

**METAL CHALCOGENIDES AND PHOSPHIDES BASED
ELECTRODE MATERIALS: AN EFFICIENT CATALYST
FOR ENERGY CONVERSION AND STORAGE
APPLICATIONS**

By

JIBAN KRUSHNA DAS

CHEM11201604004

**National Institute of Science Education and Research
Jatni, Odisha-752050**

A thesis submitted to the

Board of Studies in Chemical Sciences

*In partial fulfillment of requirements
for the Degree of*

DOCTOR OF PHILOSOPHY

of

HOMI BHABHA NATIONAL INSTITUTE





November, 2021

Homi Bhabha National Institute¹

Recommendations of the Viva Voce Committee

As members of the Viva Voce Committee, we certify that we have read the dissertation prepared by JIBAN KRUSHNA DAS entitled “Metal Chalcogenides and Phosphides Based Electrode Materials: An Efficient Catalyst for Energy Conversion and Storage Applications” and recommend that it may be accepted as fulfilling the thesis requirement for the award of Degree of Doctor of Philosophy.

Chairman – Prof. A. Srinivasan		Date: 19.11.2021
Guide / Convener – Dr. J. N. Behera		Date: 19.11.2021
Examiner – Prof. Satoshi Horike		Date: 19.11.2021
Member 1- Dr. C. S. Purohit		Date: 19.11.21
Member 2- Dr. Sanjib Kar		Date: 19.11.21
Member 3- Dr. Joydeep Bhattacharjee		Date: 19/11/21

Final approval and acceptance of this thesis is contingent upon the candidate's submission of the final copies of the thesis to HBNI.

I/We hereby certify that I/we have read this thesis prepared under my/our direction and recommend that it may be accepted as fulfilling the thesis requirement.

Date: 19/11/2021

Place: NISER, Bhubaneswar


(Dr. J. N. Behera)

Guide

¹ This page is to be included only for final submission after successful completion of viva voce.

STATEMENT BY AUTHOR

This dissertation has been submitted in partial fulfillment of requirements for an advanced degree at Homi Bhabha National Institute (HBNI) and is deposited in the Library to be made available to borrowers under rules of the HBNI.

Brief quotations from this dissertation are allowable without special permission, provided that accurate acknowledgment of source is made. Requests for permission for extended quotation from or reproduction of this manuscript in whole or in part may be granted by the Competent Authority of HBNI when in his or her judgment the proposed use of the material is in the interests of scholarship. In all other instances, however, permission must be obtained from the author.

Jiban Krushna Das

Jiban Krushna Das

DECLARATION

I, hereby declare that the investigation presented in the thesis has been carried out by me. The work is original and has not been submitted earlier as a whole or in part for a degree / diploma at this or any other Institution / University.

Jiban Krushna Das
Jiban Krushna Das

List of Publications

a) Published

1. “VS₂: An efficient catalyst for electrochemical hydrogen evolution reaction in the acid medium”, **Jiban K. Das**, Aneeya K. Samantara, Arpan K. Nayak, Debabrata Pradhan, and J. N. Behera, *Dalton Trans.*, **2018**, *47*, 13792-13799.

2. “Synthesis of Ge₄Se₉ nanoplates and its reduced graphene oxide composite for electrochemical energy storage application”, **Jiban K. Das**, Aneeya K. Samantara, Sree Raj K. A, Chandra Sekhar Rout, and J. N. Behera, *Dalton Trans.*, **2019**, *48*, 15955–15961.

3. “3D NiCoP hollow spheres; efficient electrode material for hydrogen evolution reaction and supercapacitor application”, **Jiban K. Das**, Aneeya K. Samantara, S. Satyarthi, C. S. Rout, and J. N. Behera, *RSC Adv.*, **2020**, *10*, 4650-4656.

4. “Synthesis of 3D free standing crystalline NiSe_x matrix for electrochemical energy storage application”, S. M. Dinara, A. K. Samantara, **Jiban K. Das**, J. N. Behera, S. K. Nayak, D. Late, C. S. Rout, *Dalton Trans.*, **2019**, *48*, 16873–16881.

5. “Enhanced oxygen evolution reaction with a ternary hybrid of patronite-carbon nanotubes-reduced graphene oxide: A synergy between experiments and theory”, A. K. Samantara,[‡] **Jiban K. Das**,[‡] Satyajit Rath, Naresh K. Jena, Brahmananda Chakraborty, and J. N. Behera, *ACS Appl. Mater. Interfaces.*, **2021**, *13*, 35828–35836 (‡ **Equal Contribution**)

6. “MOF-derived flower-shaped CoSe₂ nanoplates as a superior bifunctional electrocatalyst for both oxygen and hydrogen evolution reactions”, Nachiketa Sahu, **Jiban K. Das**, and J. N. Behera, *Sustainable Energy Fuels*, **2021**, 5, 4992–5000

b) Communicated

1. “NiSe₂ nanoparticles encapsulated in N-doped carbon matrix derived from an one-dimensional Ni-MOF: an efficient and sustained electrocatalyst for hydrogen evolution reaction”, Nachiketa Sahu, **Jiban K. Das**, and J. N. Behera, *Inorganic chemistry (Under Review)*

c) Chapters in books

1. “Supercapacitors based on graphene and its hybrids”, A.K. Samantara, **Jiban K. Das**, J. N. Behera, Elsevier, **2021**, Paperback ISBN: 9780128219935.

Conferences attended

1. **Participated** in an international conference on Nanomaterials at Utkal University, Bhubaneswar, in Feb–2017.
2. Presented a **poster** at Inter IISER & NISER Chemistry Meet (IINCM–2017), 22–24 December 2017. “VS₂: an efficient catalyst for electrochemical hydrogen evolution reaction”.
3. National conference on recent advancement in material science (RAIIMS) 17–18th March 2018 held at VSST Burla, Sambalpur presented a **poster** entitled “VS₂: an efficient catalyst for electrochemical hydrogen evolution reaction” having **best poster presentation** achievement.
4. Presented a **poster** in ACS ON CAMPUS at NISER Bhubaneswar on July 23, 2018, presented a poster entitled “VS₂: an efficient catalyst for electrochemical hydrogen evolution reaction”.
5. **Participated** in the National bioorganic chemistry conference (NBCC) at NISER Bhubaneswar on 22–24 December 2018.
6. National conference on industrial coatings 24–25th January 2019 held at CSIR-IMMT Bhubaneswar, delivered an **Oral lecture** entitled “Synthesis of Ge₄Se₉ nanoplates and its reduced graphene oxide composite for electrochemical energy storage application”.

Jiban Krushna Das
Jiban Krushna Das

**Dedicated to
My Father**

ACKNOWLEDGEMENTS

I would like to express my gratitude to Dr. Jogendra Nath Behera, my supervisor, for continuous support, encouragement, patience exhibited, and freedom provided for free thinking. I am thankful to Prof. Sudhakar Panda, Director-NISER, for the laboratory facilities and financial support.

I thank my Doctoral committee members, Prof. A. Srinivasan and Dr. C. S. Purohit, Dr. S. Kar, Dr. Joydeep Bhattacharjee, and all other faculties in SCS. Also, I appreciate the help provided by Dr. Pratap Deheri and Dr. Tapas Kumar Ghosh for collecting Raman and TEM data. I remember our collaborators, Prof. Debabrata Pradhan (IIT-KGP), Dr. C. S. Rout (JAIN UNIVERSITY, BENGALURU), Satyajit Rath (IIT-BBSR), immense pleasure for their valuable contributions. I thank all my past lab members Dr. Jitendra Kumar, Dr. Subba Reddy Marri, Dr. Ranjay Kumar Tiwari, Niharika, Saumya, Ipsha, and Rambabu, who have worked with me in different periods for their help and support. Thank my present lab members Dr. Aneeya Kumar Samantara, Rajat, Malay, Abhisek, Nachiketa, Manisha, Nisa, Radhamadhab, Vamsi Krishna, Nikhil, Rahul, Smruti, and Deepak, for creating a healthy atmosphere in the lab and their fruitful discussions. I remember all my friends with great gratitude, especially Kanhu, Yajna, Prasant, Dipti, Sushanta, Prabhu, Rajendra, Hemanta, Ullash (U.U. Batch-2011-2013), and Srini, Bibhu, Samser, Pragati, Sajal, Somnath, Sarat, Nabin (NISER-2016-2020). Finally, above all, I thank my father (Murali), mother (Minati), my teachers, my beloved wife (Gayatri), daughter (Jagruti) and brother (Bhabashankar & Amar) for their unconditional love, care, affection, and support.

Jiban Krushna Das
Jiban Krushna Das

CONTENTS

	Page No
Thesis title	1
Recommendations of Viva-Voce Board	2
Statement by the Author	3
Declaration	4
Publication List	5
Dedications	8
Acknowledgments	9
Contents	10
Synopsis	11
List of Figures	21
List of Tables	29
List of Abbreviations	30
Chapter-1	33
Chapter-2	88
Chapter-3	142
Chapter-4	167

SYNOPSIS

The present thesis contains four chapters. Chapter 1 is the introduction part, which gives a detailed study of energy conversion and storage applications. Chapter 2 is basing upon the hydrothermal synthesis and energy conversion applications of vanadium-based metal chalcogenides and their hybridization of the reduced form of graphene oxide (RGO) and functionalized carbon nanotubes (FCNTs). Chapter 3 deals with the developments of tetra germanium nonaselenide (Ge_4Se_9) and reduced graphene oxide (RGO) hybrids for energy storage applications. Chapter 4 gives the hydrothermal synthesis of a three-dimensional nickel-cobalt phosphide hollow sphere for coupled applications such as energy conversion and storage.

Chapter-1: Introduction of Energy Conversion and Storage Applications

The current energy demands are more concerned about renewable energy sources such as hydrogen (H_2) or oxygen (O_2) to ignore greenhouse gases and create a clean and green environment through a simple electrochemical water splitting process.¹ This chapter describes the general introduction about the energy conversion process, corresponding to the half-cell reaction in the respective electrodes of a cathode (hydrogen evolution) and anode (oxygen evolution), basic concepts of working principle, reaction mechanism of overall surface reaction, different precious or non-precious materials used for the catalytic evolution, various carbon-based materials used for the mechanical support and further improvement of electrocatalytic performances of the as-prepared catalyst, the different synthetic techniques from which they can be synthesized, and standard parameters used for the energy conversion process.²⁻⁴ Likewise energy conversion process, the energy storage system towards supercapacitor plays a vital role in the recent energy sector. It opens up a new

window to fulfill future energy demands.^{5,6} Based on the energy storage applications, this chapter also describes the importance of supercapacitor compared to commercial capacitor and battery.⁷ Particularly, the working principle, types of charge storage mechanism, electrode materials used to improve the supercapacitor performance, and different electrochemical measurements and their calculations for storage capacitance were also discussed.

Chapter-2: Energy Conversion based on Pristine Vanadium Chalcogenides and their Reduced Graphene Oxide (RGO) and Functionalization Carbon Nanotubes (FCNTs) Hybrids

This chapter deals with the hydrothermal synthesis of vanadium-based metal chalcogenides and their composites of reduced graphene oxide (RGO) and functionalization of carbon nanotubes (FCNTs) like pristine VS_2 , RGO/ VS_4 , FCNTs/ VS_4 , and RGO/FCNTs/ VS_4 hybrids electrode materials respectively. After successfully synthesizing and proper step-wise characterization analysis, the electrochemical performances towards hydrogen and oxygen evolution were studied in a two-compartment of three-electrode measurements setup. Hydrogen evolution reactions of pristine VS_2 and the composites of VS_4 /rGO have been carried out in a 0.1 M H_2SO_4 electrolytic medium. The presence of large catalytic active sites and rough surface area of the two-dimensional hexagonal crystal system of VS_2 might show enhanced HER activity compared to the linear 1D monoclinic crystal system of VS_4 /rGO composites. The pristine VS_2 shows good hydrogen evolution activity in the points of lower onset value (15 mV vs. RHE), small Tafel value (36 mV dec^{-1}), and the overpotential of 41 mV required to reach the predefined current density of 10 mA/cm², as shown in Figure 1.⁸ Pristine VS_2 is metallic but shows poor oxygen

evolution reaction because of the absence of any mechanical and electrochemical supporting template like reduced graphene oxide (RGO) or functionalized carbon nanotubes. The synergistic effects of RGO and FCNTs demonstrate the VS_2 is converted to VS_4 in a simple hydrothermal technique, corresponding to form a ternary hybrid of RGO/FCNTs/ VS_4 .⁹ The enhanced OER activity is noticed in the supporting electrolyte of 1 M KOH. Figure 2 displays the RGO/FCNTs/ VS_4 hybrids show better oxygen evolution performances with 330 mV overpotential needed to deliver 10 mA cm^{-2} current density. Besides, with an appreciable Tafel value and the 15 hours of constant electrolysis in an alkaline solution compared to various as-prepared catalysts. Furthermore, the electrochemical measurements are supported by calculating the higher ECSA (electrochemical active surface area) and roughness factor (R_f) value of RGO/FCNTs/ VS_4 hybrids. The constancy and efficacy of the electrode material of bare VS_2 and RGO/FCNTs/ VS_4 hybrids have been tested by the post-HER and OER analysis, respectively. The above studies demonstrated that the vanadium-based chalcogenides and its hybrids have been illustrated as the suitable electrode material for the water splitting process and open a new window in the field of ternary hybrids.

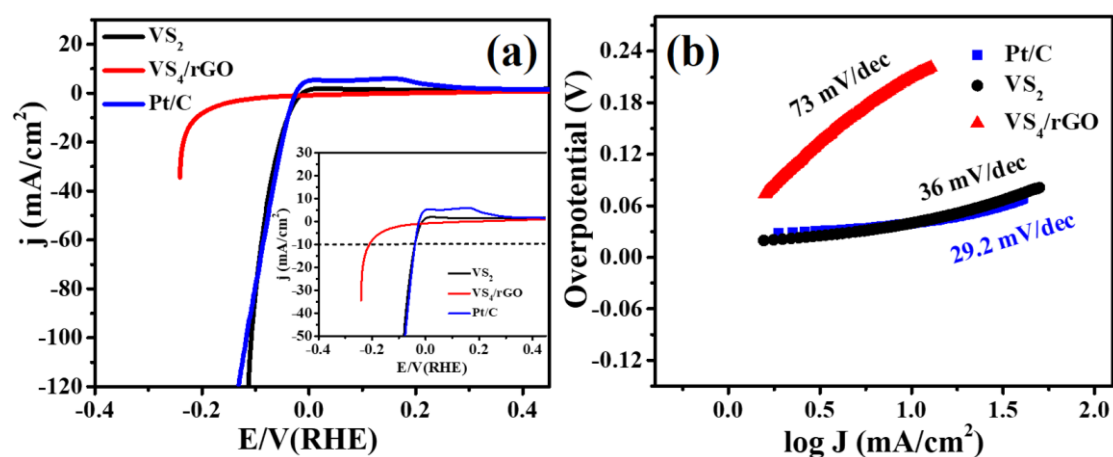


Figure 1 (a) Polarization curve or linear sweep voltammetry (LSVs) curve for pristine VS₂, VS₄/rGO hybrids and precious metal of Pt/C modified electrode (GCE) in the acidic medium at a potential of 5 mV/s and (b) is the Tafel plots.

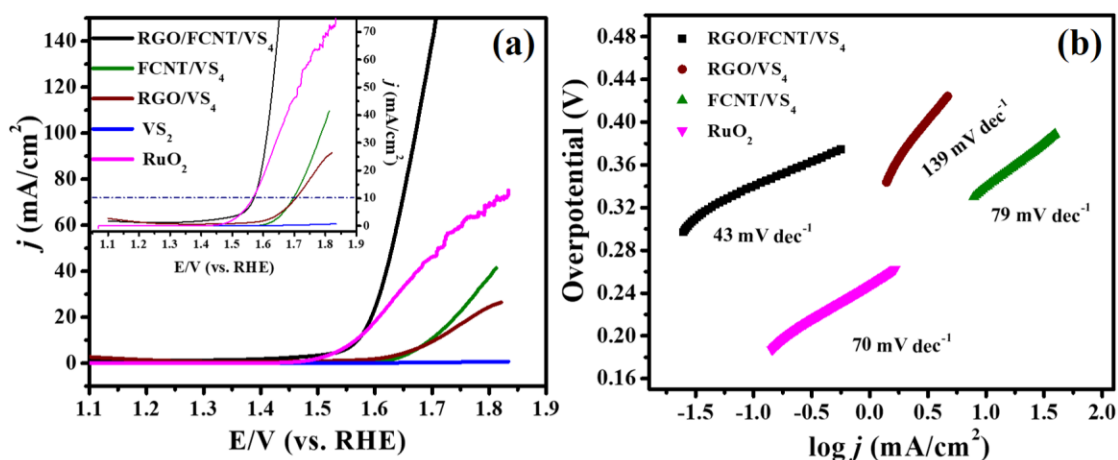


Figure 2 (a) Polarization curve for OER by the catalyst-ink modified samples of VS₂, RGO/VS₄, FCNT/VS₄, RuO₂, and RGO/FCNT/VS₄ in 1 M KOH at an applied potential of 5 mV/s and (b) is the fitting parameter termed as Tafel plots.

Chapter-3: Supercapacitor based on Germanium Selenide (Ge₄Se₉) and RGO Hybrids

This chapter describes a facial hydrothermal synthesis of tetra germanium nonaselenide (Ge₄Se₉) and their hybrids of different weight percentages (%) of the reduced form of graphene oxide (RGO). Moreover, the electrochemical measurements towards supercapacitor applications of Ge₄Se₉/RGO composite are explored. Tetra germanium nonaselenide (Ge₄Se₉) is a two-dimensional layered structure corresponding to the orthorhombic crystal system. The crystal arrangement of Ge₄Se₉ is similar to the monoclinic binary germanium selenide (GeSe₂). The tetrahedral (T_d) GeSe₄ unit is a common structural fragment in both the monoclinic and orthorhombic crystal systems of GeSe₂ and Ge₄Se₉. In the case of GeSe₂, the tetrahedral unit of

GeSe₄ is connected in both the corner and edge-sharing centers. But in Ge₄Se₉ unit, GeSe₄ sharing an additional Se-Se dimer in the corner. However, the orthorhombic crystal system of Ge₄Se₉ can be easily differentiated from the binary monoclinic GeSe₂, with an extra corner-shared Se-Se pair that is linked with tetrahedral GeSe₄ units throughout the structures. The crystal structure with a different atomic arrangement have reproduced and redrawn from Fjellvåg et al. in Figure 3.¹⁰

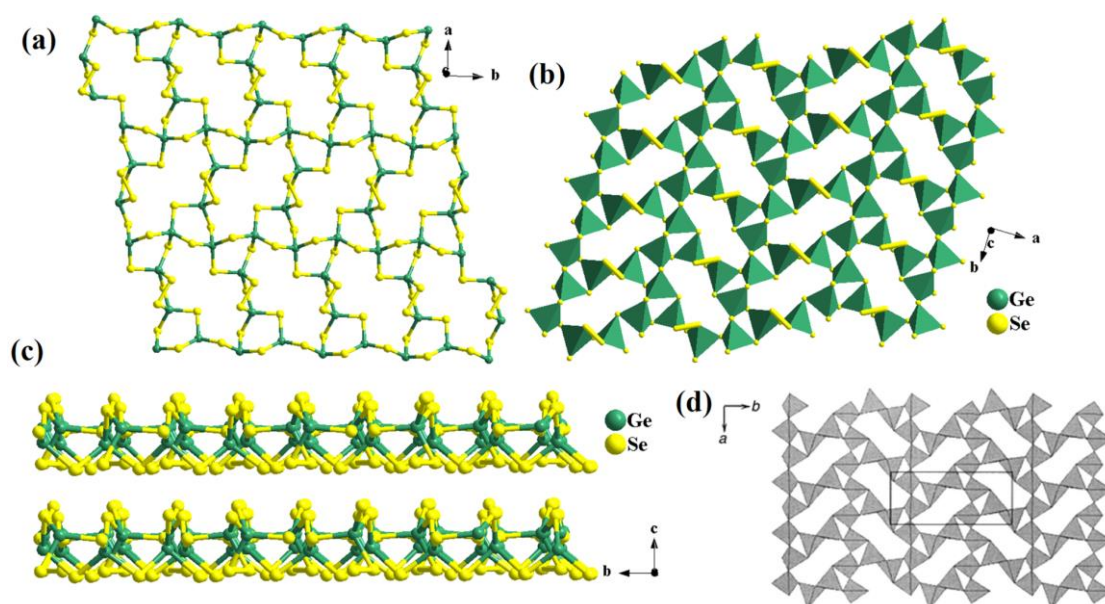


Figure 3 (a) 2D layers structure having the ball and stick model, (b) polyhedral crystal arrangement, (c) stacking 2D picture of Ge₄Se₉ layers, and (d) polyhedral design of monoclinic GeSe₂.

Herein, the electrochemical studies of Ge₄Se₉ with reduced graphene oxide composites have been tested. Pristine germanium selenide (Ge₄Se₉) and their graphene oxide of different weight percentages (%) hybrids such as 0.30 wt% and 0.60 wt% have been synthesized hydrothermally. The graphene oxide having 0.30 wt% of Ge₄Se₉ hybrid termed as Ge₄Se₉/RG1 shows acceptable energy storage performances than pristine and other as-prepared hybrids (Ge₄Se₉/RG2). The charge storage performances of

Ge₄Se₉/RG1 show a better specific capacitance value of 220 F g⁻¹ at 2 A/g, the energy density of 12 Wh/kg, and power density of 4.6 kW/kg, respectively.¹¹ Moreover, the hybrids show 91% of retention capacitance after the cyclic stability of repeated 10000 charge-discharge cycles. Furthermore, a post-stability study depicts the robustness and efficiency of the composites. We believe that the hydrothermal synthesis of a new kind of tetra germanium nonaselenide (Ge₄Se₉) electrode material and its various weight percentage of GO hybrids having better supercapacitor performances could bring a new avenue in the field of main group metal chalcogenides to fulfill the future energy demands.

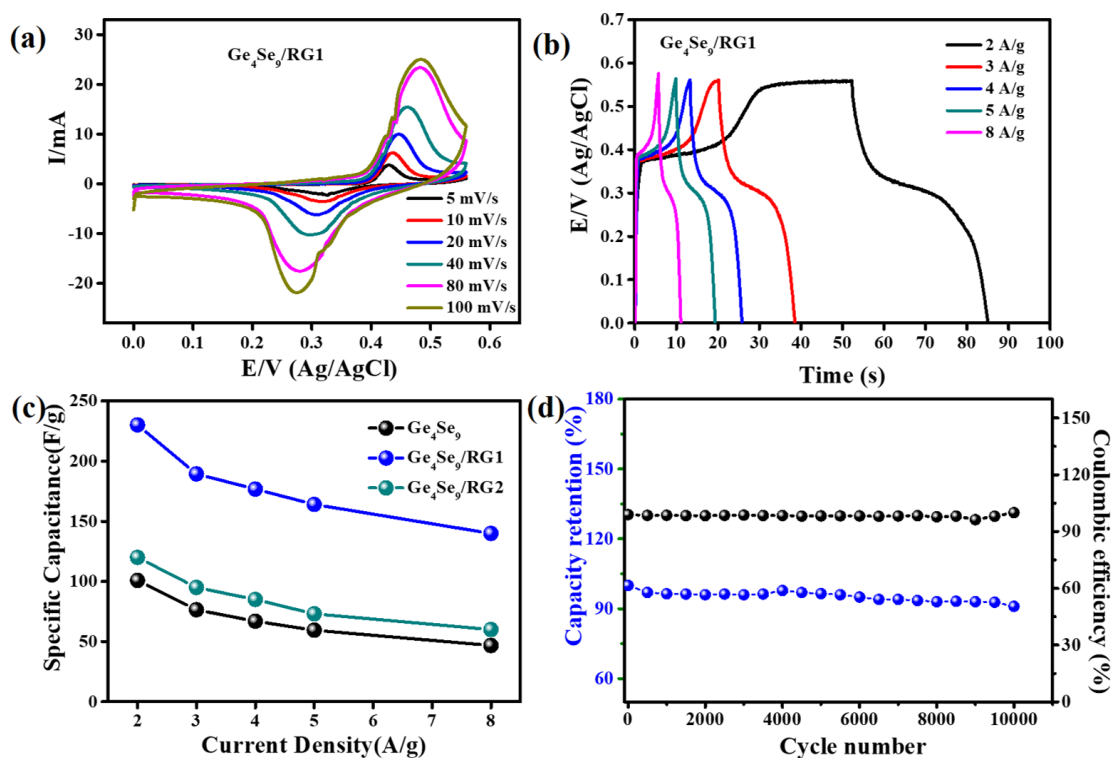


Figure 4 (a, b) Graph of cyclic voltammetry (CV) and galvanostatic charge-discharge (GCD) curve for Ge₄Se₉/RG1, (c) graph of specific capacitance vs. various current densities, (d) long cyclic number for stability test with coulombic efficiency for the Ge₄Se₉/RG1 hybrids.

Chapter-4: 3D NiCoP Hollow Spheres: Efficient Electrode Material for Hydrogen Evolution Reaction and Supercapacitor Application

This chapter gives a detailed study on the synthesis of 3D hollow sphere-like morphology of nickel cobalt phosphide (NiCoP) and its electrochemical analysis towards hydrogen evolution reaction and the charges storage performances corresponding to supercapacitor applications. The complete and step-wise characterization technique displays the high crystalline nature and 3D hollow sphere-like morphology of bimetallic NiCoP. For hydrogen evolution reaction, all the electrochemical studies have been carried out in an acidic medium of 0.5 M H₂SO₄, as shown in Figure 5. Electrolysis of water to the evolution of hydrogen offers better performances, and an acceptable overpotential of 160 mV needs to give 10 mA/cm² current density, a Tafel value of 70 mV/dec, respectively. Furthermore, the impedance spectrum used to verify the faster charge transfer process and the stability test of the 3D hollow sphere NiCoP catalyst observed by the chronopotentiometry technique show a deviation of 15 mV overpotential even after 18 hours of constant electrolysis process have been noticed in Figure 6.

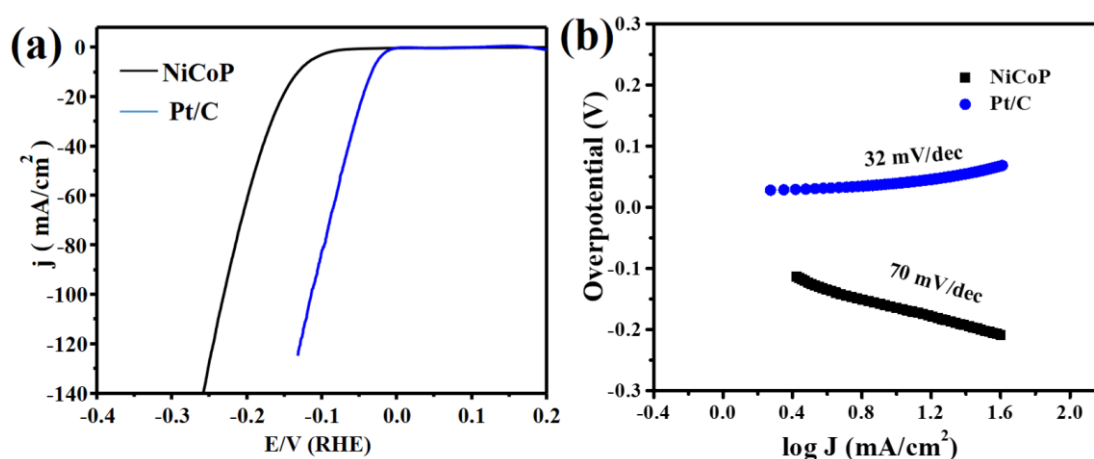


Figure 5 (a) Polarization curve and (b) Tafel plot for NiCoP and precious Pt/C.

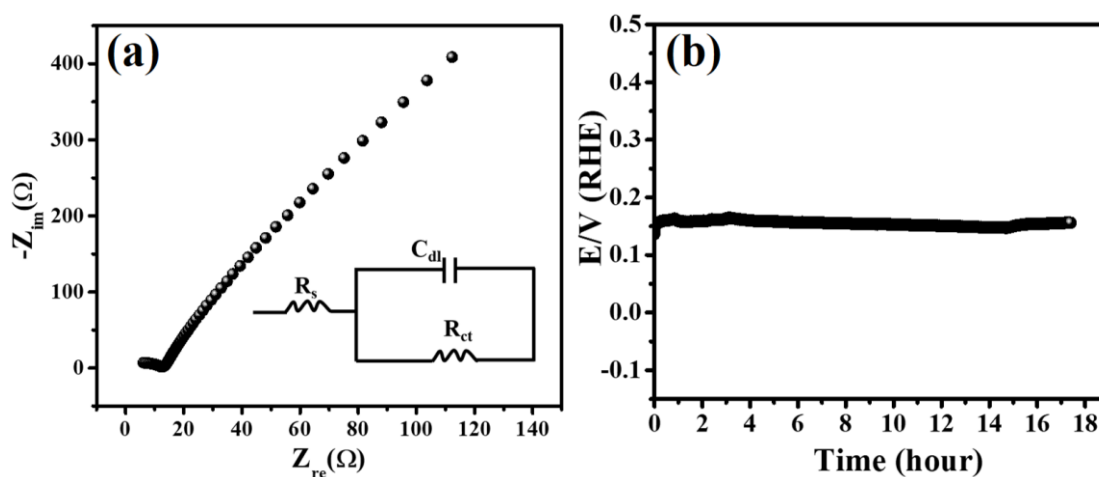


Figure 6 (a) Impedance diagram and (b) long cyclic test. Inset of (a) represents Randles circuit diagram.

Likewise, in hydrogen evolution reaction, the bimetallic NiCoP shows excellent supercapacitor performances in an electrolyte of 5 M KOH and shown in Figure 7. The obtained specific capacitance of 960 F g^{-1} at 1 mV/s , the energy density of 33.3 Wh/kg , and power density of 11.8 kW/kg signifying the charge storage and supply efficacy of the as-prepared NiCoP.¹² A graph of energy density vs. power density known as Ragone plot for NiCoP and 95% of its initial retention capacitance after continuous repeated 10000 charge-discharge cycles demonstrated the robustness of the bimetallic phosphide material as illustrated in Figure 8. The post stability measurements also verified the efficiency and constancy performances of the bimetallic NiCoP electrode material. Both hydrogen evolution and supercapacitor performances of the 3D sphere-like morphology of NiCoP implying as the front line bimetallic phosphide electrode material compared to other reported phosphide materials.

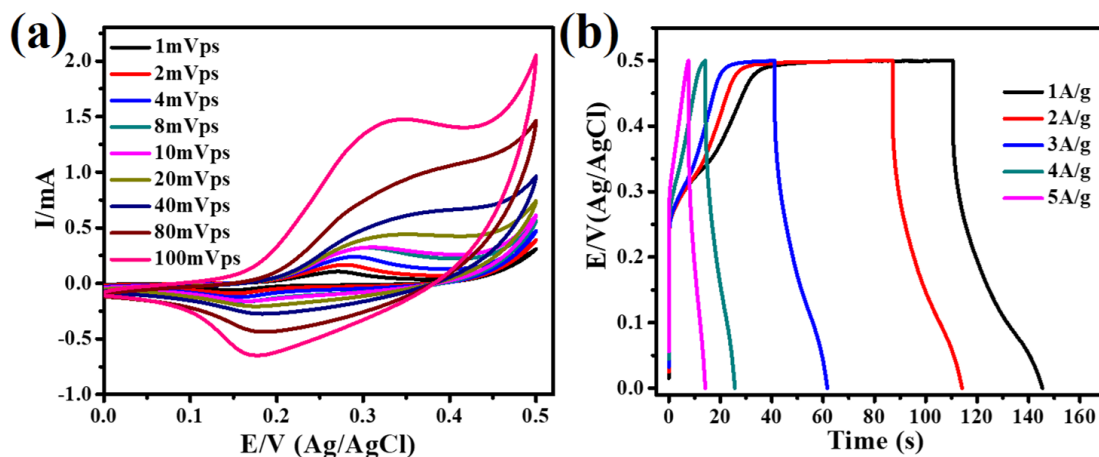


Figure 7 (a) Graph of cyclic voltammety at different scan values, (b) charge-discharge process at various current densities.

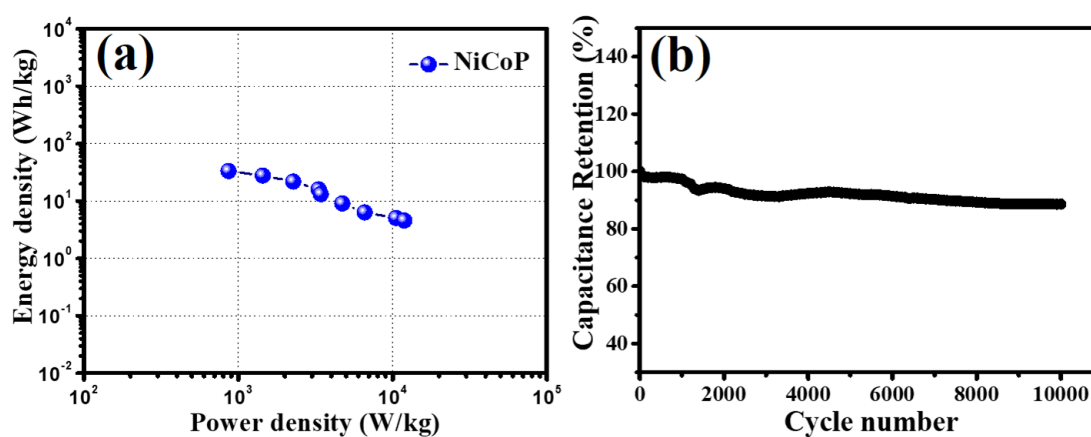


Figure 8 (a) Energy density vs. power density, corresponding Ragone plot, and (b) cyclic number for the stability test of NiCoP.

References

- 1 X. Zou and Y. Zhang, *Chem. Soc. Rev.*, 2015, **44**, 5148–5180.
- 2 S. Anantharaj, S. R. Ede, K. Sakthikumar, K. Karthick, S. Mishra and S. Kundu, *ACS Catal.*, 2016, **6**, 8069–8097.
- 3 N. T. Suen, S. F. Hung, Q. Quan, N. Zhang, Y. J. Xu and H. M. Chen, *Chem. Soc. Rev.*, 2017, **46**, 337–365.

- 4 Y. Yan, T. He, B. Zhao, K. Qi, H. Liu and B. Y. Xia, *J. Mater. Chem. A*, 2018, **6**, 15905–15926.
- 5 G. Wang, L. Zhang and J. Zhang, *Chem. Soc. Rev.*, 2012, **41**, 797–828.
- 6 S. Ratha, S. R. Marri, N. A. Lanzillo, S. Moshkalev, S. K. Nayak, J. N. Behera and C. S. Rout, *J. Mater. Chem. A*, 2015, **3**, 18874–18881.
- 7 M. Winter and R. J. Brodd, *Chem. Rev.*, 2004, **104**, 4245–4269.
- 8 J. K. Das, A. K. Samantara, A. K. Nayak, D. Pradhan and J. N. Behera, *Dalton Trans.*, 2018, **47**, 13792–13799.
- 9 S. Ratha, S. R. Marri, J. N. Behera and C. S. Rout, *Eur. J. Inorg. Chem.*, 2016, **2016**, 259–265.
- 10 H. Fjellvåg, K. O. Kongshaug and S. Stølen, *J. Chem. Soc. Dalton Trans.*, 2001, 1043–1045.
- 11 J. K. Das, A. K. Samantara, S. R. K. A., C. S. Rout and J. N. Behera, *Dalton Trans.*, 2019, **48**, 15955–15961.
- 12 J. K. Das, A. K. Samantara, S. Satyarthi, C. S. Rout and J. N. Behera, *RSC Adv.*, 2020, **10**, 4650–4656.

List of Schemes

Page No

- | | | | |
|----|------------|---|-----|
| 1. | Scheme 1.1 | Schematic diagram of surface oxidized NiCoP during electrochemical measurements towards SCs in 5 M KOH. | 186 |
|----|------------|---|-----|

List of Figures

- | | | | |
|----|------------|--|----|
| 1. | Figure 1.1 | Worldwide transition from fossil fuel to renewable fuel is required. | 35 |
| 2. | Figure 1.2 | Schematic presentation of the two-electrode system in electrolysis process. | 37 |
| 3. | Figure 1.3 | Schematic presentation of polarization curve in electrolysis process. | 38 |
| 4. | Figure 1.4 | A three-electrode measurement setup of an electrochemical cell. | 39 |
| 5. | Figure 1.5 | Reaction mechanism path followed by HER in acidic electrolytes. | 41 |
| 6. | Figure 1.6 | A step-wise reaction mechanism for OER displays in the acidic process in blue line and alkaline in red line conditions. This overall reaction mechanism follows the formation of reaction intermediates of peroxide (M–OOH) and oxo (M–O) intermediate to generate molecular oxygen. | 43 |
| 7. | Figure 1.7 | Schematic presentation of linear fitted Tafel region. | 46 |
| 8. | Figure 1.8 | Impedance spectrum for pristine and Fe/P dual doping CoS ₂ polycrystalline nanowire for HER. | 48 |
| 9. | Figure 1.9 | Schematic diagram of CV showing the ideal non-faradic from which C_{dl} value to be calculated (a), CV of the non-faradic | 50 |

	portion at various scan rates (b), and Figure (c) shows the fitting parameter of cathodic and anodic points determined the slope.	
10.	Figure 1.10 The cyclic stability of VS ₂ for HER in 0.1 M H ₂ SO ₄ electrolytic solution at a higher applied current density of 30 mA/cm ² .	53
11.	Figure 1.11 Elements used for the preparation of HER-based electrocatalyst in the periodic table.	54
12.	Figure 1.12 Volcano plot (activity vs. calculated Gibb's free energy) used for HER electrocatalyst.	55
13.	Figure 1.13 Metal chalcogenides have a layered structure, and every single nanocrystal contains multilayers with weak van der Waals force attraction stacked along the <i>c</i> -axis.	60
14.	Figure 1.14 Ragone plot showing the representative of different energy storage devices.	65
15.	Figure 1.15 Schematic diagram of a supercapacitor cell.	66
16.	Figure 1.16 Cyclic voltammetry of VSe ₂ /RGO (0.3 wt%) curves at various scan rates.	71
17.	Figure 1.17 Charge discharge curve of VSe ₂ /RGO (0.3 wt%) at different current densities.	72
18.	Figure 1.18 EIS of VSe ₂ /RGO (0.3 wt%) and other as-synthesized material.	73
19.	Figure 1.19 Long-term cyclic number of VSe ₂ /RGO (0.3 wt%) hybrids.	74
20.	Figure 1.20 Helmholtz model for the electrical double-layers.	75
21.	Figure 1.21 Representation of charge accumulation process in EDL type capacitor.	76
22.	Figure 1.22 Schematic of hybrid capacitor in 1 M H ₂ SO ₄ electrolyte.	77

23.	Figure 2.1	FTIR for graphene oxide and VS ₄ /rGO composite.	101
24.	Figure 2.2	PXRD study for bare VS ₂ and rGO composite of VS ₄	101
25.	Figure 2.3	XPS for the V 2p and S 2p orbitals of bare VS ₂ .	103
26.	Figure 2.4	XPS scan for V 2p, S 2p, O 1s, and C 1s of VS ₄ /rGO	103
27.	Figure 2.5	(a), (b) Different magnification ranges of field emission scanning electron microscopic picture of VS ₂ .	104
28.	Figure 2.6	(a-c) Elemental mapping images of Pristine VS ₂ .	104
29.	Figure 2.7	(a) Low and higher (b) magnifications study of FESEM picture for VS ₄ /rGO composites.	105
30.	Figure 2.8	Thermogravimetric analysis for VS ₂ and VS ₄ /rGO.	106
31.	Figure 2.9	Nyquist impedance spectrum for the VS ₂ (a) and (b) VS ₄ /rGO composites.	107
32.	Figure 2.10	(a),(b) Polarization curve and Tafel plot for VS ₂ , VS ₄ /rGO composites, along with commercial Pt/C moderate GCE in 0.1 M H ₂ SO ₄ .	108
33.	Figure 2.11	Linear sweep voltammograms for bare VS ₂ , VS ₄ /rGO and precious Pt/C before and after <i>iR</i> compensation in 0.1 M H ₂ SO ₄ electrolyte.	109
34.	Figure 2.12	(a, b) are the cyclic voltammograms in 0.1 M H ₂ SO ₄ at individual scan rates (10 to 400 mV s ⁻¹), and (c, d) is the profile of scan rate vs. cathodic and anodic current at -0.05 V for VS ₂ and VS ₄ /rGO.	110
35.	Figure 2.13	Durability test of VS ₂ and VS ₄ /rGO modified electrode surface for HER in 0.1 M H ₂ SO ₄ electrolytic solution.	111

36.	Figure 2.14	Electrolysis experiments of VS ₂ modified electrode at a larger current density of 30 mA/cm ² in the acidic electrolyte medium.	112
37.	Figure 2.15	(a),(b) FESEM images for the VS ₂ after the chronopotentiometry measurement at 10 mA/cm ² .	113
38.	Figure 2.16	High resolution XPS spectrum of V 2p and S 2p for VS ₂ after chronopotentiometry measurement at 10 mA/cm ² .	113
39.	Figure 2.17	(a, b) High and low magnification of captured SEM images.	115
40.	Figure 2.18	Transmission electron microscopic pictures (a, b) of RGO/FCNT/VS ₄ composite at a distinct magnification range. (c) HRTEM analysis and the SAED pattern are carried out and inset in figure (a).	116
41.	Figure 2.19	EDS spectrum of the RGO/FCNT/VS ₄ hybrid showing V, S, C, and O at different atomic and weight percentages.	116
42.	Figure 2.20	EDS mapping of RGO/FCNT/VS ₄ hybrid showing V, S, C, and O elements.	117
43.	Figure 2.21	(a) Powder X-ray diffraction of RGO/FCNT/VS ₄ .	118
44.	Figure 2.22	FESEM and TEM images of VS ₂ , RGO/VS ₄ , and FCNT/VS ₄ .	118
45.	Figure 2.23	Powder pattern for (a) pristine VS ₂ , (b) RGO/VS ₄ , and (c) FCNT/VS ₄ .	119
46.	Figure 2.24	(a) Raman spectra of RGO/FCNT/VS ₄ composite before and after OER and (b) Raman study of RGO/FCNT/VS ₄ , RGO/VS ₄ , RGO, and GO showing the D- and G-bands.	120
47.	Figure 2.25	(a), (b) High resolution XPS study of V 2p, S 2p, and (c), (d) C 1s, O 1s of RGO/FCNT/VS ₄ hybrid.	122

48.	Figure 2.26	Thermogravimetric analysis of the RGO/FCNT/VS ₄ hybrids.	122
49.	Figure 2.27	(a) LSVs curve for OER by glassy carbon electrode modified with VS ₂ , RGO/VS ₄ , FCNT/VS ₄ , RuO ₂ , and RGO/FCNT/VS ₄ in 1 M KOH electrolytic solution at a sweep rate of 5 mV/s, having a mass loading of 0.25 mg/cm ² and (b) Tafel plots (overpotential vs.log of current density).	123
50.	Figure 2.28	Linear sweep voltammograms of RGO/FCNT/VS ₄ , FCNT/VS ₄ , RGO/VS ₄ , and RuO ₂ for OER before along with after <i>iR</i> correction. All the LSVs data are measured at a sweep rate of 5 mV/s with an applied electrode rotation speed of 1600 rpm.	124
51.	Figure 2.29	(a) The complete cyclic voltammogram of RGO/FCNT/VS ₄ for oxygen evolution reaction and (b) cyclic voltammogram before and after <i>iR</i> correction.	125
52.	Figure 2.30	(a) Nyquist plots for RGO/FCNT/VS ₄ , FCNT/VS ₄ , and RGO/VS ₄ , (b) OER stability test for RGO/FCNT/VS ₄ . The inset in (b) is the photograph of the electrode taken before and during the electrolysis.	126
53.	Figure 2.31	(a, b) Cyclic voltammograms and the fitting parameter plot are used to observe the non-faradic parameters such as <i>C_{dl}</i> , ECSA, and <i>R_f</i> value at 0.14 V vs. sweep rate for RGO/FCNT/VS ₄ hybrid.	127
54.	Figure 2.32	The cyclic voltammograms for (a) FCNT/VS ₄ , (c) RGO/VS ₄ ,	128

	at various sweep rates, and (b, d) displays the graph of current at 0.14 V vs. different sweep rate to calculated the value of double-layer capacitance (C_{dl}), electrochemical accessible surface area (ECSA), and roughness factor (R_f) of active catalysts.	
55.	Figure 2.33 (a) Powder X-ray diffraction spectrum, and (b) FESEM image of RGO/FCNT/VS ₄ hybrid after the chronopotentiometry (CP) stability test.	129
56.	Figure 2.34 In-situ X-ray photoelectron study of (a) V 2p, (b) S 2p, (c) C 1s, and (d) O 1s of RGO/FCNT/VS ₄ hybrid after OER stability measurement.	130
57.	Figure 2.35 HRTEM analysis of RGO/FCNT/VS ₄ hybrid after OER stability measurement.	131
58.	Figure 2.36 Linear sweep voltammogram of commercial V ₂ (SO ₄) ₃ , and V ₂ O ₅ in alkaline solution at 5 mV/s.	132
59.	Figure 3.1 Layered 2D structure (a) ball and stick model, (b) polyhedral crystal structure, (c) stacking arrangements of a 2D layer of bare Ge ₄ Se ₉ , and (d) monoclinic polyhedral structure of GeSe ₂ . The crystal structure was reproduced and redrawn from Fjellvåg et al.	146
60.	Figure 3.2 (a) FESEM images of pristine Ge ₄ Se ₉ and (b, c) different magnification picture of Ge ₄ Se ₉ /RG1 composite.	151
61.	Figure 3.3 Elemental mapping for Ge ₄ Se ₉ /RG1 hybrid.	152
62.	Figure 3.4 EDAX spectrum for Ge ₄ Se ₉ /RG1 composite. And	152

	the table showing the weight percentage and atomic percentage of C, Ge, and Se in the Ge ₄ Se ₉ /RG1 composite.	
63.	Figure 3.5 TEM analysis at different magnifications (a, b) and (c) High-resolution images of Ge ₄ Se ₉ /RG1 composite.	154
64.	Figure 3.6 (a) Powder diffraction pattern for Ge ₄ Se ₉ , Ge ₄ Se ₉ /RG1, and Fourier transform infrared spectrum for graphene oxide and Ge ₄ Se ₉ /RG1 composite.	154
65.	Figure 3.7 (a) Raman study for pristine Ge ₄ Se ₉ and Ge ₄ Se ₉ /RG1 hybrids and (b) shows for <i>I_D</i> and <i>I_G</i> bands of graphene in GO, RGO, and Ge ₄ Se ₉ /RG1 hybrids.	155
67.	Figure 3.8 Scans of X-ray photoelectron spectra for Ge 3d, Se 3d, C 1s, and O 1s of graphene hybrid Ge ₄ Se ₉ .	156
68.	Figure 3.9 TGA results for bare Ge ₄ Se ₉ , Ge ₄ Se ₉ /RG1, and Ge ₄ Se ₉ /RG2 hybrids.	157
69.	Figure 3.10 (a, b) Graph of cyclic voltammetry (CV) and Galvanostatic charge-discharge (GCD) for Ge ₄ Se ₉ /RG1, (c) graph of specific capacitance vs. various current densities, (d) long cyclic number for stability test with columbic efficiency for the Ge ₄ Se ₉ /RG1 hybrids.	158
70.	Figure 3.11 (a) Cyclic voltammetry with Galvanostatic charge-discharge curve for bare Ge ₄ Se ₉ and Ge ₄ Se ₉ /RG2 hybrids.	159
71.	Figure 3.12 (a) Post stability analysis of Ge ₄ Se ₉ /RG1 hybrids having the electrochemical study and characterization of impedance diagram before and after stability, (b) SEM image. The inset	160

		in (a) corresponded to the circuit diagram.	
72.	Figure 3.13	(a) PXRD and (b) Raman study for after electrolysis measurements.	160
73.	Figure 4.1	X-ray diffraction pattern for NiCoP hollow sphere.	175
74.	Figure 4.2	(a, b) Low and high magnification of field emission scanning electron microscope images.	175
75.	Figure 4.3	(a-d) TEM pictures for the NiCoP at different magnifications.	176
76.	Figure 4.4	Elemental dispersive X-ray spectrometry mapping of NiCoP microspheres.	177
77.	Figure 4.5	(a) Polarization curve (LSVs), along with Tafel plot (b) for both NiCoP and precious Pt/C.	178
78.	Figure 4.6	(a) Impedance diagram and (b) long cyclic test. The inset of (a) an equivalent circuit diagram.	179
79.	Figure 4.7	(a) Linear sweep voltammograms of NiCoP microsphere, (b) commercial Pt/C before with after iR compensation.	179
80.	Figure 4.8	(a),(b) Powder pattern and FESEM pictures of NiCoP after constant stability test for 18 hours in an acidic solution at 10 mA/cm^2 .	180
81.	Figure 4.9	(a) CV cycles at different sweep rate, (b) CD plots at various applied current densities.	183
82.	Figure 4.10	(a) Profile of Ragone plot for NiCoP and (b) durability test in 5 M KOH.	184
83.	Figure 4.11	(a) X-ray diffraction pattern (b) FESEM study, with (c) HRTEM Image of NiCoP after stability test in 5 M KOH.	185

List of Tables

1.	Table 2.1	A brief literature survey on transition metal sulfide catalysts for HER.	113
2.	Table 2.2	Balancing table of electrocatalytic performance of some recently developed materials towards oxygen evolution reaction.	133
3.	Table 3.1	Supercapacitor performance Comparison of Ge ₄ Se ₉ /RG2, Ge ₄ Se ₉ /RG1, bare Ge ₄ Se ₉ , and other reported metal selenides and oxide.	161
4.	Table 4.1	Comparison table for HER performance of different electro-catalysts.	180
5.	Table 4.2	Energy storage performance of NiCoP along with various transition metal phosphides.	186

List of Abbreviations

FCNTs	Functionalized carbon nanotubes
RGO	Reduced graphene oxide
1D	One dimensional
HER	Hydrogen evolution reaction
OER	Oxygen evolution reaction
LSVs	Linear sweep voltammetry
R_f	Roughness factor
R_s	Solution resistance
R_{ct}	Charge transfer resistance
C_{dl}	Double-layer capacitance
CPE	Constant phase elements
ECSA	Electrochemical active surface area
CP	Chronopotentiometry
TOF	Turn over frequency
FE	Faradaic efficiency
T_d	Tetrahedral
GO	Graphene oxide
RG	Reduced graphene
WE	Working electrode
GCE	Glassy carbon electrode
SCE	Saturated calomel electrode
NMP	N-Methyl-2-pyrrolidone
CE	Counter electrode

RE	Reference electrode
RHE	Reversible hydrogen electrode
NHE	Normal hydrogen electrode
TGA	Thermogravimetric analysis
PXRD	Powder X-ray diffraction
FTIR	Fourier transform infrared
FESEM	Field emission scanning electron microscope
TEM	Transmission electron microscope
HRTEM	High resolution transmission electron microscopy
EDAX	Energy dispersive analysis of X-rays
3D	Three-dimensional
2D	Two-dimensional
SC	Supercapacitor
C_{sp}	Specific capacitance
PD	Power density
ED	Energy density
PPC	Propylene carbonate
ILs	Ionic liquids
CNTs	Carbon nanotubes
TMOs	Transition metal oxides
CPs	Conducting polymers
PANI	Polyaniline
PPY	Polypyrrole
CV	Cyclic voltammetry

CCCD	Constant current charge/discharge
EIS	Electrochemical impedance spectroscopy
EDLC	Electrical double-layer capacitance
PC	Pseudocapacitance
PCS	Pseudocapacitance supercapacitor
HS	Hybrid supercapacitors
MCs	Metal chalcogenides
TMDCs	Transition metal dichalcogenides
TMPs	Transition metal-based phosphides
CVD	Chemical vapour deposition
SWCNTs	Single walled carbon nanotubes
MWCNTs	Multi walled carbon nanotubes
DI	De-ionized
GCRDE	Glassy carbon rotating disk electrode
ICP-OES	Inductively coupled plasma optical- emission spectrometry
XPS	X-ray photoelectron spectroscopy

CHAPTER – 1

Energy Conversion through Water Splitting and the Supercapacitor:

A Brief Overview

- 1.1 Introduction
- 1.2 Electrolysis
 - 1.2.1 Types of electrolysis
- 1.3 Electrochemical cell
- 1.4 Mechanism of electrolysis process
 - 1.4.1 Mechanism involved in hydrogen evolution reaction
 - 1.4.2 Mechanism involved in oxygen evolution reaction
- 1.5 Common parameters for catalytic evolution process
 - 1.5.1 Overpotential
 - 1.5.2 Tafel slope
 - 1.5.3 Electrochemical impedance spectroscopy
 - 1.5.4 Electrochemical active surface area
 - 1.5.5 Mass activity
 - 1.5.6 Turn over frequency
 - 1.5.7 Faradic efficiency
 - 1.5.8 Cyclic stability
- 1.6 Types of electrode materials used
 - 1.6.1 Noble metal based catalysts
 - 1.6.2 Carbon based materials
 - 1.6.3 Transition metal oxides
 - 1.6.4 Metal chalcogenides

1.1 Introduction

A growing economy always has a high energy demand. Till now, the consumption of traditional fossil fuels is feeding 80% of global energy demand. However, serious environmental issues and the rising level of global warming are caused by hydrocarbon combustion sources.¹ The low operating cost and ease of access, renewable sources of energy show growth in demand in this present time.² Atomic reactors have a history of catastrophic disasters. Solar and wind energy, at this stage, are not capable of providing high power in a continuous manner irrespective of the time of the day or weather conditions. In the recent decade, hydrogen portrays as an efficient and green source of energy. But the evolution of hydrogen gas still depends upon the steam reform of fossil fuels, which not only uses exhaustible energy resources but also produces CO₂ as a byproduct.³⁻⁵

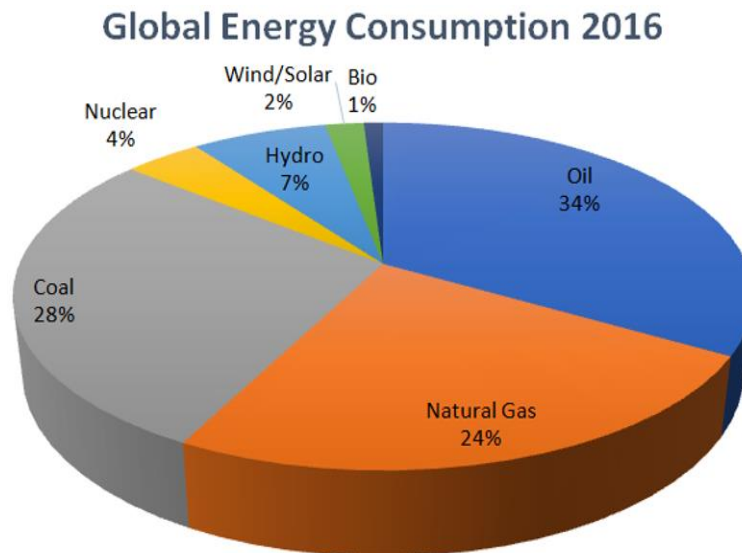


Figure 1.1 Worldwide transition from fossil fuel to renewable fuel is required.¹

Hydrogen, produced through a simple electrolytic splitting of water, is a cheap, safe, and clean, renewable fuel. The best feature of this process is water is both fuel and a

by-product. Along with this advantage, the highest gravimetric energy density of hydrogen (~120 kilo-joule per gram) makes electrolytically produced hydrogen a preferable candidate for the source of green energy.⁶ The electrolytic cell is divided into two halves. The half-cell is containing the positive electrode or the anode for OER (oxygen evolution reaction) process. And the negatively charged electrode or the cathode is responsible for HER (hydrogen evolution reaction). Theoretically, the potential of 1.23 V is necessitated for the electrolysis of water molecules. But in practical application, due to various internal and external factors, a higher cell voltage is required, leading to an overall decrease in efficiency.⁷ Though some noble metals like platinum, iridium, and rhodium have shown excellent electrocatalytic performance⁸⁻¹² as their precious metal so using them on an industrial scale would be very expensive.⁴ So, to make the production of electrocatalysts economically viable several earth-abundant transition metal-based catalysts called noble metal-free electrocatalyst (metal oxide/hydroxide, metal chalcogenides, and metal phosphides, etc.) are being explored in the past decade.¹³⁻¹⁶ As electrode materials are the key in determining the energy storage device performances, and research has been devoted to developing new electrode materials with salient structural characteristics and unique functions.

1.2 Electrolysis

Electrolysis reduces water molecules into hydrogen and oxygen by the passage of external voltage through the current collector onto the electrode in an aqueous electrolyte medium. The hydrogen evolution occurs at the catalyst coated cathode electrode surface, and oxygen evolution occurs at the anode electrode surface, comprising two half-cell reactions. In this process, hydrogen gas is stored for fuel

purposes, and oxygen is liberated into the atmosphere at the respective electrodes. The common term is used for electrolysis is water splitting. The overall water splitting in different media and splitting reaction can be represented in various ways as follow:^{4,17}

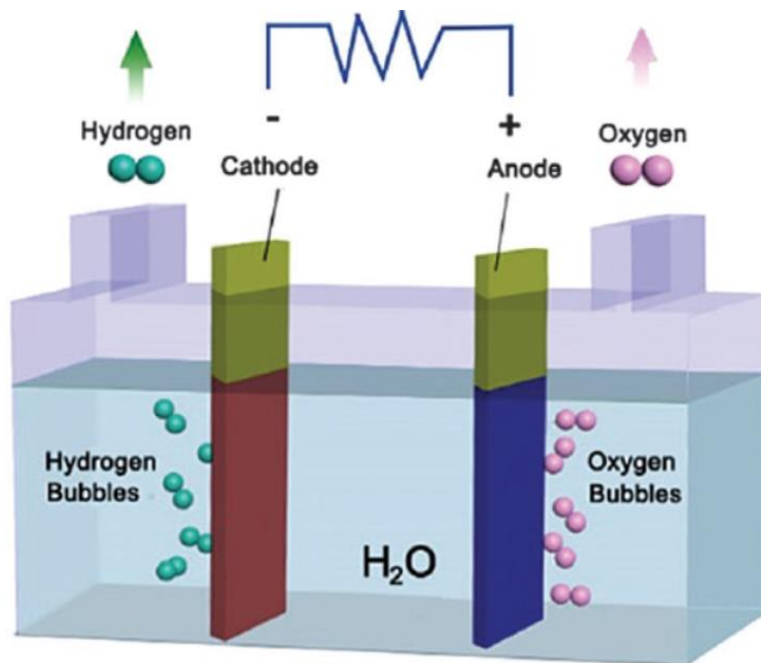
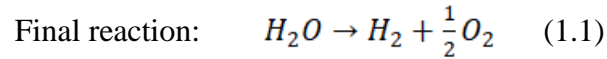
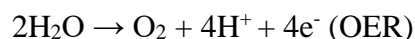


Figure 1.2 Schematic presentation of the two-electrode system in electrolysis process.¹⁸

1.2.1 Types of electrolysis

Depending upon the sort of solution media and active H^+/OH^- ions, the electrolysis process occurs concerning hydrogen evolution reaction (HER) with oxygen evolution reaction (OER) within the respective cathode and anode electrodes. In an acidic medium, proton (H^+) and alkaline medium (OH^-) are the active ions.^{4,7,18} The water splitting process can be expressed in the different medium as follows:





In basic condition:

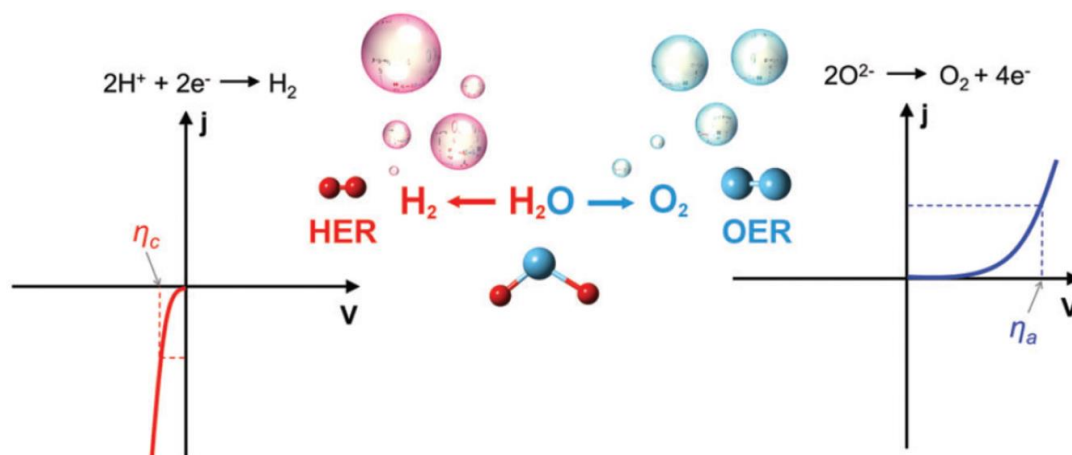
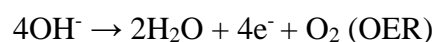


Figure 1.3 Schematic presentation of polarization curve in electrolysis process.¹⁹

The above reaction mechanism for the electrolysis process towards the evolution of molecular H_2 or O_2 gases has been carried out by the passage of external current at a specific potential is known as thermodynamic potential. While this potential is calculated from the equation as follows:

$$\Delta G = -nFE^0 \quad (1.2)$$

Where ΔG = Change in Gibb's free energy

n = No. of free electron

F = Faraday constant (96500 C)

Thermodynamically, the standard voltage required for the overall water splitting and the value calculated from the above equation for both the HER and OER processes to be 1.23 V at 25 °C and 1 atm. However, HER and OER processes are very sluggish reactions, and in practice, more voltage is required for water electrolysis.²⁰ The potential at which electrolysis occurs is called onset potential. Whereas, η_c and η_a

represent the symbols of the cathodic/anodic electrodes extra potential to overcome the thermodynamic potential. The additional potential is called overpotential.

1.3 Electrochemical cell

The electrochemical cell is the setup of a three-electrode system where the electrolysis process was occurring. This type of electrochemical cell comprises a three-electrode arrangement whereas, as catalyst modified working electrode (WE) named as GCE (glassy carbon electrode), bare platinum is auxiliary or counter (CE), along with aqueous silver/silver chloride (Ag/AgCl) as reference electrode (RE) respectively. Although the respective electrodes are immersed in the supporting electrolytes, some potential has been applied to initiate the electrolysis process.

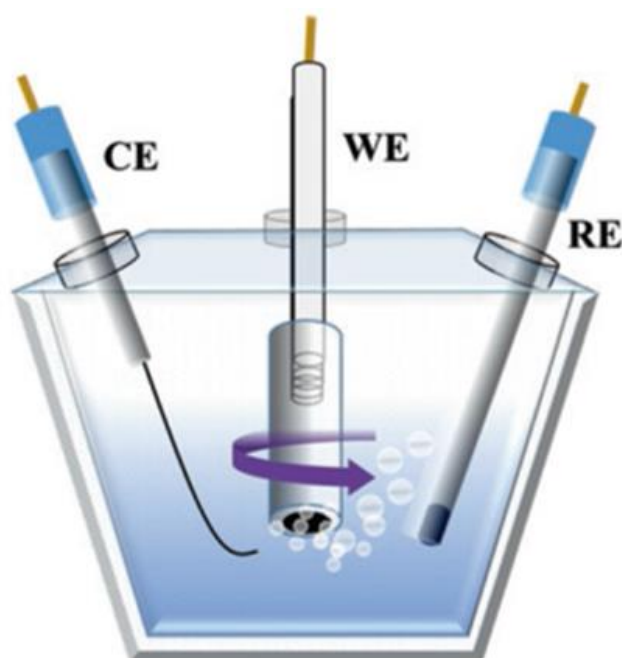
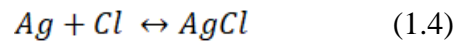
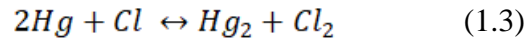


Figure 1.4 The three-electrode measurement setup of an electrochemical cell.⁴

The catalyst-modified working electrode is prepared by the mixture of a solvent and a binder-like nafion with an optimal quantity of the as-prepared catalyst followed by ultra-sonication to make a homogeneous catalyst slurry, and the slurry was drop cast

onto the surface of GCE. The preparation of the electrode material strongly depends upon the type of electrocatalyst used. Likewise, the working electrode, the reference electrode of silver, and calomel electrodes are used in the saturated solution of KCl. While for this type of reference electrodes, the chemical redox reaction generally as follows:



Sometimes, chlorine leaching from the above reference electrode was occurred during the electrolysis process and further enhanced the as-prepared electrode material catalytic activity. To avoid leaching possibility, mercury oxide (Hg/HgO) or sulfate type of reference electrode is used to analyze the actual catalytic activity. The use of different references electrode for the evolution of renewable (H₂ or O₂) gases through water splitting are calibrated into RHE (reversible hydrogen electrode) by well-known Nernst equation as follows:

In the case of aqueous Ag/AgCl reference electrode,

$$E_{RHE} = E_{Ag/AgCl} + E^0_{Ag/AgCl} + 0.059 p^H; E^0_{Ag/AgCl} = 0.21 V$$

For saturated calomel electrode (SCE),

$$E_{RHE} = E_{SCE} + E^0_{SCE} + 0.059 p^H; E^0_{SCE} = 0.24 V$$

For Hg/HgO electrode,

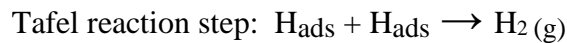
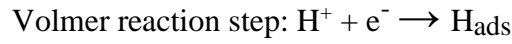
$$E_{RHE} = E_{Hg/HgO} + E^0_{SCE} + 0.059 p^H; E^0_{Hg/HgO} = 0.897 V$$

1.4 Mechanism of the electrolysis process

Through a simple water splitting process, the HER and OER mechanism follow a multi-electron path in all kinds of electrolytic mediums like acidic, alkaline, and neutral mediums, respectively.

1.4.1 Mechanism involved in hydrogen evolution reaction

The reduction of hydrogen ion to the generation of molecular H₂ gases in acidic medium corresponding to cathodic cell reaction during water electrolysis process which represented as three steps reaction mechanism as follows:^{4,21}



Firstly, in the Volmer process, the electron coupled hydronium ion (H⁺) gets transfer at the active catalytic sites to form an adsorbed hydrogen (H_{ads}) atom. The further step is considered the Heyrovsky process, whereas the adsorbed hydrogen atom is simultaneously combined with another electron coupled proton to form molecular hydrogen. Finally, the adsorbed hydrogen atom onto the electrode surface unites to produce hydrogen molecules called the Tafel reaction path. The formation of molecular hydrogen takes place by reducing bare protons (H⁺) or water in the acidic medium. And following either the Volmer-Tafel or Volmer-Heyrovsky reaction path has been shown in Figure 1.5.

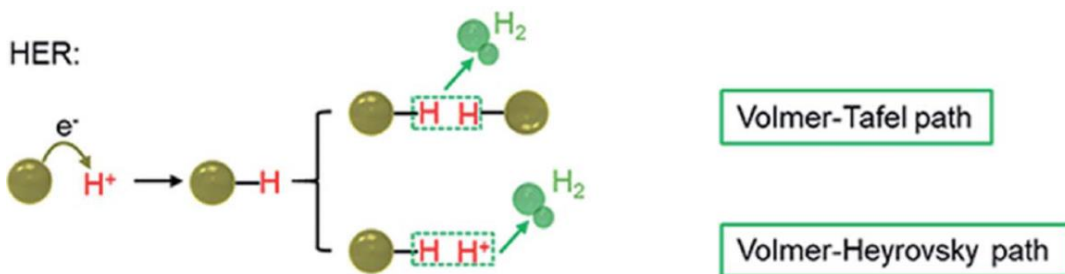
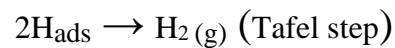
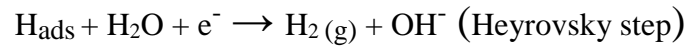
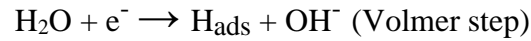


Figure 1.5 Reaction mechanism path followed by HER in acidic electrolytes.²²

Similarly, HER reaction in basic medium occurs with the presence of more active OH⁻ ion and the proton in the form of water molecules, and the reaction path follows as:²³⁻

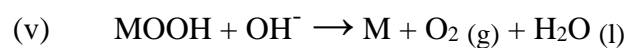
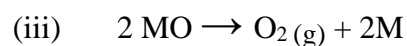
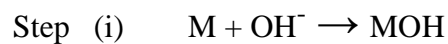
25



Firstly, the electron combined with the water molecules corresponding to discharge an adsorbed hydrogen atom and an active hydroxide ion to the electrolyte. After that, the adsorbed hydrogen atom coupled with another electron combined water molecules to form hydrogen gases. Finally, two H_{ads} atoms combined to form molecular H₂, which is named as Tafel reaction step.

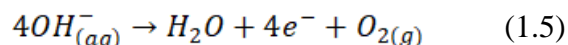
1.4.2 Mechanism involved in oxygen evolution reaction

During the electrolysis process, the oxidation of water molecules acquires molecular oxygen at the anode electrode surface. It follows four electrons of oxide/hydroxide reaction path in acidic and basic electrolyte medium. The reaction mechanism path in an alkaline medium represented as^{7,26}



Where M represents the catalytic surface sites

The overall anodic reaction is,



The mechanism for the evolution of molecular oxygen from both the acidic and alkaline electrolytic mediums has been shown in Figure 1.6.

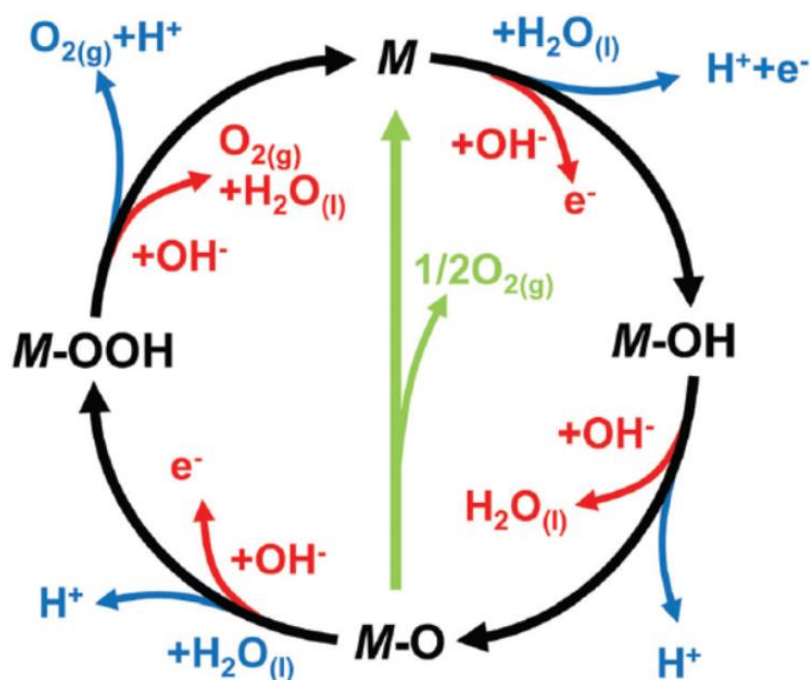


Figure 1.6 A step-wise reaction mechanism for OER displays in the acidic process in blue line and alkaline in red line conditions. This overall reaction mechanism follows the formation of reaction intermediates of peroxide (M–OOH) and oxo (M–O) intermediate to generate molecular oxygen.¹⁹

It has been observed that the intermediate MO follows two different reaction paths to form molecular oxygen. In an alkaline medium, the decomposition of oxide (MO) intermediates simultaneously with the combination of peroxide (MOOH) with the hydroxide to form O₂. But in the case of acidic medium, the direct decomposition of MO intermediates and the coupled of peroxide (MOOH) with water to form molecular

oxygen, respectively. However, the formation and decomposition of M-O bond (generally M-O bonding interaction in metal hydroxide (MOH), oxide (MO), and peroxide (MOOH)) are determining the performances of the overall electrolysis process.^{19,21}

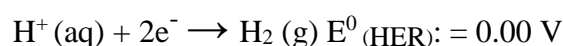
1.5 Common parameters for the catalytic evolution process

The electrocatalytic performances are calculated by various key parameters such as overpotential, Tafel plot, Nyquist plots, electrochemical active surface area (ECSA) with roughness factor or active sites, mass activity, turn over frequency, faradic efficiency, and cyclic stability, respectively. Simultaneously, the surface reaction mechanism involvement during the catalytic process is also evaluated by these above parameters.

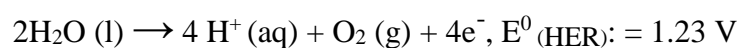
1.5.1 Overpotential (η)

As per the known Nernst equation, theoretically, a standard thermodynamic potential (E^0) of 1.23 V and 0.0 V (vs. NHE) is required to perform electrochemical oxidation and reduce water reaction. In practice, no such electrochemical reaction occurs in such standard potential (E^0) due to the sluggish reaction kinetics and low energy efficacy. Therefore some additional energy is required in terms of overpotential (η) to initiate the HER/OER process.

In HER process



In OER process



An electrocatalyst having a lower value of overpotential (η) shows better electrochemical activity in both HER and OER processes. But there are three types of overpotential associated with the HER and OER process to hinder the reaction path during catalytic activity and minimizing the efficiency of an electrocatalyst. Generally, the overpotential origin is focused on the overpotential of activation, concentration overpotential, and the overpotential concerning the presence of uncompensated solution resistance during the period of electrochemical study.²⁰ The activation overpotential is implying as an in-situ property of the electrode surface and can be removed by the presence of a suitable electrocatalyst. The concentration overpotential has been observed due to the slower charge carrier diffusion near the electrolyte/electrode interface, and it can be reduced by steady solution stirring. Further arises of overpotential due to uncompensated resistance can be eliminated through ohmic drop (iR) correction. While this can be analyzed by the facility available in different electrochemical workstation set-up²⁷ and calculated manually by knowing the solution resistance from impedance spectroscopy.^{27,28} A resultant solution resistance is multiplying with the current density to get the ohmic drop (iR) and subtracted from the recorded experimental data to observe the electrocatalyst intrinsic HER/OER activity. However, the potential at a particular current density such as 10 mA/cm² was broadly accepted as a predefined current density corresponding to the HER/OER process to evaluate an efficient electrocatalyst. The predefined current density of (10 mA/cm²) is anticipated to match the 12.3% efficiency of solar cell energy under the illumination of 1 sun.^{29,30} Therefore, the smaller overpotential value determined in current density of (standard as 10 mA/cm²) implies a cost-effective electrocatalyst towards water electrolysis.

1.5.2 Tafel slope

The Tafel slope simplifies surface kinetics and the reaction mechanism on an electrocatalyst surface throughout the overall HER and OER processes. The lower Tafel slope value of an electrocatalyst indicates the higher efficiency nature of HER or OER catalyst, corresponding to an increase of cathodic/anodic current density at a lower value of overpotential. Generally, the Tafel slope is derived from the fitted linear region of the Tafel plot.^{31,32} The Tafel plot is represented as a profile of the current density $\log(j)$ versus overpotential (η). While this relation between $\log(j)$ versus overpotential (η) is determined by using the following equation.

$$d \log(j)/d \eta = 2.303 RT/\alpha nF \quad (1.6)$$

From equation (1.6), it has been observed that the Tafel slope region is inversely proportional to the charge transfer coefficient (α). The rest parameter (Likewise, R = gas constant, T = temperature, and F = Faraday constant) are constant, and n is the involvements of electrons of two and four for HER as well as OER, respectively.

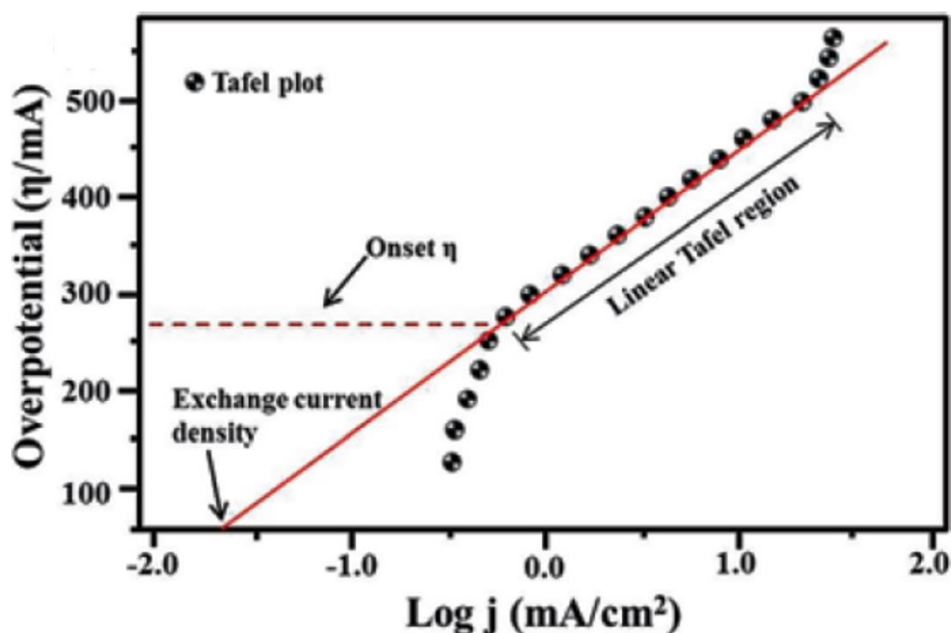


Figure 1.7 Schematic presentation of linear fitted Tafel region.⁴

The linearly fitted Tafel region of the Tafel plot is represented as an equation as follows:³³

$$\eta = a + b \log j \quad (1.7)$$

From equation (1.7), η is overpotential, a and b are Tafel constant, Tafel slope, and j is the obtained current density. Moreover, the exchange current density (j_0) value is also derived from the Tafel plot at the zero overpotential. The higher value of (j_0) indicates the larger availability of the active site on the catalyst surface. However, the higher active surface gives a higher value of exchange current density (j_0).²⁰

1.5.3 Electrochemical impedance spectroscopy (Nyquist plot)

The impedance spectrum or Nyquist plot has been applied to investigate a charge transfer resistance (R_{ct}), the resistance of the solution (R_s) used, and mass transfer activity on an electrocatalyst surface during the electrochemical water splitting process. The impedance spectrum was plotted as the plot of an imaginary axis (Z'') versus the real axis (Z') in a supporting electrolyte. The potential applies to get some response through conduction of lower to higher charge transfer between the electrode surface and an electrolyte. A lower charge transfer activity refers to the electrode material's higher conductivity, which accompanies the efficient nature and metal doping characteristics of the electrocatalyst. The lower R_{ct} value can be boosting the HER and OER performances of an electrocatalyst, which have been illustrated in Figure 1.8. Randles circuit has been observed inside the Nyquist plot. Where R_s , R_{ct} is denoted as solution resistance and charge transfer resistance. In contrast, the CPE (constant phase elements) is noted as double-layer capacitance.

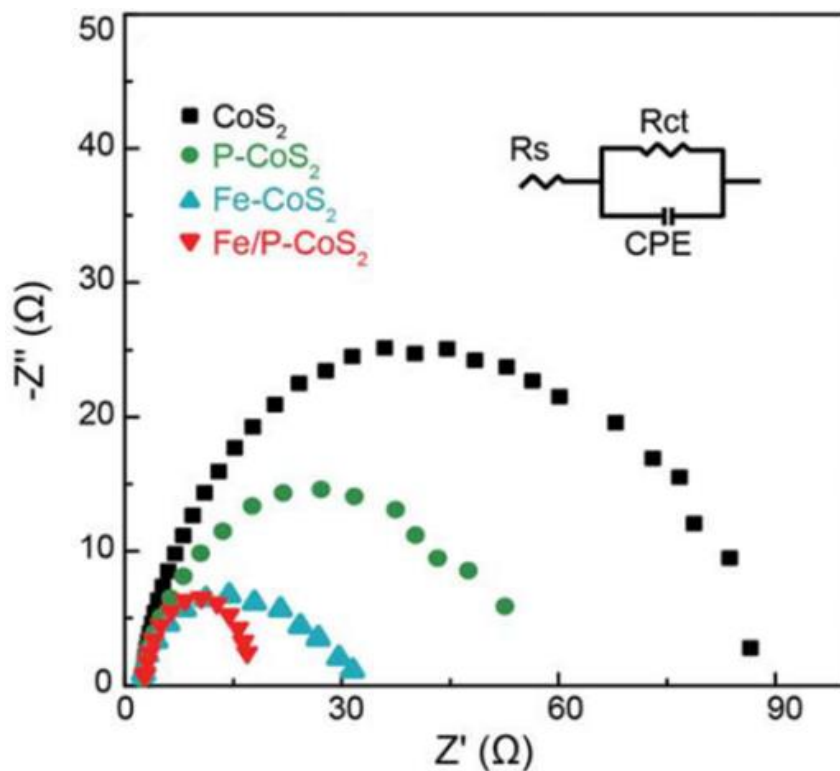


Figure 1.8 Impedance spectrum for pristine and Fe/P dual doping CoS₂ polycrystalline nanowire for HER.³⁴

Moreover, the specific capacitance or energy stored performances of active material is derived through the EIS measurements by considering the equation as follows:^{35,36}

$$C_m = \frac{1}{m \times j \times 2\pi f \times Z''} \quad (1.8)$$

Herein, C_m a specific capacitance, the mass of sample represents m , f and Z'' are the frequency and imaginary part.

1.5.4 Electrochemical active surface area (ECSA)

The ECSA value has been calculated by following double-layer capacitance (C_{dl}) from a non-faradic region of cyclic voltammetry curve and a similar non-faradic potential region electrochemical impedance spectroscopy. The ECSA value strongly depends

on the surface of the electrocatalyst having very rough and porous. The double-layer capacitance is evaluated only due to the charge accumulation process corresponding to a charge of layers at the electrode interface without any redox behavior. The current (i) generates from the CV curve is directly proportional to the applied scan values (ϑ) and the capacitance of double layer (C_{dl}) by considering the below equation as follows:^{37,38}

$$i = \vartheta C_{dl} \quad (1.9)$$

The C_{dl} value was obtained with the plotting of current (i) vs. sweep rate (ϑ).

Further the equation for ECSA,³⁹

$$ECSA = \frac{C_{dl}}{C_s} \quad (1.10)$$

Herein C_s denotes as specific capacitance, and it is varying in the range of 20-60 $\mu\text{F}/\text{cm}^2$.⁴⁰⁻⁴²

The presence of electrochemically active sites per unit surface area named as roughness factor (R_f) is derived by dividing the ECSA value with the geometrical surface area (S_{geo}) of as-prepared sample modified GCE (glassy carbon electrode material) from the below equation as follows:

$$R_f = \frac{ECSA}{S_{geo}} \quad (1.11)$$

Generally, the geometrical surface area (S_{geo}) of modified GCE material is used to normalize the measured cathodic (HER) and anodic (OER) current value.

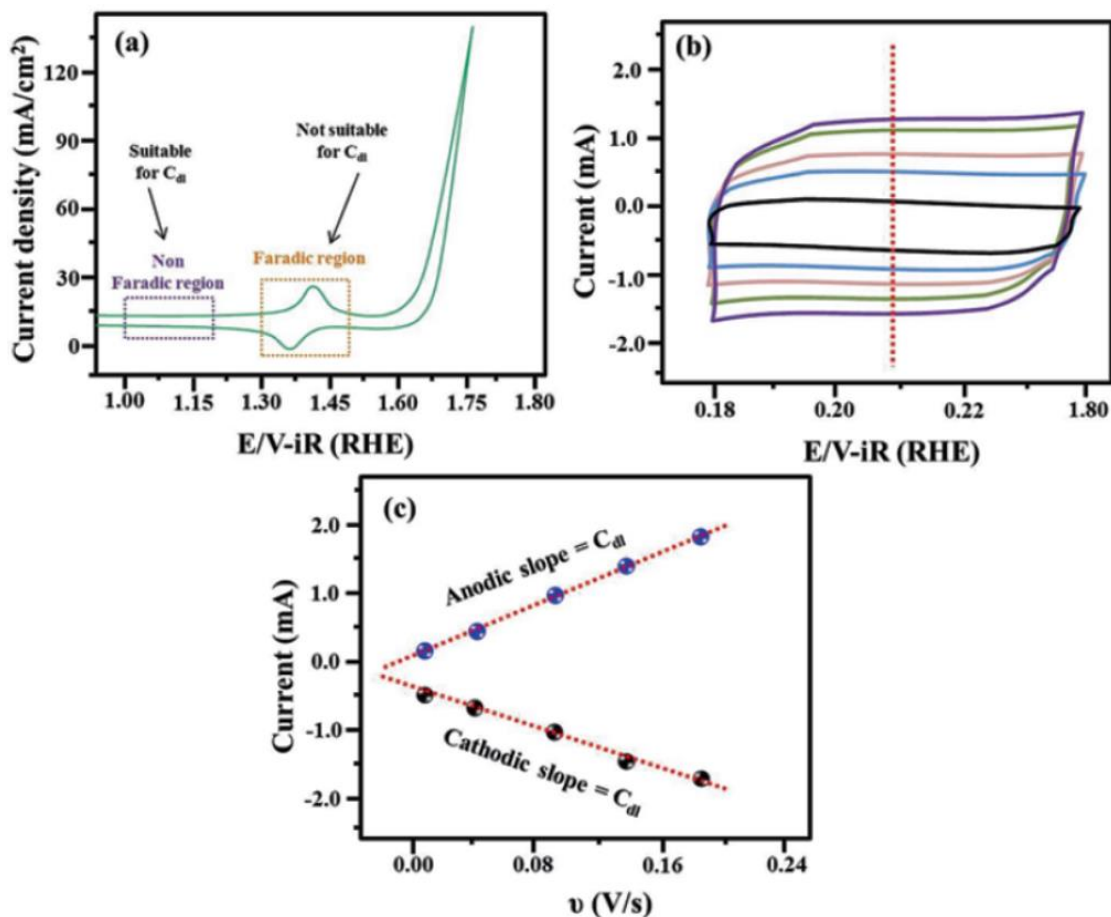


Figure 1.9 Schematic diagram of CV showing the ideal non-faradic region from which C_{dl} value to be calculated (a), CV of the chosen non-faradic portion at various scan rates (b), and Figure (c) represents the fitting parameter of cathodic and anodic points determined the slope value.⁴

1.5.5 Mass activity

The mass activity is the geometrical normalization of the as-prepared sample was carried out by dividing calculated current density (J) by mass (m) of the catalyst-ink drop cast on to the working electrode by following the equation as below,⁴³

$$\text{Mass activity (mA/g)} = \frac{J}{m} \quad (1.12)$$

1.5.6 Turn over frequency

The turnover frequency of an electrocatalyst gives a detailed study about the evolution of no. of moles of H₂ or O₂ molecules per unit time.^{44,45} However, the value of turn over frequency can be calculated as per the following equations:

$$TOF = \frac{\text{Number of H}_2 \text{ or O}_2 \text{ evolved per unit time}}{\text{Number of active sites}}$$

$$\text{Or } (TOF)_{HER} = \frac{IN_A}{AF_n\Gamma} \quad (1.13)$$

Herein, I , N_A , A , and n are observed as current, Avogadro constant, geometrical surface area, no. of electron transferred along with Γ as a symbol of surface, respectively. In HER study, two-electrons required to evolve H₂ molecules and four-electron in the case of OER as follows,⁴

$$(TOF)_{HER} = \frac{I}{2F_n} \quad (1.14)$$

$$(TOF)_{OER} = \frac{I}{4F_n} \quad (1.15)$$

Here, I is the current measured in the LSVs curve, F denotes as Faraday constant, and n is the no. of active surface sites.

1.5.7 Faradic efficiency

Faradic efficiency is a key parameter used to measure the efficacy and the ratio of electrons participating to the number of electrons supplied throughout the electrochemical process. But in HER/OER, the Faradic efficiency depicts the amount of hydrogen or oxygen molecules detected practically to the amount of H₂ or O₂ molecules theoretically.^{18,27}

After that, the Faradaic efficiency (FE) has been evaluated by using the below equation as follows,

$$\text{Faradaic Efficiency} = \frac{I_R \times n_D}{I_D \times n_R \times N_{CL}} \quad (1.16)$$

In the above equation, I_R and I_D are the ring and disk current, respectively. Where n_D and n_R represent the involvements of countable electrons number in the overall electrochemical study.

1.5.8 Cyclic stability

Likewise, different active parameters, the durability or cyclic stability measurement was carried out by chronopotentiometry (variation of overpotential observed at a sustained current density of 10 mA/cm² or higher). Moreover, the chronoamperometric (at a particular overpotential change in current density) technique evaluates to observed the constancy performances and practical application of the as-prepared active electrode material. However, the stability performances were also done by repeating the CV cycle between the predefined potential ranges at a specific scan value. Generally, the polarization curve of an electrocatalyst has been recorded after the stability test and compare with before stability data to observe any such kind of change in overpotential obtained, corresponding to the poor electrochemical performances. Moreover, the further shift in diffraction pattern (phase purity), surface morphology, and elemental composition (XPS spectrum) were studied after the post stability analysis to confirm the efficacy of as-prepared active materials.

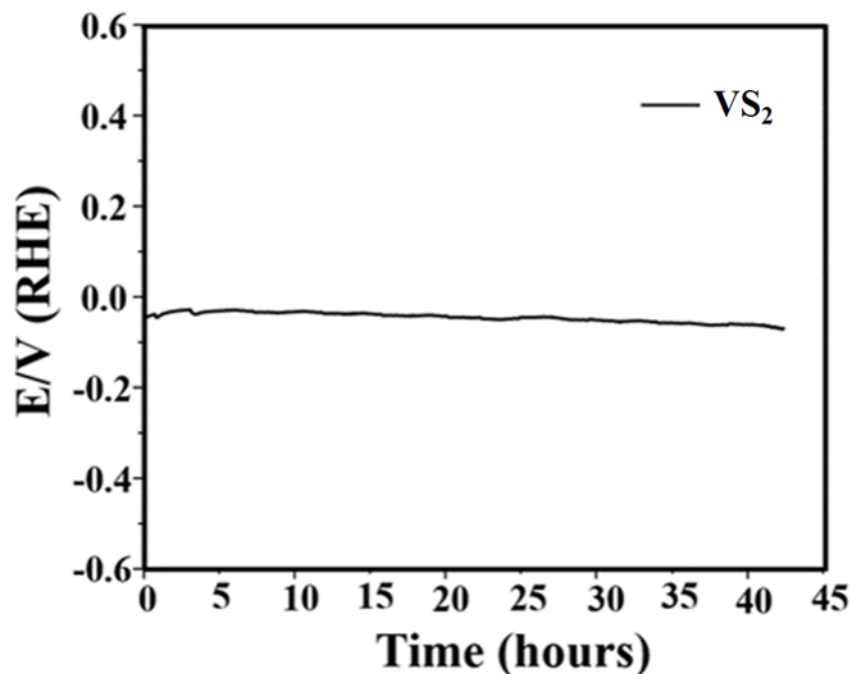


Figure 1.10 The cyclic stability of VS₂ for HER in 0.1 M H₂SO₄ electrolytic solution at a higher applied current density of 30 mA/cm².³⁷

1.6 Types of electrode materials used

The electrocatalytic evolution of renewable hydrogen/oxygen molecules strongly depends on the various precious and non-precious electrode material elements. The noble metal of platinum (Pt) or palladium (Pd) and oxide-based precious metals like ruthenium (RuO₂), iridium oxide (IrO₂) are used as benchmark catalysts for the simplest electrolysis process. Besides this precious metal-based catalyst, various metal and non-metal-based electrocatalysts are used to replace the noble metal-based catalyst. Nowadays, the noble metal-free electrocatalyst with efficient HER/OER performances has been synthesized by following various unique synthetic techniques and check their catalytic activity competes with the precious one.

1	2	3	4	5	6	7	8	9	10	11	12	13	14	15	16	17	18
H	Periodic Table of Elements																He
Li	Be											B	C	N	O	F	Ne
Na	Mg											Al	Si	P	S	Cl	Ar
K	Ca	Sc	Ti	V	Cr	Mn	Fe	Co	Ni	Cu	Zn	Ga	Ge	As	Se	Br	Kr
Rb	Sr	Y	Zr	Nb	Mo	Tc	Ru	Rh	Pd	Ag	Cd	In	Sn	Sb	Te	I	Xe
Cs	Ba	La	Hf	Ta	W	Re	Os	Ir	Pt	Au	Hg	Ti	Pb	Bi	Po	At	Rn

- Pt-containing noble metal HER catalysts
- Metals that are used for constructing noble metal-free HER catalysts
- Nonmetals that are used for constructing noble metal-free HER catalysts

Figure 1.11 Elements used for the preparation of HER-based electrocatalyst in the periodic table.¹⁸

1.6.1 Noble metal-based catalysts

As per the theoretical study, the thermodynamic potential of 0 V and 1.23 V (versus RHE) is required to proceed with two and four-electron reaction mechanisms to generate molecular hydrogen and oxygen gases from the water electrochemical process. The electrocatalytic process is the surface phenomenon, and practically it needs a high value of overpotential to split the water. Generally, the high value of additional potential (overpotential) is reduced by precious noble metals of platinum (Pt), palladium (Pd), oxide of ruthenium (RuO₂), and the oxide of iridium (IrO₂), respectively.²¹ A profile of HER activity for the precious metal concerning free energy change is shown in Figure 1.12. platinum (Pt) is the benchmark catalyst for the HER process. It's required a lower value of additional potential to extend the broadly accepted 10 mA /cm² (as a standard current density value). Likewise, in the case of

OER, both ruthenium (RuO_2) and iridium oxide (IrO_2) are used as the reference electrocatalyst owing to enhance the oxygen evolution activity in the supporting electrolytes.¹¹ However, its high price, sketchy availability, and poor electrochemical stability are prohibited in the enormous practical applications.

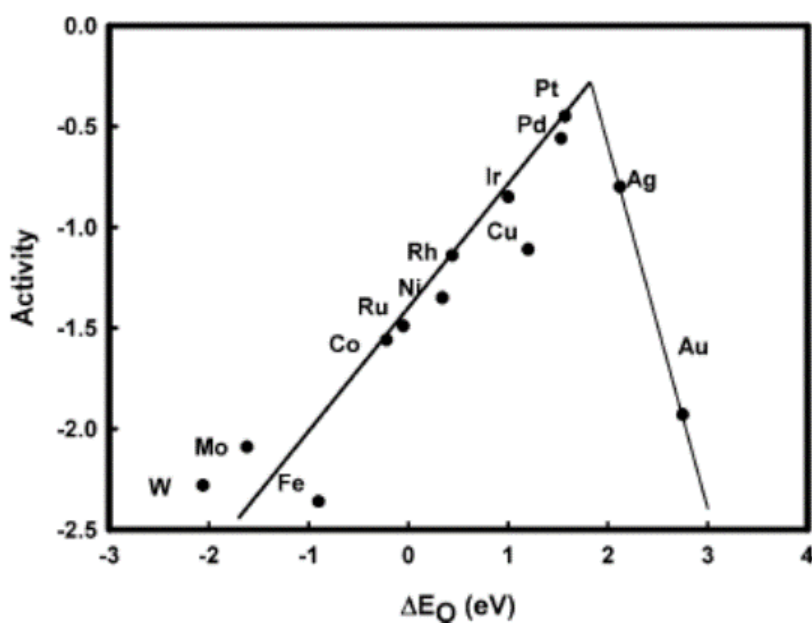


Figure 1.12 Volcano plot (activity vs. calculated Gibbs free energy) used for HER electrocatalyst.⁴⁶

Therefore, the researchers are giving more effort to develop a noble metal-free electrocatalyst than a catalytic activity like precious metal. And their low-cost value due to low precious metal content and good durability has the advantage to use over the precious metal. In this regard, various carbon-based materials, both the pristine and carbon hybrids of metal oxide/hydroxide, metal chalcogenides, and metal phosphides electrode material, are demonstrated as non-precious electrode material for the electrocatalytic and energy storage process. Moreover, precious metal also plays a vital role in supercapacitor application. For example, Patake *et al.* prepared RuO_2

chemically with the lowest capacitance value of 50 F/g.⁴⁷ Similarly, the nanotubular array of RuO₂ · xH₂O in aqueous solution depicts an enhanced specific capacitance of 1300 F g⁻¹.⁴⁸

1.6.2 Carbon based materials

The carbon-based electrode material having 2D layers analogous corresponding to pristine graphene⁴⁹ and other carbon material includes activated carbon,⁵⁰⁻⁵² carbon nanotubes,⁵³ carbon nanofibers,⁵⁴ template or hetero atom carbon,⁵⁵ and carbon aerogels⁵⁶ are used as a template or hybrid materials to enhance the storage performances and catalytic activity in both the field of energy storage and conversion application.^{14,57} Although 2D graphene material has good attention because of its low price value, high natural abundance, better surface-to-volume ratio, good electrical conductivity, elevated thermal and chemical stability and can be operated in a broad range of temperatures. Likewise, graphene, the surface functionalization of carbon nanotubes material that tunes the pore size, pore-volume, and the nanostructures that help enhance electrocatalytic (HER/OER) and storage capacitance (Supercapacitor) values besides other carbonaceous material.^{58,59} Carbon nanotubes were first discovered by scientist Iijima in the year 1991.⁶⁰ However, carbon nanotubes having single graphene sheets wrapped into cylindrical nanotube form denoted as single-walled carbon nanotubes (SWCNTs), and In the case of multiwalled carbon nanotubes (MWCNTs), there is a hierarchical carbon nanotube structure. The main advantage of the CNTs is it has no edge plane which can prevent the irreversible electrochemical reaction.⁶¹ These unique properties make CNTs an efficient composite material with graphene for energy conversion and storage study. But the presence of limited accessible surface area and EDLC behavior, these carbonaceous materials have some

limitations to hybrids with pseudo material for showing better HER/OER performances.⁶¹ The hydrogen evolution reaction of pure RGO films was obtained from the measured polarization curve, which signifying the poor catalytic activity without any hybrids of redox-active material. The HER performance of the graphene is enhanced by doping than the pristine one. The dual-doped (N, P) graphene shows better HER activity than the bare graphite and single-doped graphene electrode material. It needed only 420 mV of additional potential to reach 10 mA/cm² of predefined current density and a lower Tafel slope value than other electrodes materials.⁶² Likewise graphenes, MWCNTs is shown poor electrocatalytic performances without any hybrids or doping.⁶³

Similarly, the charge storage performance towards supercapacitor (SCs) application was reported above carbonaceous material due to its various physiochemical properties. Both the energy conversion and storage performances of the electrode material are essential to prove the efficiency of the material. The super capacitance calculated with regards to specific capacitance and the specific capacitance value of reduced form graphene oxide (RGO) was 144 F/g in the previously reported data.⁶⁴ The activated carbon depicts the specific capacitance of 60 F/g.⁶⁵ Moreover, activated carbon and carbon nanotubes' hybrids showed specific capacitance (90 F/g) in an organic electrolytic medium.⁶⁶ But the poor rate capability and lower energy density of the bare CNTs, pristine graphene, and graphene/CNTs hybrids think to develop an advanced electrode material. So the researchers have investigated a new kind of semiconductor electrode material with pseudocapacitor behavior or surface oxidation-reduction reaction to enhance the charge storage efficiency and better active catalytic sites for further energy conversion applications.

These materials are transition metal oxide, metal chalcogenides, and meta phosphides which can be composited with the carbon material for other energy enhancements.

1.6.3 Transition metal oxides (TMOs)

The semiconducting behavior of metal oxide and hydroxide is a prominent candidate for the HER/OER process and high storage performance towards supercapacitor (SCs). The advantages of the non-precious metal oxide or hydroxide have a variable oxidation state, higher electrochemical stability, and an electrically conductive nature, implying a suitable candidate for the energy fields.⁶⁷ The noble metal of oxide of ruthenium (RuO_2) or iridium (IrO_2) is used as a standard electrode material for higher electrocatalytic performances towards oxygen evolution reaction (OER).¹¹ But its expensive nature and limited availability motivate us to search for a noble metal-free electrocatalyst. Remarkably, the non-precious metal oxide of Co_3O_4 , NiO , and MnO_2 was explored and considered anode material for overall water splitting. Silva *et al.* synthesized the NiO nanofibers and observed the OER activity in lower overpotential (322 mV) to register at a standard current density (10 mA/cm^2).⁶⁸ Similarly, $\text{Co}_{3-x}\text{O}_4$ investigated their higher oxygen evolution performances with a lower value of overpotential (268 mV) and a Tafel value of 38.2 mV/dec, respectively.⁶⁹ Besides these, the binary metal oxide of 1D NiCo_2O_4 /graphene hybrids shows excellent OER and supercapacitor performances.¹⁴ The small overpotential value (313 mV) was obtained to deliver the predefined current density of 10 mA/cm^2 , a lower Tafel value of 35 mV/dec, and a better specific capacitance of 1315 F g^{-1} . The long-term stability test observed the efficacy of the electrode material in the area of energy storage and conversion. Moreover, other low-cost and nature-friendly single transition metal oxide with graphene hybrids electrode materials like $\text{rGO/Fe}_3\text{O}_4$,⁷⁰ $\text{rGO/Co}_3\text{O}_4$,⁷¹ extended

their research in the energy storage field. However, its poor cyclic stability is restricted to developing an alternative efficient electrode material for energy storage performance. For example, Gao *et al.* synthesized the electrodeposition of Co_3O_4 nanowire /NF having storage capacitance of 746 F g^{-1} at 5 mA/cm^2 of applied current density.⁷¹ Likewise, MnO_2 is the amorphous nanostructured electrode material with the storage value of 250 F g^{-1} , and a long test cyclic process of the electrode was observed with the repeated 1200 cycle number.⁷²

1.6.4 Metal chalcogenides

Transition metal chalcogenides (TMCs) are the most attracted inorganic graphene analogous of two-dimensional layered semiconductor material having simple formula MX_2 , where M represents different transition metal ($\text{M} = \text{V}, \text{Mo}, \text{Co}, \text{W}, \text{Nb}, \text{Sn}$) and the chalcogens are ($\text{X} = \text{S}, \text{Se}, \text{Te}$). A transition metal atom is sandwiched between two chalcogen atoms through a covalent bond to produce layer structures. Every layer is bounded with weak van der Waal's force of interaction which can be easily exfoliated. The compounds of TMCs exhibit different electrochemical measurements (such as energy storage or energy conversion) related to requisition like a solar cell, supercapacitor, lithium-ion battery, and the splitting of water to the evolution of renewable gases like H_2 or O_2 .⁷³⁻⁷⁵ The flat surface area of the transition metal compounds shows enhanced electrical and mechanical properties. The transfer of electrons occurs through MX_2 nanostructured metal chalcogenides, resulting in faster diffusion of ions between the MX_2 layer and electrolyte, which gives enhanced specific capacitance value and shows better HER/OER results. The charge storage mechanism in TMCs follows a faradic reaction mechanism in which both oxidation and reduction occur at the electrode surface. The popularity of the TMCs is not

because of their immense applications but also the facile technique through which they can be synthesized.⁷⁶

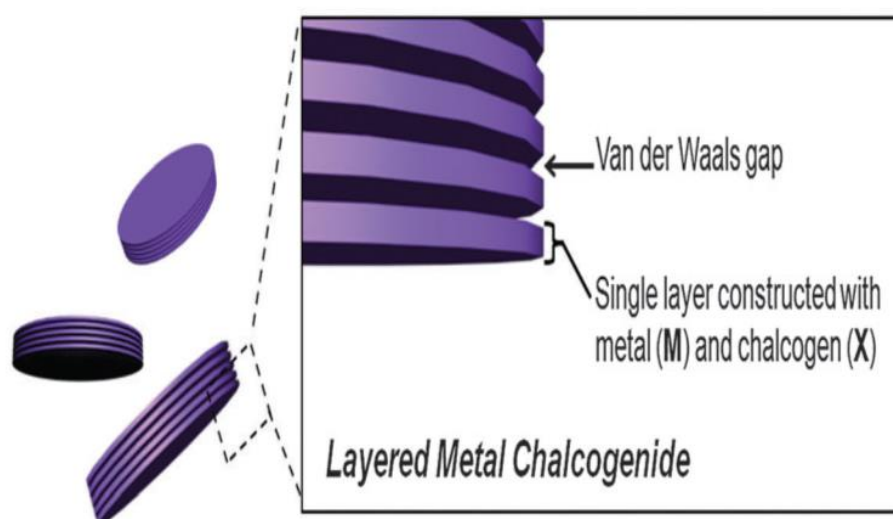


Figure 1.13 Metal chalcogenides have a layered structure, and every single nanocrystal contains multilayers with weak van der Waals force attraction stacked along the *c*-axis.⁷⁷

Different pristine metal chalcogenides electrode materials observed the catalytic evolution of renewable H₂ or O₂ gas molecules through water splitting and energy storage capability. Pristine metal chalcogenides such as NiSe₂, CoSe₂, MoS₂, WS₂, NbS₂, *etc.*, are the noble metal-free electrocatalyst that enhances electrochemical activity towards HER/OER and compare the catalytic activity with precious metal. Yu *et al.* studied the superior HER performances of NiSe₂ nanocrystal have a lower value of Tafel slope (29.4 mV/dec). While the obtained value is lower than other reported NiSe₂ and the noble metal platinum (Pt) of 30.8 mV/dec.⁷⁸ Guo *et al.* hydrothermally synthesized hollow micro/nano MoS₂ nanomaterial and explored their HER study of overpotential (214 mV) for 10 mA/cm⁻² current density, Tafel value (74 mV/dec) in supporting electrolytes of 0.5 M H₂SO₄.⁷⁹ However, Kwak groups represents the

synthesis of NiSe₂ and CoSe₂ nanocrystal involving dual behavior (HER or OER) applications for the observation of electrochemical study.⁸⁰ Similarly, transition metal chalcogenides like WS₂,⁸¹ VS₂,⁶⁴ MoS₂⁸² show good electrochemical charge storage performances without any hybrid of supporting material (graphene, carbon nanotubes, etc.).

1.6.4.1 Metal chalcogenides and Graphene hybrids

The higher surface-to-volume ratio and good electrical properties of graphene and various carbonaceous material used as a composite materials with TMCs promote nucleation growth, cyclic stability, and improve the physiochemical properties.^{49,61,65} To avoiding the easily restacking nature of 2D metal chalcogenides, some additional templating agents of carbon-based electrode material (graphene, CNTs, etc.) are used.⁸³ The pristine form of TMCs and graphene composite is mainly synthesized using the solution method, hydrothermal method, and chemical vapor deposition method.^{74,75} Moreover, the graphene/TMCs composite facilitates high dispersibility in aqueous and an organic solvent, high surface area to volume ratio, and high chemical with mechanical stability.⁸⁴ Graphene composites of metal chalcogenides are shown much better electrochemical performances (both HER/OER and SCs) than pristine ones. Likewise, Ahn and the group following the hydrothermal method synthesized CoS₂ nanoparticles on the graphene layer and tested their HER performances. While the electrode-modified HER catalysts need only 150 mV to acquire the standard 10 mA/cm⁻² current density with the calculated fitting value of the Tafel plot of 48 mV/dec.⁸⁵ Similarly, Kagkoura *et al.* following the solution method synthesis of optimized MoS₂/RGO composites, which shows better HER activity than the pristine one. It required only 154 mV of overpotential to achieve the current density of 10

mA/cm^{-2} , Tafel value of 77 mV/dec are implying the enhanced activity.⁸⁶ Tang groups investigated NiSe nanowire's synthesis on the supported nickel foam. This efficient electrode material has a dual functional behavior of HER and OER activity in a harsh alkaline solution.⁸⁷ Additionally, supercapacitor performances are also improved by an active template of graphene hybrids material. For example, the graphene hybrid of MoS_2 shows better specific capacitance or charge storage capacitance (282 F/g) in comparison to pristine MoS_2 (156 F/g).⁸² Similarly, WS_2/RGO composites having a five times higher capacitance value (350 F/g) than the pristine WS_2 .⁸¹

1.6.4.2 Metal chalcogenides and carbon nanotubes (CNTs) composites

Likewise graphene, carbon nanotubes have an excellent attraction in the energy field (energy conversion and storage) than other carbon-based electrode materials due to their large surface area, good conductive nature, higher thermal conductivity, better thermal stability, and good mechanical properties.^{60,88,89} However, pristine CNTs electrode material has not shown any electrochemical performances towards energy storage and conversion without any hybrids or doping.⁵⁸ Therefore, a new kind of electrode material used called composite materials. The composites of CNTs with various transition metal-based chalcogenides or transition metal-based oxides (TMOs) give faster reversible surface redox reactions between the electrolyte and electrode interface, which improved the electrochemical activity.^{40,58,59} The easy restacking character and low theoretical specific capacity of the TMDCs sheet are further enhanced by hybridizing functionalized carbon nanotubes and optimized energy performances. For example, Kim *et al.* developed microporous nanostructured of CoSe_2 -CNTs composites having optimized microsphere morphology for hydrogen evolution reaction. Catalytic performances measured concerning overpotential (174

mV at a predefined current density of 10 mA cm^{-2}), Tafel slope of 37.8 mV dec^{-1} for microsphere CoSe_2 -CNTs composites is lower than bare CoSe_2 .⁶³ Similarly, the carbon nanotubes composites of MoS_2 ,⁹⁰ and WSe_2 ,⁹¹ and CoS_2 ⁵⁸ are used as advanced electrocatalyst towards overall water splitting in the respective electrolyte solution.

1.6.5 Metal phosphides

Transition metal-based phosphides (TMPs) are examined as a prominent catalyst in producing renewable gas molecules like H_2 or O_2 through simple water-splitting reaction and considered an efficient electrode material to replace the precious metal (Pt, Ru, and Ir, etc.) based electrocatalysts.²⁷ The phosphorous atom with a more electronegative character facilitates the withdrawal of electrons from the metal center atom. The phosphorous atom's negative chemical state acts as a base and withdraws the electrons, corresponding to forming positively charged ions during hydrogen evolution reaction. In this period, the atomic percentage of the phosphorous for the same metal phosphides increases, signifying HER activity enhancements. The improvements of HER performances because of the P content in TMPs have some specific limit, and after that, the activity decreases. But an optimized metal to phosphorous ratio can execute the HER activity.⁹² Recently, mono and bimetallic of TMPs (FeP , Ni_xP , CoP , MoP , NiCoP , WP_2 , etc.) have been synthesized by following different synthetic routes and the electrocatalytic performances towards HER have been analyzed through the supporting electrolytic medium of the aqueous acidic and basic solution.^{38,92–96} For example, Tian *et al.* synthesized iron phosphides (FeP) nanoparticles and observed their HER performances in acidic media. The HER efficiency of this phosphide material was determined by a lower overpotential of 154

mV at 10 mA/cm^{-2} and a Tafel slope of 65 mV/dec^{-1} , respectively.⁹⁷ Masud groups reported FeP nano particles' synthesis and explored their OER performances in an alkaline electrolytic medium.⁹³ Similarly, the variation of nickel to phosphorous ratio implies the formation of a different phase of Ni_xP nanoparticles, which shows enhanced HER activity in acidic and alkaline electrolyte conditions.⁹⁴

1.7 Supercapacitor (SCs) or Ultra capacitor

The growing energy demand because of the industrial revolution has reached a level where highly efficient and sustainable energy storage devices towards supercapacitors need to be explored. The consumption of traditional fossil fuels fulfills the global energy demands of 80%. However, fossil fuel consumption relies upon the increase in greenhouse effect gases with pollution intact environment remarkably. Therefore it is urgent to develop an alternative, clean, and high energy source device which might be full-filled the future energy demand.^{1,5} Electrochemical capacitors or Supercapacitors (SCs) signifying as a competitive candidate in modern energy device systems because of their more excellent power supply capability and higher energy density than different used batteries and traditional capacitors. Moreover, its long cycle life without any chemical reaction, more significant charge propagation nature, and simple operating principle signify an efficient charge storage device.⁹⁸ The comparison of electrochemical performances for supercapacitor, capacitor, and various lithium-ion battery have been illustrated by Ragone plot in Figure 1.14.⁹⁹

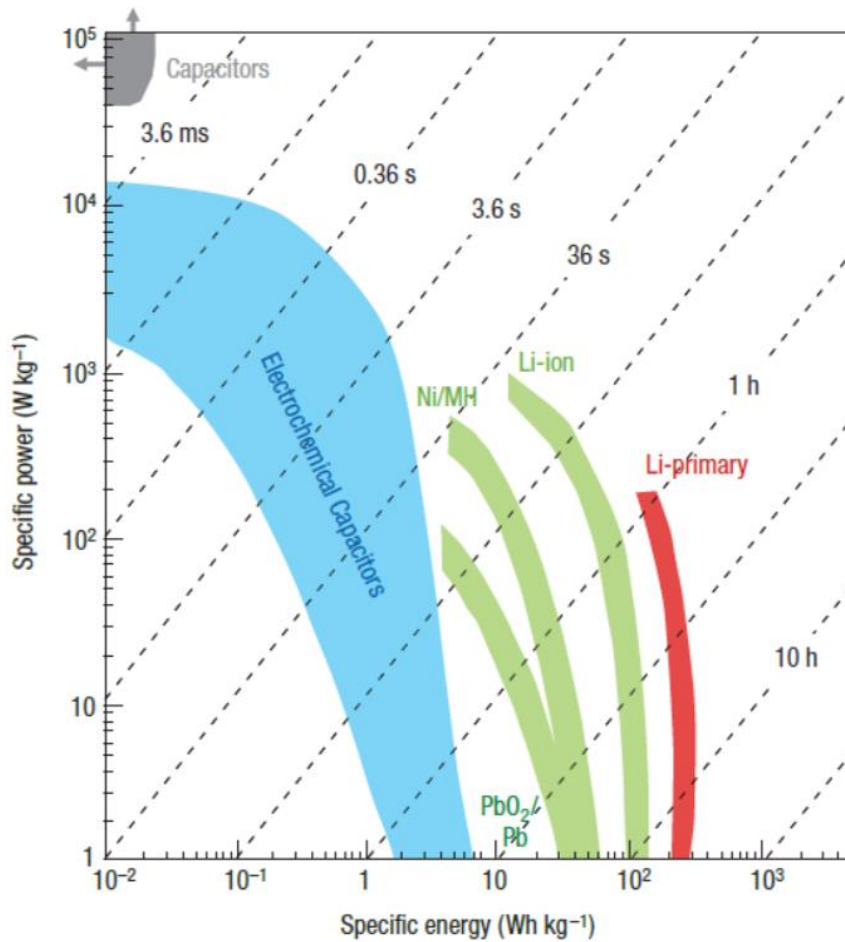


Figure 1.14 Ragone plot showing the representative of different energy storage devices.⁹⁹

1.7.1. Basic Components of Supercapacitor (SCs)

The supercapacitor is an electrochemical energy storage device that can operate to store electrical energy quickly and very slow discharge process as compared to commercial batteries and capacitors. The basic setup consists of two electrodes, two current collectors, a separator, and an electrolyte solution. Generally, the two porous electrodes having respective electro-active material coating by connecting with the current collector and dipped in the suitable electrolytic medium. The dielectric separator acts as an insulation between the two electrodes which can avoid the short circuit but allows the respective charge carriers to pass through it. While applying a

voltage through the current collector to the individual electrode corresponds to the ions of opposite charge towards itself. As a result, each ion accumulated on the surface of two electrodes and creates a layer of opposite ions, which generates energy during the discharging process. The performances of the SCs strongly depend on the components (such as types of electrodes, current collector, separator, and the electrolyte used, etc.) by which it is made up. The following advantages make SCs a suitable electrochemical cell than other devices.¹⁰⁰

- (1) Higher power density (greater than the battery)
- (2) High energy density (larger than capacitor)
- (3) Low-cost value
- (4) Safety system with easy operation.
- (5) Better cycle stability than battery
- (6) Faster charge/discharge in a second and very slow self-discharge process.

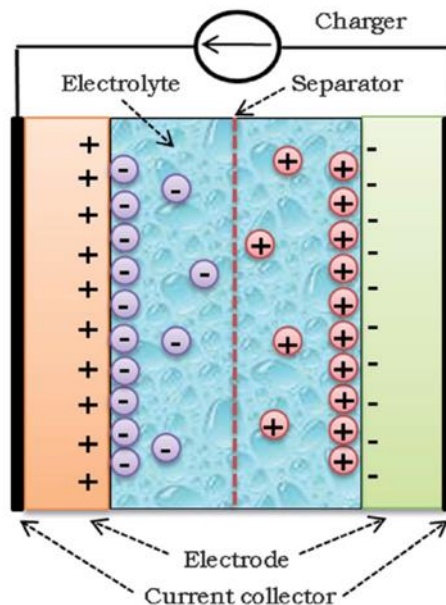


Figure 1.15 Schematic diagram of a supercapacitor cell.¹⁰⁰

1.7.2 Key parameters used in supercapacitor

The supercapacitor performances are evaluated through the standard parameter of specific capacitance or charge storage performances, energy density, power density, and cyclic stability with coulombic efficiency, respectively.

1.7.2.1 Specific capacitance

Specific capacitance (C_s) is portrayed as the capacitance of an as-prepared electrode active material obtained by the amount of charge stored with a potential change. And the observed capacitance was normalized to mass called gravimetric capacitance (F/g) for an area called areal capacitance (F/cm²), respectively. The value of specific capacitance for various electrode materials is monitored by a mass of sample loaded on the electrode surface, separator, presence of the electrolytic medium, the thickness, and the dimension of active material, are used. The value of specific capacitance (C_s) has been calculated from the cyclic voltammetry technique as well as the galvanostatic charge-discharge process.^{81,98}

1.7.2.2 Specific energy and Specific power

Specific energy or energy density and specific power or power density are two major factors that can be determined the further super capacitance performances of an ultra-capacitor. Both the specific energy and specific power of a supercapacitor device were evaluated from the obtained measurements of cyclic voltammetry (CV) and galvanostatic charge-discharge (GCD) techniques. The energy density of an as-prepared active material was calculated by using CV curve and represented in the equation (1.17),^{92,101}

$$E_d = \frac{1}{2} C_s (\Delta V)^2 \quad (1.17)$$

Similarly, the specific power or power density was evaluated from the CV data by using the equation as follows (1.18),^{59,101}

$$P_d = \frac{1}{2} C_s (\Delta V)r \quad (1.18)$$

Herein, E_d and P_d are the energy density in terms of Wh kg⁻¹ and power density of kW kg⁻¹, respectively. C_s is the specific capacitance, ΔV represents the specified potential window, and r is depicted as the scan rate at which all CV cycles were performed.

1.7.2.3 Cyclic stability and Coulombic efficiency

The supercapacitor efficiency was evaluated at a particular scan rate or current density by performing cyclic stability measurements. And the coulombic efficiency (η) was calculated by using the equation as follows:¹⁰¹

$$\eta = \frac{t_D}{t_C} \times 100\% \quad (1.19)$$

Where t_D is the discharge time in second, t_C is the charging time in second, and η represents the coulombic efficiency. While this the ratio of charging and discharging time in second.

1.7.3 Electrolytes used

The requirements of ideal electrolytes in the electrochemical capacitor (ES) are not only significantly enhance the charge storage capacity but also improves the high electrical stability, low solvated ionic radius, low resistivity, high ionic concentration and low toxicity, wide operational potential window, low volatility, light expensive with pure form availability.¹⁰⁰ Generally, the liquid electrolytes are used as aqueous and non-aqueous electrolytes. However, the ionic and organic electrolytes are corresponding to the non-aqueous electrolyte.

1.7.3.1 Aqueous electrolytes

The aqueous electrolytes have been prepared by using various inorganic compounds and from the group of salt materials. The aqueous electrolytes are highly conductive due to the availability of many solvated ions, which correspond to enhance the charge storage performances. Depending upon the P^H of the electrolyte solution, it has been group into acidic (H_2SO_4), alkaline (KOH, NaOH, etc.), and neutral solution (K_2SO_4 , Na_2SO_4 , KCl, etc.), respectively. The lower resistance and higher ionic concentration make as better electrolytes than the non-aqueous organic electrolyte. The electrochemical capacitor shows a higher value of storage capacitance and enhanced power density because of the lower ionic radius and higher ionic concentration. There is no need for a particular synthetic method and condition for the aqueous electrolytes. But the narrow range of operational voltage windows restricts to improves both the energy and power density.¹⁰⁰ Therefore, non-aqueous electrolytes of ionic liquid and organic electrolytes have come into the picture.

1.7.3.2 Non-aqueous electrolytes

Supreme advantages of non-aqueous electrolytes corresponding to a wide range of potential operational windows of voltage as high as 2.5-3.5 V compared to aqueous electrolytes. However, non-aqueous electrolytes are organic electrolytes and ionic liquids. Generally, the organic electrolytes of acetonitrile, propylene carbonate (PPC) are used in SCs cells due to the wide range of operational temperature and voltage window. But the use of propylene carbonate (PPC) is more favorable over acetonitrile because of its less toxic and environment-friendly nature.¹⁰⁰ Besides the ionic liquids are used, which is the mixture of cations and anions.¹⁰⁰ The cations refer to as organic or inorganic and anions as inorganic. The commonly used cationic/anionic ionic liquids in the fabrication of SCs devices such as sulfonium, imidazolium,

phosphonium, pyrrolidinium, ammonium salts, and the anions such as hexafluorophosphate, tetrafluoroborate, trifluoromethanesulfate, and bis(trifluoromethanesulfonyl) imide.^{102,103} Moreover, the high thermal and electrical stability, low vapor pressure, high electrochemical stability, and the high range of voltage windows make them use as a suitable electrolyte in SCs devices.^{102,104,105}

1.7.4 Calculation of super capacitance from various techniques

Different instrumental measurement techniques are used to evaluate the storage capacitance, specific energy, power density, cyclic stability, and the equivalent series resistance of an SCs device by using cyclic voltammetry (CV), galvanostatic charge-discharge (GCD), and the impedance spectroscopy or Nyquist plot respectively.

1.7.4.1 Cyclic voltammetry technique

The capacitance of the as-prepared electrode material is evaluated by the first characterization technique of cyclic voltammetry. The CV curve with a rectangular shape is obtained for an electric double-layer capacitor (EDLC) or some pseudo capacitor type (PC) material. In the case of EDLC, there is no faradic reaction of oxidation and reduction peaks to be observed. But the PC material shows prominent redox peaks, which is a highly reversible redox reaction. However, this information is insufficient to distinguish the EDLC and PC materials from the obtained CV curve. Both the two and three-electrode systems are used to record the CV data. In a specified potential window range, the specific capacitance of a supercapacitor electrode material is calculated at various scan rates in a suitable electrolytic medium. Behera *et al.* observed the value of specific capacitance of VSe₂/RGO (0.3 wt%) hybrids of 680 F/g at an applied current density of 1 A/g.⁵⁷ The value of specific capacitance is obtained by using the equation as follows:

$$C_s = \frac{1}{mv(V_a - V_b)} \int_{V_a}^{V_b} I(V) dV \quad (1.20)$$

Herein $\int_{V_a}^{V_b} I(V) dV$ is the area under the curve, m denotes the mass of the sample, s is the sweep rate, and $(V_a - V_b)$ represents the potential operating window, respectively.

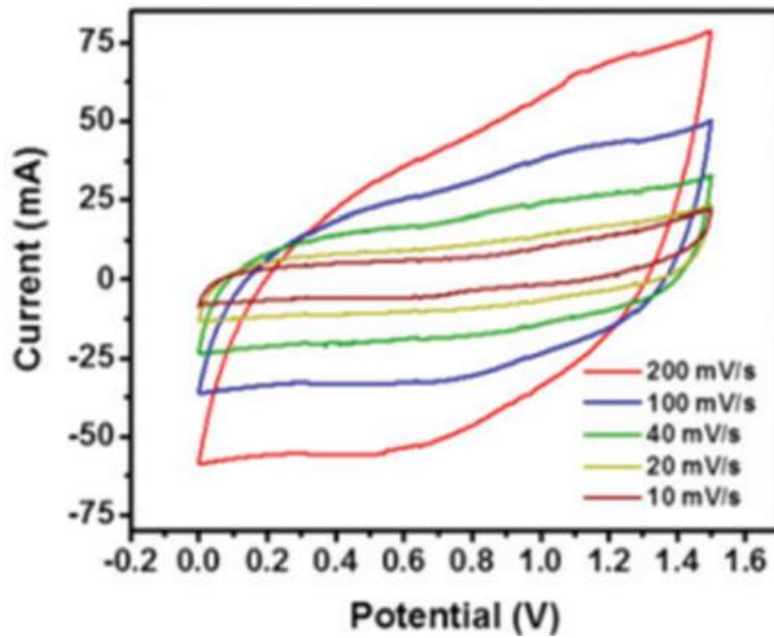


Figure 1.16 Cyclic voltammetry of VSe₂/RGO (0.3 wt%) curves at various scan rates.⁵⁷

1.7.4.2 Constant current charge/discharge

The significant advantage of this technique over CV measurements is not only due to the calculation of key parameters such as specific capacitance but also the energy density and power density, respectively. Moreover, the leakage, and the peak current, was measured by this technique. The constant current charge-discharge (CCCD) technique is also used for cyclic stability measurements. The modified electrode material's charge storage capacitance is determined from the CD curve as per the

following equations (1.21). The charge/discharge curve of VSe₂/RGO (0.3 wt%) is shown in Figure 1.17.⁵⁷

$$C = \frac{I \times \Delta t}{\Delta V \times m} F/g \quad (1.21)$$

I represent the discharge current in ampere (A), and Δt, Δv, m are the discharging time, discharging voltage, and mass of electrode material .

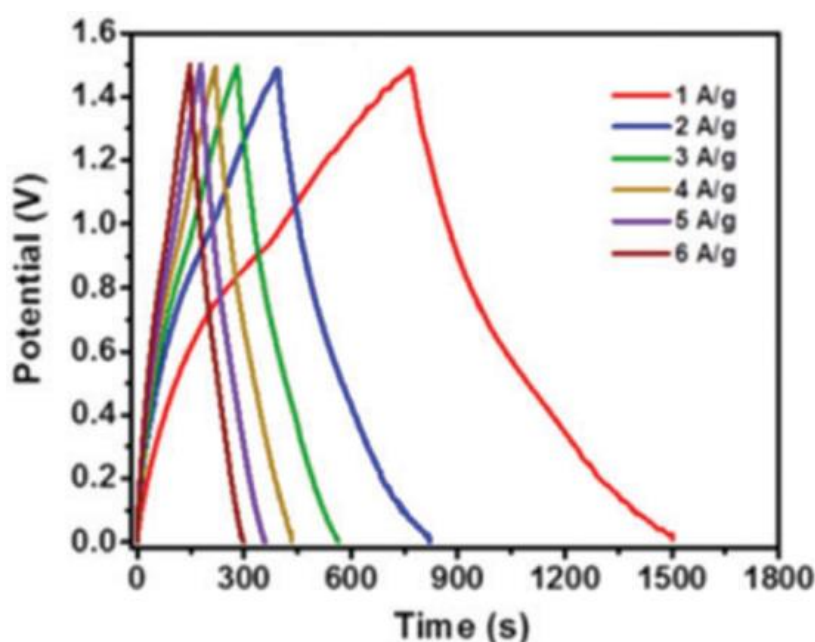


Figure 1.17 Charge discharge curve of VSe₂/RGO (0.3 wt%) at different current densities.⁵⁷

1.7.4.3 Electrochemical impedance spectroscopy (EIS)

The electrochemical impedance spectrum is used to analyze the intrinsic parameter of the modified electrode material and the electrolytes. Notably, this technique was done by calculating solution resistance, charge transfer resistance, mass transfer, specific capacitance value, specific energy, specific power, and charge storage mechanism. Generally, the graph represents the plots of imaginary part (Z'') versus real part (Z') in an electrolyte solution. The semi-circle region of the graph represents the charge

transfer resistance (R_{ct}). Further, the value of capacitance can be calculated in this region. Specific power or power density of active material increases with the decrease of charge transfer resistance. The diffusion of ions observed in the Warburg impedance region is the 45° phase angle from the semicircle region.^{98,100} The EIS spectrum of optimized 0.30 wt% of RGO hybrid VSe_2 sample with other compared material is shown in Figure 1.18, and the insert picture represents as the Randles circuit diagram.⁵⁷

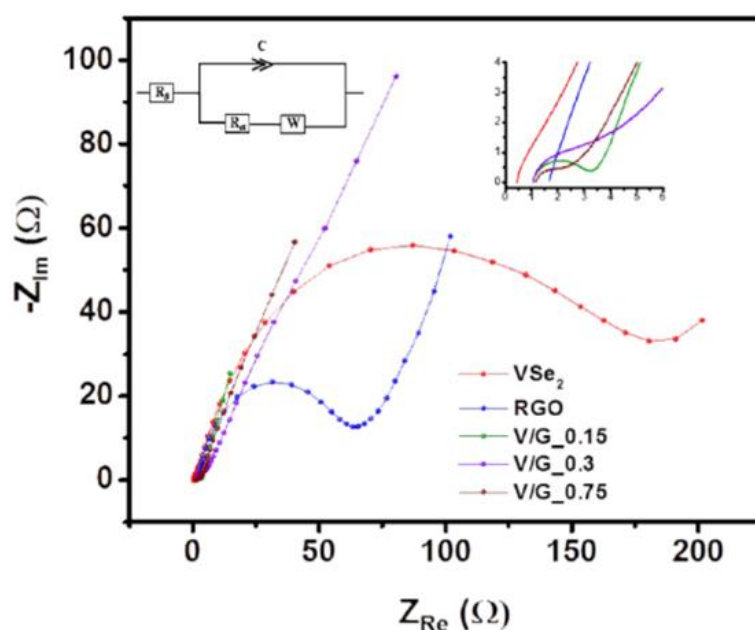


Figure 1.18 EIS of VSe_2 /RGO (0.3 wt%) and other as-synthesized material.⁵⁷

1.7.4.4 Cyclic stability

The verification of long-term performances and usability of the as-synthesized electrode material was dependent upon the cyclic stability performances. Both the CV and CD techniques are used at a particular scan value or current density to observe the stability test. The capacitance retention was also calculated in terms of percentage after the stability measurements.

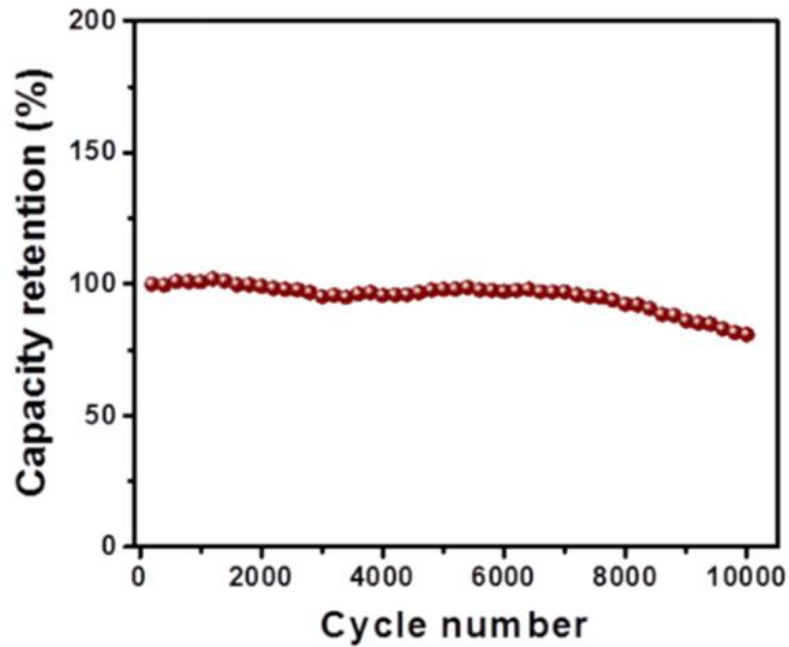
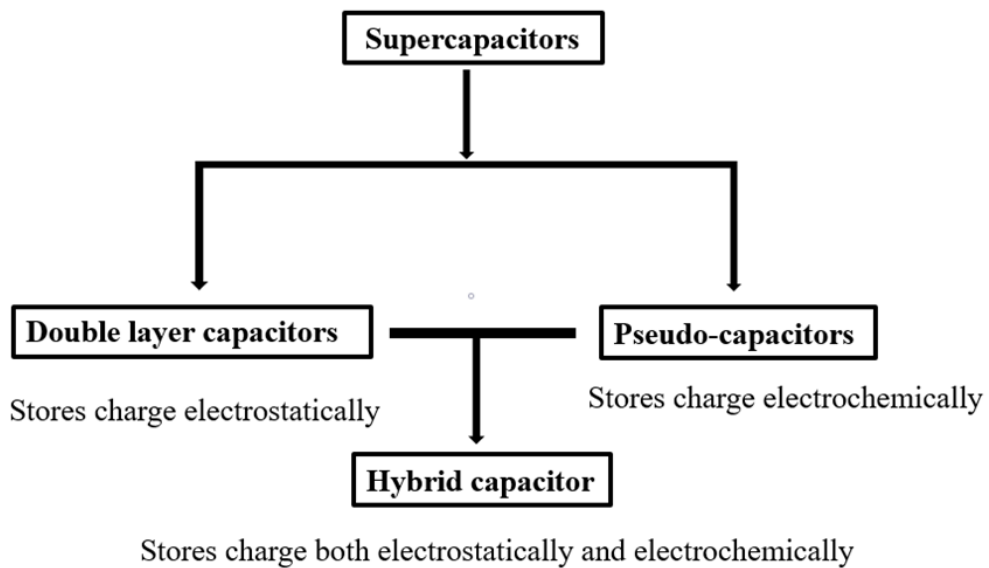


Figure 1.19 Long term cyclic number of VSe₂/RGO (0.3 wt%) hybrids.⁵⁷

1.7.5 Mechanism involved in SCs

The classification and mechanism of a supercapacitor are basing upon the material used for an energy storage system. The SCs are categorized as,



1.7.5.1 Electrical double-layer mechanism

The electric double layer (EDL) type capacitors are following non-faradic reactions. The mechanism of stores charge and energy is a completely electrostatic process. The electric double layer concept belongs to forming the two layers of opposite charge on two interfaces consisting of a minimal distance separating a molecular dielectric. As the voltage is applied, the movements of ions or the accumulation of charge take place on the respective electrode of the opposite charge. The electrolyte is used for the creation of an ion-rich environment. In the 19th century, Helmholtz proposed the first theoretical model for the EDL-type capacitor. According to the Helmholtz model, the charge accumulation process forming the inner and outer layers of the Helmholtz plane between the surface of the current collector and the electrolyte. The stores of electric charge are directly proportional to the voltage applied to the EDL system. Generally, the carbon-based electrode material (graphene, activated carbon, carbon nanotubes, etc.) is shown this type of mechanism.

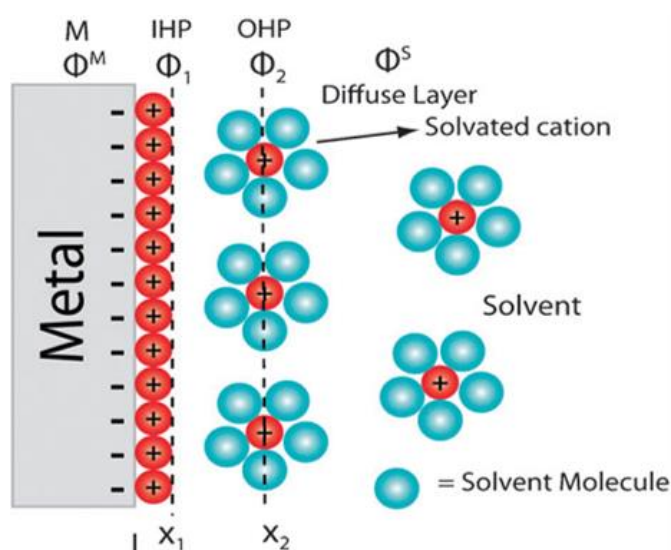


Figure 1.20 Helmholtz model for the electrical double-layers.¹⁰⁶

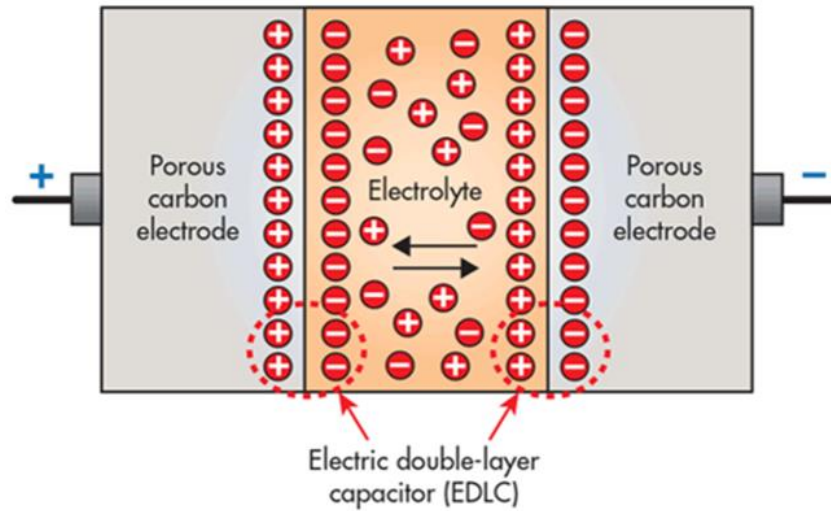


Figure 1.21 Representation of charge accumulation process in EDL type capacitor.¹⁰⁷

1.7.5.2 Mechanism of Pseudocapacitance (PC)

The electrode material used for the pseudocapacitor belongs to the faradic reaction that corresponds to both oxidation and reduction reactions. Different metal oxides like RuO_2 , Co_3O_4 , MnO_2 , and the conducting polymer shows the redox type behavior during the electrochemical measurements. The energy stores in the pseudocapacitor are due to the conduct of charge between the active electrode material and the aqueous electrolyte solution. A mechanism of charge transfer arises from the intercalation of ions, redox reaction, and adsorption process. The high energy density and higher capacitance value are the main advantages of PC over the EDL-type capacitor. But the redox behavior of this capacitor is giving poor results during the stability test. It has been observed that the slower faradic process of the pseudo capacitor as compared to the double-layer capacitor exhibits a lower power density.

1.7.5.3 Hybrid Supercapacitor (HS)

The hybrid capacitor is used for the design of highly efficient asymmetric-type supercapacitor devices. The hybridization of carbon-based electrode material (EDLC

type mechanism) and redox-active electrode material (pseudocapacitance mechanism) gives a hybrid capacitor. Therefore the observed specific capacitance for a hybrid capacitor is the combination of both mechanisms, where one is dominant over the other. The hybrid supercapacitor performances strongly depend upon the type of electrode material, electrolyte, separator, and other core components of the current collector during the fabrication process. The advantage of HS's belongs to high energy and power density with high cell voltage. For example, Wang et al. fabricated a hybrid capacitor, corresponding to highly porous graphitic carbon fibers (HPGCFs) as a positive electrode and anthraquinone functionalized HPGCFs as negative electrodes, respectively. While this hybrid capacitor gives excellent SCs performances in terms of higher energy density (19.3 Wh kg^{-1}) with better power supplying capability.¹⁰⁸

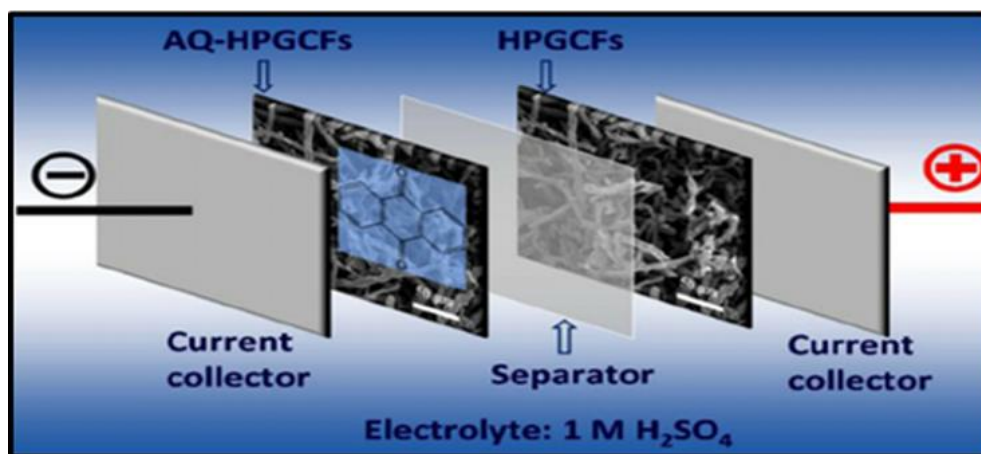


Figure 1.22 Schematic diagram of hybrid capacitor in 1 M H₂SO₄ electrolyte.¹⁰⁸

1.8 Supercapacitance of TMCs and Graphene hybrids

The electrochemical and physical properties of pristine TMCs were further improved by the hybridization of graphene material, which exhibits enhanced super capacitance performances.⁵⁹ The super capacitance of the hybrid material exhibits in terms of specific capacitance, higher energy density, and greater supply of power density value.

The extraordinary mechanical support and electronic properties make graphene a suitable composite material than other carbon-based materials. The uniform pore size and high surface area of graphene draw an expansive attraction in the energy field area.⁴⁹ Besides specific capacitance, it has been observed that the efficiency of the electrode material in SCs corresponding to the higher value of power supply capability and larger cycle number obtained during the stability test. The TMCs/RGO hybrids electrode material shows a better value of power density and coulombic efficacy than other pseudocapacitors/EDL hybrid material. Likely, Rout *et al.* investigated the hydrothermal method of synthesis of ternary hybrids having a higher value of power density (13.85 kW/kg) and obtained the retention of 80% after 5000 of constant charge/discharge cycle.⁵⁹ Likewise, VSe₂/RGO hybrids material performed 10000 of the repeated charge-discharge process and shows the power density of 3.3 kW/kg to check the usability in practical application.⁵⁷

1.9 Supercapacitance of TMPs

Transition metal phosphides (TMPs) have drawn great heed for the energy storage system developments because of the superior electrical conductivity, metallic features, and rich chemical state.¹⁰⁹ The transition metal of single or binary-based phosphides electrode material has already demonstrated their electrocatalytic performances towards HER/OER in much-reported literature.^{92,94,96,110} Particularly, the bimetallic phosphides electrode material is higher in electrochemical activity than that of single metal phosphides due to the availability of a multimetal charge transfer center.^{92,110} Interestingly, several reports on TMPs act as a non-hybrids electrode material to improve super capacitance performances.^{111,112} While this efficient nature of TMPs strongly depends on the various synthetic methods and controlled reaction conditions

from which it can be synthesized.^{27,112} For example, Gao *et al.* developed a novel urchin-like bimetallic NiCoP hollow sphere by following the two-step synthetic method corresponding to hydrothermal synthesis followed by phosphorization. It exhibits the specific capacity of 761 mAh/g at an applied current density of 1 A/g.¹¹³ Wang *et al.* have been synthesized Co₂P nanoflowers and observed a specific capacitance of 416 F/g at a current value of 1 A/g.¹¹⁴

2.0 References

- 1 <https://www.bernini-impianti.it/it/news-eventi-bernini-impianti.html?cat=1>
- 2 A. K. Samantara and S. Ratha, eds. A. K. Samantara and S. Ratha, Springer International Publishing, Cham, 2019, pp. 69–77.
- 3 J. O. Bockris, *Int. J. Hydrogen Energy*, 2002, **27**, 731–740.
- 4 A. K. Samantara and S. Ratha, *Metal Oxides/Chalcogenides and Composites: Emerging Materials for Electrochemical Water Splitting*, Springer International Publishing, 2019.
- 5 M. D. Leonard, E. E. Michaelides and D. N. Michaelides, *Renew. Energy*, 2020, **145**, 951–962.
- 6 K. T. Møller, T. R. Jensen, E. Akiba and H. Li, *Prog. Nat. Sci. Mater. Int.*, 2017, **27**, 34–40.
- 7 Y. Jiao, Y. Zheng, M. Jaroniec and S. Z. Qiao, *Chem. Soc. Rev.*, 2015, **44**, 2060–2086.
- 8 X. Wang, Y. Oriyasa and Y. Uchimoto, *ACS Catal.*, 2016, **6**, 4195–4198.
- 9 Y. Lee, J. Suntivich, K. J. May, E. E. Perry and Y. Shao-Horn, *J. Phys. Chem. Lett.*, 2012, **3**, 399–404.

- 10 S. M. Alia, S. Shulda, C. Ngo, S. Pylypenko and B. S. Pivovarov, *ACS Catal.*, 2018, **8**, 2111–2120.
- 11 N. Mamaca, E. Mayousse, S. Arrii-Clacens, T. W. Napporn, K. Servat, N. Guillet and K. B. Kokoh, *Appl. Catal. B Environ.*, 2012, **111–112**, 376–380.
- 12 N. Cheng, S. Stambula, D. Wang, M. N. Banis, J. Liu, A. Riese, B. Xiao, R. Li, T.-K. Sham, L.-M. Liu, G. A. Botton and X. Sun, *Nat. Commun.*, 2016, **7**, 13638.
- 13 X. Chia, A. Y. S. Eng, A. Ambrosi, S. M. Tan and M. Pumera, *Chem. Rev.*, 2015, **115**, 11941–11966.
- 14 A. K. Samantara, S. Kamila, A. Ghosh and B. K. Jena, *Electrochim. Acta*, 2018, **263**, 147–157.
- 15 J. Zhou, C. Zhang, T. Niu, R. Huang, S. Li, J. Z. Zhang and J. G. Chen, *ACS Appl. Energy Mater.*, 2018, **1**, 4599–4605.
- 16 Y. Pei, Y. Cheng, J. Chen, W. Smith, P. Dong, P. M. Ajayan, M. Ye and J. Shen, *J. Mater. Chem. A*, 2018, **6**, 23220–23243.
- 17 Q. Wang, C.-S. Cha, J. Lu and L. Zhuang, *Phys. Chem. Chem. Phys.*, 2009, **11**, 679–687.
- 18 X. Zou and Y. Zhang, *Chem. Soc. Rev.*, 2015, **44**, 5148–5180.
- 19 N.-T. Suen, S.-F. Hung, Q. Quan, N. Zhang, Y.-J. Xu and H. M. Chen, *Chem. Soc. Rev.*, 2017, **46**, 337–365.
- 20 S. Anantharaj, S. R. Ede, K. Sakthikumar, K. Karthick, S. Mishra and S. Kundu, *ACS Catal.*, 2016, **6**, 8069–8097.
- 21 M. Zeng and Y. Li, *J. Mater. Chem. A*, 2015, **3**, 14942–14962.
- 22 Y. Yan, T. He, B. Zhao, K. Qi, H. Liu and B. Y. Xia, *J. Mater. Chem. A*, 2018,

- 6, 15905–15926.
- 23 J. Wei, M. Zhou, A. Long, Y. Xue, H. Liao, C. Wei and Z. J. Xu, *Nano-Micro Lett.*, 2018, **10**, 75.
- 24 J. Mohammed-Ibrahim and X. Sun, *J. Energy Chem.*, 2019, **34**, 111–160.
- 25 N. Dubouis and A. Grimaud, *Chem. Sci.*, 2019, **10**, 9165–9181.
- 26 Z. Cai, X. Bu, P. Wang, J. C. Ho, J. Yang and X. Wang, *J. Mater. Chem. A*, 2019, **7**, 5069–5089.
- 27 Y. Shi and B. Zhang, *Chem. Soc. Rev.*, 2016, **45**, 1529–1541.
- 28 K. R. Cooper and M. Smith, *J. Power Sources*, 2006, **160**, 1088–1095.
- 29 Q. Gao, W. Zhang, Z. Shi, L. Yang and Y. Tang, *Adv. Mater.*, 2019, **31**, 1802880.
- 30 J. D. Benck, T. R. Hellstern, J. Kibsgaard, P. Chakthranont and T. F. Jaramillo, *ACS Catal.*, 2014, **4**, 3957.
- 31 E. Fabbri, A. Habereder, K. Waltar, R. Kötz and T. J. Schmidt, *Catal. Sci. Technol.*, 2014, **4**, 3800–3821.
- 32 R. D. L. Smith, M. S. Prévot, R. D. Fagan, S. Trudel and C. P. Berlinguette, *J. Am. Chem. Soc.*, 2013, **135**, 11580–11586.
- 33 P. Xiao, M. A. Sk, L. Thia, X. Ge, R. J. Lim, J.-Y. Wang, K. H. Lim and X. Wang, *Energy Environ. Sci.*, 2014, **7**, 2624–2629.
- 34 Y.-Y. Zhang, X. Zhang, Z.-Y. Wu, B.-B. Zhang, Y. Zhang, W.-J. Jiang, Y.-G. Yang, Q.-H. Kong and J.-S. Hu, *J. Mater. Chem. A*, 2019, **7**, 5195–5200.
- 35 J. Zang, S.-J. Bao, C. M. Li, H. Bian, X. Cui, Q. Bao, C. Q. Sun, J. Guo and K. Lian, *J. Phys. Chem. C*, 2008, **112**, 14843–14847.
- 36 Y.-Y. Liang, H. L. Li and X.-G. Zhang, *J. Power Sources*, 2007, **173**, 599–605.

- 37 J. K. Das, A. K. Samantara, A. K. Nayak, D. Pradhan and J. N. Behera, *Dalton Trans.*, 2018, **47**, 13792–13799.
- 38 A. Dutta, A. K. Samantara, S. K. Dutta, B. K. Jena and N. Pradhan, *ACS Energy Lett.*, 2016, **1**, 169–174.
- 39 C. C. L. McCrory, S. Jung, J. C. Peters and T. F. Jaramillo, *J. Am. Chem. Soc.*, 2013, **135**, 16977–16987.
- 40 T. Y. Ma, S. Dai, M. Jaroniec and S. Z. Qiao, *J. Am. Chem. Soc.*, 2014, **136**, 13925–13931.
- 41 C. Tang, W. Wang, A. Sun, C. Qi, D. Zhang, Z. Wu and D. Wang, *ACS Catal.*, 2015, **5**, 6956–6963.
- 42 C. Zhang, Y. Huang, Y. Yu, J. Zhang, S. Zhuo and B. Zhang, *Chem. Sci.*, 2017, **8**, 2769–2775.
- 43 M. Gao, W. Sheng, Z. Zhuang, Q. Fang, S. Gu, J. Jiang and Y. Yan, *J. Am. Chem. Soc.*, 2014, **136**, 7077–7084.
- 44 G. Zhao, K. Rui, S. X. Dou and W. Sun, *Adv. Funct. Mater.*, 2018, **28**, 1803291.
- 45 C. Costentin, S. Drouet, M. Robert and J.-M. Savéant, *J. Am. Chem. Soc.*, 2012, **134**, 11235–11242.
- 46 J. J. Lingane, *J. Electroanal. Chem.*, 1961, **2**, 296–309.
- 47 V. D. Patake and C. D. Lokhande, *Appl. Surf. Sci.*, 2008, **254**, 2820–2824.
- 48 C.-C. Hu, K.-H. Chang, M.-C. Lin and Y.-T. Wu, *Nano Lett.*, 2006, **6**, 2690–2695.
- 49 Q. Tang and Z. Zhou, *Prog. Mater. Sci.*, 2013, **58**, 1244.
- 50 M. Endo, T. Maeda, T. Takeda, Y. J. Kim, K. Koshiba, H. Hara and M. S. Dresselhaus, *J. Electrochem. Soc.*, 2001, **148**, A910.

- 51 E. Raymundo-Piñero, K. Kierzek, J. Machnikowski and F. Béguin, *Carbon N. Y.*, 2006, **44**, 2498–2507.
- 52 D. Qu and H. Shi, *J. Power Sources*, 1998, **74**, 99–107.
- 53 S. Shiraishi, H. Kurihara, K. Okabe, D. Hulicova and A. Oya, *Electrochem. commun.*, 2002, **4**, 593–598.
- 54 B. Xu, F. Wu, R. Chen, G. Cao, S. Chen, Z. Zhou and Y. Yang, *Electrochem. commun.*, 2008, **10**, 795–797.
- 55 J. Lee, J. Kim and T. Hyeon, *Adv. Mater.*, 2006, **18**, 2073–2094.
- 56 B. Fang and L. Binder, *J. Power Sources*, 2006, **163**, 616–622.
- 57 S. R. Marri, S. Ratha, C. S. Rout and J. N. Behera, *Chem. Commun.*, 2017, **53**, 228–231.
- 58 H. Wang, Z. Li, G. Li, F. Peng and H. Yu, *Catal. Today*, 2015, **245**, 74–78.
- 59 S. Ratha, S. R. Marri, J. N. Behera and C. S. Rout, *Eur. J. Inorg. Chem.*, 2016, **2016**, 259–265.
- 60 P. M. Ajayan and O. Z. Zhou, eds. M. S. Dresselhaus, G. Dresselhaus and P. Avouris, Springer Berlin Heidelberg, Berlin, Heidelberg, 2001, pp. 391–425.
- 61 M. Inagaki, H. Konno and O. Tanaike, *J. Power Sources*, 2010, **195**, 7880–7903.
- 62 Y. Zheng, Y. Jiao, L. H. Li, T. Xing, Y. Chen, M. Jaroniec and S. Z. Qiao, *ACS Nano*, 2014, **8**, 5290–5296.
- 63 J. K. Kim, G. D. Park, J. H. Kim, S.-K. Park and Y. C. Kang, *Small*, 2017, **13**, 1700068.
- 64 S. Ratha, S. R. Marri, N. A. Lanzillo, S. Moshkalev, S. K. Nayak, J. N. Behera and C. S. Rout, *J. Mater. Chem. A*, 2015, **3**, 18874–18881.

- 65 C. Merino, P. Soto, E. Vilaplana-Ortego, J. M. Gomez de Salazar, F. Pico and J. M. Rojo, *Carbon N. Y.*, 2005, **43**, 551–557.
- 66 C. Portet, P. L. Taberna, P. Simon and E. Flahaut, *J. Power Sources*, 2005, **139**, 371–378.
- 67 D.-D. Zhao, S.-J. Bao, W.-J. Zhou and H.-L. Li, *Electrochem. commun.*, 2007, **9**, 869–874.
- 68 V. D. Silva, T. A. Simões, J. P. F. Grilo, E. S. Medeiros and D. A. Macedo, *J. Mater. Sci.*, 2020, **55**, 6648–6659.
- 69 R. Zhang, Y.-C. Zhang, L. Pan, G.-Q. Shen, N. Mahmood, Y.-H. Ma, Y. Shi, W. Jia, L. Wang, X. Zhang, W. Xu and J.-J. Zou, *ACS Catal.*, 2018, **8**, 3803–3811.
- 70 M. Li, F. Pan, E. S. G. Choo, Y. Lv, Y. Chen and J. Xue, *ACS Appl. Mater. Interfaces*, 2016, **8**, 6972–6981.
- 71 Y. Gao, S. Chen, D. Cao, G. Wang and J. Yin, *J. Power Sources*, 2010, **195**, 1757–1760.
- 72 P. Ragupathy, D. H. Park, G. Campet, H. N. Vasan, S.-J. Hwang, J.-H. Choy and N. Munichandraiah, *J. Phys. Chem. C*, 2009, **113**, 6303–6309.
- 73 M. Chhowalla, H. S. Shin, G. Eda, L.-J. Li, K. P. Loh and H. Zhang, *Nat. Chem.*, 2013, **5**, 263.
- 74 X. Huang, Z. Zeng and H. Zhang, *Chem. Soc. Rev.*, 2013, **42**, 1934–1946.
- 75 M. R. Gao, Y. F. Xu, J. Jiang and S. H. Yu, *Chem. Soc. Rev.*, 2013, **42**, 2986.
- 76 C. Tan and H. Zhang, *Chem. Soc. Rev.*, 2015, **44**, 2713–2731.
- 77 J. H. Han, S. Lee and J. Cheon, *Chem. Soc. Rev.*, 2013, **42**, 2581–2591.
- 78 B. Yu, X. Wang, F. Qi, B. Zheng, J. He, J. Lin, W. Zhang, Y. Li and Y. Chen,

- ACS Appl. Mater. Interfaces*, 2017, **9**, 7154–7159.
- 79 B. Guo, K. Yu, H. Li, H. Song, Y. Zhang, X. Lei, H. Fu, Y. Tan and Z. Zhu, *ACS Appl. Mater. Interfaces*, 2016, **8**, 5517–5525.
- 80 I. H. Kwak, H. S. Im, D. M. Jang, Y. W. Kim, K. Park, Y. R. Lim, E. H. Cha and J. Park, *ACS Appl. Mater. Interfaces*, 2016, **8**, 5327–5334.
- 81 S. Ratha and C. S. Rout, *ACS Appl. Mater. Interfaces*, 2013, **5**, 11427.
- 82 X. Wang, J. Ding, S. Yao, X. Wu, Q. Feng, Z. Wang and B. Geng, *J. Mater. Chem. A*, 2014, **2**, 15958.
- 83 X. Rui, H. Tan and Q. Yan, *Nanoscale*, 2014, **6**, 9889–9924.
- 84 D. Li, M. B. Müller, S. Gilje, R. B. Kaner and G. G. Wallace, *Nat. Nanotechnol.*, 2008, **3**, 101–105.
- 85 S. Ahn, J. Yang, H. Lim and H. S. Shin, *Nano Converg.*, 2016, **3**, 5.
- 86 A. Kagkoura, I. Tzanidis, V. Dracopoulos, N. Tagmatarchis and D. Tasis, *Chem. Commun.*, 2019, **55**, 2078–2081.
- 87 C. Tang, N. Cheng, Z. Pu, W. Xing and X. Sun, *Angew. Chemie Int. Ed.*, 2015, **54**, 9351–9355.
- 88 K. Yurekli, C. A. Mitchell and R. Krishnamoorti, *J. Am. Chem. Soc.*, 2004, **126**, 9902–9903.
- 89 A. Garg and S. B. Sinnott, *Chem. Phys. Lett.*, 1998, **295**, 273–278.
- 90 H. Yuan, J. Li, C. Yuan and Z. He, *ChemElectroChem*, 2014, **1**, 1828–1833.
- 91 G. Zhang, X. Zheng, Q. Xu, J. Zhang, W. Liu and J. Chen, *J. Mater. Chem. A*, 2018, **6**, 4793–4800.
- 92 J. K. Das, A. K. Samantara, S. Satyarthi, C. S. Rout and J. N. Behera, *RSC Adv.*, 2020, **10**, 4650–4656.

- 93 J. Masud, S. Umapathi, N. Ashokaan and M. Nath, *J. Mater. Chem. A*, 2016, **4**, 9750–9754.
- 94 P. Jiang, Q. Liu and X. Sun, *Nanoscale*, 2014, **6**, 13440–13445.
- 95 X. Zhang, X. Yu, L. Zhang, F. Zhou, Y. Liang and R. Wang, *Adv. Funct. Mater.*, 2018, **28**, 1706523.
- 96 M. Pi, T. Wu, D. Zhang, S. Chen and S. Wang, *Nanoscale*, 2016, **8**, 19779–19786.
- 97 L. Tian, X. Yan and X. Chen, *ACS Catal.*, 2016, **6**, 5441–5448.
- 98 M. Winter and R. J. Brodd, *Chem. Rev.*, 2004, **104**, 4245–4270.
- 99 P. Simon and Y. Gogotsi, *Nat. Mater.*, 2008, **7**, 845.
- 100 G. Wang, L. Zhang and J. Zhang, *Chem. Soc. Rev.*, 2012, **41**, 797–828.
- 101 J. K. Das, A. K. Samantara, S. R. K. A., C. S. Rout and J. N. Behera, *Dalton Trans.*, 2019, **48**, 15955–15961.
- 102 M. Galiński, A. Lewandowski and I. Stepniak, *Electrochim. Acta*, 2006, **51**, 5567–5580.
- 103 A. Lewandowski and M. Galiński, *J. Phys. Chem. Solids*, 2004, **65**, 281–286.
- 104 G. A. Snook, P. Kao and A. S. Best, *J. Power Sources*, 2011, **196**, 1–12.
- 105 H. OHNO and K. FUKUMOTO, *Electrochemistry*, 2008, **76**, 16–23.
- 106 H. Du, X. Lin, Z. Xu and D. Chu, *J. Mater. Sci.*, 2015, **50**, 5641–5673.
- 107 M. Faisal, M. A. Hannan, P. J. Ker, A. Hussain, M. B. Mansor and F. Blaabjerg, *IEEE Access*, 2018, **6**, 35143–35164.
- 108 H. Wang, H. Yi, C. Zhu, X. Wang and H. Jin Fan, *Nano Energy*, 2015, **13**, 658–669.
- 109 X. Wang, H.-M. Kim, Y. Xiao and Y.-K. Sun, *J. Mater. Chem. A*, 2016, **4**,

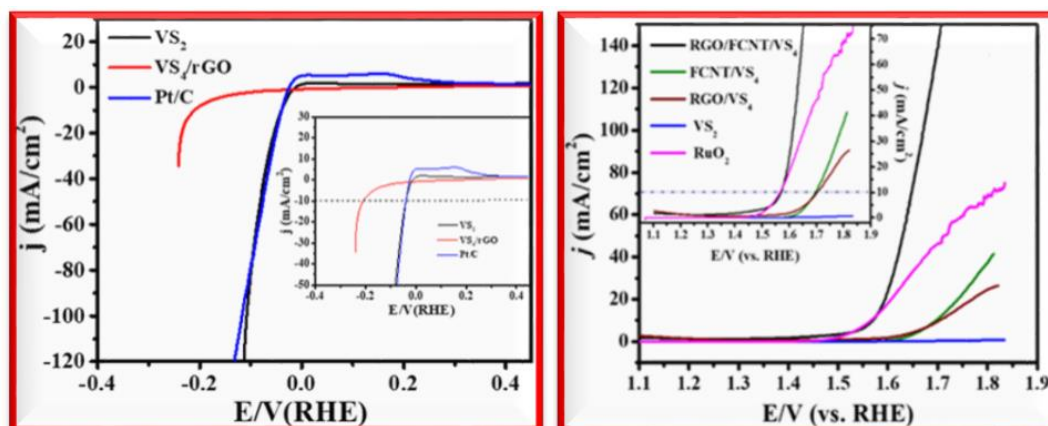
- 14915–14931.
- 110 C. Du, L. Yang, F. Yang, G. Cheng and W. Luo, *ACS Catal.*, 2017, **7**, 4131–4137.
- 111 Y. Jin, C. Zhao, Y. Wang, Q. Jiang, C. Ji and M. Jia, *Ionics (Kiel)*, 2017, **23**, 3249–3254.
- 112 J. Theerthagiri, G. Durai, K. Karuppasamy, P. Arunachalam, V. Elakkiya, P. Kuppusami, T. Maiyalagan and H.-S. Kim, *J. Ind. Eng. Chem.*, 2018, **67**, 12–27.
- 113 M. Gao, W.-K. Wang, X. Zhang, J. Jiang and H.-Q. Yu, *J. Phys. Chem. C*, 2018, **122**, 25174–25182.
- 114 X. Chen, M. Cheng, D. Chen and R. Wang, *ACS Appl. Mater. Interfaces*, 2016, **8**, 3892–3900.

CHAPTER-2

Energy Conversion based on VS₂ and RGO/FCNTs/VS₄ Hybrids

- 2.1** Abstract section
- 2.2** Introduction part
- 2.3** Motivational work
- 2.4** Experimental section
 - 2.4.1** Synthesis of GO and functionalization of CNTs
 - 2.4.2** Synthesis of pristine VS₂ layers
 - 2.4.3** Synthesis of RGO/ VS₄ hybrids
 - 2.4.4** Synthesis of FCNTs/ VS₄ hybrids
 - 2.4.5** Synthesis of RGO/FCNTs/VS₄ hybrids
- 2.5** Characterization
- 2.6** Electrochemical measurements
- 2.7** Calculations of ECSA and R_f
- 2.8** Results and discussions
- 2.9** Conclusions
- 2.10** References

2.1 Abstract



This chapter includes simple hydrothermal synthesis of 2D VS₂ layers and 1D patronite hybrids of RGO/FCNTs/VS₄. The detailed electrocatalytic studied of bare Vanadium chalcogenides, and RGO/FCNTs hybrids showed enhanced hydrogen evolution reaction (HER) and oxygen evolution reaction (OER) in an acidic (0.1 M H₂SO₄) and alkaline (1 M KOH) electrolytic medium. VS₂ modified electrode material shows better hydrogen evolution activity in terms of lower onset value (15 mV vs. RHE) with a notably low Tafel slope (36 mV/dec, close to Pt/C). It needed only 41 mV of overpotential to deliver 10 mA/cm² current density. Further cyclic stability of VS₂ electrode material displays a small change in overpotential even after 10 h and 43 h of constant electrolysis. Secondly, the patronite hybrids of RGO/FCNTs/VS₄ significantly enhanced the oxygen evolution activity by the synergistic effects of individual components of VS₄, RGO, and functionalized single-walled CNTs. The hybrids electrode material needs only 330 mV overpotential to achieve the benchmarked current density of 10 mA/cm² and a lower Tafel slope of 43 mV/dec, respectively. Moreover, substantial active sites, higher ECSA values, and 15 h of constant electrolysis or durability make the composites electrocatalytic more active.

2.2 Introduction

Electrochemical water splitting is the simple and cleanest path for renewable energy sources that display hydrogen and oxygen production, such as chemical fuels. It consists of two half-cell reactions, whereas hydrogen evolution occurs at the cathode, simultaneously oxygen evolution occurs at the anode involving two and four-step electron processes in the respective solution media to evolve the renewable gases.^{1,2} Electrochemical process is a surface phenomenon, and the additional potential required to overcome the energy barrier is called overpotential, which could break the hydrogen bond associated with water molecules. noble metal-based highly active electrocatalyst like platinum (Pt) for HER and oxide of ruthenium and iridium (RuO_2 , IrO_2 , etc.) for OER are used to minimize the kinetic barrier in the electrolysis process.³ But their low availability, high expensive nature, and poor durability limit their use in commercial applications. Therefore, it's urgent to develop an efficient, inexpensive, and sustainable electrocatalyst, which performances close to precious metals in the HER and OER processes. A recent study focused on developing 2D layered structures of transition metal dichalcogenides (TMDCs) gathers excellent attention due to their physicochemical properties and likely to replace precious metal in terms of earth-abundant nature as well as good electrocatalytic activity.⁴⁻⁶ The TMDCs have been reported in their hybrids and their pristine form. The popularity of the electrode material is well known in the energy storage and conversion process and the one-step synthetic route through which it can be synthesized.⁷ Besides, the use of RGO (reduced graphene oxide) and CNTs (carbon nanotubes) are the supporting hybrids or composite materials that give mechanical support and improve the charge transport process of the bare TMDCs.^{8,9} The pristine and hybrids form of metal chalcogenides

were synthesized, and their various performances were explored in the energy fields. For example, pristine sulfides or selenides such as WS_2 , MoS_2 , NiS_2 , CoS_2 , and carbon-based RGO or CNTs hybrid materials MoS_2/RGO , WS_2/RGO are reported in the various research fields and yield even superior results.^{10–16} However, from the group of TMDCs compounds, Vanadium based chalcogenides (sulfides/selenides) have shown significant consequences for both the energy storage and the conversion process.^{5,17–20} Besides these, the lower specific capacity values and restacking characters of TMDCs are further resolved by the hybridization of different carbonaceous materials such as a reduced form of graphene oxide named RGO. The functionalization of single/multi-ordered carbon nanotubes as FCNTs, corresponding to catalytic site improvements, increase in surface area, good electrical conductivity, and faster ions transportation.^{8,21} In this chapter, we synthesized vanadium chalcogenides and their hybrid material forms of bare VS_2 layers, VS_4 with reduced graphene oxide hybrids, and both the FCNTs and RGO composites of patronite VS_4 in a well-known hydrothermal method. We explored its electrocatalytic study towards hydrogen and oxygen evolution reaction. The two-dimensional layered hexagonal type crystal arrangements of VS_2 may spare more active sites regarding the basal plane and edge site. These active sites further improve the HER performances of VS_2 compared to the one-dimensional crystal structure of RGO hybrids VS_4 . The patronite VS_4 has a 1D linear chain structure and consists of two sulfides (S_2^{2-}) dimer units. The conversion of VS_2 to VS_4 was carried out by graphene oxide in the hydrothermal method.⁵ However, the presence of RGO in VS_4 hybrids shows poor HER activity compared to pristine VS_2 layers. Additionally, considering the advantages of FCNTs,^{22–27} we synthesized RGO/FCNTs/ VS_4 , a ternary hybrids material, and

explored the performances in the field of electrolysis towards oxygen evolution reaction (OER). The synergistic effect of both RGO and FCNTs like carbonaceous materials provide the proper nucleation route for the conversions of VS_2 to VS_4 and activate the catalytic sites of 1D VS_4 with accessible surface area, easy charge transportation, better conductivity, and well mechanical stability, which optimized the ternary hybrid to catalytically more active.⁸ The electrochemical measurements of RGO/FCNTs/ VS_4 towards oxygen evolution are rarely reported. Interestingly, the OER activity of RGO/FCNTs/ VS_4 shows better performances than the synthesized pristine VS_2 layers, RGO/ VS_4 and FCNTs/ VS_4 , respectively.

2.3 Motivation of our Work

Vanadium chalcogenides of pristine VS_2 layers, RGO hybrid of VS_4 , and both RGO/FCNTs hybrids of VS_4 have been successfully synthesized hydrothermally and used as an alternative electrocatalyst to replace the precious metal such as platinum (Pt) for HER and ruthenium oxide (RuO_2) for OER. Hydrogen evolution performances of both VS_2 and VS_4/rGO have been studied in an acidic medium and observed their superior HER activity of pristine hexagonal 2D VS_2 layers over 1D crystal structure of VS_4/rGO hybrids. A large surface area with accessible active sites of 2D VS_2 layers shows better performance than the 1D crystal chain structure of VS_4/rGO . The VS_4/rGO hybrid has fewer active sites with reduced graphene oxide as supporting carbonaceous materials. Further, the electrocatalytic performances of RGO/FCNTs/ VS_4 towards OER have been observed by the hybridization of RGO and FCNTs with VS_4 . The transformation of 2D VS_2 layers to 1D VS_4 crystal chain was carried out with both the synergistic effect of carbonaceous materials. It enhanced the OER performances of ternary RGO/FCNTs/ VS_4 hybrids. This chapter gives a detailed

electrocatalytic study of pristine as well as hybrid forms of vanadium chalcogenides. However, the superior HER activity of modified VS₂ layers as cathode electrode material over single-chain monoclinic crystal structure of VS₄/rGO and the enhanced OER performances of ternary hybrids of RGO/FCNTs/Vs₄ is rarely reported.

2.4 Experimental section

2.4.1 Synthesis of GO and Functionalization of CNTs

Graphite oxidation was done successfully from the graphite powder by a well-known hummers' modified method.²⁸⁻³⁰ Firstly, 2 g of bulk graphite powder was taken in a 250 ml capacity of a beaker and 30 ml of conc. H₂SO₄ (98%) was added slowly to the graphite-containing beaker and kept in an ice bath under constant stirring. Then under the stirring condition, KMnO₄ (6 g) was added gradually into the acid precursor and left stirring in a water container for the next 2 hours and maintained the system temperature below 20 °C. The as-prepared reaction slurry was cooled by adding 60 ml of deionized water under an ice bath. A copious amount of 30% of H₂O₂ was added till the effervescence took place and the color of the precursor changes to brownish-yellow. Furthermore, the as-synthesized brownish-yellow product was collected through centrifugation and washed continuously with 0.1 M HCl to obtain unreacted SO₄²⁻ free graphene oxide. The as-prepared graphene oxide product was dried and stored for future use.

The single-walled carbon nanotubes functionalization (FCNTs) was done with an acid mixture of (1:3) ratios of concentrated HNO₃ and H₂SO₄. The final black color product obtained through centrifugation was repeatedly washed with ethanol and water to separate the unreacted acid impurities.

2.4.2 Synthesis of VS₂ layers

Vanadium disulfide (VS_2) has been synthesized through a hydrothermal method. In detail, 1 mmol of sodium orthovanadate (0.55 g) and 2 mmol of thioacetamide ($\text{C}_2\text{H}_5\text{NS}$, 1.12 g) were added to a 50 ml capacity beaker containing 40 ml of deionized water, and the reaction mixture free to stir for the next 30 minutes to get a homogeneous transparent solution. Further, the whole reaction precursor was transferred into a 50 ml capacity of stainless steel autoclave and placed in a running oven at 160 °C for 24 h. After cooling naturally, an obtained black-colored sample was collected through centrifuge by repeatedly washed with acetone/deionized water to remove unreacted sulfide impurities. Moreover, the collected material was dried by a vacuum oven and stored to use for further characterization study.

2.4.3 Synthesis of VS_4/RGO hybrids

VS_4/RGO hybrids have been synthesized by following similar reaction conditions during the synthesis of VS_2 . The use of graphene oxide solution was a templating agent to promote the nucleation growth of VS_2 to VS_4 at 160 °C for 24 hours. The reduction of graphene oxide (GO) to reduced graphene oxide (RGO) occurred during this hydrothermal treatment.

2.4.4 Synthesis of FCNTs/ VS_4 hybrids

Firstly, 100 mg of functionalized carbon nanotubes were dissolved thoroughly in deionized water by sonication to prepared solution (1) reaction mixture. Additionally, the second solution (2) mixture was prepared by reacting 0.55 g of Na_3VO_4 and 1.12 g of $\text{C}_2\text{H}_5\text{NS}$ in 40 ml DI water. The above solution (1) and (2) was mixed and continually stirred for the next 1 hour. The final reaction precursor was then transferred to a Teflon-lined stainless autoclave (volume of autoclave: 50 ml) and placed in a hot air oven at 160 °C for 24 h. After cool down, the precipitates were

collected, washed with water and ethanol, dried in a vacuum oven (at 60 °C), and stored for further characterization and application.

2.4.5 Synthesis of RGO/FCNTs/VS₄ hybrids

At first, 100 mg of functionalized carbon nanotubes and 60 mg of graphene oxide were dispersed in deionized water separately and continued for one hour of ultrasonication to form a homogeneous solution mixture. Then (1:2) ratio of Na₃VO₄ and C₂H₅NS was added in deionized water to prepare the reaction precursor. Further, all the above reaction mixtures were mixed and left for stirring to form a uniform solution. The total reaction mixture was shifted to a 50 ml capacity of digestion bomb, and a one-day reaction was carried out through hydrothermal treatment at 160 °C. Finally, a black-colored powder sample was collected through the centrifugation process and stored for future use.

2.5 Characterization

The phase purity with different crystal systems of all the as-prepared materials was analyzed by recording the powder X-ray diffraction pattern with the help of a Bruker D8 Advanced diffractometer equipped with Cu-K α radiation ($\lambda = 1.5418 \text{ \AA}$) at a scan rate of 1° per minute. Morphological structure and elemental detection of the samples were observed through the field emission scanning electron microscope (FESEM, Merlin Compact with GEMINI-I column, Zeiss Pvt. Ltd, Germany), transmission electron microscope (HRTEM, JEOL 2100F, working at 200 kV), and the elemental mapping data. For the TEM study, the dilute form of an as-synthesized sample on a carbon-coated copper grid was prepared by drop-casting with vacuum drying. The oxidation state with elemental composition was determined by X-ray photoelectron spectroscopy (PHI Versa Probe III). Moreover, thermal analysis was performed with

the help of TA Instruments-Waters Lab at the ramping process of $10\text{ }^{\circ}\text{C min}^{-1}$. Raman study of all samples was recorded using Horiba Scientific instruments at a Laser excitation wavelength of 532 nm.

2.6 Electrochemical measurements

A typical three-electrode measurement setup was used for the electrochemical study (electrochemical workstation of CHI 760D). Firstly, a suitable proportion of catalyst was dispersed in N-Methyl-2-pyrrolidone (NMP) followed by polyvinyl pyrrolidone as a binder of 10 wt. % for the preparation of the active material slurry. Further, the active slurry was coated on the surface of a glassy carbon plate electrode (GCE) and dried at $85\text{ }^{\circ}\text{C}$ for 1 hour. The material-coated electrode plate is working, bare platinum wire as an auxiliary, and the saturated calomel electrode (SCE) electrode was used for reference. The supporting electrolytes were taken for HER measurements as 0.1 M H_2SO_4 . Surface wettability can influence the gas evolution behavior, enhancing the durability of the electrocatalysts.^{31–33} Therefore, after drying, the electrode was pretreated electrochemically by running 50 CV cycles in a potential window, from 0.45 to -0.30 V vs. reversible hydrogen electrode (RHE) scale. The polarization curve profiles were recorded at a 5 mV/s sweep rate followed by the same potential window during the above CV cycles. All of the measurement potentials are recorded with SCE and calibrated in terms of the RHE scale as per the equation (2.1).^{29,34}

$$E_{RHE} = E_{SCE} + 0.059 (P_H) + 0.244\text{ V} \quad (2.1)$$

Where 0.244 V represented the potential value of saturated calomel electrode (SCE). The Nyquist plot was performed with an applying voltage of 5 mV, having an open circuit of frequency value from a scale of 1 mHz to 1 MHz. All the recording data

are presented in iR corrected/compensated and displayed through the $E-iR$, where “ i ” gives observed negative current and “ R ” represents an uncompensated solution of resistance obtained from plotted impedance data. The actual reaction mechanism behind the electrolysis process (HER) derived from the Tafel plots. The slope value was obtained by using the following equation (2.2),^{35,36}

$$\eta = a + b \log j \quad (2.2)$$

Herein, η denoted as the overpotential, a , b are represented as Tafel constant and Tafel slope, and j the measured current density. In a similar electrolytic condition, the stability test was performed by the chronopotentiometry technique at 10 mA cm^{-2} .

Similarly, in the oxygen evolution reaction (OER), all the electrochemical measurements were carried out using Autolab PGSTAT100N in a two-compartment three-electrode electrochemical cell. For the electrochemical investigation, the samples of (VS_2 , RGO/VS_4 , FCNT/VS_4 , RGO/FCNT/VS_4 , and RuO_2) having a concentration of 3.5 mg/ml was used to prepare an electrocatalyst ink by dispersing in a (9:1) mixing ratios of ethanol and Nafion solution followed by bath-sonication. Then $5 \mu\text{l}$ of catalyst ink was used onto the glassy carbon rotating disk electrode (GCRDE) surface and dried for further measurements. The mass of sample loading (0.25 mg/cm^2) was kept for the overall electrochemical study. A catalyst ink modified GCRDE was taken as working, bare platinum as auxiliary, and aqueous Ag/AgCl as reference electrodes for OER, respectively. The polarization curve data were recorded in an alkaline electrolyte medium of 1 M KOH . For better interaction with the electrolytic alkaline medium with the material-coated working electrode surface was cycled

between a potential ranges of 1.20 to 1.65 V (vs. RHE). Here, the measurement was recorded with an aqueous Ag/AgCl reference electrode. The conversion of saturated calomel electrode (SCE) to RHE scale (reversible hydrogen electrode) was done through a standard procedure reported elsewhere.³⁷ The electrochemical impedance spectroscopy (EIS) has been recorded by potentiometric technique, at 1.65 V (vs. RHE) with an input sinusoidal ac signal of small amplitude 5 mV, within a frequency range of 1 MHz to 0.1 Hz. The iR compensation of all the recorded data was done by noting the uncompensated solution resistance ($R_s = \sim 6.45$ for 1.0 M KOH) from the Nyquist plot. The compensated data shows the intrinsic electrocatalytic activity of the electrocatalyst by eliminating the undesired electrolytic effect and the catalyst resistance. Additionally, the Tafel slopes give the actual surface mechanism, and the slope value was obtained by using the following equation (2.3),^{29,34,38}

$$\eta = E \text{ (vs. RHE)} - 1.23 \text{ V} \quad (2.3)$$

Although the long cycle life of a modified electrocatalyst was tested by chronopotentiometry method at a predefined current density of 10 mA/cm², during the period of stability test, mass losses of the electrocatalyst have been analyzed through the inductively coupled plasma optical emission spectrometry (ICP-OES) instruments conducted by Perkin Elmer Optima 2100 DV. Further conformational analysis, the percentage of mass losses or dissolved in the modified electrocatalyst film's electrolyte have been calculated after stability and compared the values with the initial mass % of the electrode material before the stability test.

2.7 Evaluation of Electrochemical accessible surface area (ECSA) and surface roughness factor (R_f)

The ECSA values of as-synthesized samples were calculated from the double-layer capacitance (C_{dl}) followed by a non-faradic cyclic voltammogram region

with the potential window of -0.15 to 0.05 V and -0.16 to 0.04 V vs. Ag/AgCl for VS₂ and VS₄/rGO respectively.²⁹ The sample modified GCE (surface area: 0.07 cm²) denotes as working electrode, bare Pt wire, and aqueous Ag/AgCl electrodes are used as auxiliary and reference, respectively. Cyclic voltammograms were measured in the acidic (0.1 M H₂SO₄) electrolyte solution of various scan values ($10, 20, 40, 80, 100, 200, 400$ mV s⁻¹). Particularly, the current that arises during the CV measurements is due to the accumulation of positive/negative charged ions at the double layers interface rather than following any faradic reactions.^{34,39} Since the current is directly proportional to the double layer capacitance as per the following equation (2.4), the average double-layer capacitance (C_{dl}) value has been calculated by plotting different scan rate vs. current of cathodic and anodic at -0.05 V vs. Ag/AgCl,³⁴

$$i = \nu C_{dl} \quad (2.4)$$

The ECSA value was evaluated by the equation as follows,³⁹

$$ECSA = \frac{C_{dl}}{C_s} \quad (2.5)$$

Where C_s is the specific capacitance, for the calculation of ECSA, C_s are taken to be 0.035 mF/cm². Further, the R_f (roughness factor) value was calculated from the ECSA by dividing the geometrical surface area of the used GCE.

Similarly, for OER, the ECSA value for RGO/FCNT/VS₄, FCNT/VS₄, and RGO/VS₄ were recorded in a non-faradic region ($0.1 - 0.21$ V vs. Ag/AgCl) in 1 M KOH electrolyte at different scan rates ($10, 20, 40, 80, \text{ and } 100$ mV/s). The values of ECSA and R_f for OER electrode materials have been calculated by following the above equation (2.4) and (2.5), which have already been used for HER electrocatalyst. Here, C_s is the specific capacitance (0.04 mF cm⁻²) of an atomically smoothed material

under similar electrolytic conditions to estimate C_{dl} .^{40,41} Also, R_f was evaluated by dividing the results of ECSA with a geometrical surface area of the catalyst-ink modified working electrode (0.07 cm^2).⁴¹

2.8 Results and discussions

A one-route hydrothermal technique was carried out to develop VS_2 layers and reduced graphene oxide (rGO) hybrids. The reduction of graphene oxide (GO) occurred during the hydrothermal synthesis of VS_4/rGO . The FTIR spectral analysis in Figure 2.1 shown the detailed reduction process. The sharp, intense peaks of GO attributed to the presence of different stretching vibration of oxygen-containing functional groups, like hydroxyl (O-H) groups, adsorbed H_2O molecules, carbonyl (C=O) of aldehyde or acids or ketone groups, along with different alcoholic or epoxy groups at the wavenumber value of 3400 cm^{-1} , 1722 cm^{-1} , and 1050 cm^{-1} respectively.^{42,43} All these intense peaks of GO have been diminished during the high-temperature reduction process. The peak position appeared at a wavenumber of 1635 cm^{-1} for (C=C) displaying rGO layer developments.⁴⁴ Figure 2.2 shows the X-ray powder of the crystal phase for both the VS_2 layers and VS_4/rGO composites. The PXRD data gives the crystallinity and phase purity information of the samples. The three-strong peak positions at 2θ value of 15.4° , 35.77° , and 45.26° displays as hexagonal crystal lattice for VS_2 layers (JCPDS data file no 89-1640). In contrast, the diffraction pattern at 15.8° and 17° attributed to (110) and (020) diffraction plane of 1D monoclinic VS_4 crystal system (JCPDS: 72-1294) in the VS_4/rGO composite. The diffraction peak expected at 2θ of 26° for rGO in the VS_4/rGO composite was disappeared compared to highly crystalline VS_4 peaks.

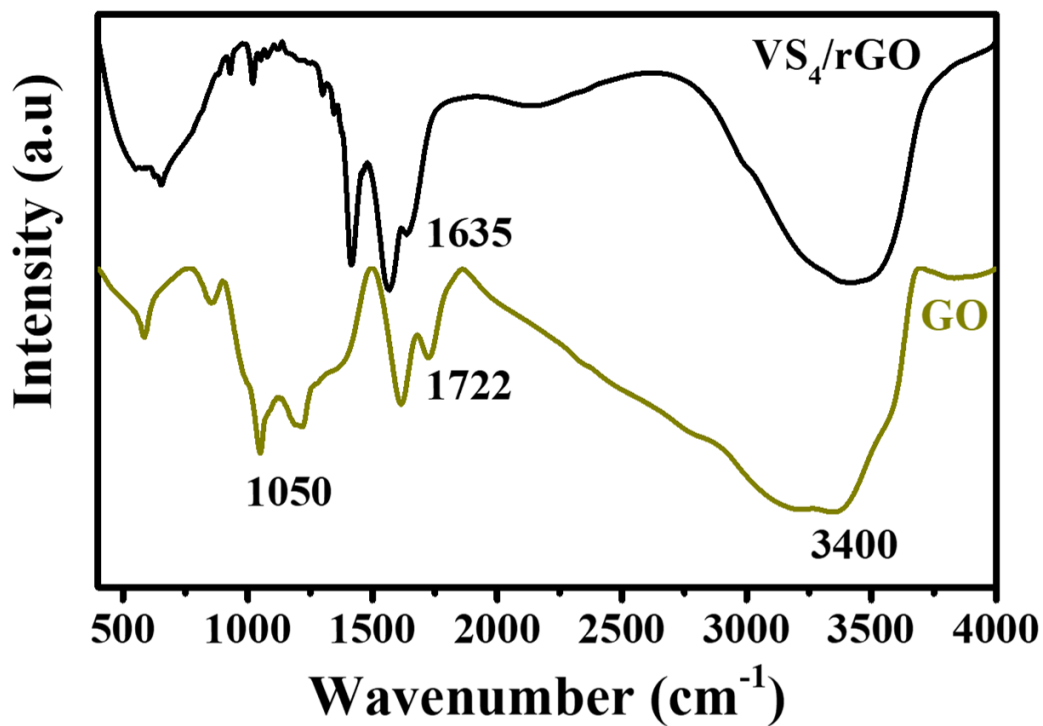


Figure 2.1 FTIR spectrum of graphene oxide and VS_4/rGO composite.

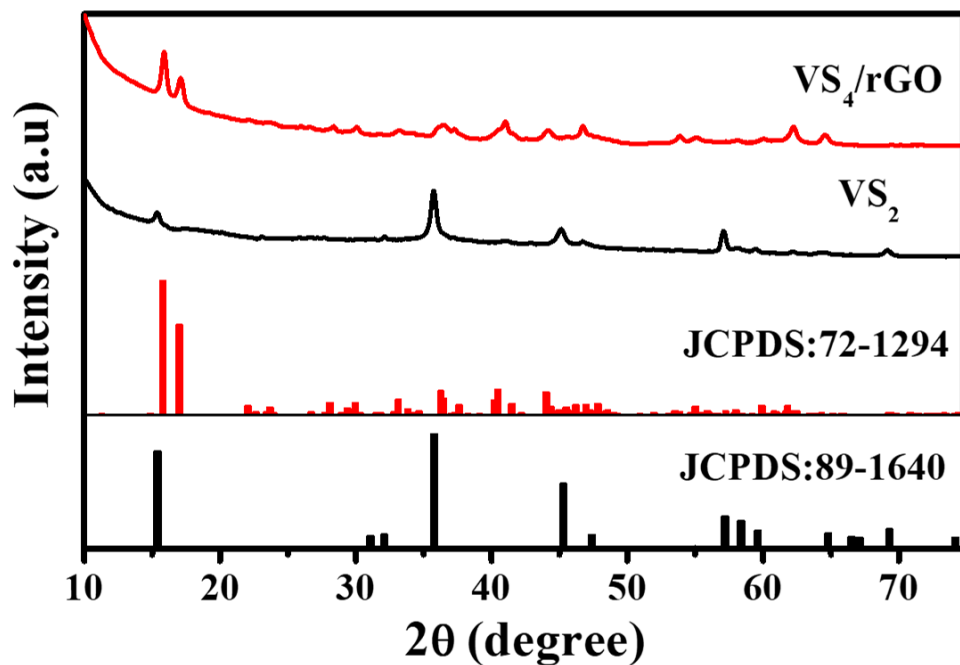


Figure 2.2 X-ray powder diffraction study of bare VS_2 and rGO composite of VS_4 .

X-ray photoelectron spectroscopy depicts the oxidation state, elemental composition, and binding energy of bare VS₂ and VS₄/rGO composites. Figure 2.3 shows the XPS peaks for pristine VS₂, and the vanadium peaks located at 516.6 and 523.7 eV are ascribed to the V 2p_{3/2} and V 2p_{1/2} orbitals, corresponding to +4 chemical state.^{45,46} A conformation study of sulfide (S²⁻) peaks at the binding energy of 162.9 and 164.1 eV, obtained from fitted S spectrum attributed to the orbitals of S 2p_{3/2} and S 2p_{1/2}, respectively. Similarly, four XPS fitting V spectrums were observed for VS₄/rGO composite in Figure 2.4. The two characteristics peaks are detected at 513.6 and 521.1 eV have been signifying the orbital of V 2p_{3/2} and V 2p_{1/2}, which assigned as +4 oxidation state of vanadium. Whereas VS₄/rGO composites might be oxidized in air, the peaks show at 517.1, and 524.1 eV are for V₂O₅ which attribute to V 2p_{3/2} V 2p_{1/2} orbital, respectively.⁴⁷ High-resolution spectrum of S 2p observed a small peak around 168.4 eV assigned the presence of sulfate group, which indicates the surface of VS₂ getting oxidized.⁴⁸ Moreover, the existence of rGO verified by the presence of carbon peaks at 285 eV for C 1s and the other three peaks at 284.6, 286, and 288.5 eV are notifying through the high-resolution deconvoluted spectrum with references to the carbonyl carbon (-C=O-), epoxy or hydroxyl (-C-O-C- or -O-H), ethylene (C=C) in the rGO composites.⁴⁶ These above results suggested that the developments of VS₂ layers and the composite form of VS₄/rGO are confirmed in hydrothermal reaction conditions.

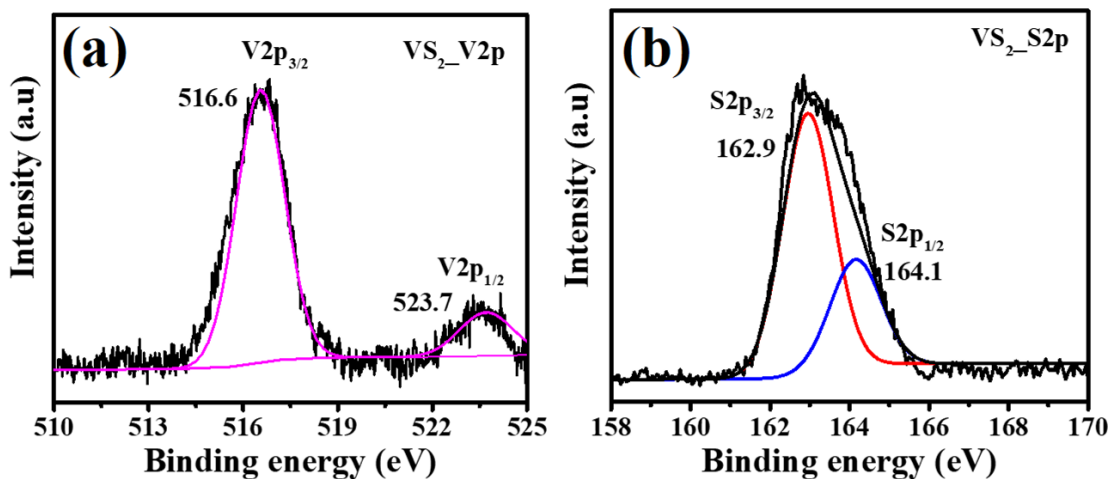


Figure 2.3 X-ray photoelectron scans of the V 2p and S 2p orbitals of bare VS₂.

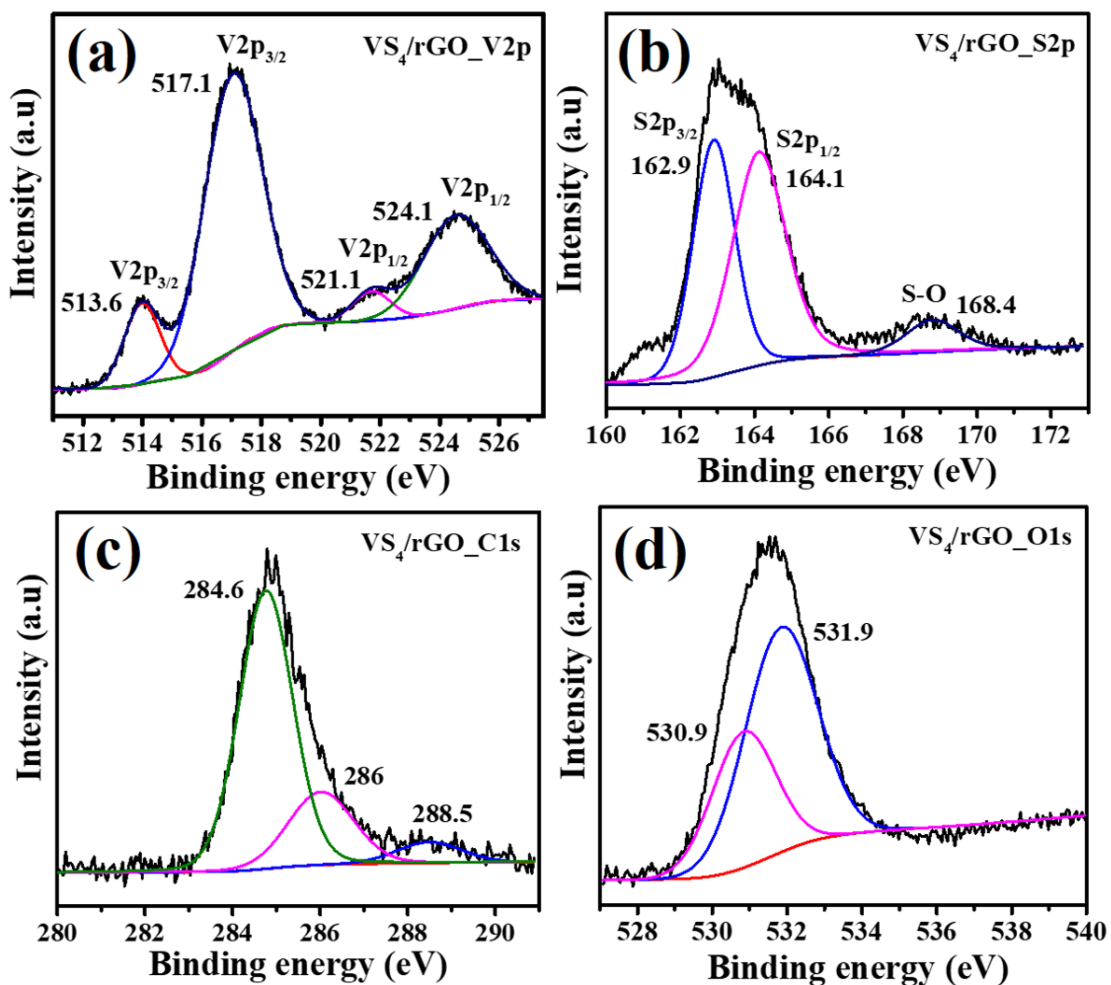


Figure 2.4 XPS scan of V 2p, S 2p, O 1s, and C 1s of VS₄/rGO composite.

As-prepared pristine VS_2 possesses layer by layers morphology with ~ 100 nm thick at different magnifications shown in Figure 2.5a-b. Further, the EDS spectrum shows the vanadium and sulfur molar ratio is about 1:1.93, and the elemental position of V and S are observed in the overall VS_2 sample in Figure 2.6a-c. However, in rGO hybrids VS_4 , the grown of microscopic flake-like morphology was noticed on the graphene surface shown in Figure 2.7.

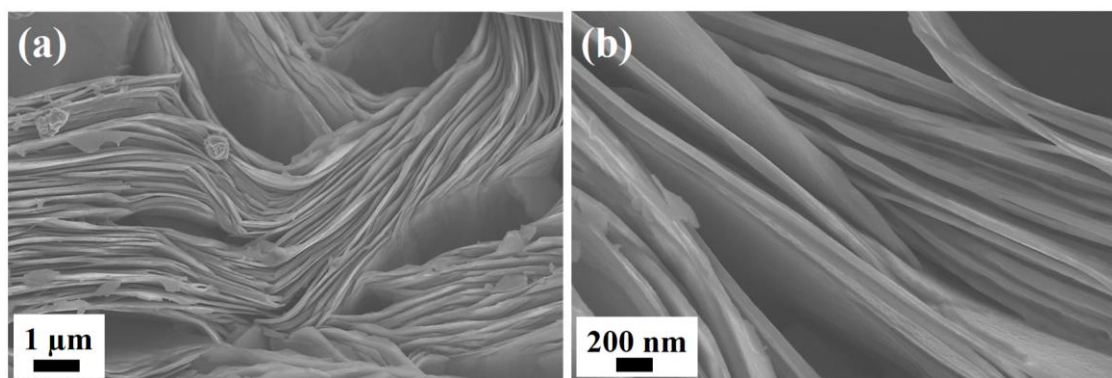


Figure 2.5 (a), (b) Different magnification ranges of field emission scanning electron microscopic pictures of VS_2 .

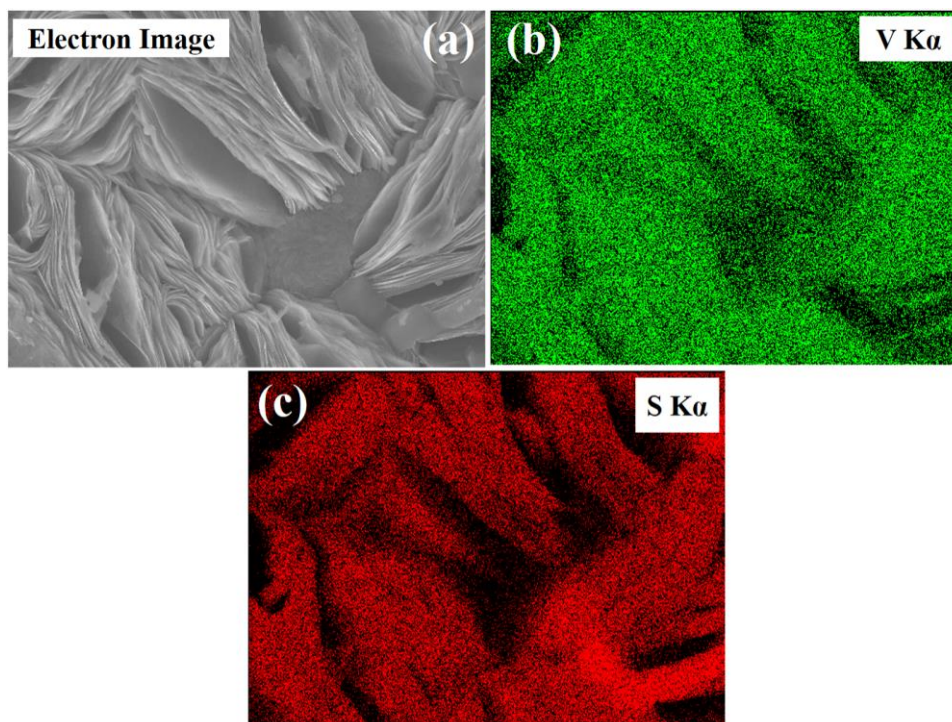


Figure 2.6 (a-c) Elemental mapping images of Pristine VS₂.

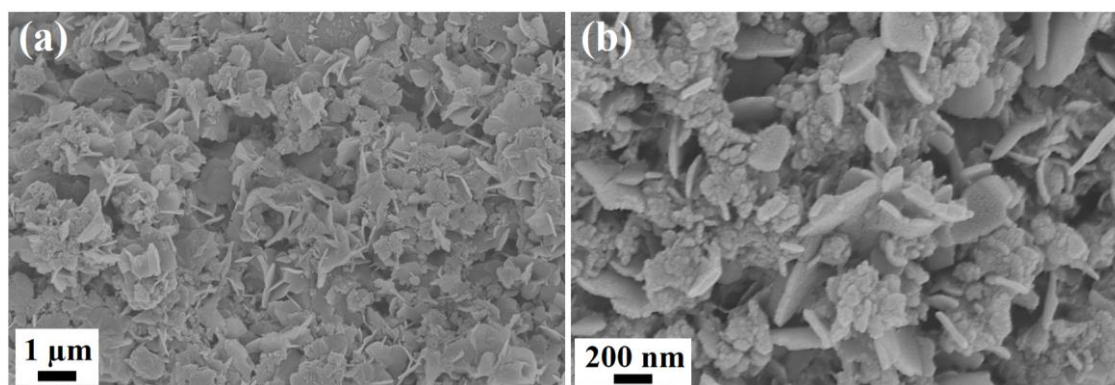


Figure 2.7 (a) Low and higher (b) magnifications study of FESEM pictures for VS₄/rGO composites.

With an increase in temperature, the variation of weight loss of the sample was investigated by TGA (thermogravimetric analysis) in Figure 2.8. The thermogravimetric study of pristine VS₂ and VS₄/rGO composite was done within the temperature range of 25–600 °C. A multi-step weight loss of both the samples taken place with a slow increase in temperature. At the first step, below 150 °C temperature, the weight loss nearly equal to 10% for bare VS₂ because of the desorption of moisture and water molecule.⁴⁹ The second step weight loss for the VS₂ sample sudden increase to 30% due to the removal of some sulfur units between the temperature windows of 150 to 300 °C. The final weight loss was shown by 4 wt% within the temperature of 400–500 °C because of the elimination of rest sulphur units inside the VS₂ layers and after that sample weight loss was stabilised.⁵⁰ Similarly in VS₄/rGO composite, first sample weight loss to be noticed about of 5% by the removal of water molecules below 200 °C. Further sample weight loss about 25% attributed for the decomposition of rGO layers was noticed between 200–300 °C. Finally the weight loss 10% between the temperatures of 380–520 °C indicating by

desorption of sulphur units from VS_4 crystalline structure followed by the conversion of VS_2 .

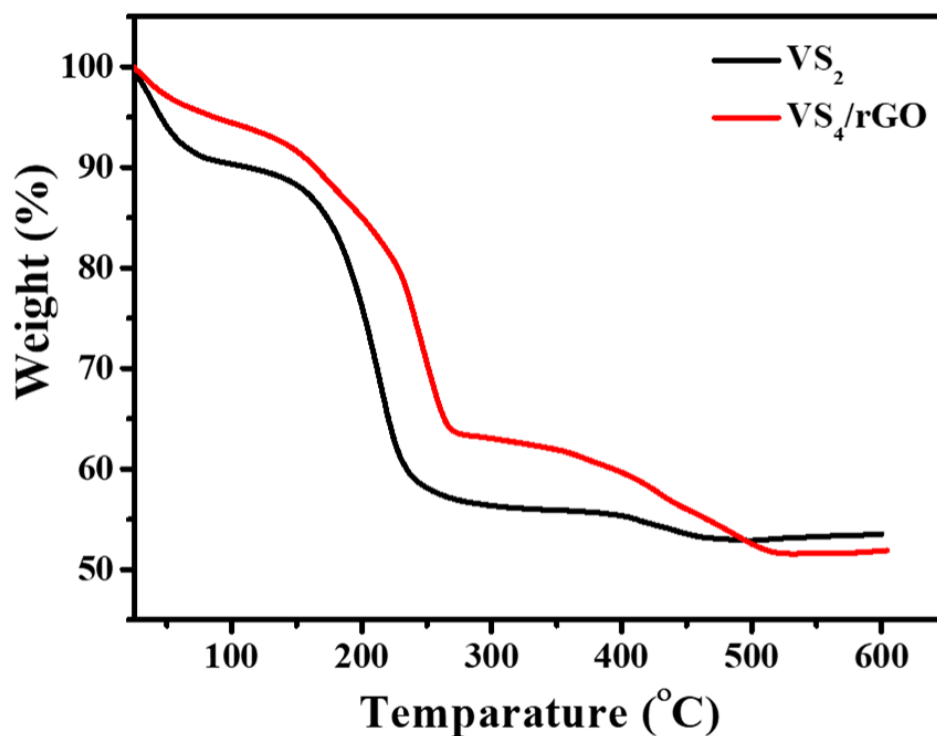


Figure 2.8 Thermogravimetric analysis for VS_2 and VS_4/rGO .

The simple synthetic technique and step-wise characterization process of the as-prepared VS_2 and VS_4/rGO composites gave overall knowledge about the samples. Besides these, evaluating the electrocatalytic response towards HER has been carried out in a three-electrode measurement setup. The mass used on the surface of glassy carbon electrodes was 0.5 mg/cm^2 as working, bare platinum as an auxiliary, and aqueous Ag/AgCl as the standard reference electrode. The catalytic activity in terms of different measurement techniques such as linear sweep voltammetry (LSVs) or polarization curve, cyclic voltammetry (CV), Nyquist diagram, and chronoamperometry technique was evaluated to check the HER efficiency of the

electrode material. While the electrolyte used for the overall measurements is 0.1 M H_2SO_4 . Figures 2.9a and b depict the Nyquist diagram for both pristine VS_2 of solution resistance (4.5Ω) and VS_4/rGO composites with solution resistance (3.8Ω), respectively.

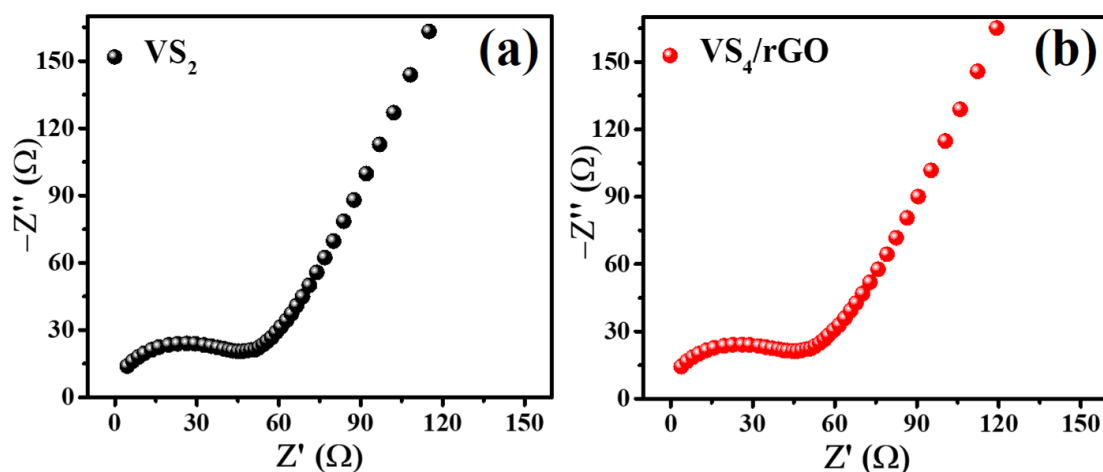


Figure 2.9 Nyquist impedance spectrum for the VS_2 (a) and (b) VS_4/rGO composites.

The iR corrected LSVs profile was carried out at a sweep rate of 5 mV/s (Figure 2.10a). It has been noticed that the VS_2 modified electrode shows enhance HER activity in respect of sharp negative current and lower onset potential value (15 mV vs. RHE) as compared to bare GCE and VS_4/rGO within the prescribed potential window. Moreover, bare VS_2 demands only 41 mV of extra potential or overpotential to attain the current density of 10 mA/cm^2 . This value is less than 210 mV of VS_4/rGO and very proximate to the precious Pt/C (40 mV) electrode materials. Figure 2.11 signifying the before and after iR correction LSV plots of all samples. The reaction mechanism path for HER has been analyzed by fitting the polarization curve regarding the log of current density (j) vs. overpotential named Tafel plot in Figure 2.10b. The Tafel value obtained for Pt/C is 29.2 mV/dec is accompanying by the earlier

reports.^{51,52} The Tafel slopes for VS₂ and VS₄/rGO composites are evaluated individually as 36 mV/dec and 73 mV/dec. However, the actual reaction mechanism of electrolysis is unclear. Considering the obtained Tafel value and theoretical calculation, the HER mechanism for both VS₂ and VS₄/rGO composites follows the Volmer-Heyrovsky path than the Volmer-Tafel path for noble Pt/C.^{36,53} Moreover, the exchange current density was obtained by interpolating the linear fitted Tafel graph line to zero overpotential. Furthermore, the pristine VS₂ shows higher exchange current density (60.54 mA/cm²) in comparison to rGO composite VS₄ (16.4 mA/cm²), with other described TMDCs.^{54–57}

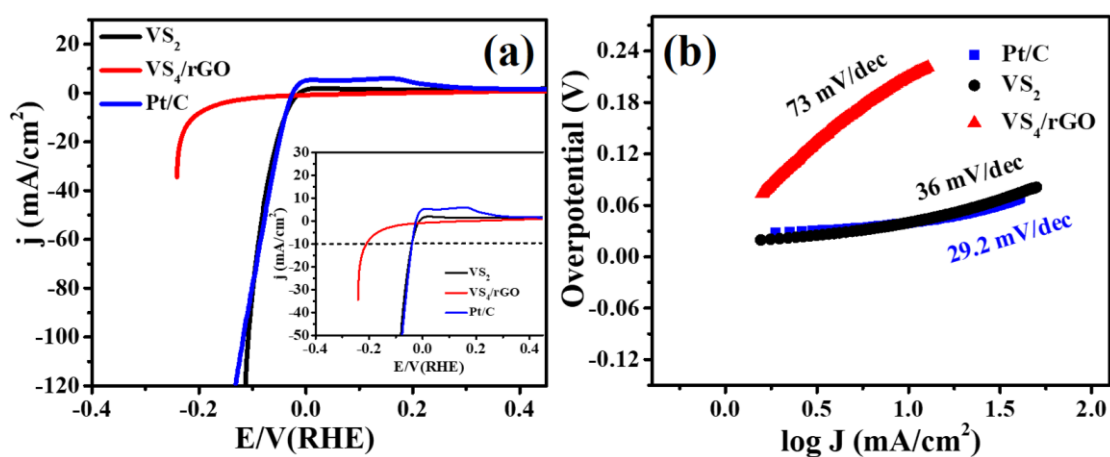


Figure 2.10 (a), (b) Polarization curve and Tafel plot for VS₂, VS₄/rGO composites, along with commercial Pt/C moderate GCE in 0.1 M H₂SO₄.

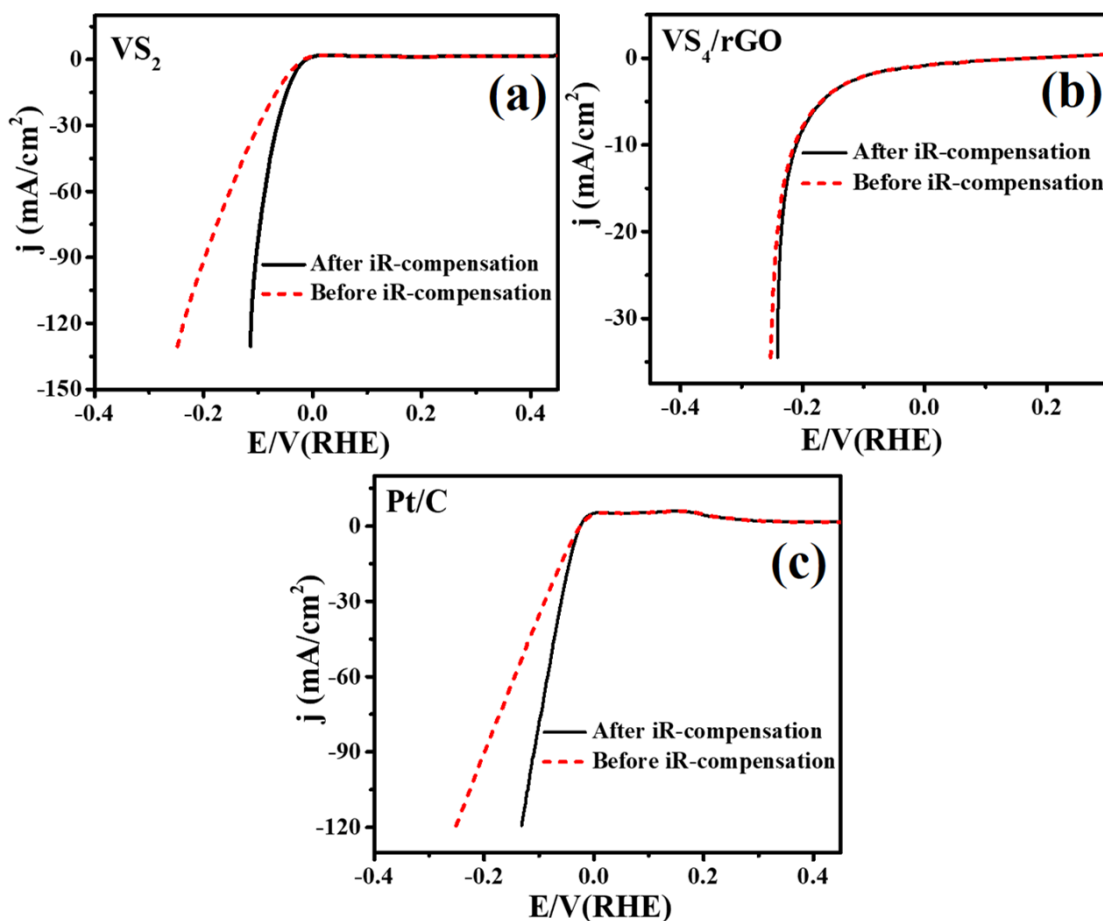


Figure 2.11 Linear sweep voltammograms for bare VS_2 , VS_4/rGO composite, along with precious Pt/C before and after iR compensation in 0.1 M H_2SO_4 electrolyte.

As the electrolysis process towards hydrogen evolution reaction is an in-situ surface appearance and the detailed crystal system results of bare VS_2 and VS_4/rGO composites presume that the surface of VS_2 exhibits a 2D hexagonal crystal system, it may provide a large surface area with greater catalytic active sites as compared to rGO composite of 1D linear chain structure of VS_4 . The higher active sites of VS_2 are more beneficial for HER than the VS_4/rGO . The detailed crystal analysis is supported with the obtained value of ECSA measurements and calculated from the non-faradic portion of cyclic voltammograms within a specified electrochemical window. However, the detailed electrochemical study is provided in Figure 2.12.

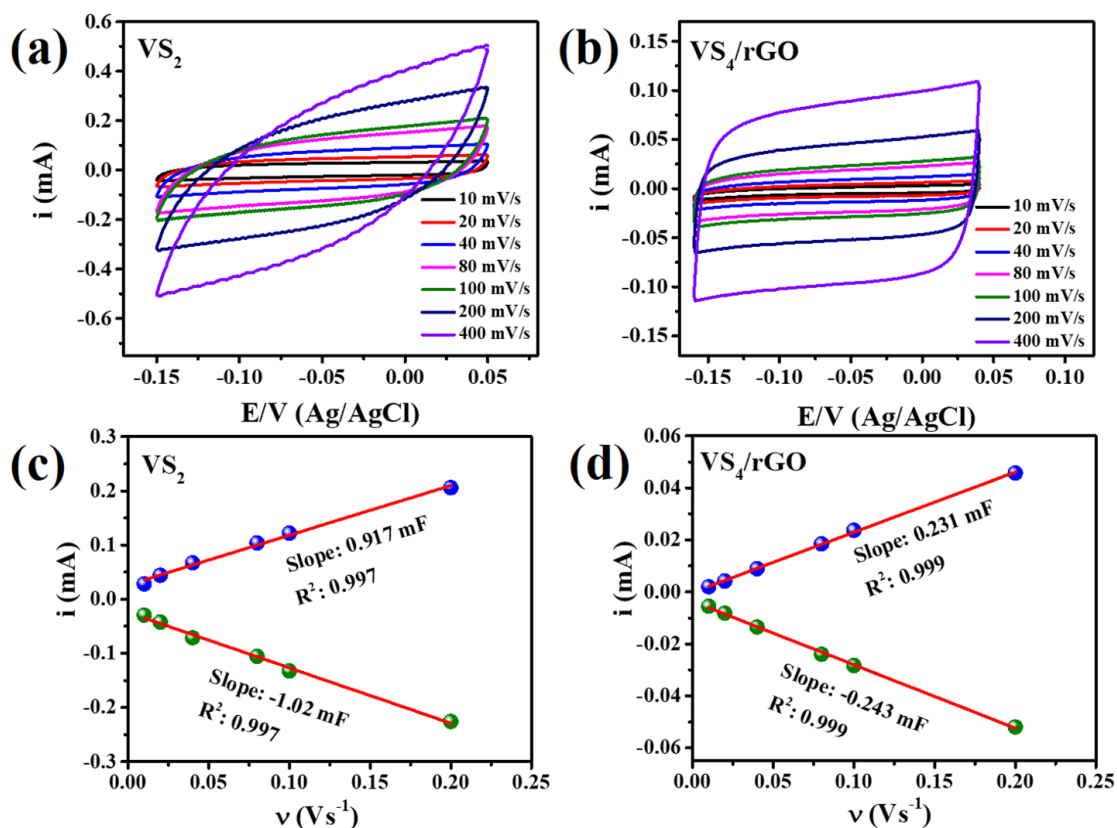


Figure 2.12 (a, b) are the cyclic voltammograms in 0.1 M H₂SO₄ at individual scan rates (10 to 400 mV s⁻¹), and (c, d) is the profile of scan rate vs. cathodic and anodic current at -0.05 V for VS₂ and VS₄/rGO.

Besides these, the current arises at the double-layer interface because of the charge accumulation process, and the double-layer capacitance (C_{dl}) is directly related to the measured current (above equation 4, section 2.7). Furthermore, the C_{dl} of the VS₂ sample was evaluated to be 0.969 mF/cm² providing a larger ECSA value (27.7 cm²) than the rGO hybrid of the VS₄ chain (C_{dl} of 0.237 mF/cm² and ECSA of 6.77 cm²) and the roughness factor (R_f) for VS₂, VS₄/rGO composite were found to be 395.71 and 96.73, respectively. In comparison, the R_f value of VS₂ is four times higher than the composite form of VS₄/rGO. The above results, such as the larger ECSA and R_f values, confirm that VS₂ shows better HER activity over the VS₄/rGO hybrids and

other published HER electrocatalysts in Table 2.1. The chronopotentiometry technique carried out an essential key parameter for practical application in the long-term stability test. Interestingly, both catalyst (pristine VS₂, VS₄/rGO composite) demonstrate robust durability even after 10 h of constant electrolysis in 0.1 M H₂SO₄ solution and shows a negligible diminishment of the overpotential shown in Figure 2.13.

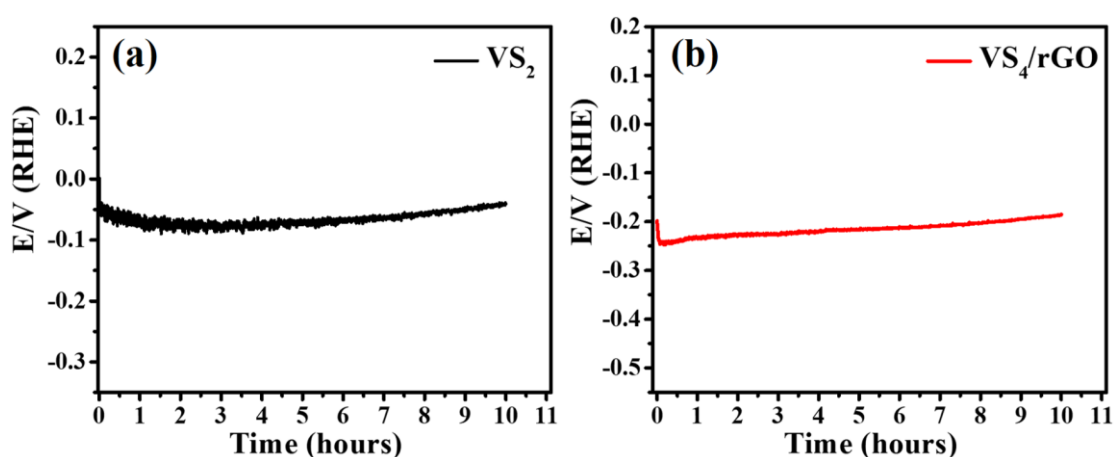


Figure 2.13 Durability test of VS₂ and VS₄/rGO modified electrode surface for HER in 0.1 M H₂SO₄ electrolytic solution.

Additionally, the stability test of VS₂ was also performed at a higher current density of 30 mA/cm² under constant 43 hours of electrolysis in the same electrolytic solution with a negligible decrease of overpotential in Figure 2.14. The robustness of the VS₂ material has also been verified by analyzing the characterization technique of FESEM and the XPS spectrum after the stability test.

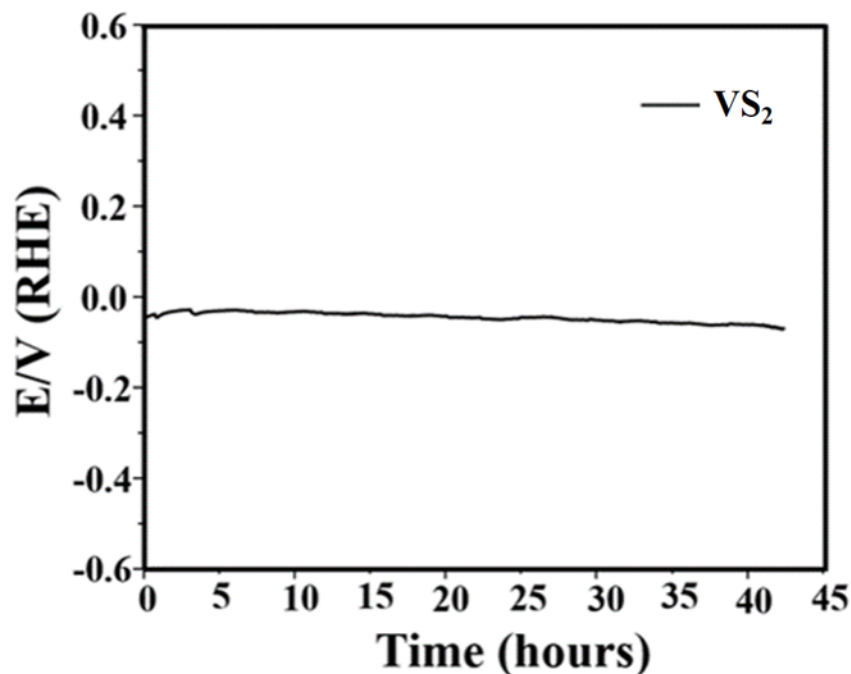


Figure 2.14 Electrolysis experiments of VS₂ modified electrode at a larger current density of 30 mA/cm² in the acidic electrolyte medium.

Figure 2.15a-b is the surface morphology of the VS₂ electrocatalyst that has been recorded after the stability test, which implies a little distortion of the surface morphology of VS₂ that may be due to the constant electrolysis process. Further, the high-resolution XPS spectrum was performed after the post stability test and is presented in Figure 2.16. The characteristics peak position at the binding energy of 516.6 and 523.7 for V 2p_{3/2} and V 2p_{1/2} eV orbitals suggests vanadium metal is in +4 oxidation state and the fitted two peaks of binding energy at 162.9 and 164.1 eV for S ascribed as S 2p_{3/2} and S 2p_{1/2} orbitals respectively. While the analysis of XPS data after HER stability is well correlated with the before electrolysis XPS data of the VS₂ sample. From these above studies, we presume that a small overpotential value, lower Tafel slope, larger ECSA with good roughness factor (R_f), and excellent cyclic stability of the 2D hexagonal crystal system of VS₂ modified cathode electrode

material will efficient to substitute the precious electrocatalysts and fulfill their future energy demand.

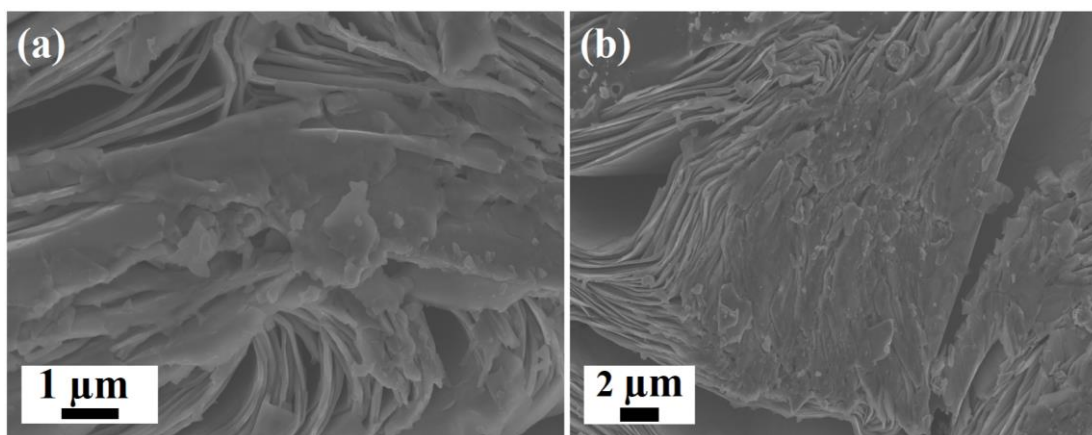


Figure 2.15 (a), (b) FESEM images for the VS_2 after the chronopotentiometry measurement at 10 mA/cm^2 .

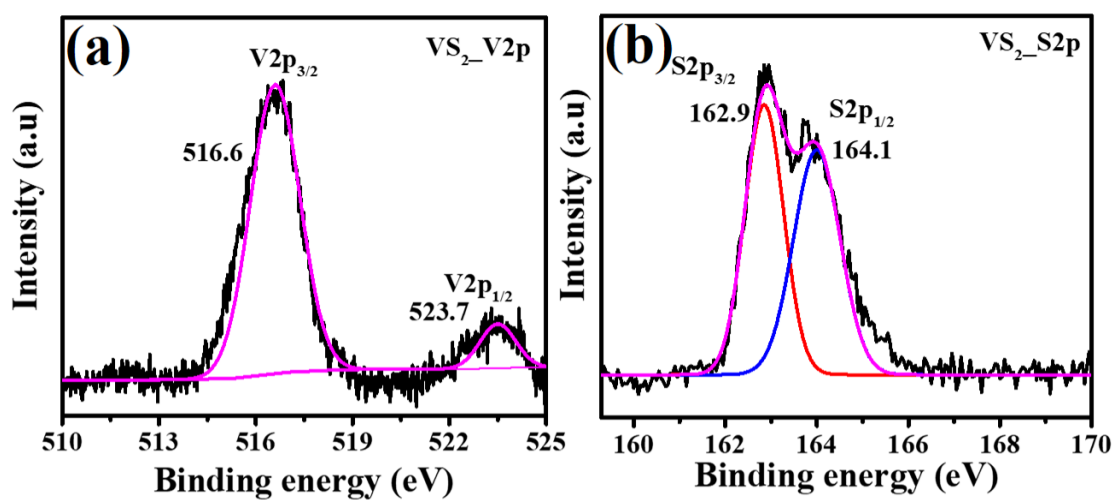


Figure 2.16 High-resolution XPS spectrum of V 2p and S 2p for VS_2 after chronopotentiometry measurement at 10 mA/cm^2 .

Table 2.1 A brief literature survey on transition metal sulfide catalysts for HER.

Sample	Electrolyte H ₂ SO ₄ (M)	Over potential at 10 mA/cm ² in (mV)	Tafel value in mV/dec	References
Co doped VSe ₂	0.5	230	63.4	ACS Appl. Energy Mater. 2019, 2, 644–653
1T-VS ₂	0.5	68	34	Adv. Mater. 2015, 27, 5605
CoSe ₂ -160 microcubes	0.5	156	40	Inorg. Chem. 2020, 59, 12778–12787
NiS ₂ /rGO	0.5	200	52	Catalysis Communications, 2016, 85, 26
2H-MoS ₂ triangle, Mo edge	0.5	201	68	Adv. Mater. 2017, 1701955
CoSe ₂ @N/C-CNT	0.5	185	98	J. Colloid Interf. Sci. 2020, 566, 296-303
1T'-MoS ₂ basal plane	0.5	356	84	Adv. Mater. 2017, 1701955
H-Co/MoS ₂	0.5	156	58	Nano Energy, 2017, 39, 409
WS ₂	0.5	337	80	Nanoscale, 2017, 9, 13515
MOF derived CoSe ₂	0.5	195	43	Sustainable Energy Fuels, 2021, 5, 4992
3D WS ₂ /graphene/Ni	0.5	87	79	Int. Journal of hydrogen energy, 2017, 7811.
Ni _{0.75} Fe _{0.25} Se ₂	0.5	197	107	Int. J. Hydrogen Energy, 2019, 44, 22796–22805
RGO/CoSe ₂ -180	0.5	172	35.2	Int. J. Hydrogen Energy, 2020, 45, 1738-1747
VS ₂ Nano plate	0.5	42	36	Chem. Mater. 2016, 28, 5587
VS₂	0.1	41	36	This Work
VS₄/rGO	0.1	210	73	This Work

Likewise, the oxygen evolution reaction for the vanadium chalcogenides and its carbon-based hybrid materials were successfully synthesized by following single-step hydrothermal routes under controlled reaction conditions as briefly discussed in the above experimental section 2.4. FESEM and TEM were studied to give the core

information of the surface morphologies and crystallographic structures for pristine VS_2 , RGO/VS_4 , FCNT/VS_4 , $\text{RGO}/\text{FCNT}/\text{VS}_4$ hybrids. The petal-like structure of VS_4 crystal with thickness $\sim 5\text{-}10$ nm is uniformly distributed over the surface of the RGO/FCNT template in Figure 2.17a-b. It has been noticed that the surfaces of the VS_4 nanosheets are seemed to be rough, which obeys the criterion for enhanced redox activities and good charge transportation.

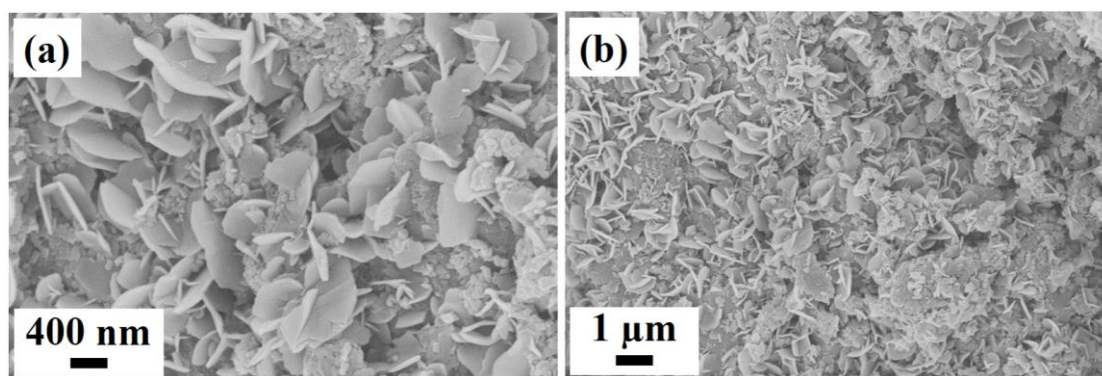


Figure 2.17 (a, b) High and low magnification of captured SEM images.

A similar investigation has been carried out through the HRTEM images shown in Figure 2.18a-b. Moreover, the well-resolved lattice spacing was observed from the high-resolution transmission electron microscopic image, which corresponded to [110] plane for VS_4 crystal, along with [100] plane of graphitic part in Figure 2.18c.^{58,59} Figure 2.19 and Figure 2.20 are the EDS and elemental mapping analysis, which displays the presence of the elements of vanadium, sulfur, and carbon in the hybrid electrode materials.

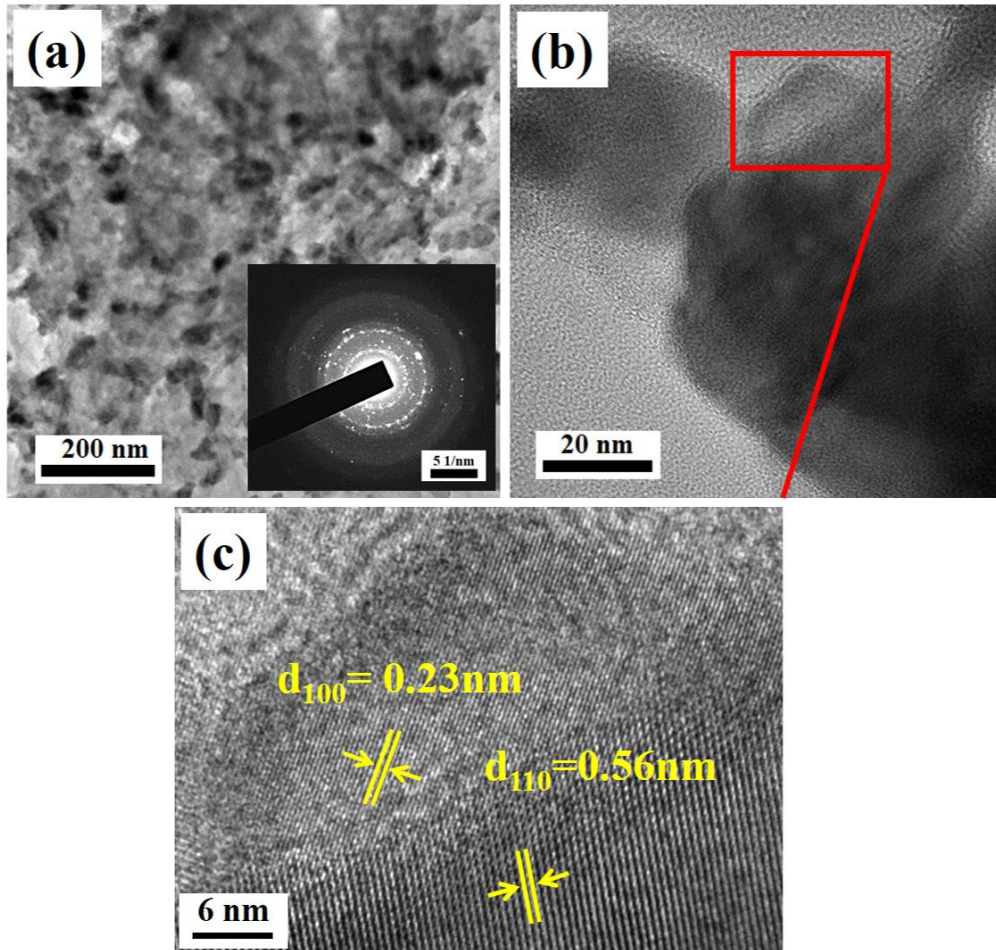


Figure 2.18 Transmission electron microscopic pictures (a, b) of RGO/FCNT/VS₄ composite at a distinct magnification range. (c) HRTEM analysis and the SAED pattern are carried out and inset in Figure (a).

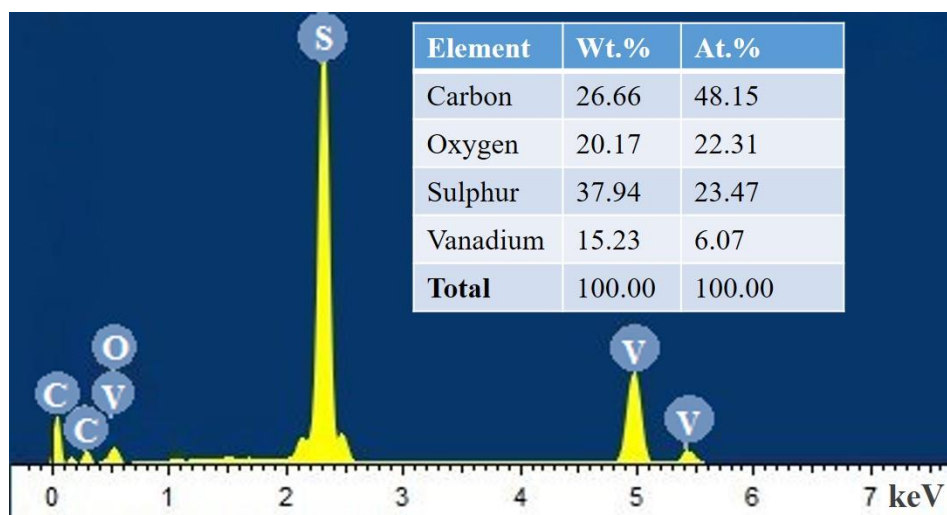


Figure 2.19 EDS spectrum of the RGO/FCNT/VS₄ hybrid showing V, S, C, and O at different atomic and weight percentages.

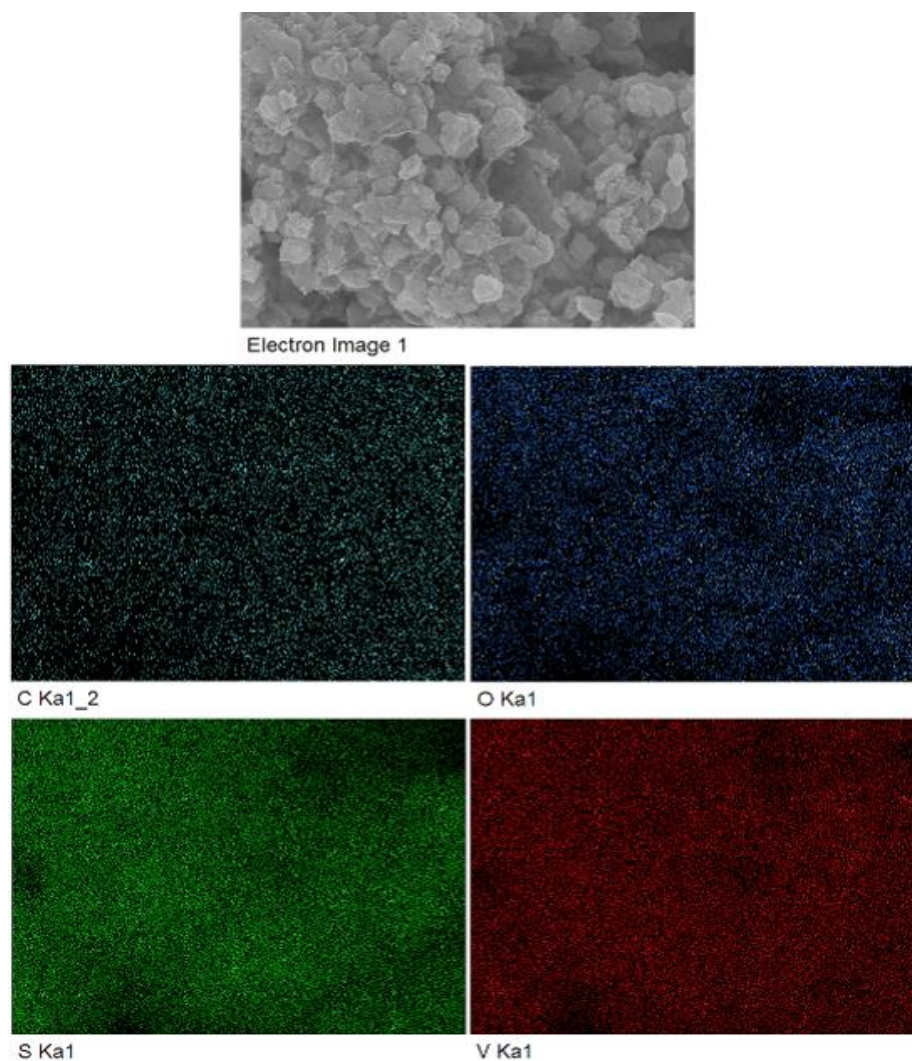


Figure 2.20 EDS pattern of RGO/FCNT/VS₄ hybrid showing the presence of V, S, C, and O elements.

Figure 2.21 shows the PXRD pattern of the ternary hybrid of RGO/FCNT/VS₄. The two major peaks that could be identified at 2θ values of ~ 15.8 and 17° were indexed to the phase growth along the direction of (110) and (020) planes. The peaks were identified from the diffraction pattern because of the monoclinic crystal system of patronite VS₄ (JCPDS file no-72-1294).

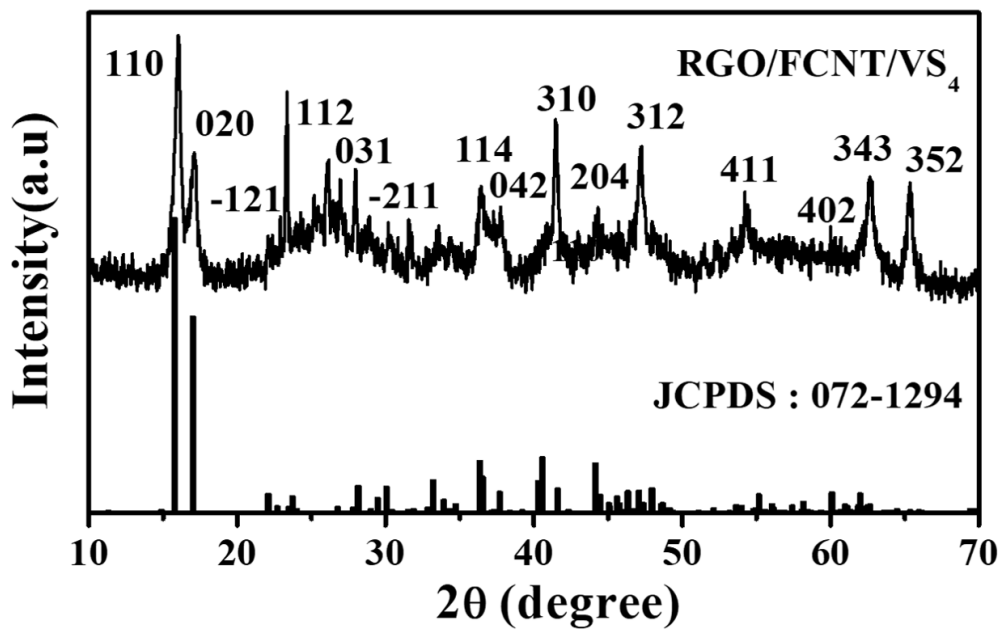


Figure 2.21 (a) Powder X-ray diffraction of RGO/FCNT/VS₄.

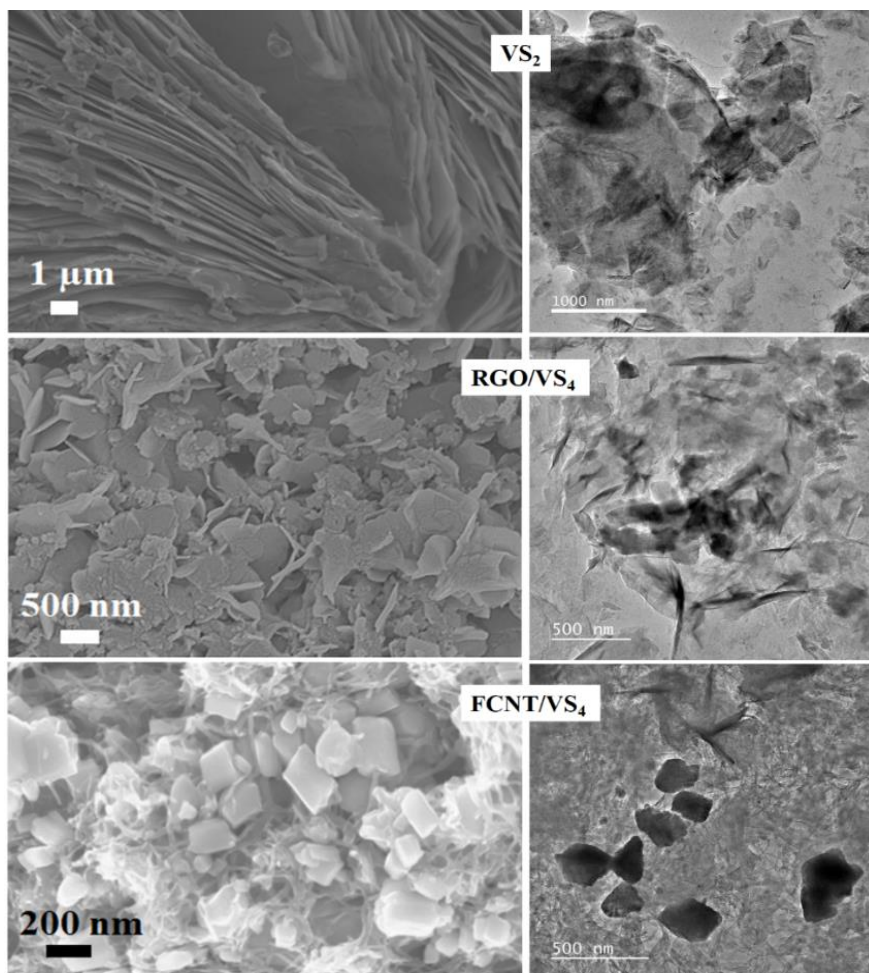


Figure 2.22 FESEM and TEM images of VS₂, RGO/V_S₄, and FCNT/V_S₄.

Figure 2.22 and Figure 2.23 have been illustrated for the surface morphology and powder pattern of VS₂, RGO/V_S₄, and FCNT/V_S₄ samples by the characterization technique PXRD, FESEM, and TEM, respectively. All the diffraction patterns were well matched with the corresponding crystallographic JCPDS files.

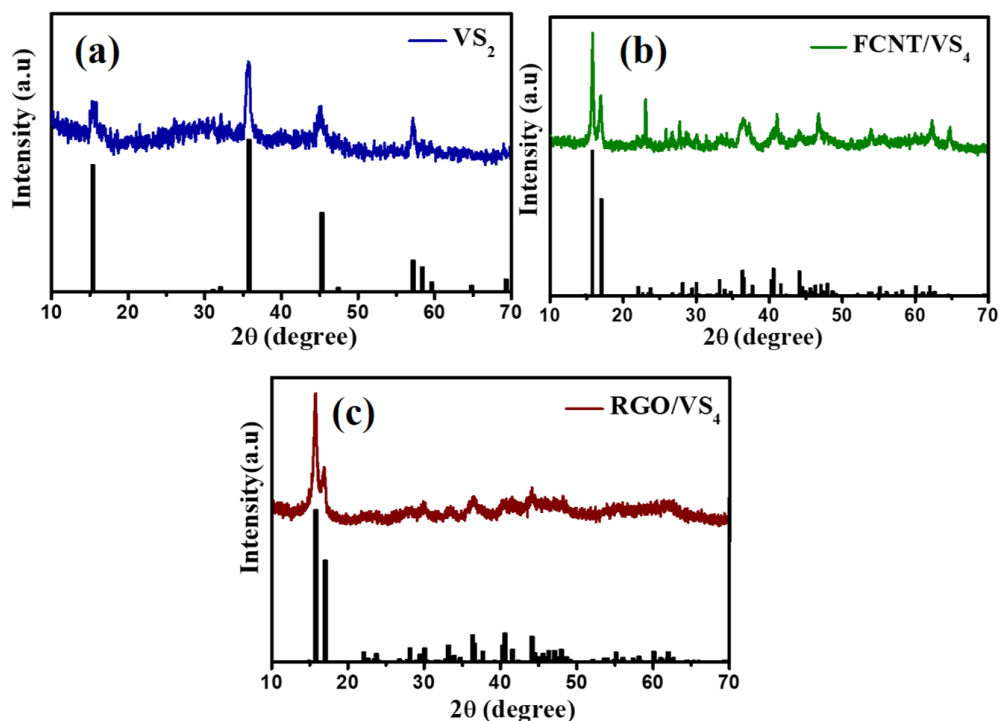


Figure 2.23 Powder pattern for (a) pristine VS₂, (b) RGO/V_S₄, and (c) FCNT/V_S₄.

The Raman spectra of RGO/FCNT/V_S₄ hybrids clearly show two distinct bands at 190 and 279 cm⁻¹ because of the stretching (A₁) and bending (B₁) modes V-S as shown in Figure 2.24a. The presence of graphene oxide and its effective reduction during hydrothermal treatment in the different composites such as pristine GO, RGO, RGO/V_S₄, and RGO/FCNT/V_S₄ have been analyzed from the Raman spectra shown in Figure 2.24b. It has been observed that the position of the peak at ~1345 and ~1577 cm⁻¹ are for the D-band and G-band of graphene. The obtained intensity ratio (I_D/I_G)

for GO, RGO, RGO hybrids VS₄, and RGO/FCNT/V_S₄ were evaluated as the value of 1.04, 1.13, 1.4, and 1.65, respectively. An increased I_D/I_G ratio has been noticed for pristine RGO and the RGO hybrid samples of RGO/V_S₄ and RGO/FCNT/V_S₄ compared to bare GO. While the variation in the intensity ratio confirms the restoration of in-plane sp² carbons and the formation of numerous smaller sp² graphitic domains. It persistent the effective reduction of GO were taken place to RGO in the hydrothermal treatment.^{60,61} Additionally, the linkage between V and C of patronite VS₄ and RGO/FCNT was observed by a weak and broad Raman band at 856 cm⁻¹. The above results suggest the high phase purity of the as-prepared samples was observed in the previous reports.^{62,63}

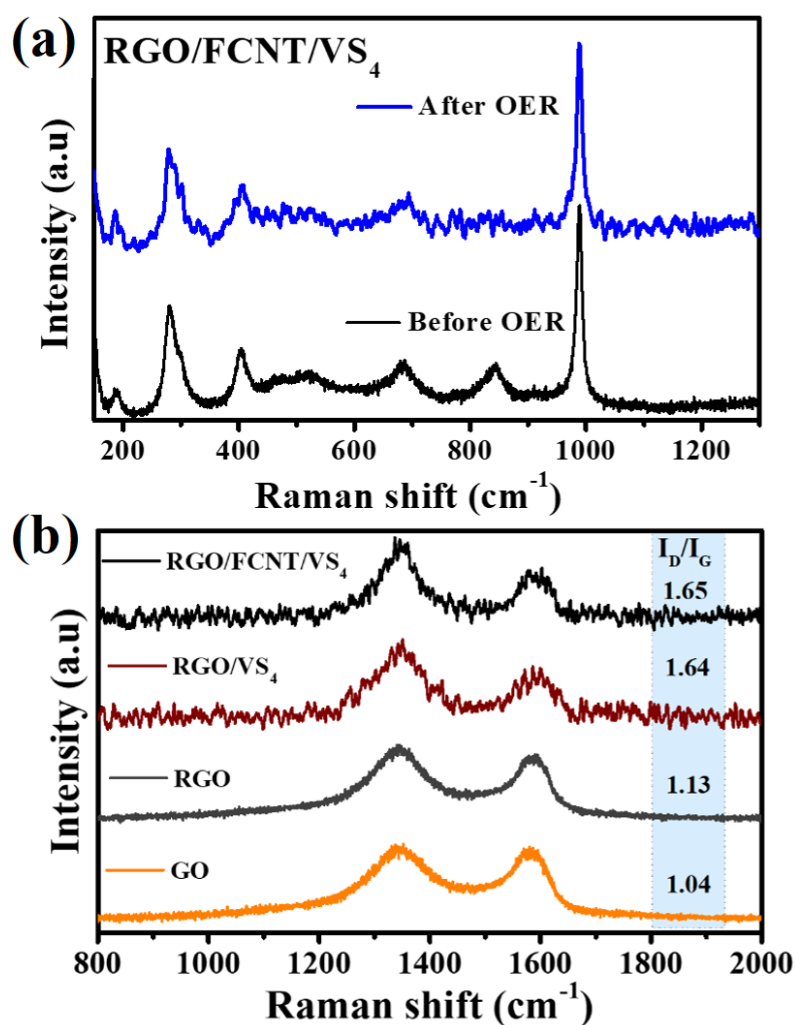


Figure 2.24 (a) Raman spectrum of RGO/FCNT/VS₄ composite before and after OER and (b) Raman spectrum of RGO/FCNT/VS₄, RGO/VS₄, RGO, and GO showing the D- and G-bands.

Figure 2.25 shows the XPS measurements of V 2p, S 2p, C 1s, and O 1s of VS₄/RGO/FCNT. A V 2p spectrum present two major peaks at 515.90 and 523.11 eV, corresponding to the V 2p_{3/2} and V 2p_{1/2} orbitals and confirmed the vanadium is in +4 oxidation states.^{5,64} Further, two characteristics peaks at 162.30 eV and 163.47 eV are the signals for S 2p_{3/2} and S 2p_{1/2} orbitals and existence of sulfide (S_2^{2-}) dimer in patronite VS₄.⁶⁴ Figure 2.25c shows for C 1s, band position at 284.70 eV attribute to the availability of non-oxygenated sp² C of RGO and FCNT. However, the peak present at 285.45 eV exhibits oxygen-containing functionalities of hydroxyl (-OH) or epoxy (-C-O-C-) groups.^{12,28} While the further co-existence of these groups is also conveyed by the O 1s XPS spectrum of peak position at ~531 eV. These XPS results demonstrated the in-situ study of ternary RGO/FCNT/VS₄ hybrids. The thermal stability of ternary RGO/FCNT/VS₄ hybrids was carried out by thermogravimetric analysis (TGA) in Figure 2.26. The sample weight loss with increasing temperature has been recorded under a nitrogen atmosphere within a temperature window of 25 – 800 °C. Firstly, the weight loss (10 %) corresponding to the elimination of involved water molecules and moisture below in the temperature region of 140 °C.^{5,49} The steady weight loss of about 30% followed by desorption of RGO and FCNT hybrids occurs between the temperature range 150 – 300 °C. The slight weight loss (6-7%) occurs within the temperature region of 350 –700 °C, and after that, the material was found to be stable (up to ~800 °C).

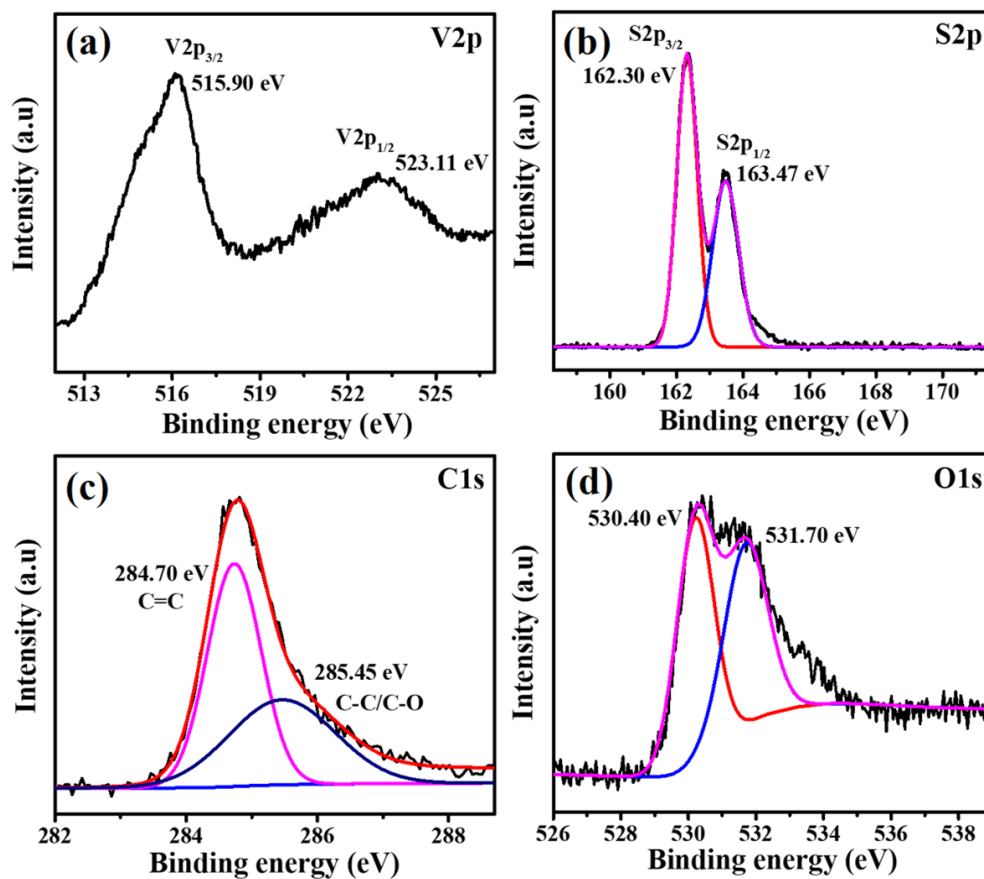


Figure 2.25 (a), (b) High resolution XPS study of V 2p, S 2p, and (c), (d) C 1s, O 1s of RGO/FCNT/VS₄ hybrid.

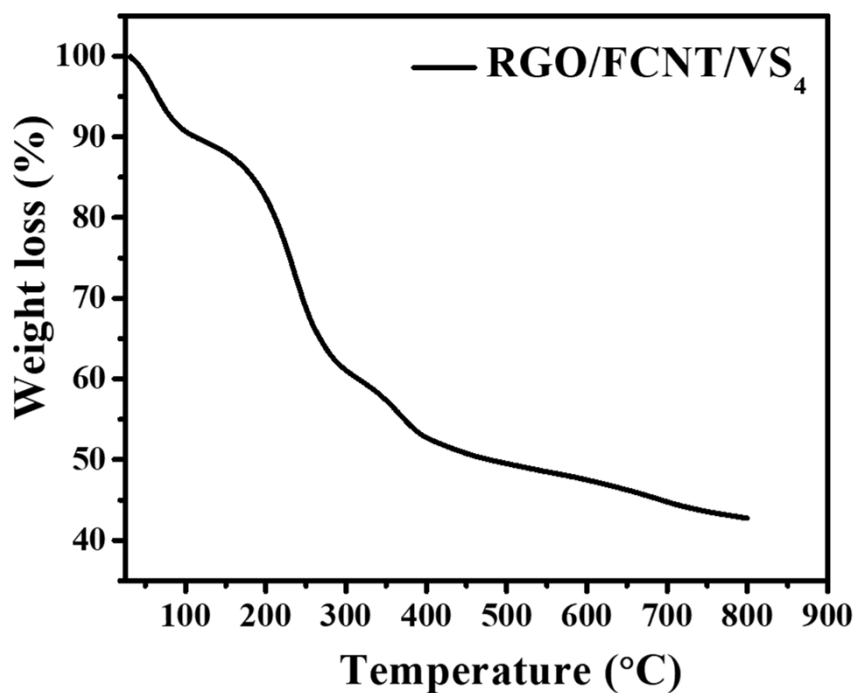


Figure 2.26 Thermogravimetric analysis of the RGO/FCNT/VS₄ hybrids.

The OER activity of the materials is tested by recording the linear sweep voltammetry (LSV) in the electrolyte medium of 1.0 M KOH solution and shown in Figure 2.27a. All the potential data of the LSV curves were *iR*-compensated and presented here as in Figure 2.28. The onset potential of the ternary RGO/FCNT/VS₄ hybrid is found to be ~1.45 V (vs. RHE), which is lower in comparison to RGO/VS₄ (1.55 V), FCNT/VS₄ (1.53 V), and bare VS₂ (1.57 V) under similar electrolytic conditions. Moreover, RGO/FCNT/VS₄ hybrid gives only the overpotential of 330 mV to gain the standard current density of 10 mA/cm². This overpotential value was significantly lower than FCNT/VS₄ (460 mV), RGO/VS₄ (480 mV), and some reported OER electrode materials that have been shown in Table 2.2. The OER kinetics of all the samples were measured by following Tafel plots derived from the corresponding LSV curve have been illustrated in Figure 2.27b.

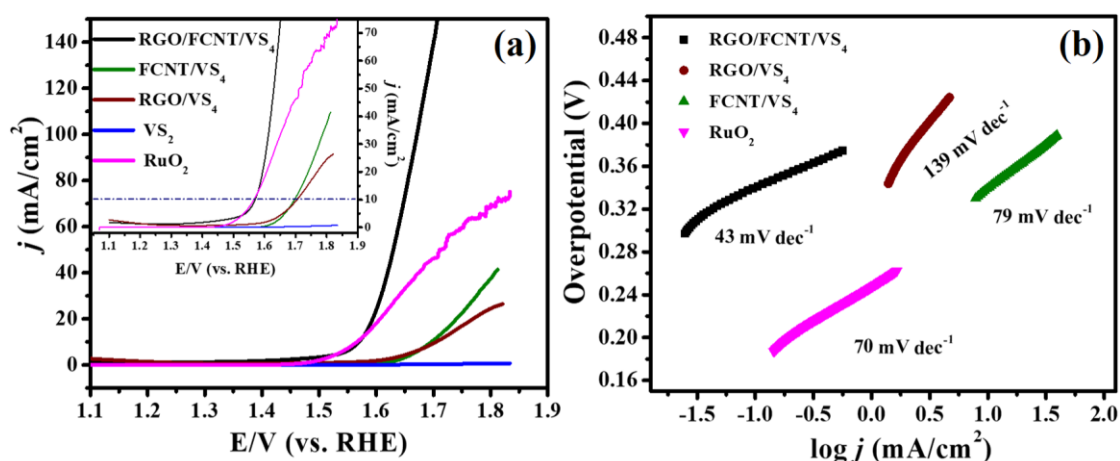


Figure 2.27 (a) Linear sweep voltammogram for OER by glassy carbon rotating disk electrode modified with VS₂, RGO/VS₄, FCNT/VS₄, RuO₂, and RGO/FCNT/VS₄ in 1

M KOH at a sweep rate of 5 mV/s with a mass loading of 0.25 mg/cm² and (b) the corresponding Tafel plots (overpotential vs. log of current density).

A linear Tafel fitting line gives the slope value of 43, 70, 79, and 139 mV/dec with regards to RGO/FCNT/VS₄, RuO₂, FCNT/VS₄, and RGO/VS₄ hybrid, respectively. Besides these, the lower Tafel value of RGO/FCNT/VS₄ hybrid electrode material accelerated faster OER kinetics than other studied materials. Figure 2.29 displays as the complete CV cycle for RGO/FCNT/VS₄ hybrid is recorded at a scan rate of 5 mV/s, and the observation gives the redox behavior of as-prepared electrode material. However, no such oxidation and reduction peaks of the material are noticed in the complete CV cycle.

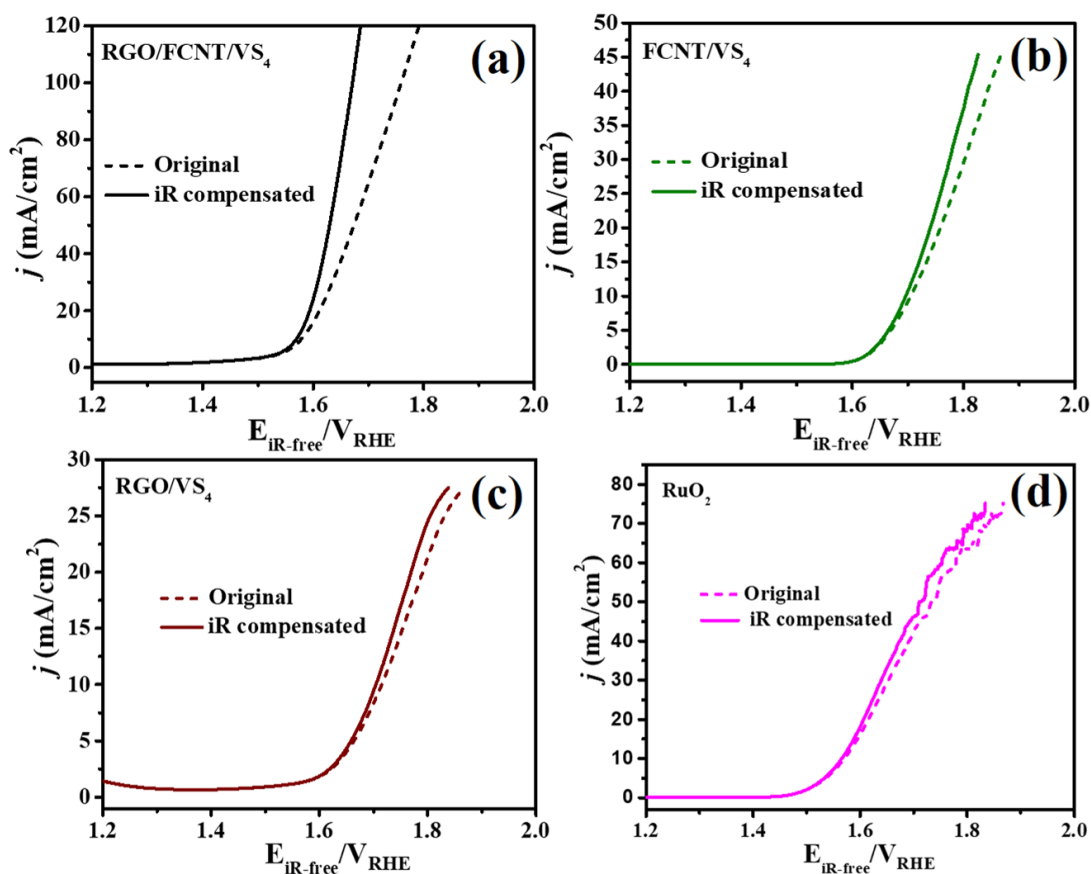


Figure 2.28 Linear sweep voltammograms of RGO/FCNT/VS₄, FCNT/VS₄, RGO/VS₄, and RuO₂ for OER before along with after *iR* correction. All the LSVs data were measured at a sweep rate of 5 mV/s with an applied electrode rotation speed of 1600 rpm.

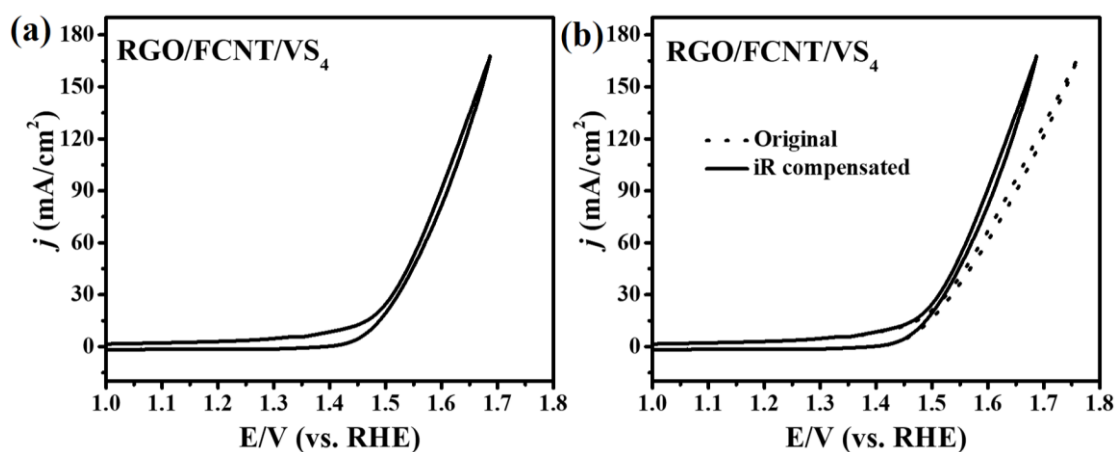


Figure 2.29 (a) The complete cyclic voltammogram of RGO/FCNT/VS₄ for oxygen evolution reaction and (b) cyclic voltammogram before and after *iR* correction.

Moreover, the electrochemical performances were studied through the electrochemical impedance spectrum (EIS) technique in Figure 2.30a. The charge transfer resistance (R_{CT}) was obtained from the EIS spectra for all the samples. And the lower (R_{CT}) value indicates the faster charge transfer and mass transfer rate onto the electrode surface. The R_{CT} values of 40, 400, and 300 Ω were obtained for RGO/FCNT/VS₄, RGO/VS₄, and FCNT/VS₄ hybrid electrode material, respectively. EIS study suggests that the RGO/FCNT/VS₄ hybrids electrode material was a superior electrocatalyst compared to the other two catalysts. The metallic nature of VS₂ shows low charge transfer resistance (R_{ct}) and poor OER activity because of the absence of an effective mechanical support material such as RGO or CNTs based carbon material. Since electrochemical water splitting is a surface phenomenon, the presence of carbon-based

material of RGO/CNTs hybrids gives mechanical support, faster charge transfer, and better electrical conductivity, increasing the number of active centers on the electrocatalyst surface. Further, the electrochemical durability of the RGO/FCNT/VS₄ hybrid was measured by the chronopotentiometry (CP) at 10 mA/cm² current density in Figure 2.30b. The overpotential increased by only 10 mV even after 15 h of constant electrolysis. Afterward, a gradual increase in overpotential has been noticed due to the peeling off of the deposited hybrid material from the electrode surface. Further, the durability test is also supported by the ICP-OES measurements. The remaining ternary hybrid material was collected from the glassy plate electrode surface after 15 h of constant electrolysis. From the as-coated electrode surface, the composition was measured by ICP-OES. The loss of the catalyst mass of 20% is observed, which might occur because of the partial dissolution of the modified ternary hybrids electrode material into the electrolyte solution during the stability test. The loss of active mass reduces active catalytic sites, which implies a decrease in OER performance. In comparison, the OER study is required of 10 mV more overpotential to reach the predefined 10 mA/cm² current density.

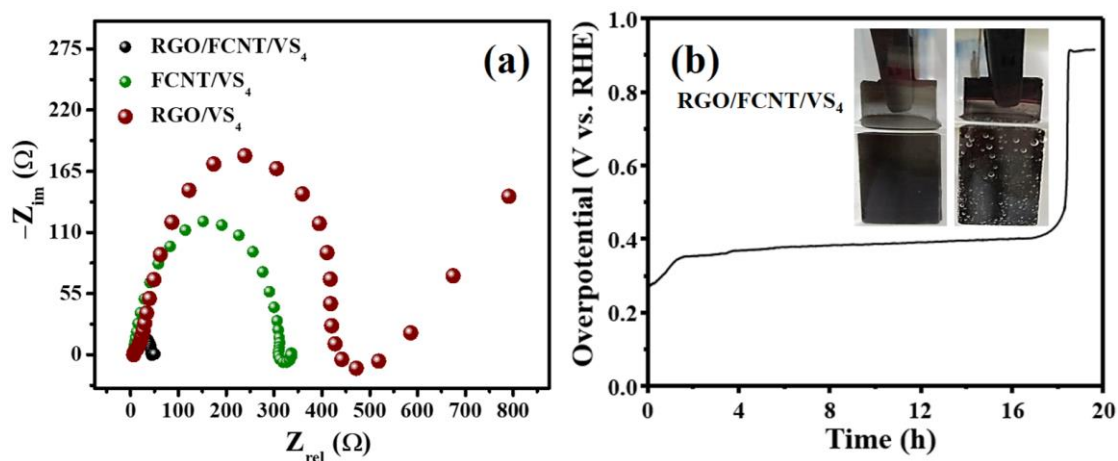


Figure 2.30 (a) Nyquist plots for RGO/FCNT/VS₄, FCNT/VS₄, and RGO/VS₄, (b) OER stability test for RGO/FCNT/VS₄. The inset in (b) is the photograph of the electrode taken before and during the electrolysis.

Electrochemical accessible surface area (ECSA) and the presence of active sites named as roughness factor (R_f) for all the as-prepared electrocatalysts have been calculated from double-layer capacitance (C_{dl}) are displayed in Figure 2.31 and Figure 2.32, respectively. Further, the C_{dl} and ECSA value of 2.69 mF, 67.25 cm² are calculated for the RGO/FCNT/VS₄ hybrid, which is significantly higher in comparison to the values obtained from RGO/VS₄ (0.196 mF, 4.9 cm²) and FCNT/VS₄ (0.59 mF, 14.75 cm²). Moreover, the Roughness factor (R_f) evaluated for RGO/FCNT/VS₄, RGO/VS₄, and FCNT/VS₄ were found to be 960.7, 70, and 210.71, respectively. The above-detailed investigations confirm that the ternary hybrid has a higher electrochemically active surface and a large active center than the other samples.

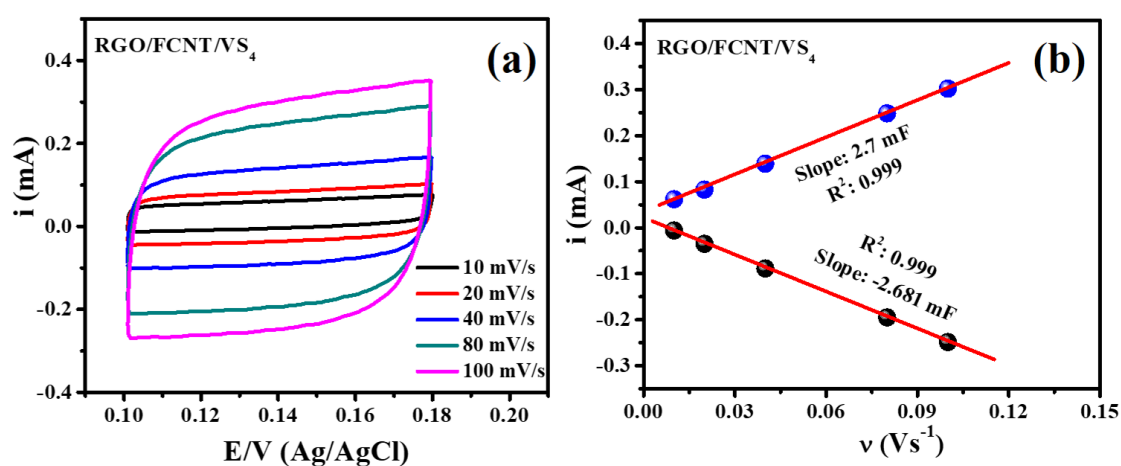


Figure 2.31 (a, b) Cyclic voltammograms and the fitting parameter plot are used to observe the non-faradic parameters (such as C_{dl} , ECSA, and R_f) value at 0.14 V vs. sweep rate for RGO/FCNT/VS₄ hybrid.

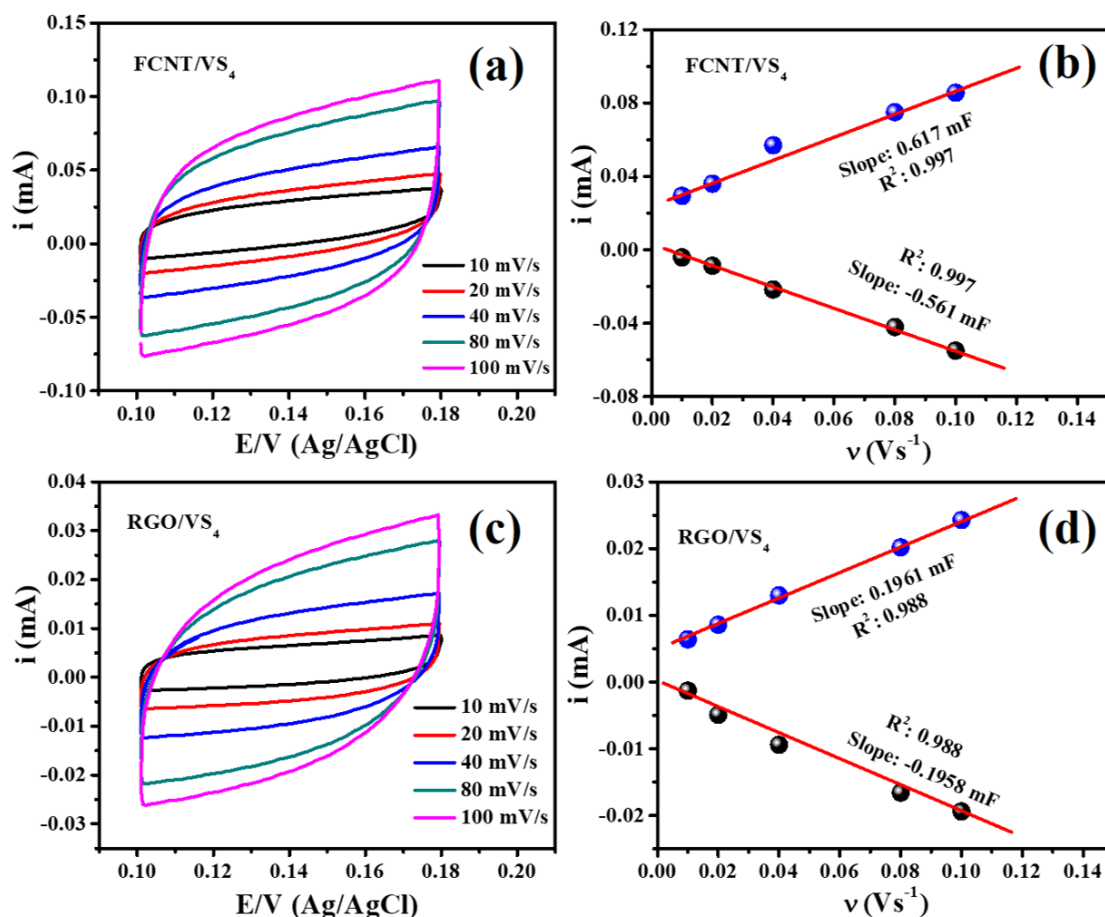


Figure 2.32 The cyclic voltammograms for (a) FCNT/VS₄, (c) RGO/VS₄, at various sweep rates, and (b, d) displays the graph of current at 0.14 V vs. different sweep rate to calculated the value of double-layer capacitance (C_{dl}), electrochemical accessible surface area (ECSA), and roughness factor (R_f) of active catalysts.

The post stability analysis has been demonstrated by Raman, PXRD, and FESEM, respectively, which further confirm the changes in the phase pattern and surface morphology of the as-prepared ternary hybrid as shown in Figure 2.24a and Figure 2.33. Figure 2.33 shows the PXRD and FESEM analysis of RGO/FCNT/VS₄ hybrids after the stability test investigates the surface study of the catalyst. In contrast, VS_x gets converted into the corresponding metal sulfates [V₂(SO₄)₃], metal oxide (V₂O₅), and metal peroxide (VOOH) moieties, respectively, during the period of continuous

electrolysis. Moreover, partial morphological changes are observed after the stability test for the RGO/FCNT/VS₄. Further Raman study after electrolysis shown in Figure 2.24a suggests weakening recorded peak position at 856 cm⁻¹ correspondings to V-C linkage. The obtained weakened position because of the leaching of VS₄ from the hybrids graphitic layers surface RGO/CNTs of RGO/FCNT/VS₄ hybrids.⁶⁵

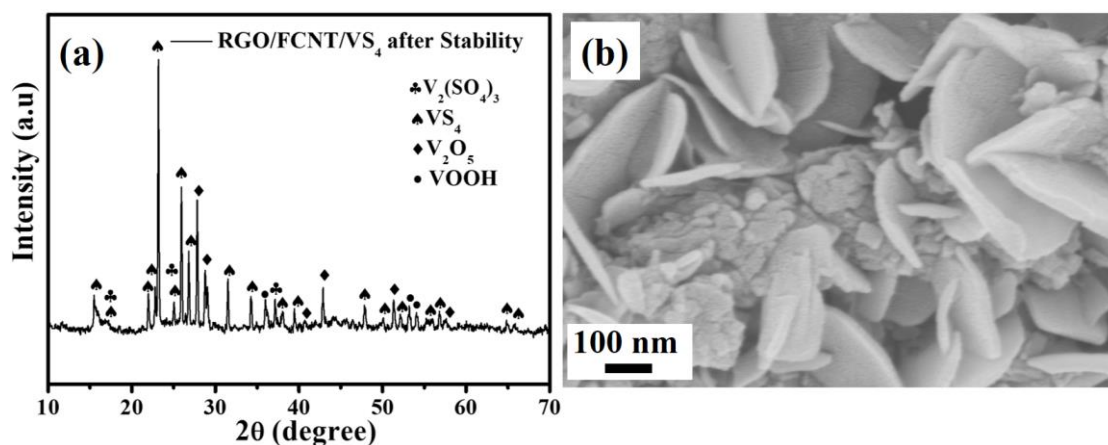


Figure 2.33 (a) Powder X-ray diffraction spectrum, and (b) FESEM image of RGO/FCNT/VS₄ hybrid after the chronopotentiometry (CP) stability test.

The post-stability XPS spectrum of the sample was well shown in Figure 2.34. There is four characteristics peak obtained from the XPS study of V 2p. The peak position obtained with the binding energy of 516.90 eV and 524.40 eV is assigned to V 2p_{3/2} with V 2p_{1/2} orbitals of vanadium, as in +5 oxidation state for V₂O₅. However, the presence of +4 and +3 chemical states of vanadium are observed for the VS₄ and VOOH or V₂(SO₄)₃ having a binding energy of 515.65 eV (V 2p_{3/2}) and 523.20 eV (V 2p_{1/2}), respectively.⁶⁶ The oxidation nature of V clearly shows the presence of +3, +4, and +5 oxidation states after the post-OER test. In S 2p core-level XPS analysis, three different wide bands at 162.27 eV, 163.47 eV, and 168.39 eV were observed. The first two broad bands of S 2p_{3/2} and S 2p_{1/2} orbitals are assigned to S₂²⁻ species in the

ternary hybrids.⁶⁴ However, the band center is about 168.39 eV, indicating oxidized S–O linkage on the surface species.⁴⁸ Additionally, C and O presence is confirmed from the binding energy at 285 eV for C 1s and 530 eV for O 1s. Figure 2.34c shows the C 1s spectra at 284.68, 285.41, and 286.30 eV are regarding C=C along with the C–O bond, respectively. Further, an O 1s peak centered at ~530 eV, indicating the oxygen functional group's involvement.

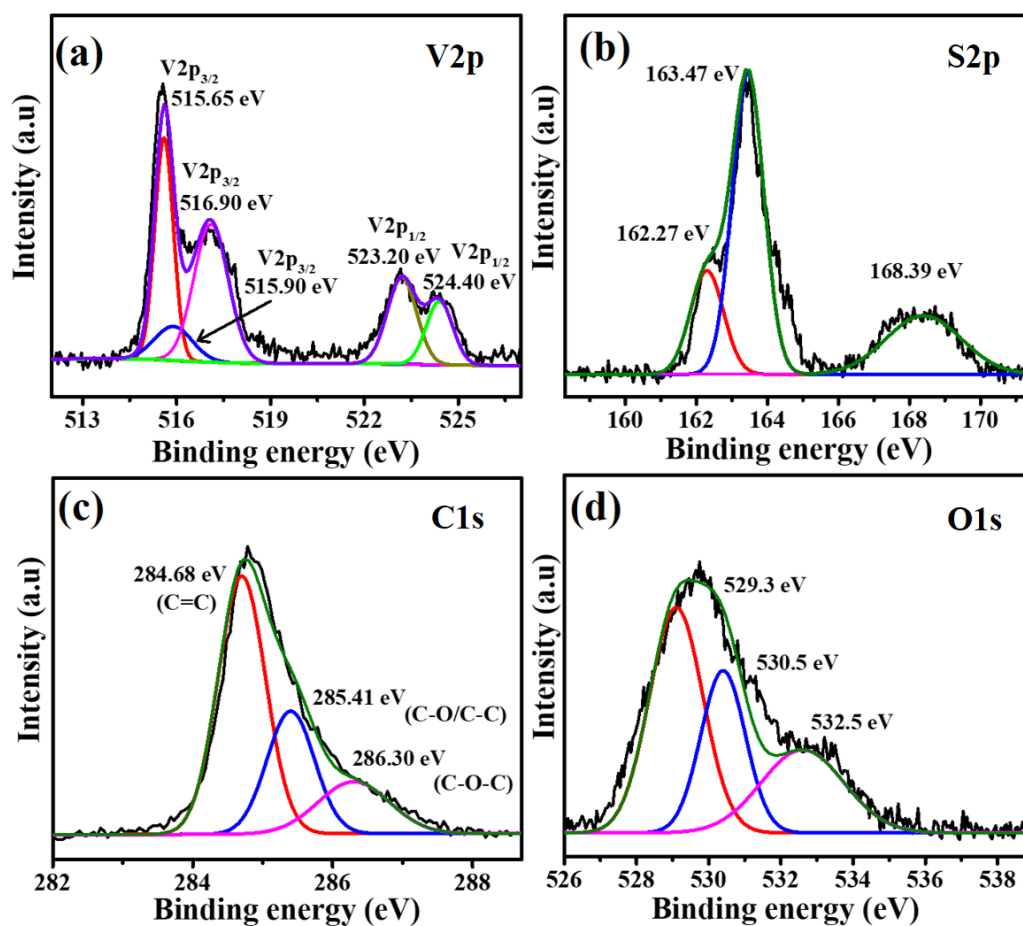


Figure 2.34 In-situ X-ray photoelectron study of (a) V 2p, (b) S 2p, (c) C 1s, and (d) O 1s of RGO/FCNT/VS₄ hybrid after OER stability measurement.

Both before and after stability tests of the RGO/FCNT/VS₄ samples indicate V, S, C, and O elements, respectively. Compared with RGO/FCNT/VS₄ hybrid, a modest change in the atomic percentage of the elements has been noticed after the post-OER

test. The RGO/FCNT/ VS_4 hybrid contains the atomic ratio of 52.18%, 16.65%, 24.13%, and 7.04% for C, O, S, and V, respectively. Whereas after the stability test, the ternary hybrids constitute the atomic percentage of 45.18% of C, 27.37% of O, 21.33% of S, and 6.12% of V. This demonstrates that the surface of ternary hybrids might be oxidized during the post OER measurements. The above XPS analysis clearly shows the in-situ conversion of VS_4 to vanadium oxide, hydroxide, and vanadium sulfate species during the OER test. This observation is supported by the obtained lattice fringes spacing corresponding to the diffraction planes from the HRTEM images after the stability test shown in Figure 2.35.

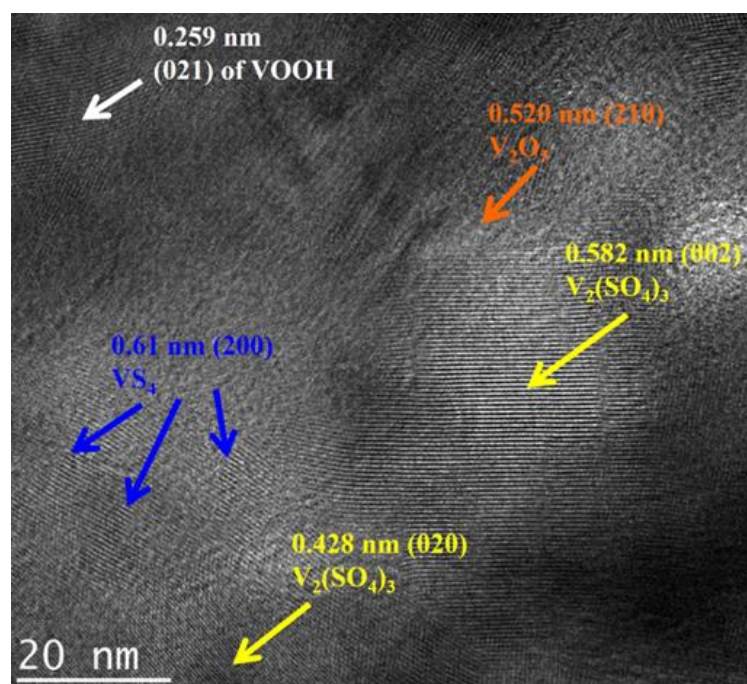


Figure 2.35 HRTEM analysis of RGO/FCNT/ VS_4 hybrid after OER stability measurement.

To verify RGO/FCNT/ VS_4 hybrid enhanced OER performance because of the metal oxides or not, we have measured the anodic current density through the LSV curve for the commercial availability of $\text{V}_2(\text{SO}_4)_3$ and V_2O_5 , which are illustrated in Figure 2.36.

Interestingly, V_2O_5 and $V_2(SO_4)_3$ shows poor OER activity under similar electrolytic condition. In harsh alkaline conditions, the surface of metal sulfides transformed into metal oxides, hydroxides, and oxy-hydroxides during OER measurements.^{67,68} However, some reports have claimed that the sulfide surfaces are not completely diminished even after the long-term durability test.⁶⁹⁻⁷² In this present study, we noticed that the surface of the RGO/FCNT/ VS_4 hybrids partially transformed from metal sulfide to metal oxides/oxo-hydroxide and metal sulfate, respectively. The surface oxidized VS_x is still showing good electrocatalytic performance, similar to other OER-based electrocatalysts like metal chalcogenides and phosphides.⁷³⁻⁷⁶ Besides these, the better electrical conductivity even in partially oxidized form and greater charge transport character of VS_x electrode surface is still responsible for sustained oxygen evolution reaction.^{77,78}

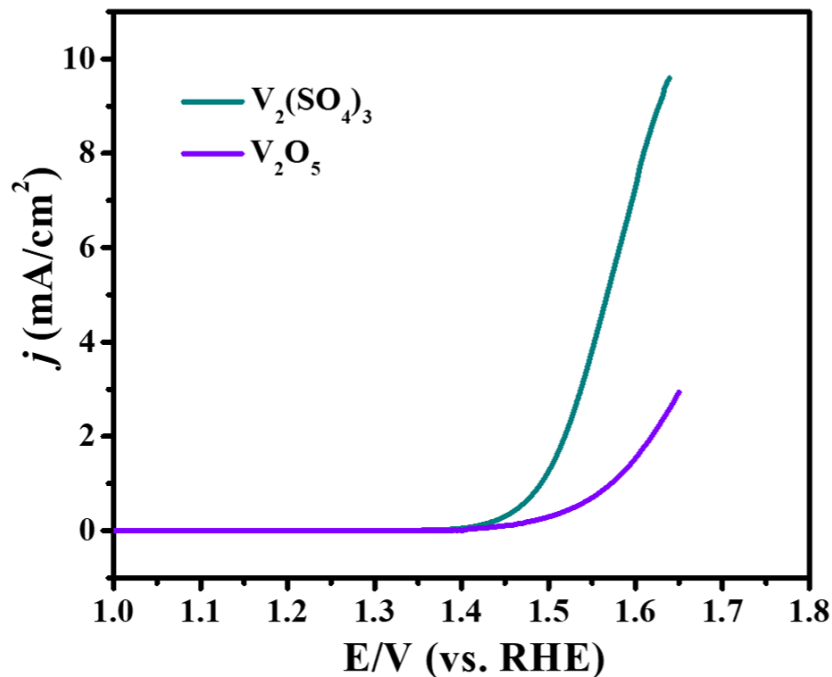


Figure 2.36 Linear sweep voltammogram of commercial $V_2(SO_4)_3$ and V_2O_5 in alkaline solution at 5 mV/s.

Table 2.2 Balancing table of electrocatalytic performance of some recently developed materials towards oxygen evolution reaction.

Sample	Electrolyte KOH (M)	Over potential 10mA/cm ² (mV)	Tafel slope (mV/dec)	Onset potential (V)	Reference
CoO-280-5CoO Nanosheets	1	320	70	1.47	ACS Omega 2018, 3, 10092–10098
CoSe ₂ -160 microcubes	1	328	73		Inorg. Chem. 2020, 59, 12778–12787
FeCoSe ₂ /Co _{0.8} Se	1	330	50.8		J. Alloy. Compd. 2020, 825, 154073
CoSe ₂ /CNTs	1	324	76		Electrochim. Acta 2020, 331, 135362
Hierarchical cobalt sulfide	1	275	30		Electrochimica Acta 281, 2018, 348-356
CoSe ₂ @NC nanorods	1	310	95		J. Alloy. Compound 2019, 778, 134-140
Ni _{0.13} Co _{0.87} S _{1.09}	1	316	54.72		ACS Appl. Energy Mater, 2018, 1 (2), 495–502
Ni ₂ FeO _x @-G-Ph-SN	1	265	60		Sustainable Energy Fuels, 2018, 2, 2160
NiFeP	1	330	39		Chem. Commun., 2018, 54, 8630
MOF derived CoSe ₂	1	320	60		Sustainable Energy Fuels, 2021, 5, 4992
CoSe ₂ @N/C-CNT	1	340	103		J. Colloid Interf. Sci. 2020, 566, 296-303
RGO/FCNT/VS₄	1	330	43	1.45	Present Work

2.9 Conclusions

In summary, the synthesis of both pristine VS₂ and RGO/FCNT/VS₄ hybrid was done by a facile one-step hydrothermal process and its applications towards water splitting

(like hydrogen evolution and oxygen evolution reaction) are investigated. The 2D hexagonal crystal structure of pristine VS₂ owing to greater catalytic active center and large accessible surface area showing enhanced HER performances compared to the 1D monoclinic crystal system of VS₄/rGO composites. VS₂ needs an overpotential of 41 mV to deliver the predefined 10 mA/cm² current density. Additionally, the better HER activity of VS₂ was also explained by the lower onset value (15 mV vs. RHE), small Tafel value (36 mVdec⁻¹), and the durability test, respectively. Likewise, ternary hybrids of the RGO/FCNT/VS₄ sample show better OER performances because of the synergistic effect of RGO/FCNTs hybrids in VS₄. The presence of a higher value of ECSA and R_f makes the ternary hybrids catalytically more active, and it requires an overpotential of 330 mV to reach 10 mA/cm² current density. Therefore, we conclude that the vanadium-based pristine sulfide and their hybrid electrode materials are suitable HER/OER catalysts like other reported electrode materials and simultaneously creates a new window in the field of ternary hybrid materials.

2.10 References

- 1 X. Li, L. Zhao, J. Yu, X. Liu, X. Zhang, H. Liu and W. Zhou, *Nano-Micro Lett.*, 2020, **12**, 131.
- 2 J. Wang, X. Yue, Y. Yang, S. Sirisomboonchai, P. Wang, X. Ma, A. Abudula and G. Guan, *J. Alloys Compd.*, 2020, **819**, 153346.
- 3 Y. Jiao, Y. Zheng, M. Jaroniec and S. Z. Qiao, *Chem. Soc. Rev.*, 2015, **44**, 2060–2086.
- 4 M. Chhowalla, H. S. Shin, G. Eda, L.-J. Li, K. P. Loh and H. Zhang, *Nat. Chem.*, 2013, **5**, 263.

- 5 J. K. Das, A. K. Samantara, A. K. Nayak, D. Pradhan and J. N. Behera, *Dalton Trans.*, 2018, **47**, 13792–13799.
- 6 Y.-Y. Zhang, X. Zhang, Z.-Y. Wu, B.-B. Zhang, Y. Zhang, W.-J. Jiang, Y.-G. Yang, Q.-H. Kong and J.-S. Hu, *J. Mater. Chem. A*, 2019, **7**, 5195–5200.
- 7 C. Tan and H. Zhang, *Chem. Soc. Rev.*, 2015, **44**, 2713–2731.
- 8 S. Ratha, S. R. Marri, J. N. Behera and C. S. Rout, *Eur. J. Inorg. Chem.*, 2016, **2016**, 259–265.
- 9 S. Ratha, S. R. Marri, N. A. Lanzillo, S. Moshkalev, S. K. Nayak, J. N. Behera and C. S. Rout, *J. Mater. Chem. A*, 2015, **3**, 18874–18881.
- 10 L. Wu, A. J. F. van Hoof, N. Y. Dzade, L. Gao, M.-I. Richard, H. Friedrich, N. H. De Leeuw, E. J. M. Hensen and J. P. Hofmann, *Phys. Chem. Chem. Phys.*, 2019, **21**, 6071–6079.
- 11 S. Ratha and C. S. Rout, *ACS Appl. Mater. Interfaces*, 2013, **5**, 11427.
- 12 Y. Li, H. Wang, L. Xie, Y. Liang, G. Hong and H. Dai, *J. Am. Chem. Soc.*, 2011, **133**, 7296.
- 13 S. Wei, R. Zhou and G. Wang, *ACS Omega*, 2019, **4**, 15780–15788.
- 14 K. Hernandez Ruiz, J. Liu, R. Tu, M. Li, S. Zhang, J. R. Vargas Garcia, S. Mu, H. Li, T. Goto and L. Zhang, *J. Alloys Compd.*, 2018, **747**, 100–108.
- 15 J. Li, J. Li, D. Yan, S. Hou, X. Xu, T. Lu, Y. Yao, W. Mai and L. Pan, *J. Mater. Chem. A*, 2018, **6**, 6595–6605.
- 16 Y. Guo, C. Shang and E. Wang, *J. Mater. Chem. A*, 2017, **5**, 2504–2507.
- 17 T. G. Ulusoy Ghobadi, B. Patil, F. Karadas, A. K. Okyay and E. Yilmaz, *ACS Omega*, 2017, **2**, 8319–8329.
- 18 S. R. Marri, S. Ratha, C. S. Rout and J. N. Behera, *Chem. Commun.*, 2017, **53**,

- 228–231.
- 19 C. Wang, X. Wu, Y. Ma, G. Mu, Y. Li, C. Luo, H. Xu, Y. Zhang, J. Yang, X. Tang, J. Zhang, W. Bao and C. Duan, *J. Mater. Chem. A*, 2018, **6**, 8299–8306.
- 20 F. Ming, H. Liang, Y. Lei, W. Zhang and H. N. Alshareef, *Nano Energy*, 2018, **53**, 11–16.
- 21 X. Rui, H. Tan and Q. Yan, *Nanoscale*, 2014, **6**, 9889–9924.
- 22 P. M. Ajayan and O. Z. Zhou, eds. M. S. Dresselhaus, G. Dresselhaus and P. Avouris, Springer Berlin Heidelberg, Berlin, Heidelberg, 2001, pp. 391–425.
- 23 C. A. Mitchell, J. L. Bahr, S. Arepalli, J. M. Tour and R. Krishnamoorti, *Macromolecules*, 2002, **35**, 8825–8830.
- 24 K. Yurekli, C. A. Mitchell and R. Krishnamoorti, *J. Am. Chem. Soc.*, 2004, **126**, 9902–9903.
- 25 A. Garg and S. B. Sinnott, *Chem. Phys. Lett.*, 1998, **295**, 273–278.
- 26 B. I. Yakobson and P. Avouris, eds. M. S. Dresselhaus, G. Dresselhaus and P. Avouris, Springer Berlin Heidelberg, Berlin, Heidelberg, 2001, pp. 287–327.
- 27 J. Chen, M. A. Hamon, H. Hu, Y. Chen, A. M. Rao, P. C. Eklund and R. C. Haddon, *Science (80-.)*, 1998, **282**, 95 LP – 98.
- 28 A. K. Samantara, S. Chandra Sahu, A. Ghosh and B. K. Jena, *J. Mater. Chem. A*, 2015, **3**, 16961–16970.
- 29 A. K. Samantara, S. Kamila, A. Ghosh and B. K. Jena, *Electrochim. Acta*, 2018, **263**, 147–157.
- 30 J. K. Das, A. K. Samantara, S. R. K. A., C. S. Rout and J. N. Behera, *Dalton Trans.*, 2019, **48**, 15955–15961.
- 31 W. Xu, Z. Lu, X. Sun, L. Jiang and X. Duan, *Acc. Chem. Res.*, ,

DOI:10.1021/acs.accounts.8b00070.

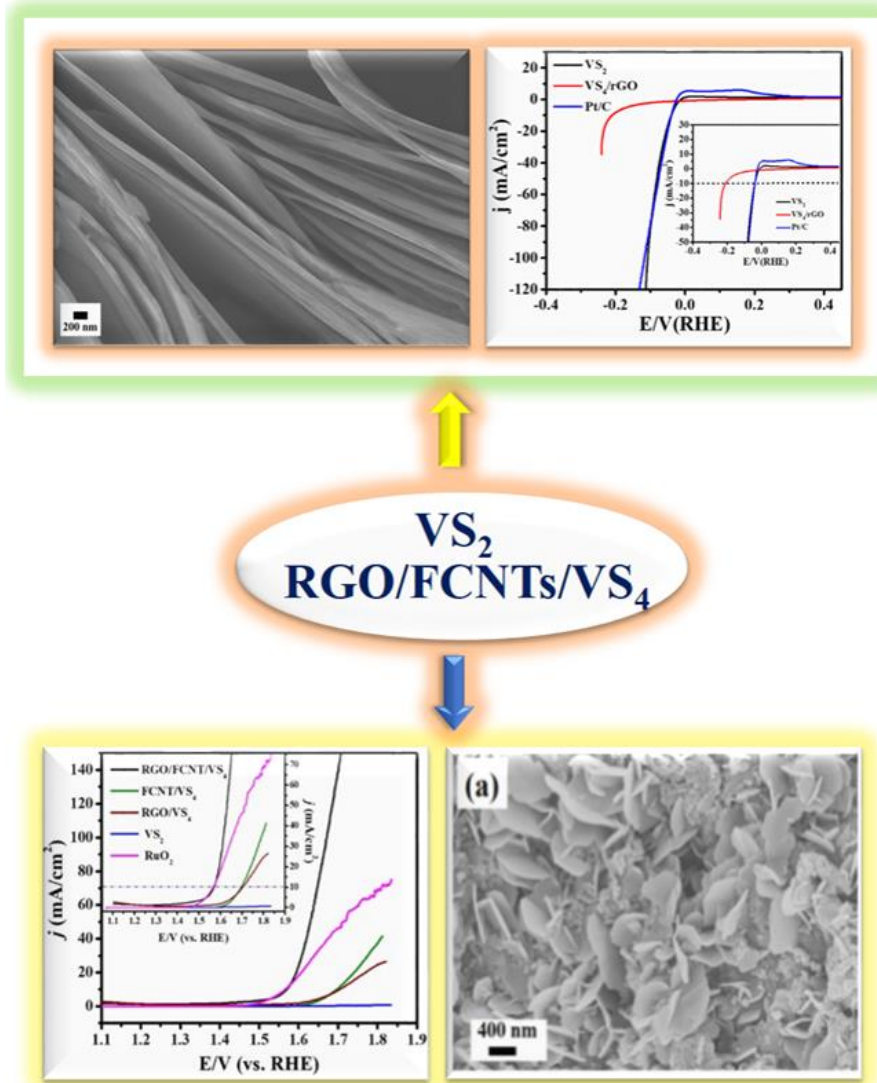
- 32 Z. Lu, W. Zhu, X. Yu, H. Zhang, Y. Li, X. Sun, X. Wang, H. Wang, J. Wang, J. Luo, X. Lei and L. Jiang, *Adv. Mater.*, 2014, **26**, 2683–2687.
- 33 W. Xu, Z. Lu, P. Wan, Y. Kuang and X. Sun, *Small*, 2016, **12**, 2492–2498.
- 34 A. Dutta, A. K. Samantara, S. K. Dutta, B. K. Jena and N. Pradhan, *ACS Energy Lett.*, 2016, **1**, 169–174.
- 35 J. K. Das, A. K. Samantara, S. Satyarthi, C. S. Rout and J. N. Behera, *RSC Adv.*, 2020, **10**, 4650–4656.
- 36 P. Xiao, M. A. Sk, L. Thia, X. Ge, R. J. Lim, J.-Y. Wang, K. H. Lim and X. Wang, *Energy Environ. Sci.*, 2014, **7**, 2624–2629.
- 37 J. Yang, G. Zhu, Y. Liu, J. Xia, Z. Ji, X. Shen and S. Wu, *Adv. Funct. Mater.*, 2016, **26**, 4712–4721.
- 38 A. Dutta, S. Mutyala, A. K. Samantara, S. Bera, B. K. Jena and N. Pradhan, *ACS Energy Lett.*, 2018, **3**, 141–148.
- 39 C. C. L. McCrory, S. Jung, J. C. Peters and T. F. Jaramillo, *J. Am. Chem. Soc.*, 2013, **135**, 16977–16987.
- 40 Y. Yang, H. Fei, G. Ruan and J. M. Tour, *Adv. Mater.*, 2015, **27**, 3175–3180.
- 41 T. Y. Ma, S. Dai, M. Jaroniec and S. Z. Qiao, *J. Am. Chem. Soc.*, 2014, **136**, 13925–13931.
- 42 X. Z. Tang, Z. Cao, H. Bin Zhang, J. Liu and Z. Z. Yu, *Chem. Commun.*, 2011, **47**, 3084–3086.
- 43 C. Zhu, S. Guo, Y. Fang and S. Dong, *ACS Nano*, 2010, **4**, 2429–2437.
- 44 K. H. Liao, A. Mittal, S. Bose, C. Leighton, K. A. Mkhoyan and C. W. MacOsco, *ACS Nano*, 2011, **5**, 1253–1258.

- 45 Y. Qu, M. Shao, Y. Shao, M. Yang, J. Xu, C. T. Kwok, X. Shi, Z. Lu and H. Pan, *J. Mater. Chem. A*, 2017, **5**, 15080–15086.
- 46 P. Mohan, J. Yang, A. Jena and H. Suk Shin, *J. Solid State Chem.*, 2015, **224**, 82–87.
- 47 Y. Zhou, P. Liu, F. Jiang, J. Tian, H. Cui and J. Yang, *J. Colloid Interface Sci.*, 2017, **498**, 442–448.
- 48 H. Liang, H. Shi, D. Zhang, F. Ming, R. Wang, J. Zhuo and Z. Wang, *Chem. Mater.*, 2016, **28**, 5587–5591.
- 49 H. Huang, Y. Yu and K. H. Chung, *Int. J. Hydrogen Energy*, 2014, **39**, 13832–13837.
- 50 W. G. Wang, X. Wang, L. Y. Tian, Y. L. Wang and S. H. Ye, *J. Mater. Chem. A*, 2014, **2**, 4316–4323.
- 51 L. Yan, P. Dai, Y. Wang, X. Gu, L. Li, L. Cao and X. Zhao, *ACS Appl. Mater. Interfaces*, 2017, **9**, 11642–11650.
- 52 B. E. Conway and B. V Tilak, *Electrochim. Acta*, 2002, **47**, 3571.
- 53 W. F. Chen, S. Iyer, S. Iyer, K. Sasaki, C. H. Wang, Y. Zhu, J. T. Muckerman and E. Fujita, *Energy Environ. Sci.*, 2013, **6**, 1818–1826.
- 54 T. Wang, L. Liu, Z. Zhu, P. Papakonstantinou, J. Hu, H. Liu and M. Li, *Energy Environ. Sci.*, 2013, **6**, 625–633.
- 55 L. Yang, P. Liu, J. Li and B. Xiang, *Catalysts*, 2017, **7**, 285.
- 56 X. Hai, W. Zhou, S. Wang, H. Pang, K. Chang, F. Ichihara and J. Ye, *Nano Energy*, 2017, **39**, 409–417.
- 57 Z. Wu, B. Fang, A. Bonakdarpour, A. Sun, D. P. Wilkinson and D. Wang, *Appl. Catal. B Environ.*, 2012, **125**, 59–66.

- 58 X. Zhang, F. Wang, H. Huang, H. Li, X. Han, Y. Liu and Z. Kang, *Nanoscale*, 2013, **5**, 2274–2278.
- 59 S. N. Baker and G. A. Baker, *Angew. Chemie Int. Ed.*, 2010, **49**, 6726–6744.
- 60 S. Stankovich, D. A. Dikin, R. D. Piner, K. A. Kohlhaas, A. Kleinhammes, Y. Jia, Y. Wu, S. T. Nguyen and R. S. Ruoff, *Carbon N. Y.*, 2007, **45**, 1558–1565.
- 61 F. Tuinstra and J. L. Koenig, *J. Chem. Phys.*, 1970, **53**, 1126–1130.
- 62 Q. Li, Y. Chen, J. He, F. Fu, J. Lin and W. Zhang, *J. Alloys Compd.*, 2016, **685**, 294–299.
- 63 R. Sun, Q. Wei, Q. Li, W. Luo, Q. An, J. Sheng, D. Wang, W. Chen and L. Mai, *ACS Appl. Mater. Interfaces*, 2015, **7**, 20902–20908.
- 64 C. S. Rout, B.-H. Kim, X. Xu, J. Yang, H. Y. Jeong, D. Odkhuu, N. Park, J. Cho and H. S. Shin, *J. Am. Chem. Soc.*, 2013, **135**, 8720–8725.
- 65 K. Zhu, X. Yan, Y. Zhang, Y. Wang, A. Su, X. Bie, D. Zhang, F. Du, C. Wang, G. Chen and Y. Wei, *Chempluschem*, 2014, **79**, 447–453.
- 66 G. A. Sawatzky and D. Post, *Phys. Rev. B*, 1979, **20**, 1546–1555.
- 67 J. Jian, L. Yuan, H. Qi, X. Sun, L. Zhang, H. Li, H. Yuan and S. Feng, *ACS Appl. Mater. Interfaces*, 2018, **10**, 40568–40576.
- 68 N.-T. Suen, S.-F. Hung, Q. Quan, N. Zhang, Y.-J. Xu and H. M. Chen, *Chem. Soc. Rev.*, 2017, **46**, 337–365.
- 69 H. Wang, Z. Li, G. Li, F. Peng and H. Yu, *Catal. Today*, 2015, **245**, 74–78.
- 70 M. Shen, C. Ruan, Y. Chen, C. Jiang, K. Ai and L. Lu, *ACS Appl. Mater. Interfaces*, 2015, **7**, 1207–1218.
- 71 N. Shinde, P. Shinde, Q. X. Xia, J. M. Yun, R. Mane and K. H. Kim, *ACS Omega*, 2019, **4**, 6486–6491.

- 72 F. Li, D. Zhang, R.-C. Xu, W.-F. Fu and X.-J. Lv, *ACS Appl. Energy Mater.*, 2018, **1**, 3929–3936.
- 73 D. Yang, L. Cao, L. Feng, J. Huang, K. Kajiyoshi, Y. Feng, Q. Liu, W. Li, L. Feng and G. Hai, *Appl. Catal. B Environ.*, 2019, **257**, 117911.
- 74 W. Li, X. Gao, X. Wang, D. Xiong, P.-P. Huang, W.-G. Song, X. Bao and L. Liu, *J. Power Sources*, 2016, **330**, 156–166.
- 75 W. Li, D. Xiong, X. Gao and L. Liu, *Chem. Commun.*, 2019, **55**, 8744–8763.
- 76 D. Yang, L. Cao, J. Huang, K. Kajiyoshi, L. Feng, L. Kou, Q. Liu and L. Feng, *Nanoscale*, 2020, **12**, 2063–2070.
- 77 D. V Shinde, L. De Trizio, Z. Dang, M. Prato, R. Gaspari and L. Manna, *Chem. Mater.*, 2017, **29**, 7032–7041.
- 78 J. Du, Z. Zou, C. Liu and C. Xu, *Nanoscale*, 2018, **10**, 5163–5170.

Summary of Chapter-2

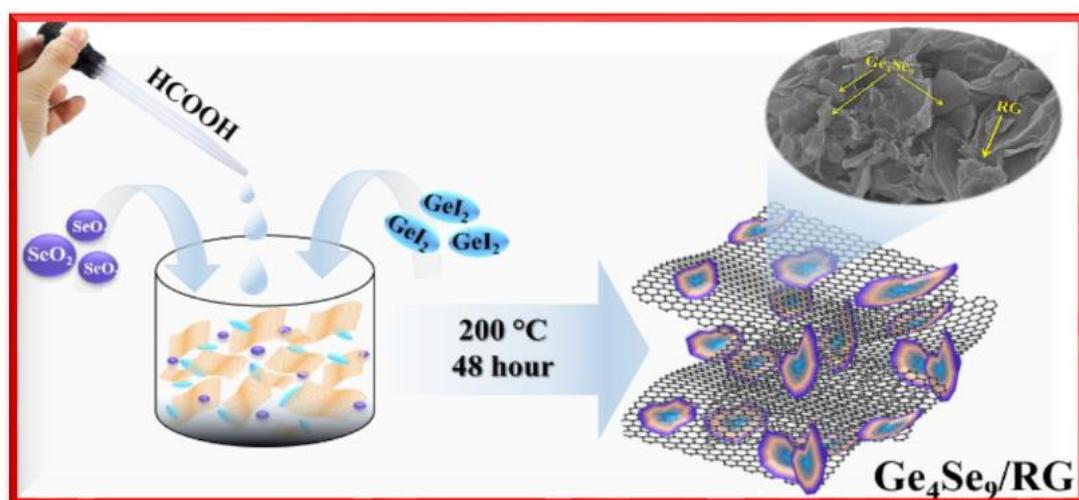


CHAPTER – 3

Supercapacitors based on Germanium Selenide (Ge_4Se_9)/RGO Hybrids

- 3.1** Abstract
- 3.2** Introduction
- 3.3** Motivation of our Work
- 3.4** Experimental Part
 - 3.4.1** Formation of RGO from GO
 - 3.4.2** Synthesis of Ge_4Se_9
 - 3.4.3** Synthesis of Ge_4Se_9 /RGO hybrids
- 3.5** Characterization
- 3.6** Electrochemical measurements
- 3.7** Results and discussions
- 3.8** Conclusions
- 3.9** References

3.1 Abstract



This chapter introduced a single-step hydrothermal synthesis of tetra germanium nonaselenide (Ge_4Se_9) and its various weight percentage (%) of reduced graphene oxide composites. For the first time, the supercapacitor application of the $\text{Ge}_4\text{Se}_9/\text{RGO}$ materials is explored. Herein the various weight percentages of graphene oxide composites play a vital role in the charge storage mechanism for the germanium chalcogenides. The different weight percentages of GO composites like 0.30 wt% and 0.60 wt% are synthesized with the pristine germanium selenide (Ge_4Se_9) precursors. Out of the pristine and two GO composites of germanium selenide (Ge_4Se_9), 0.30 wt% of GO hybrid material shows a better energy storage performances with enhanced specific capacitance (220 F/g) at a current density of 2 A/g, energy density (12 Wh/kg), and power density (4.6 kW/kg) than the other hybrids. Furthermore, the composites show additional cyclic stability of repeated 10000 charge-discharge cycles with excellent 91% of retention capacitance, and the post stability analysis signifies the robust performances of the composites.

3.2 Introduction

Till now, the high energy demands are fulfilled by the consumption of limited reserve fossil fuels. However, the dependency on fossil fuels feeds the energy demands and brings several environmental and climate changes in present human life. Therefore, researchers are more disturbed about the developments of renewable energy storage technology for a clean and carbon-free environment all over the world.¹ Nowadays, traditional batteries and conventional capacitors are emerged with great attention as alternative energy storage devices due to their unique specific power values. Although supercapacitor or ultra-capacitor signifies as a high charge storage device system by its large specific energy, fast charging or discharging capacity, excellent durability with a high power density compared to other capacitors and batteries.^{2,3} The energy or charge storage process in a supercapacitor is focused on two types of mechanism (a) charge accumulation process of formation of double layers type mechanism or EDLC and (b) oxidation or reduction of pseudo capacitor mechanism. Different metal oxides, hydroxides, metal chalcogenides, carbides, phosphides, etc., are considered electrode material, and the charge storage mechanism occurs through a Faradic oxidation-reduction reaction.⁴ Whereas the carbon-based electrode materials such as graphene oxide, carbon nanotubes, activated carbon, heteroatom-containing carbon have been significantly considered suitable carbonaceous materials and used to enhance the specific capacitance by composites with the pseudocapacitors material. The mechanism of charge storage behind in EDLCs through ions adsorption at electrode surface are completely electrostatically without any faradic reaction.⁵ However, the energy storage performances of supercapacitors strongly depend on the pseudocapacitors, EDLCs, and hybrid type electrode material used.⁶ Therefore,

researchers are drawn significant attention to 2D layered transition metal chalcogenides as an electrode material because of its layered structure, each layered structure stacked with another one by weak van der Waals force of attraction which makes easy exfoliation to form high surface area of a single-layered structure, intricateness and tunable chemical and physical properties. These properties of TMDCs, easily made them a superior electrode material and explored to use as flexible and different transparent electronics.^{7,8} Particularly different transition metal selenides like VSe₂, NiSe, WSe₂, NiSe₂, MoSe₂, CoSe₂, SnSe₂, and some other bimetallic metal centers of selenides were synthesized and extensively studied their performances in the field of energy storage.⁹⁻¹⁵ The synthesis and supercapacitor applications of germanium selenide are rarely explored. Firstly, Schaak et al. reported the synthesis of germanium sulfide/selenide (GeSe/GeS) nanostructures through a colloidal technique.¹⁶ Secondly, Rao et al. observed the growth of GeSe₂ nanowire in the process of acid hydrolysis.¹⁷ Interestingly, the crystal structure of the Ge₄Se₉ clutch is isoelectronic with the monoclinic diselenide of germanium (GeSe₂). The tetrahedral unit of the GeSe₄ structure is the common chain unit of monoclinic GeSe₂ and the orthorhombic Ge₄Se₉ crystal system. In GeSe₂, the connection via GeSe₄ tetrahedral unit is in both the corner and edge center whereas, in Ge₄Se₉ constitute, GeSe₄ sharing in corner position by the additional dimer of Se-Se pairs. The Ge₄Se₉ crystal arrangement can be easily distinguished from the GeSe₂ by sharing an extra Se-Se unit pair in the corner that linked with the tetrahedral GeSe₄ unit, as shown in Figure 3.1¹⁸

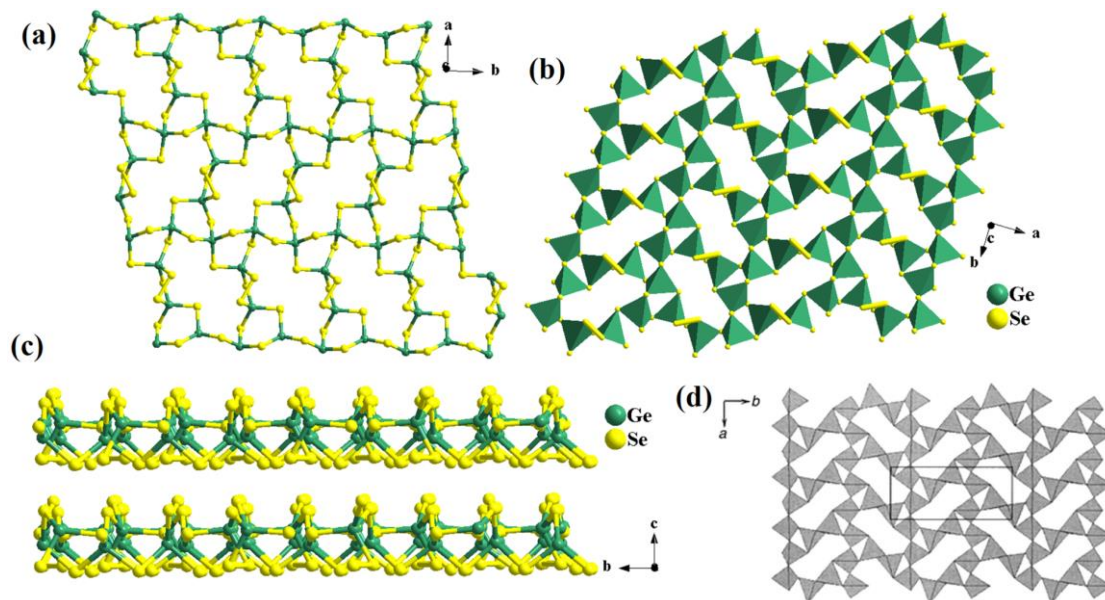


Figure 3.1 Layered 2D structure (a) ball and stick model, (b) polyhedral crystal structure, (c) stacking arrangements of a 2D layer of bare Ge₄Se₉, and (d) monoclinic polyhedral structure of GeSe₂. The crystal structure was reproduced and redrawn from Fjellvåg et al.¹⁸

After the well-discussed on crystal arrangements, the chemical state or the oxidation state of the as-prepared Ge₄Se₉ material was found to be +4 and easily explained by X-ray photoelectron spectroscopy (XPS) analysis. The simple crystal arrangement of Ge₄Se₉ material, corresponding to the common formulae of (Ge⁴⁺)₄(Se²⁻)₇(Se₂)²⁻ and the charge balance is exhibited as $4 \times (+4) = 16+$ and $7 \times (-2) + (-2) = 16-$. The charge is completely balanced with the presence of an additional Se-Se unit pair. Lastly, we briefly described a facile and one-step hydrothermal synthesis of 2D layered tetra germanium nonaselenide (Ge₄Se₉) nanoplates with reduced graphene oxide (RGO) hybrids. After the successful synthesis of yellowish color germanium selenide precursor, variable weight (%) of graphene oxides such as 0.30 wt% and 0.60 wt% composites were synthesized in a similar reaction condition. Further, the planned,

systematic characterizations, the supercapacitor performance of the hybrid material have been explored. Besides two GO composites variations, the 0.30 wt% of GO-contained composite shows good specific capacitance, specific power, and specific energy. Besides these, it gives better long-term cyclic stability. We believe that 0.30 wt% of GO-contained Ge_4Se_9 composite could be employed as an advanced electrode material for the electrochemical energy storage system. Interestingly, there is no such outline on $\text{Ge}_4\text{Se}_9/\text{RGO}$ composites as cathode electrode materials for supercapacitor performances. Preliminary, we report a single-step hydrothermal technique, planned characterization, and all the supercapacitor measurements data for bare (Ge_4Se_9) and its composite of (Ge_4Se_9)/RGO.

3.3 Motivation of our Work

For the searching of an efficient metal selenides electrode material for the energy storage applications, bare transition metal selenides and its carbonaceous materials hybrid were good for the charge storage process owing to enhance specific capacitance, specific energy, and specific power density, respectively. Researchers are considering different unique synthetic protocols and exploring electrochemical (energy storage or conversion) studies on various transition-based metal selenides electrode materials such as MoSe_2 , NiSe_2 , CoSe_2 , WSe_2 , VSe_2 layers having pristine and graphene composites. However, the research on main group-based selenide (such as germanium selenide) is rarely explored. Interestingly, we synthesized a new class of germanium selenide (Ge_4Se_9), and their variable weight percentage (%) of RGO hybrids belongs to the orthorhombic crystal structure, which is isostructure with monoclinic binary GeSe_2 , and the detailed electrochemical energy storage performances were investigated.

3.4 Experimental section

3.4.1 Formation of RGO from GO

Modified Hummers' approach functionalized graphite powder to graphene oxide, and the detailed explanation was given in the previous report.^{19,20} Further, the reduction process in which GO converted into reduced graphene oxide (RGO) was done at 160 °C for 24 h by a simple hydrothermal reaction.

3.4.2 Synthesis of bare Ge₄Se₉

Selenium-rich germanium selenide (Ge₄Se₉) was obtained by the use of a one-step hydrothermal technique involving the reaction mixture of germanium iodide (0.040 g) and SeO₂ (0.055 g) in 10 ml of deionized water. After that, a reducing agent such as formic acid of 1 ml was added slowly to the whole reaction precursor and free to stir vigorously for 1 h. Further, the total reaction precursor was transferred in a Teflon-lined autoclave and kept the total reaction mixture in a hot air oven at 200 °C for 48 h. Upon cooling down to normal temperature, obtained yellow-colored filter product was centrifuge several times with distilled water and ethanol. Further, the collected sample was dried in a vacuum oven for future use.

3.4.3 Synthesis of Ge₄Se₉/RGO hybrids

Ge₄Se₉ with varied graphene oxide composites have been used in a similar reaction condition at 200 °C for 48 h, and the presence of carbon content in the final germanium selenide samples was analyzed by elemental mapping. Particularly, varying the weight percentage (%) concentration of graphene oxide termed as the two composites of Ge₄Se₉ sample as Ge₄Se₉/RG1 (0.30 wt%) and Ge₄Se₉/RG2 (0.60 wt%) respectively.

3.5 Characterization

The initial characterization for the phase purity was determined by PXRD (powder X-ray diffraction) having a wavelength ($\lambda = 1.5418 \text{ \AA}$) of Cu-K α radiation. The morphological and elemental mapping analysis for Ge₄Se₉ and graphene oxide of Ge₄Se₉ composite were analyzed with the TEM (Transmission electron microscope of JEOL 2100F, work at 200 kV) and FESEM (Field emission scanning electron microscope) instrument of Merlin Compact having GEMINI-I electron column by Zeiss Pvt. Ltd., Germany. For FESEM and TEM study, a dilute form of the composite solution was prepared in ethanol. However, in the TEM study, a dilute solution droplet is coated on a carbon laminated copper grid (200 mesh) and dried under a vacuum pump. The thermogravimetric analysis is generally performed for the as-synthesized sample thermal stability at a slope rate of 10 °C/min (TA Instruments-Waters Lab) instruments under an inert nitrogen atmosphere. The in-situ analysis of samples further verified by the Raman spectrum under a micro Raman analyzer (Horiba Scientific) with a laser 532 nm wavelength range.

3.6 Electrochemical measurements

Electrochemical energy storage performances were carried out for nanostructure Ge₄Se₉ and Ge₄Se₉/RG composites with all systematic three-electrode measurements by using Potentiostat/Galvanostat instruments (Biologic, SP-200). The powdered sample first dispersed with the mixture of Nafion and ethanol to form a homogeneous catalyst-ink followed by bath sonication for 20 min. Moreover, a nickel foam piece having (1 cm \times 3 cm of width and length ratio) is washed continuously with freshly prepared 0.1 M HCl solution to remove the unreacted substrate. It dried for electrode preparation. Herein nickel foam coated sample (working electrode), noble platinum

(auxiliary), and aqueous Ag/AgCl (references), respectively. In electrode preparation, sample mass loading was maintained as 1 mg/cm² on 1 cm² of nickel foam throughout all measurements. A solution of 1 M KOH was used as an aqueous electrolyte for all the electrochemical experiments within the −0.1 to 0.6 V potential range.

The Nyquist impedance spectrum was recorded for the as-prepared electrode catalyst in the frequency horizon of 0.01 Hz to 1 MHz with a used amplitude of 5 mV. Further, the electrode material stability takes 10,000 repeated galvanostatic charge-discharge patterns at a constant current density of 1 A/g.

By considering the galvanostatic charge/discharge pattern, the value of specific capacitance (C_{sp}) of active material was determined from the equation as follows:^{21–23}

$$C_{sp} = \frac{I\Delta t}{m\Delta V} \quad (3.1)$$

C_{sp} is specific capacitance, I (mA), Δt is discharge current and time, m is mass of the prepared sample, and the potential working window is ΔV (V). C_{sp} is also evaluated through cyclic voltammetry by the equation as follows

$$C_{sp} = \frac{\int I dv}{2[m\vartheta(\Delta V)]} \quad (3.2)$$

The integral numerator of $\int I dv$ denotes as an area of the measured cycle, m is the mass of samples, ϑ (mV/s) and ΔV are the sweep rate and operating potential window. By following the CV technique, the subsequent calculation for energy density (ED) or specific energy and power density (PD) or specific power was done by considering the equations as,^{24,25}

$$ED = \frac{C_{sp}(\Delta V)^2}{2} \quad (3.3)$$

$$PD = \frac{C_{sp}(\Delta V)\vartheta}{2} \quad (3.4)$$

3.7 Results and discussions

Different weight percentage ratios of graphene oxide (GO) (0.30 and 0.60 wt%) with germanium selenide (Ge_4Se_9) composites have been developed in a hydrothermal method and presented as $\text{Ge}_4\text{Se}_9/\text{RG1}$ and $\text{Ge}_4\text{Se}_9/\text{RG2}$, respectively. FESEM images for pristine Ge_4Se_9 are shown in Figure 3.2a, and the reduced form of GO in $\text{Ge}_4\text{Se}_9/\text{RG1}$ (0.30 wt%) hybrid was confirmed, having plates-like morphology distributed over the RGO layer are illustrated in Figure 3.2b-c, respectively. FESEM data. Elemental mapping of the hybrid, EDAX, and a clear list of the table provided in (Figures 3.3 and Figure 3.4) confirm the presence of atomic and weight percentage of germanium, selenium, and carbon elements composites.

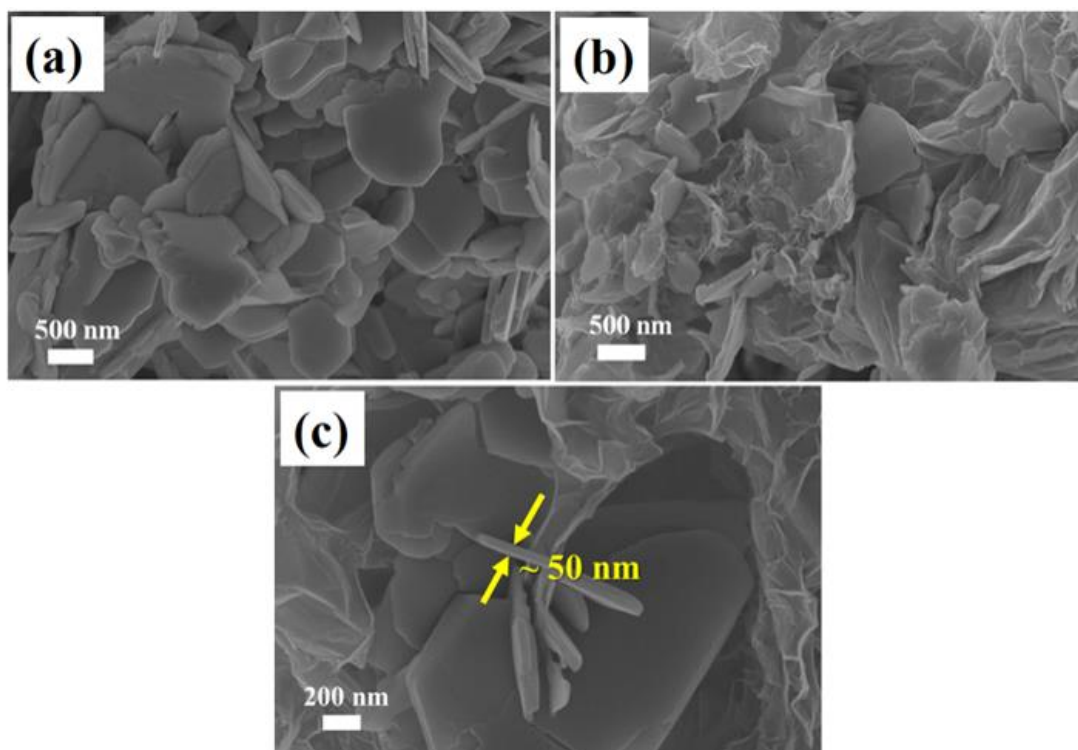


Figure 3.2 (a) FESEM image of pristine Ge_4Se_9 and (b, c) pictures of $\text{Ge}_4\text{Se}_9/\text{RG1}$ composite.

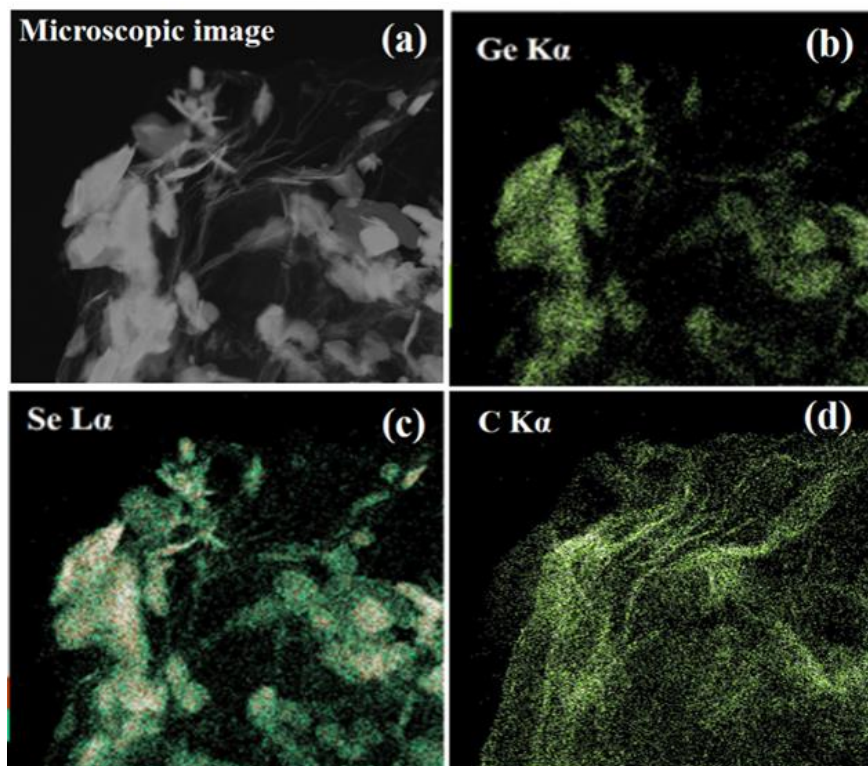
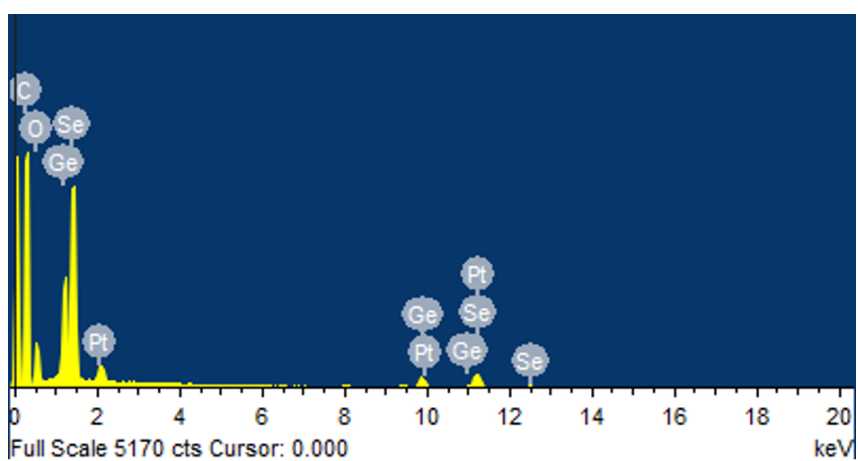


Figure 3.3 Elemental mapping for $\text{Ge}_4\text{Se}_9/\text{RG1}$ hybrids.



Element	Weight%	Atomic%
C K	72.84	94.41
Ge K	8.41	1.73
Se L	18.75	3.86
Totals	100.00	100.00

Figure 3.4 EDAX spectrum for Ge₄Se₉/RG1 composite. And the Table showing the weight percentage and atomic percentage of C, Ge, and Se in the Ge₄Se₉/RG1 composite.

Figure 3.5 shows the high-resolution TEM data of the Ge₄Se₉/RG1 (0.30 wt%) hybrid that is further supported with the The PXRD and Raman analysis denote the crystalline nanostructure of Ge₄Se₉ with the greater formation of phase purity (Figures 3.6a and 3.7a). The different plane of hkl values such as (200), (002), (111), (202), (402), (020), (113), (321), (222), and (512) shows the existence of Ge₄Se₉ having orthorhombic crystal lattice and well-matched with the existed database (PDF - 01-073-3670) without any impurity. Raman spectra observed two bands at 198 and 214 cm⁻¹ confirm the formation of Se symmetric stretching in Ge-Se-Ge linked chain. Additionally latter shows the breathing mode of edge-centered Se in the tetrahedral unit of GeSe₄.^{26,27} To confirm the further reduction process of GO in Ge₄Se₉/RG1 and RGO, we studied both FTIR and Raman spectrometer technique in (Figure 3.6b and 3.7b). In the Fourier transform infrared spectrum observed that before the reduction of GO has four intense high peaks at 3500, 1720, 1223, and 1051 cm⁻¹ respectively, which denotes to stretching vibration mode of -OH (hydroxyl group or water molecules, etc.), C=O (carbonyl group of aldehyde or ketone or acid groups), and C-O for epoxy or alcohol. After the hydrothermal reduction process of GO, some of the oxygen functional group vanished and the reduction peak at 1650 cm⁻¹ attributed to the linkage of the C=C bond. The reduction quality with the vibrational mode of GO in RGO and Ge₄Se₉/RG1 hybrids was performed in Raman spectroscopy. The increase *I_D/I_G* ratio from GO to Ge₄Se₉/RG1 (1.47) confirms the successful hybrid formation.^{28,29}

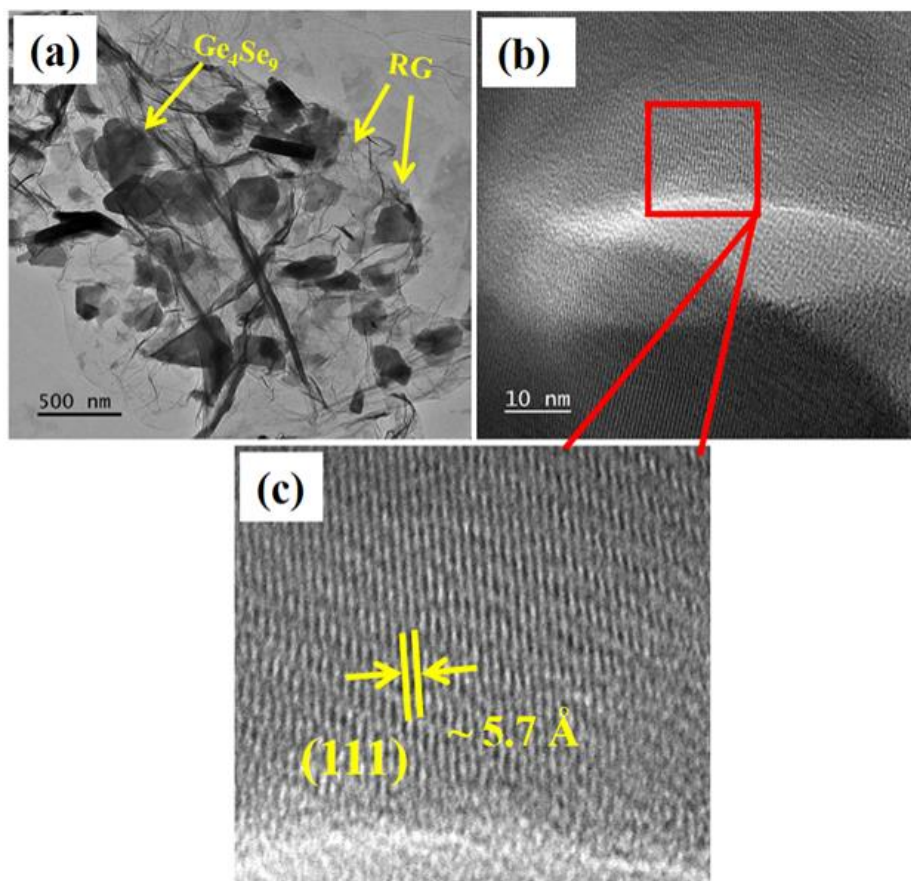


Figure 3.5 TEM analysis at different magnifications (a, b) and (c) High-resolution images of $\text{Ge}_4\text{Se}_9/\text{RG1}$ composite.

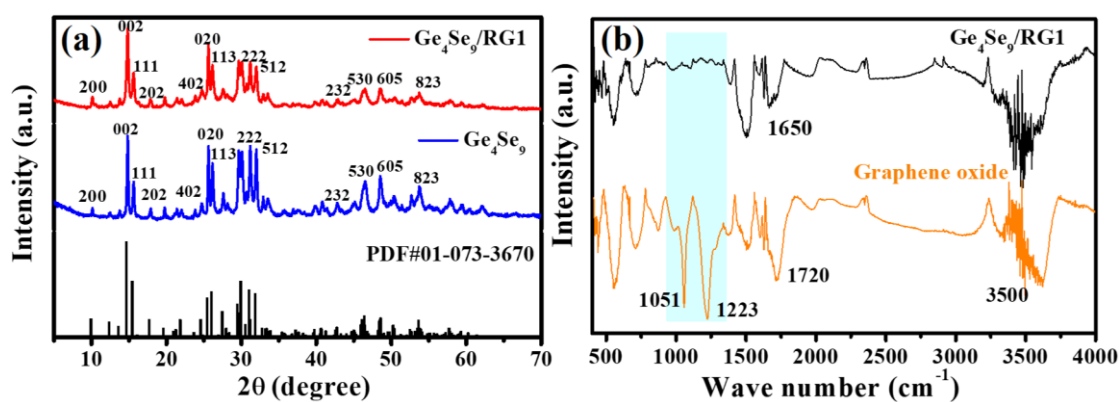


Figure 3.6 (a) Powder diffraction pattern for Ge_4Se_9 , $\text{Ge}_4\text{Se}_9/\text{RG1}$, and Fourier transform infrared spectrum for graphene oxide and $\text{Ge}_4\text{Se}_9/\text{RG1}$ composite.

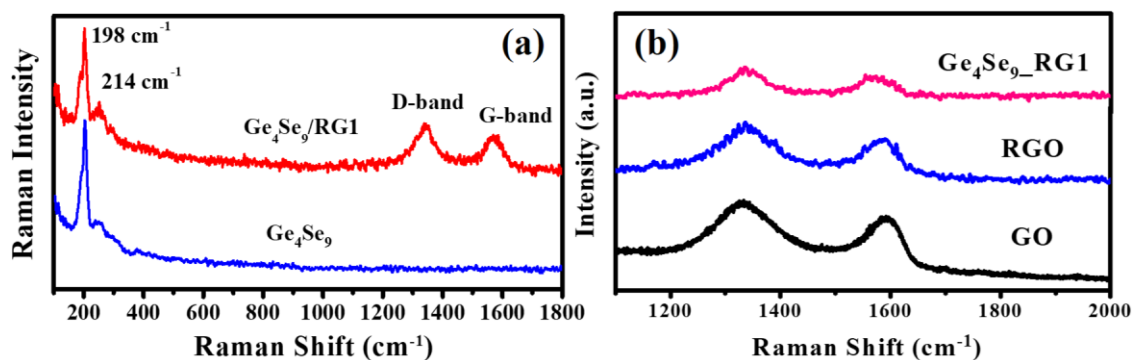


Figure 3.7 (a) Raman study for pristine Ge_4Se_9 and $\text{Ge}_4\text{Se}_9/\text{RG1}$ hybrids and (b) shows for I_D and I_G bands of graphene in GO, RGO, and $\text{Ge}_4\text{Se}_9/\text{RG1}$ hybrids.

X-ray photoelectron spectroscopy employing the elemental composition analysis of as-prepared $\text{Ge}_4\text{Se}_9/\text{RG1}$. The characteristics peak for germanium 3d at 32.1 eV shown the +4 oxidation state of Ge (Figure 3.8a).^{18,30} Also, in the case of selenium 3d spectrum, the position of the peaks at 54.1 eV, 53.2 eV, indicates Se is in $3d_{3/2}$ and $3d_{5/2}$ orbitals, which observed -2 chemical state of Se in Figure 3.8b.^{15,31} In-situ performances of the material support the developments of nonaselenides Ge_4Se_9 cluster. Further existences of both C 1s and O 1s spectrums indicate the presence of RGO layers. As shown in Figure 3.8c, the deconvolution of C 1s has two distinct peak positions at 284.4 and 285.7 eV. The O 1s in the Figure. 3.8d revealed that some quantities of $-\text{OH}$ groups are present in the final product of RGO.^{20,28,32} The thermogravimetric analysis of the Ge_4Se_9 and its different composites carried out in a nitrogen gas atmosphere at a ramping rate of $10\text{ }^\circ\text{C}/\text{min}$ is shown in Figure 3.9. The stability of bare Ge_4Se_9 material up to $500\text{ }^\circ\text{C}$ having a first weight loss of $\sim 10\%$ by removing moisture and unreacted molecules. After the temperature of $500\text{ }^\circ\text{C}$, the orthorhombic crystalline structure of Ge_4Se_9 changes to a monoclinic binary GeSe_2 system to remove rich Se-Se pairs having weight loss seems to be $\sim 65\%$. After that,

there is no more weight loss, and it appears to be stabilized.¹⁸ However, in the case of $\text{Ge}_4\text{Se}_9/\text{RG1}$ and $\text{Ge}_4\text{Se}_9/\text{RG2}$ composites, there is a weight loss of (~4%) in between 200 °C due to removal of adsorbed moisture or water. A rise in temperature $\text{Ge}_4\text{Se}_9/\text{RG1}$ composite shows 60% weight loss, and $\text{Ge}_4\text{Se}_9/\text{RG2}$ shows 20% weight loss in between 500-900 °C. The variation of weight loss confirms higher RG content in $\text{Ge}_4\text{Se}_9/\text{RG2}$ than $\text{Ge}_4\text{Se}_9/\text{RG1}$. While this shows that higher RG-containing composite material shows better stability than the lower RG content and the bare one.

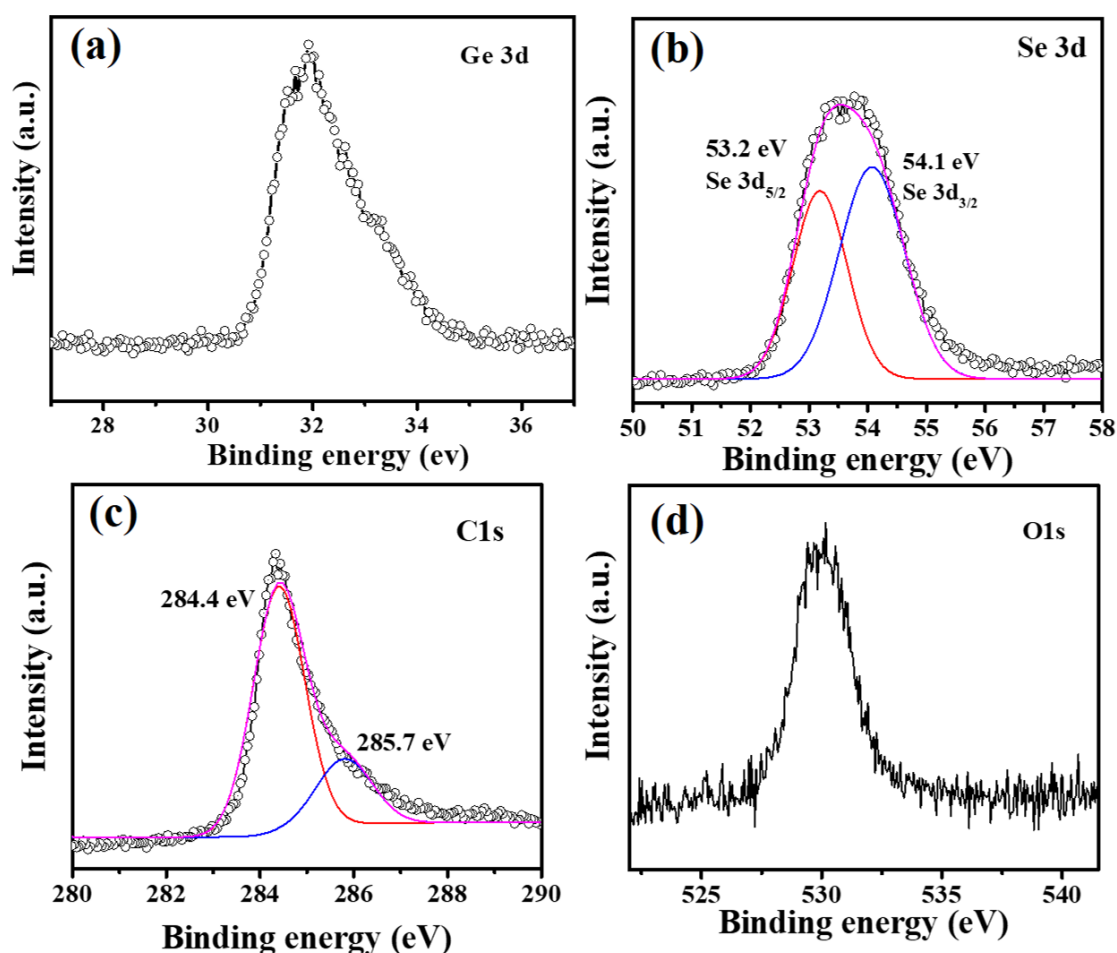


Figure 3.8 Scan of X-ray photoelectron spectra for Ge 3d, Se 3d, C 1s, and O 1s of $\text{Ge}_4\text{Se}_9/\text{RG1}$.

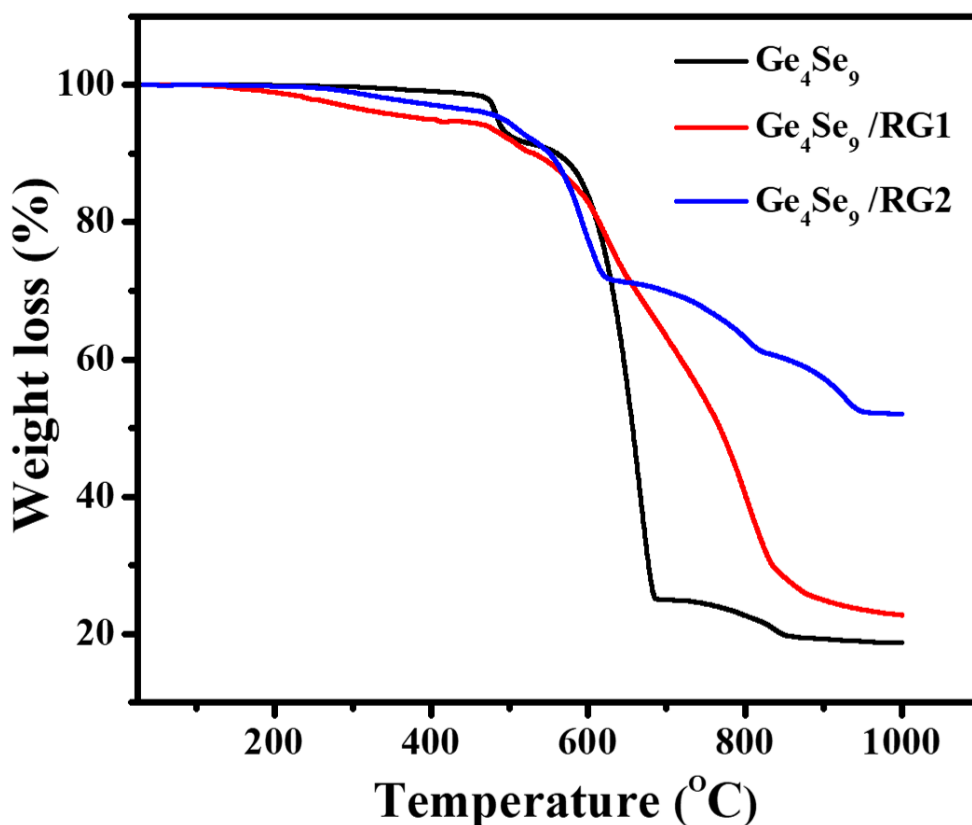


Figure 3.9 TGA results for bare Ge₄Se₉, Ge₄Se₉/RG1, and Ge₄Se₉/RG2 hybrids.

Electrochemical charge storage investigation for bare Ge₄Se₉ and graphene composites of Ge₄Se₉/RG1 and Ge₄Se₉/RG2 was done in a three-electrode of device system. Figure 3.10a is the cyclic voltammetry of Ge₄Se₉/RG1 at applied scan rates (from 5 -100 mV/s), and Figure 3.10b represented the charge-discharge curves at an applied current density of (2 to 8 A/g). All the data were recorded in 1 M KOH as a supporting electrolyte. A potential range was kept in the window value of -0.1 to 0.6 V (versus Ag/AgCl). Figure 3.10c displays the greater specific capacitance value (220 F/g) of Ge₄Se₉/RG1 compared to bare Ge₄Se₉ and Ge₄Se₉/RG2. Additionally, the values of the energy density of 12 Wh/kg, and power density of 4.6 kW/kg of Ge₄Se₉/RG1 composites, show superior electrochemical performances to the rest of

as-synthesized electrode materials. $\text{Ge}_4\text{Se}_9/\text{RG1}$ hybrids cyclic stability was done using the galvanostatic CD technique at 1 A/g, and the capacitance retention of ~91% after continuous 10,000 GCD cycles is shown in Figure 3.10d.

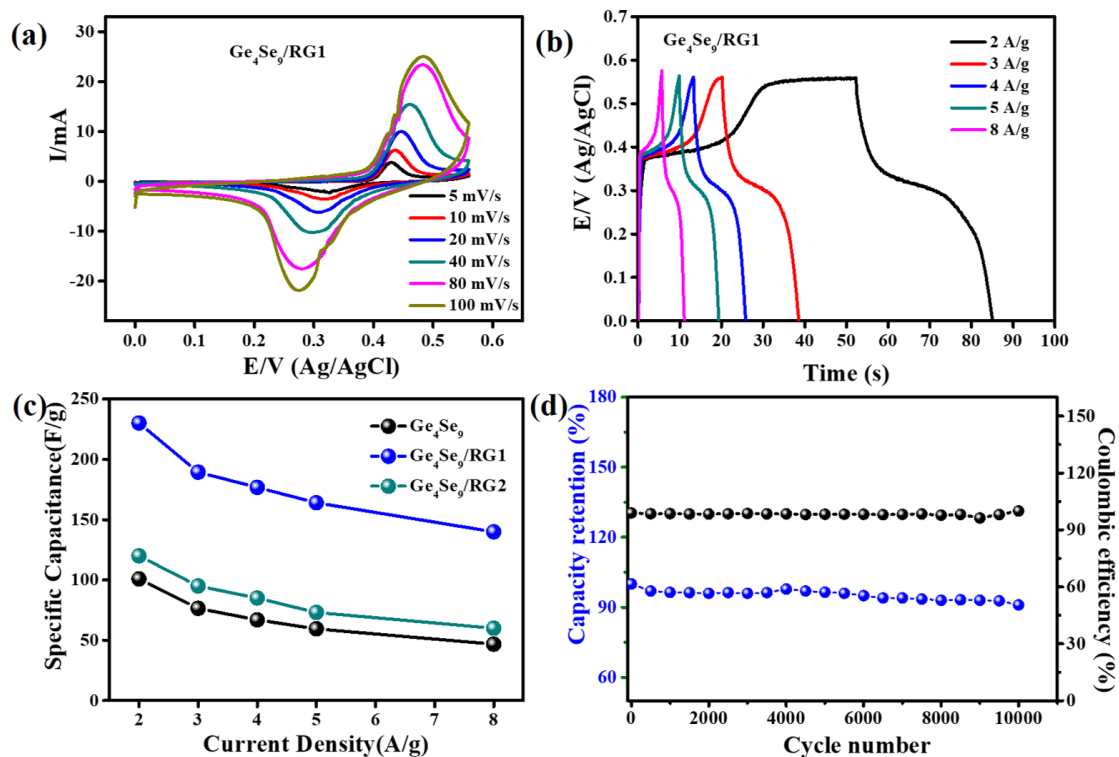


Figure 3.10 (a, b) Graph of cyclic voltammetry (CV) and Galvanostatic charge-discharge (GCD) for $\text{Ge}_4\text{Se}_9/\text{RG1}$, (c) graph of specific capacitance vs. various current densities, (d) long cyclic number for stability test with coulombic efficiency for the $\text{Ge}_4\text{Se}_9/\text{RG1}$ hybrids.

Moreover, Figure 3.11 gives the CV profile at different scan rates and GCD plots at various current densities of bare Ge_4Se_9 and $\text{Ge}_4\text{Se}_9/\text{RG2}$ hybrids in comparison to $\text{Ge}_4\text{Se}_9/\text{RG1}$ composites.

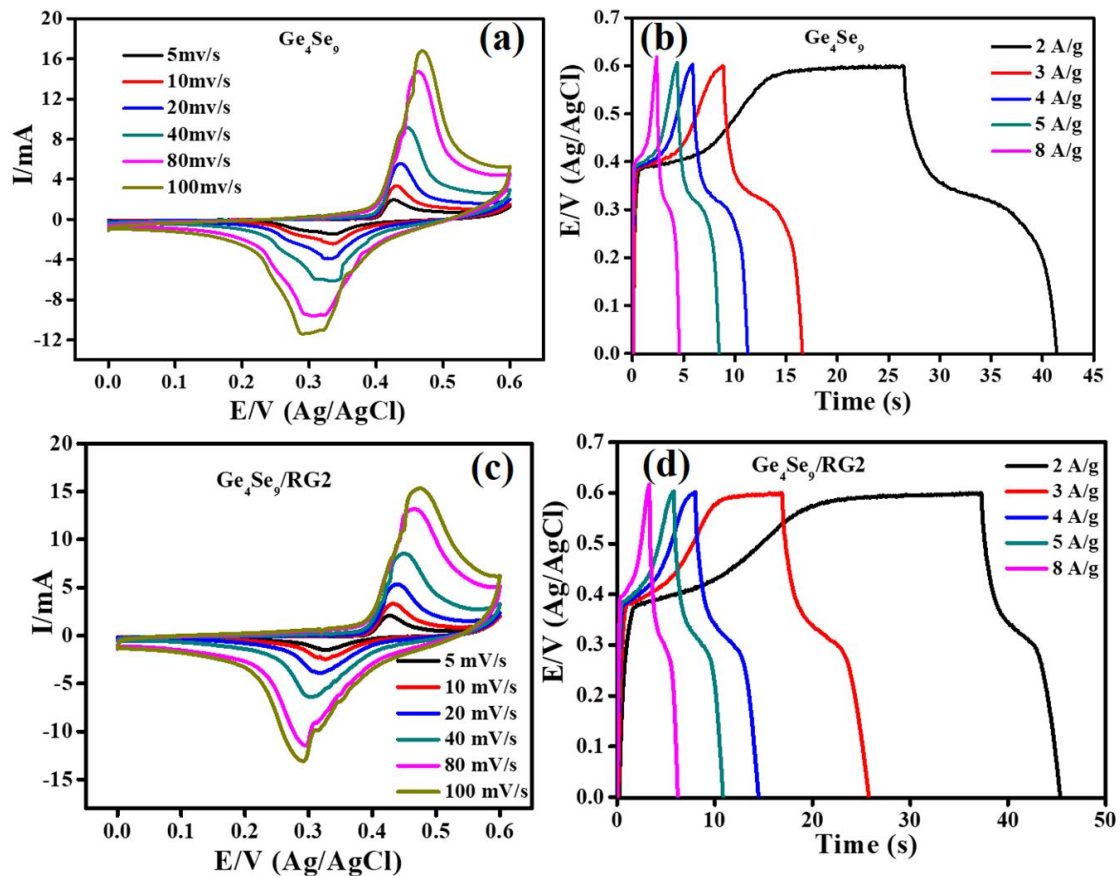


Figure 3.11 Cyclic voltammetry with Galvanostatic charge-discharge curve for bare Ge_4Se_9 (a and b) and $\text{Ge}_4\text{Se}_9/\text{RG2}$ hybrids (c and d).

A post stability analysis to impedance spectrum was studied and presented in Figure 3.12a. Electrochemical impedance study of $\text{Ge}_4\text{Se}_9/\text{RG1}$ composite for before and after post stability analysis gives similar charge transfer resistance (14.7Ω) and notice the unchanged with better electrical conductivity of the used material. The unaltered surface morphology and crystalline nature of $\text{Ge}_4\text{Se}_9/\text{RG1}$ hybrids were studied by FESEM, PXRD, and Raman spectrometry after post stability illustrated in Figure 3.12b and 3.13a-b, respectively.

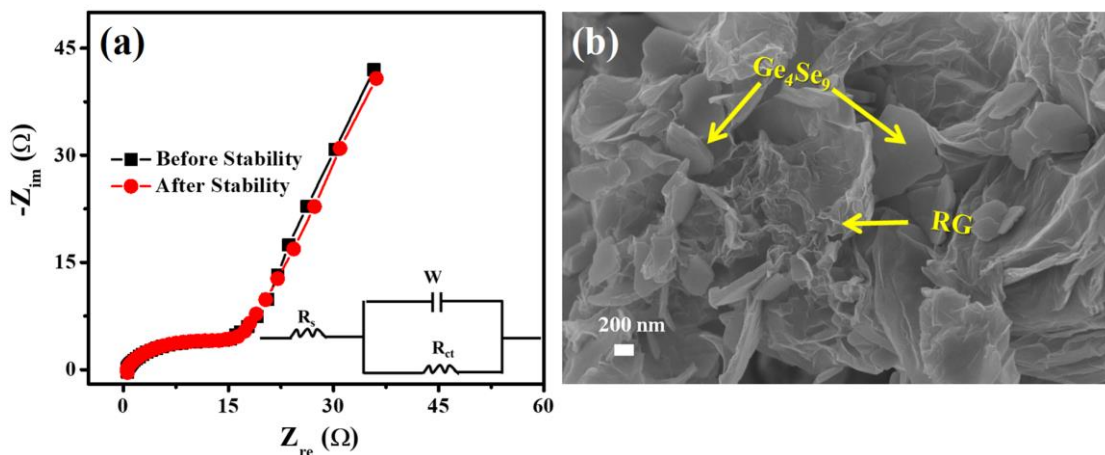


Figure 3.12 (a) Post stability analysis of Ge₄Se₉/RG1 hybrids having the electrochemical study and characterization of impedance diagram before and after stability, (b) SEM image. The inset in (a) corresponded to the circuit diagram.

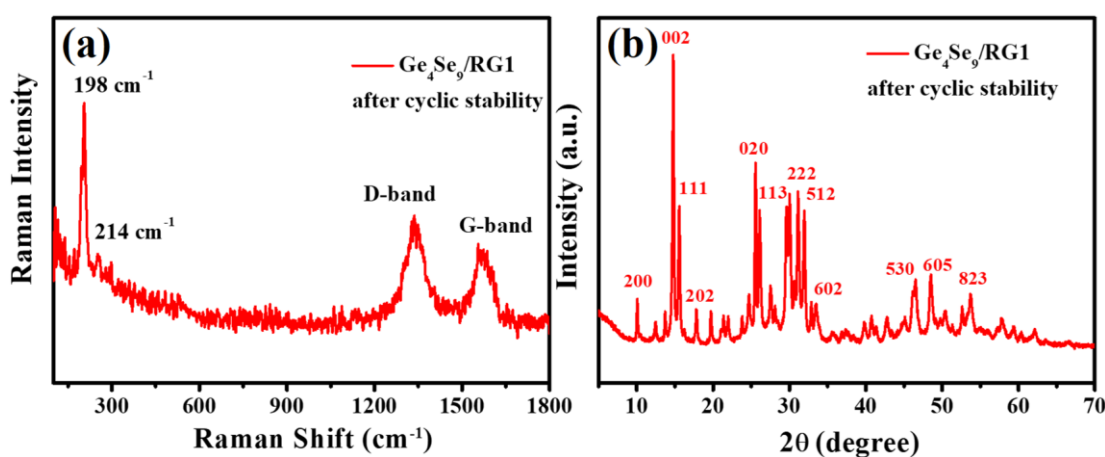


Figure 3.13 (a) Raman study for after SCs measurements and (b) is the PXRD.

A comparison table of specific capacitance, specific energy, specific power of Ge₄Se₉/RG1 composites with bare Ge₄Se₉, Ge₄Se₉/RG2, and other reported supercapacitor electrode materials have been shown in Table 3.1. The detailed electrochemical study of Ge₄Se₉/RG1 hybrids opens up an advanced directive to investigate novel and suitable electrode materials in future decades. We believe that

the scalable synthesis of various graphene hybrids with germanium selenide as a cathode electrode material is a prominent electrode material for supercapacitor device systems. systems.

Table 3.1 Supercapacitor comparison of Ge₄Se₉/RG2, Ge₄Se₉/RG1, and bare Ge₄Se₉ with other reported metal selenides and oxide literatures.

Electrode material	Energy storage capacitance (F/g)	Specific energy (W h/kg)	Specific power (k W/kg)	Stability for long cycle number	References
Mn ₂ O ₃ -MnO ₂	225	27	90	5000	ACS Appl. Energy Mater. 2020, 3, 8190–8197
3D-GeSe ₂	300	-----	-----	2000	Adv. Mater. 2013, 25, 1479–1486.
MoSe ₂ /rGO	211	-----	-----	10000	Dalton Trans., 2016, 45, 9646–9653.
SnSe ₂ Nano disk	168	-----	-----	1000	ACS Nano, 2014, 8, 3761-3770.
RuSe ₂ nanoparticles	100.8	-----	-----	1000	Chem. Commun., 2019,55, 12320-12323
WSe ₂ /GR	389	34.5	400	3000	Materials Letters, 2018, 223, 57–60.
α-MnSe	97.6 (0.1mA/cm ²)	8.60	47.05	2000	Electrochimica Acta, 2018, 268, 403-410.
Ge₄Se₉	100.8	5.04	3.56	-----	
Ge₄Se₉/RG1	220	12.0	4.6	10000	This work
Ge₄Se₉/RG2	120	6.0	3.59	-----	

3.8 Conclusions

The facile single-step hydrothermal treatment of the growth of Ge₄Se₉ plates and its RGO composite of various concentrations has been accomplished. The 2D crystalline structural arrangements, morphological studies, and the electrochemical energy storage application towards supercapacitor have been studied. Interestingly, different weight percentages (0.30 and 0.60 wt%) of GO involvement in the final reaction precursor trigger an active hybrid materials storage capacitance than the single one. The Ge₄Se₉/RG1 hybrid has 0.30 wt% of GO exhibits enhanced specific capacitance or energy storage capacitance of 220 F/g and energy density of 12 Wh/kg and a power density of 4.6 kW/kg then bare Ge₄Se₉ and Ge₄Se₉/RG2 composites. Moreover, its performance towards cyclic durability having 91% retention in starting capacitance value. And the excellent coulombic efficiency (~98%) makes it an efficient active material for SCs application. In comparison, the robustness of this electrode material was also studied by post cycle analysis.

References

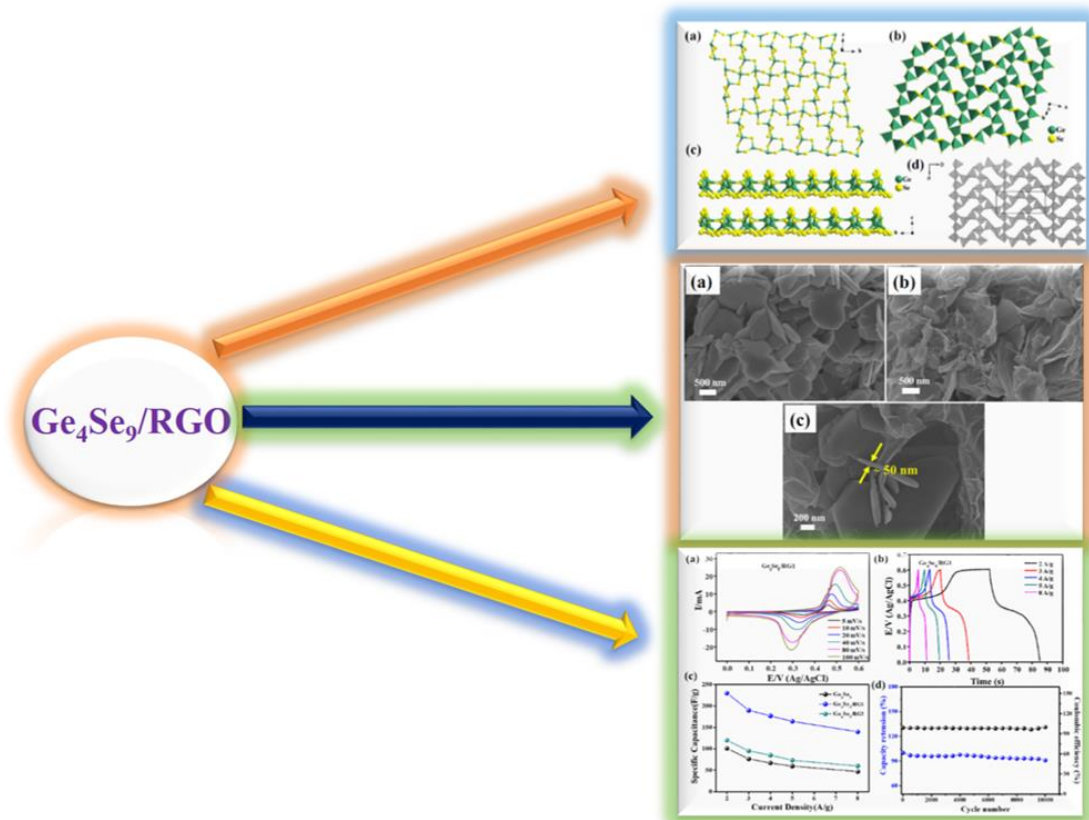
- 1 X. Zou and Y. Zhang, *Chem. Soc. Rev.*, 2015, **44**, 5148–5180.
- 2 M. Winter and R. J. Brodd, *Chem. Rev.*, 2005, **105**, 1021.
- 3 J. Zhao, Y. Li, G. Wang, T. Wei, Z. Liu, K. Cheng, K. Ye, K. Zhu, D. Cao and Z. Fan, *J. Mater. Chem. A*, 2017, **5**, 23085–23093.
- 4 A. K. Samantara and S. Ratha, *Materials Development for Active/Passive Components of a Supercapacitor: Background, Present Status and Future Perspective*, 2017.

- 5 C. Merlet, D. T. Limmer, M. Salanne, R. van Roij, P. A. Madden, D. Chandler and B. Rotenberg, *J. Phys. Chem. C*, 2014, **118**, 18291–18298.
- 6 F. Wang, X. Wu, X. Yuan, Z. Liu, Y. Zhang, L. Fu, Y. Zhu, Q. Zhou, Y. Wu and W. Huang, *Chem. Soc. Rev.*, 2017, **46**, 6816–6854.
- 7 P. Miró, M. Audiffred and T. Heine, *Chem. Soc. Rev.*, 2014, **43**, 6537–6554.
- 8 X. Chia, A. Y. S. Eng, A. Ambrosi, S. M. Tan and M. Pumera, *Chem. Rev.*, 2015, **115**, 11941–11966.
- 9 S. R. Marri, S. Ratha, C. S. Rout and J. N. Behera, *Chem. Commun.*, 2017, **53**, 228–231.
- 10 S. M. Dinara, A. K. Samantara, J. K. Das, J. N. Behera, S. K. Nayak, D. J. Late and C. S. Rout, *Dalton Trans.*, 2019, **48**, 16873–16881.
- 11 C. V. V. M. Gopi, A. E. Reddy, J.-S. Bak, I.-H. Cho and H.-J. Kim, *Mater. Lett.*, 2018, **223**, 57–60.
- 12 Y. Liu, W. Li, X. Chang, H. Chen, X. Zheng, J. Bai and Z. Ren, *J. Colloid Interface Sci.*, 2020, **562**, 483–492.
- 13 T. Chen, S. Li, J. Wen, P. Gui, Y. Guo, C. Guan, J. Liu and G. Fang, *Small*, 2018, **14**, 1700979.
- 14 X. Wang, B. Liu, Q. Xiang, Q. Wang., X. Hou, D. Chen and G. Shen, *ChemSusChem*, 2014, **7**, 308–313.
- 15 S. Xie, J. Gou, B. Liu and C. Liu, *J. Colloid Interface Sci.*, 2019, **540**, 306–314.
- 16 D. D. Vaughn, R. J. Patel, M. A. Hickner and R. E. Schaak, *J. Am. Chem. Soc.*, 2010, **132**, 15170–15172.

- 17 M. Nath, A. Choudhury and C. N. R. Rao, *Chem. Commun.*, 2004, 2698–2699.
- 18 H. Fjellvåg, K. O. Kongshaug and S. Stølen, *J. Chem. Soc. Dalton Trans.*, 2001, 1043–1045.
- 19 J. K. Das, A. K. Samantara, A. K. Nayak, D. Pradhan and J. N. Behera, *Dalton Trans.*, 2018, **47**, 13792–13799.
- 20 A. K. Samantara, S. Kamila, A. Ghosh and B. K. Jena, *Electrochim. Acta*, 2018, **263**, 147–157.
- 21 J. Zhou, C. Zhang, T. Niu, R. Huang, S. Li, J. Z. Zhang and J. G. Chen, *ACS Appl. Energy Mater.*, 2018, **1**, 4599–4605.
- 22 S. Ratha, S. R. Marri, J. N. Behera and C. S. Rout, *Eur. J. Inorg. Chem.*, 2016, **2016**, 259–265.
- 23 X. Chen, J. Ding, J. Jiang, G. Zhuang, Z. Zhang and P. Yang, *RSC Adv.*, 2018, **8**, 29488–29494.
- 24 R. Ding, L. Qi and H. Wang, *J. Solid State Electrochem.*, 2012, **16**, 3621–3633.
- 25 S. Ratha, A. K. Samantara, K. K. Singha, A. S. Gangan, B. Chakraborty, B. K. Jena and C. S. Rout, *ACS Appl. Mater. Interfaces*, 2017, **9**, 9640–9653.
- 26 T. G. Edwards and S. Sen, *J. Phys. Chem. B*, 2011, **115**, 4307–4314.
- 27 Y. Wang and K. Murase, *J. Non. Cryst. Solids*, 2003, **326–327**, 379–384.
- 28 A. K. Samantara, S. Chandra Sahu, A. Ghosh and B. K. Jena, *J. Mater. Chem. A*, 2015, **3**, 16961–16970.
- 29 H. Wang, T. Maiyalagan and X. Wang, *ACS Catal.*, 2012, **2**, 781–794.

- 30 Q. Wang, S. Z. Kang, X. Li, Y. W. Yang, L. Qin and J. Mu, *J. Alloys Compd.*, 2015, **631**, 21–25.
- 31 K. Guo, S. Cui, H. Hou, W. Chen and L. Mi, *Dalton Trans.*, 2016, **45**, 19458–19465.
- 32 Y. Li, Y. Zhao, H. Cheng, Y. Hu, G. Shi, L. Dai and L. Qu, *J. Am. Chem. Soc.*, 2012, **134**, 15–18.

Summary of Chapter-3



CHAPTER – 4

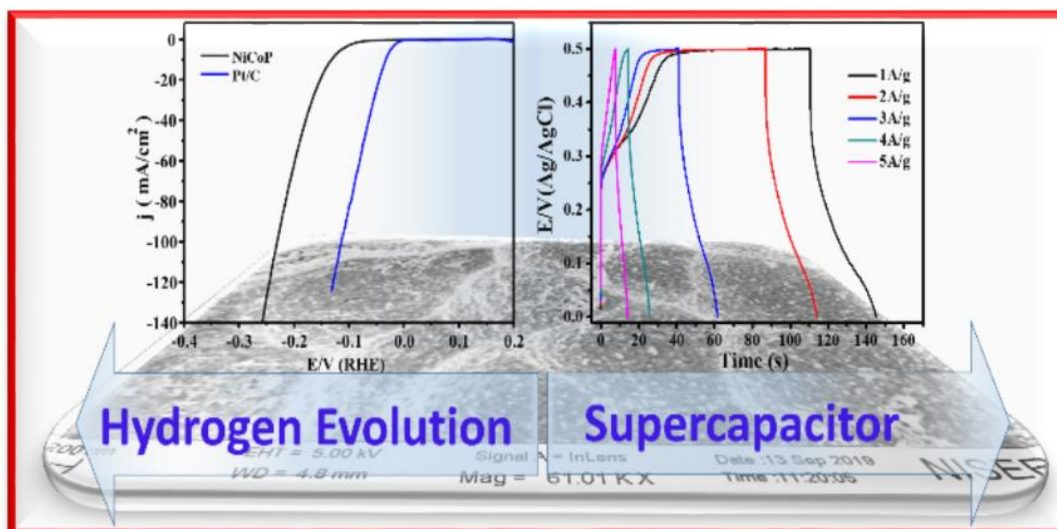
3D NiCoP Hollow Spheres: Efficient Electrode Material for

Hydrogen Evolution Reaction and Supercapacitor

Applications

- 4.1** Abstract
- 4.2** Introduction
- 4.3** Motivation of our Work
- 4.4** Experimental Part
 - 4.4.1** Synthesis of NiCoP
- 4.5** Characterization
- 4.6** Electrochemical measurements
- 4.7** Results and discussions
- 4.8** Conclusions
- 4.9** References

4.1 Abstract



This chapter represented a facile hydrothermal synthesis of bimetallic nickel cobalt phosphide (NiCoP) and studied its electrocatalytic performances for hydrogen evolution reaction and electrochemical charge storage performances towards supercapacitor applications. The systematic characterization of bimetallic nickel-cobalt phosphide confirmed the high crystalline nature and 3D sphere-like morphological nanostructures. The electrocatalytic behavior for hydrogen evolution in acidic medium shows excellent performances of 160 mV overpotential required to deliver 10 mA/cm² current density with a lower Tafel value of 70 mV/dec. The durability of the bimetallic phosphide material shows an increase of 15 mV overpotential even after 18 hours of constant electrolysis. Moreover, the supercapacitor performances of the NiCoP in an alkaline medium show better specific capacitance values of 960 F/g, energy density (33.3 Wh/kg), and power density (11.8 kW/kg), respectively. The long-term cyclic stability test was performed under a repeated 10000 charge-discharge cycle with 95% of capacitance retention of its initial value.

4.2 Introduction

Hydrogen energy is alternative renewable energy to traditional fossil fuels and can meet the future energy demands in terra watt/hour.^{1,2} The higher specific energy and carbon-free characteristic nature of hydrogen have been widely proven to be the cleanest energy fuels.³ Evolution of hydrogen and oxygen gas through the electrochemical water splitting believes to be the safest and cleanest way than other processes such as steam methane reforming, natural gas oxidation, and biomass electrolysis.⁴ Currently, researchers are busy with the development of low-cost, efficient, and highly active nature catalysts that can minimize the thermodynamic energy barrier for water electrolysis, which is termed as overpotential. Precious metals like platinum and palladium are considered the state of art hydrogen evolution catalysts due to their lower overpotential and higher electrochemical stability.^{5,6} However, its high cost and limited availability motivated the researchers to search for an alternative substitute that can replace noble metal in the electrolysis process. Various nonprecious-based transition metal electrocatalysts such as oxide,⁷ chalcogenides,⁸ carbides,⁹ nitrides,¹⁰ sulfides/selenides^{11,12} have been explored to replace the noble metal-based catalyst. From the above various electrocatalysts, transition metal phosphides have been fascinating with great attention due to their higher catalytic activity. Additionally, its electrochemical activity can be further improved by metal doping.^{13,14} Thus, bimetallic phosphides with the multivalent metal center site and more electronegative phosphorous atom improve the intrinsic hydrogen evolution activity.¹⁵ The recent studies focus on various mono and bi transition metal phosphides such as CoP, Ni_xP, WP₂, MoP, NiCoP, and FeP, and investigated through multiple synthetic techniques, which exhibited better electrochemical performances

(hydrogen evolution reaction) in both acidic as well as alkaline medium.¹⁶⁻²¹ Yuan et al. reported 3D nanostructure NiCoP as a superior HER electrocatalyst in the electrolytic medium of the acidic and basic solution.²² Chen et al. also observed nickel-cobalt phosphide having yolk-shell sphere-like nanostructures act as a bifunctional electrocatalyst.²³ These above reports suggest the importance of binary metal phosphides in the energy conversion process. However, electrode materials efficiency could be defined through the energy conversion process and gives equal priority to energy conversion and energy storage towards supercapacitor (SCs) applications. The higher power supply capability, faster charging/discharging process, and safety operating system with longer cyclic life (nearly 100 times higher than battery) of supercapacitors are the most promising energy storage system compared to the capacitors batteries.²⁴ However, supercapacitor device performances directly depend upon the type of materials used for electrode modification. For the searching of active electrode material which could give optimal charge storage performances towards supercapacitor applications, various nanostructure arrangements of pristine graphene, carbon nanotubes, metal oxides, metal chalcogenides, metal phosphides, and their hybrids were studied.^{25,26} However, still developing an efficient cathode electrode material for SCs is a big challenge. Mainly, transition metal-based phosphide material with cathode/anode type respective electrode significantly shows better performances in the energy storage or conversion process due to its larger redox sites, higher electrical conductivity, and good charge transfer process. As compared to single nickel or cobalt phosphide compounds, metal doping or bimetallic Ni-Co phosphide possess a synergistic effect that could improve the overall performance. Fu et al. reported porous NiCoP nanosheets as an asymmetric supercapacitor which

signifies high specific capacitance (1206 F g^{-1} at 1 A/g).²⁷ Similarly, Du et al. prepared a nickel foam anchored NiCoP electrode material that offers an excellent specific capacitance value of 2143 F g^{-1} at 1 A g^{-1} .²⁸ Although the above-reported metal phosphides as electrode material show its performances of either hydrogen evolution or supercapacitor, both the application showing by a single NiCoP is rarely published. Herein, we described this chapter by following a synthetic route of a simple hydrothermal method corresponding to the nucleation growth of 3D binary NiCoP nanostructured and explored their electrochemical study towards hydrogen evolution reactions and supercapacitor measurement, which was rarely reported to the best of our knowledge.

4.3 Motivation of our Work

The development of nonprecious and high efficacy electrocatalyst for energy conversion (evolution of hydrogen or oxygen gases) and charge storage (supercapacitors) performances have attracted significant attention in renewable energy technology. Nickel cobalt phosphide (NiCoP) has been stimulated by great catalytic activity over different metal oxide and metal chalcogenides due to a high electronegative phosphorous atom that facilitates the removal of an electron from the metal center and creates a positive charge center that improves the overall performances. Herein we hydrothermally synthesized 3D NiCoP and explored both the hydrogen evolution and charge storage process towards supercapacitor application. Both the existence and combined effect of Ni and Co give huge redox-active sites facilitates high electrical conductivity and high charge transfer process. The modified glassy carbon as a working electrode of NiCoP slurry gives only 160 mV overpotential to evolve H_2 gas in an acidic medium. Moreover, charge storage

performances of NiCoP modified electrode in alkaline medium shows higher specific capacitance (960 F g^{-1}), energy density (33.3 Wh kg^{-1}), and power densities of 11.8 kW/kg with robust cyclic stability. The above systematic investigation reveals that the as-synthesized bimetallic NiCoP will be a suitable candidate for the preparation of advanced and efficient electrocatalysts.

4.4 Experimental Part

4.4.1 Hydrothermal Synthesis of NiCoP

In a typical procedure, $\text{CoCl}_2 \cdot 6\text{H}_2\text{O}$ (0.5 mmol, 0.144 g) and $\text{NiCl}_2 \cdot 6\text{H}_2\text{O}$ (1 mmol, 0.237 g) were mixed in a beaker with 15 ml deionized water under constant stir for 10 min. Further, the phosphorous source of red phosphorous of 0.54 g and KOH of 0.56 g was added separately to the reaction mixture and stirred continuously for 1 hour. Then the final homogeneous precursor was transferred to a 25 ml capacity of a stainless steel-covered Teflon tube, kept in a hot running oven at $200 \text{ }^\circ\text{C}$ for 20 hours. After completing the reaction, the whole precipitate inside the Teflon was collected by washing it in deionized water/ethanol. Then it was dried and collected for further characterization use.

4.5 Characterization

The X-ray diffraction pattern was recorded on the Bruker D8 Advance diffractometer having $\text{Cu-K}\alpha$ radiation of wavelength (λ) of 1.5418 \AA . The grain size and morphological structures of NiCoP were taken by FESEM (Merlin Compact with GEMINI-I electron column, Zeiss Pvt. Ltd., Germany). The standard resolution processing of transmission electron microscope was operated using (HRTEM, JEOL 2100F, operated at voltage 200 kV). A very dilute form of the as-prepared sample was drop cast onto a carbon-covered copper grid and dried in a vacuum desiccator. Further,

the confirmation of various elements present in the samples was studied by elemental mapping analysis during the TEM studied.

4.6 Electrochemical measurements

The samples-related electrochemical responses have been carried out in an electrochemical workstation that exhibits two parts of a three-electrode system (Bio-Logic, EC-Lab, and SP 200). The sample modified GCE, commonly known as glassy carbon electrode as working, a single platinum wire and aqueous Ag/AgCl (KCl saturated) were used as auxiliary and reference, respectively. An electrolyte of 0.5 M H₂SO₄ is used for all the electrochemical studies, and the polarization curve was obtained at a sweep rate of 5 mV s⁻¹. In the preparation of homogeneous NiCoP electrocatalyst ink, 1 mg of the sample was mixed with 95 µl of ethanol and Nafion of 5 µl followed by bath sonication assistance for about 30 minutes. After that, 5 µl of the prepared slurry was loaded on the glassy carbon electrode's surface and dried at room temperature naturally. The polarization curve obtained through LSV are recorded in KCl saturated reference electrode (aqueous Ag/AgCl), obtained potential is converted into reversible hydrogen electrode (or RHE) scale by the Nernst equation as follows,^{29,30}

$$E_{RHE} = E_{Ag/AgCl} + 0.059 (pH) + E_{Ag/AgCl}^0 \quad (4.1)$$

Herein $E_{Ag/AgCl}^0$ denotes as standard electrode potential (i.e., 0.21 V) of Ag/AgCl. The Impedance Spectrum was used to record the actual kinetics of electrode surface at -0.25 V (vs. RHE scale), frequency ranges varying from 1 MHz to 0.1 Hz with an applying AC amplitude of 10 mV. Further, the measured potential curve was iR corrected or compensated to banish the unwanted solution resistance. Where “ i ”

implying to perceive current and “ R ” is the resistance obtained from the solution during the measurements. The Tafel slope value obtained by following the equation as below, ^{11,25}

$$\eta = a + b \log J \quad (4.2)$$

Here, the symbol of a , b , η , and J is represented as Tafel constant, Tafel slope value, overpotential, and measured current density, respectively. Additionally, all the related electrochemical measurements for the energy storage process (supercapacitor) are cyclic voltammetry (CV), galvanostatic charge-discharge (GCD), and cyclic stability were studied in a supporting electrolyte of 5 M KOH. The preparation of sample modified electrodes for energy storage measurements was briefly discussed in the above section. While the measurements were done within the potential windows of 0.0 to 0.5 V.

4.7 Results and discussions

After synthesizing bimetallic NiCoP, the initial characterization of X-ray powder diffraction was used to verify sample phase purity in Figure 4.1. It possesses very sharp diffraction peaks, which are attributed to different hkl values of (111), (201), (210), (300), (002), (211), (212) planes. All these diffraction peaks of bimetallic NiCoP were well matched with the existing crystal data file (JCPDS no. 01-071-2336) and indexed to forming a hexagonal crystal system. Further, no extra peaks were obtained to conferring the phase purity of the studied material. The morphological picture and mapping analysis of NiCoP surface was characterized by the field emission scanning electron microscope (FESEM) and transmission electron microscope (TEM) shown in Figure 4.2 and Figure 4.3, respectively.

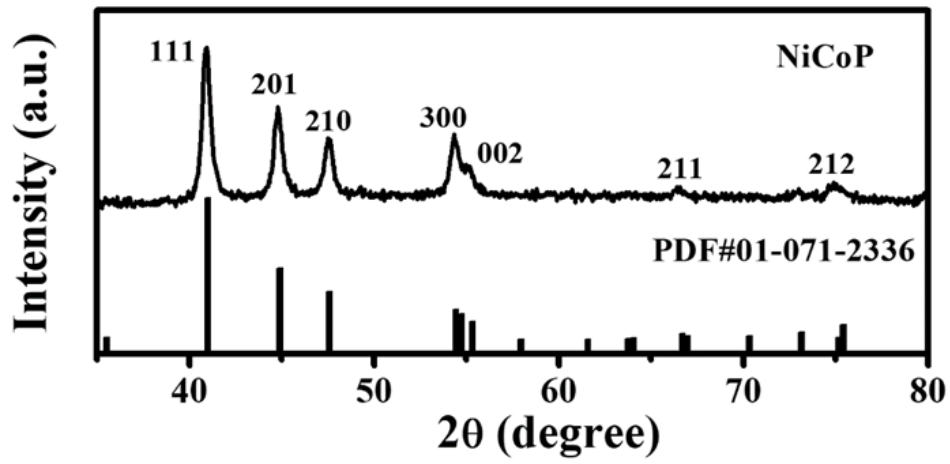


Figure 4.1 X-ray diffraction pattern for NiCoP hollow sphere.

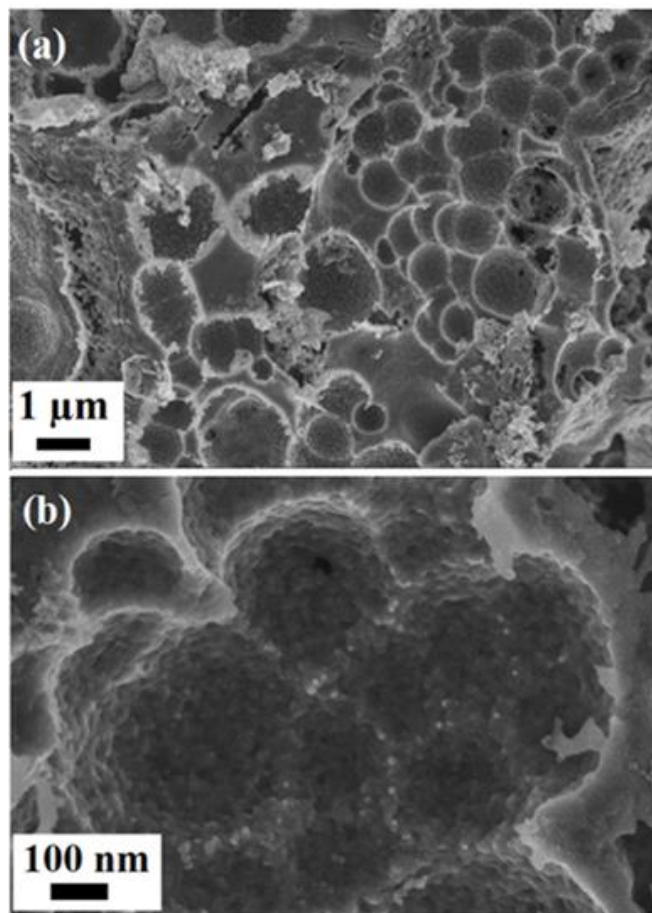


Figure 4.2 (a, b) Low and high magnification of field emission scanning electron microscope images for NiCoP.

FESEM observed the hollow sphere type morphology for NiCoP with an average diameter of 1 μm . A close study of these hollow sphere type morphology reveals that during a hydrothermal reaction, firstly, the reaction precursor converted into the metal nanoparticle and then it assembled to make such three-dimensional spheres like morphology which is very much roughened. More electroactive sites are basing upon hollow sphere morphology and the roughened surface of NiCoP, which enhanced the electrocatalytic properties for HER and energy storage performances towards supercapacitor. The HRTEM images confirm the smooth surface and well-defined lattice fringes of NiCoP in Figure 4.3c-d, indicating the interplanar distance between two adjacent fringe lines of 0.217 nm correspond to the (111) plane.

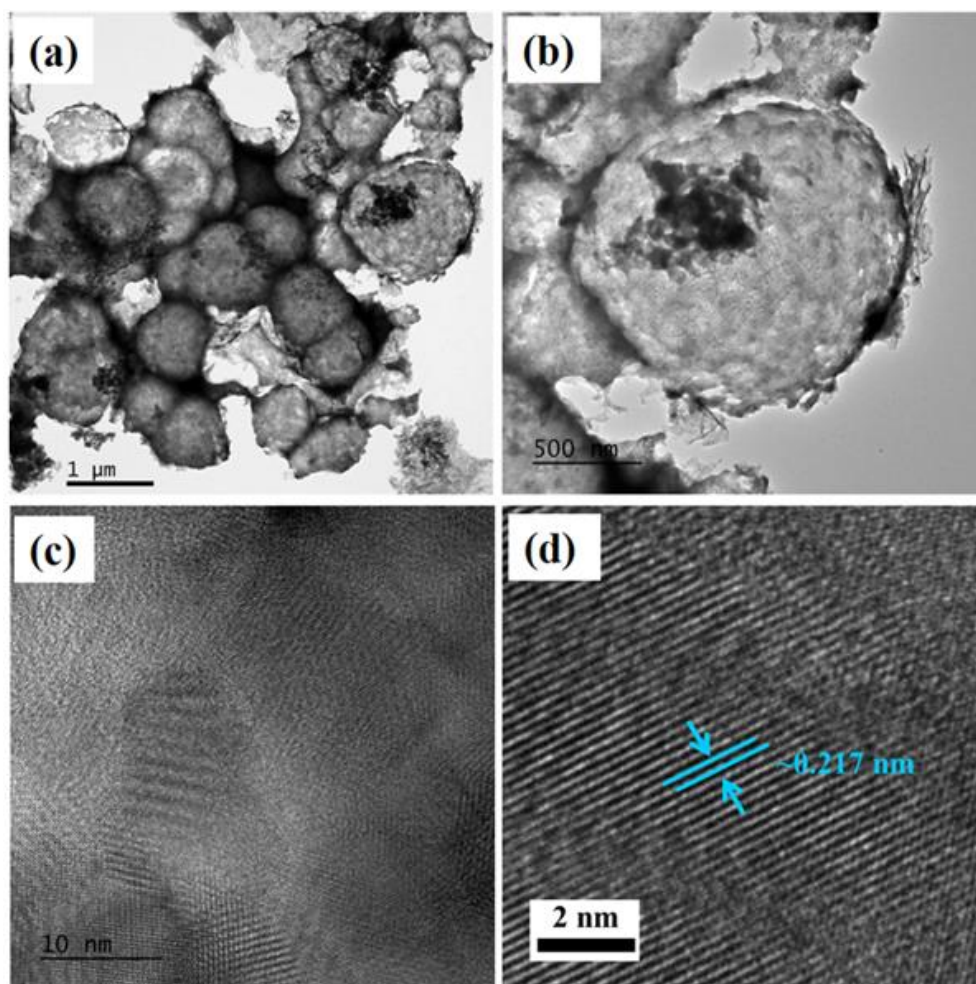


Figure 4.3 (a-d) TEM pictures for the NiCoP at different magnifications.

The energy dispersive X-ray spectrometry (EDS) verified the coexistence of Ni, Co, and P elements in the binary NiCoP hollow sphere in Figure 4.4.

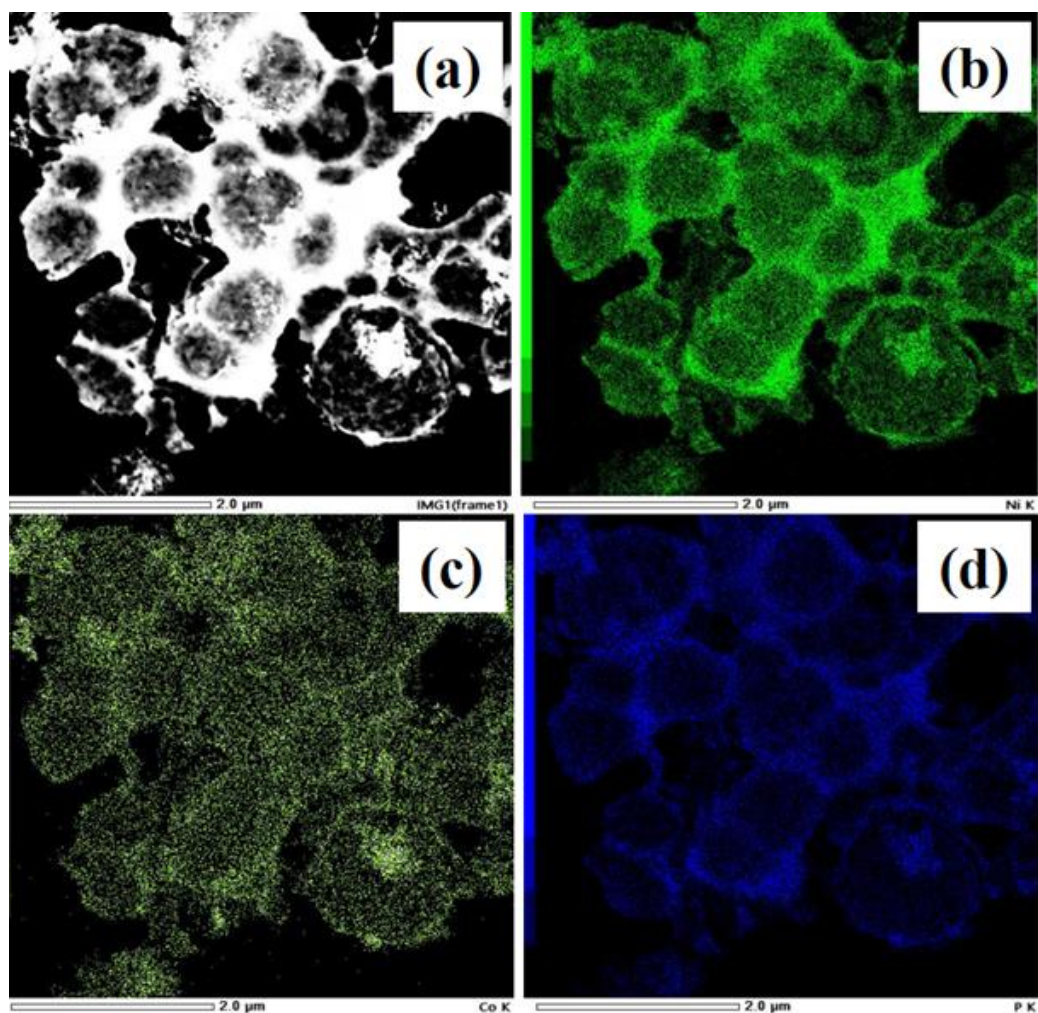


Figure 4.4 EDAX mapping of NiCoP microspheres.

The electrocatalytic activity towards hydrogen evolution was evaluated in 0.5 M H_2SO_4 , and the measurement data were recorded with the applied potential of 5 mV/s. Figure 4.5a displays the linear sweep voltammetry curve of the as-synthesized NiCoP hollow spheres and the auxiliary Pt/C. The working electrode material of NiCoP

needed only 160 and 300 mV of additional potential to reach the worldwide accepted standard current value of 10 and 300 mA/cm² respectively. The calculated lower overpotential value of an electrocatalyst shows better HER performances than other HER-based transition metal electrocatalysts.^{31–34} Furthermore, a lower Tafel slope value accessed the rapid reaction kinetics to the NiCoP surface for HER. Figure 4.5b verified the Tafel plots for NiCoP and the auxiliary Pt/C, which observed the slope of 32 and 70 mV dec⁻¹. These values demonstrated a reaction path followed by binary NiCoP and Pt/C might be Volmer-Heyrovsky and Volmer-Tafel to execute the HER.^{25,35,36}

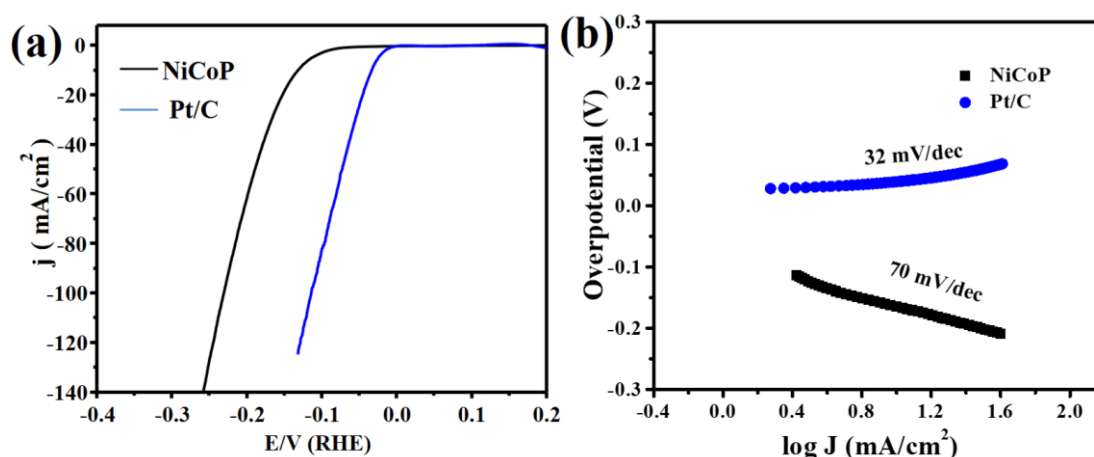


Figure 4.5 (a) Polarization curve, (b) is the Tafel plot for both NiCoP and precious Pt/C.

Electrochemical study of impedance spectrum (EIS), or Nyquist plots were observed in the varying frequency value of 1 MHz to 0.1 Hz in Figure 4.6a. The inset Figure 4.6a of EIS spectrum represented as the Randles circuit diagram, which denotes as series resistance (R_s), resistance due to charge transfer (R_{CT}), and double-layer capacitance (C_{dl}).^{37,38} the values of solution resistance and charge transfer resistance for NiCoP of 5.1 and 7.04 Ω are observed from the impedance spectrum. The above

investigation gives a clear picture of better HER kinetics and a good electron transport process of NiCoP surface. Moreover, the durability test of the electrode materials was studied under a chronopotentiometry technique, which analyzed the negligible increase of 15 mV overpotential even after 18 hours of constant electrolysis in Figure 4.6b. Before and after iR correction/compensation of LSV curves for NiCoP and Pt/C is presented in Figure 4.7.

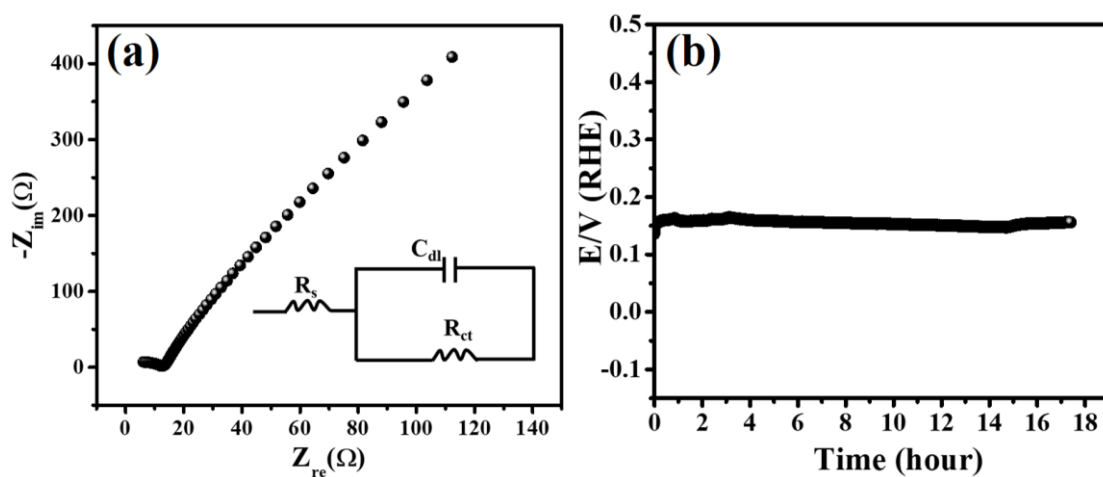


Figure 4.6 (a) Impedance diagram and (b) long cyclic test. The inset of (a) represents an equivalent circuit diagram.

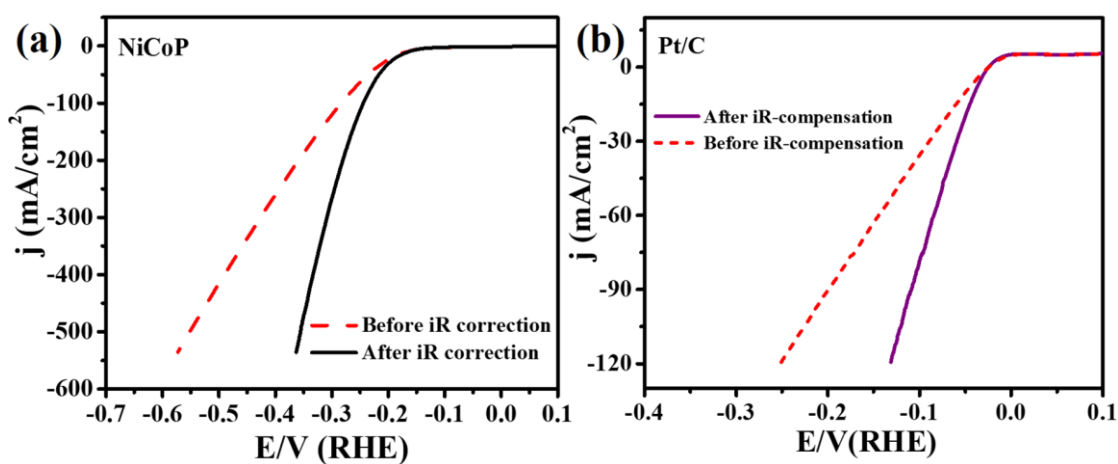


Figure 4.7 (a) Linear sweep voltammograms of NiCoP microspheres, (b) commercial Pt/C, before and after iR compensation.

The post stability measurements of the sample were done by PXRD and FESEM to verify the robustness and efficacy in Figure 4.8a and Figure 4.8b. No such phase transformation occurs in PXRD, and no morphological changes were observed after the constant long cycle electrolysis in an acidic medium that reveals the efficiency of electrode material. Table 4.1 shows the comparison table of the hydrogen evolution activity of the NiCoP with other reported electrocatalysts.

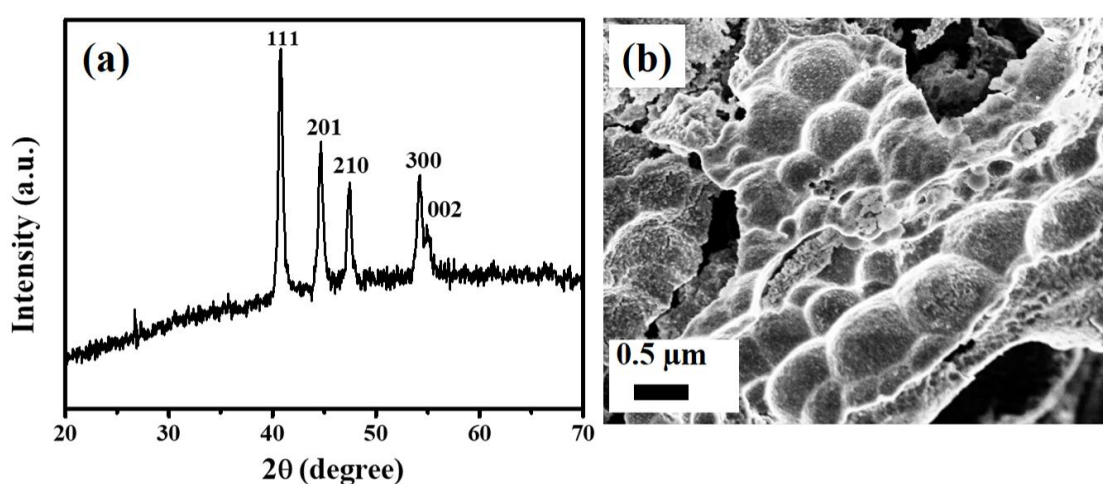


Figure 4.8 (a),(b) Powder pattern and FESEM pictures of NiCoP after 18 hours of constant stability test in an acidic solution at 10 mA/cm^2 .

Table 4.1 Comparison table for HER performance of different electrocatalysts.

Sample	Electrolyte H ₂ SO ₄ (M)	Over potential 10 mA/cm ² in (mV)	Tafel value in (mV/dec)	References
CoSe ₂ -160 microcubes	0.5	156	40	Inorg. Chem. 2020, 59 , 12778–12787
MOF derived CoSe ₂	0.5	195	43	Sustainable Energy Fuels, 2021, 5 , 4992
RGO/CoSe ₂ -180	0.5	172	35.2	Int. J. Hydrogen Energy, 2020, 45 , 1738-1747
CoSe ₂ @N/C-CNT	0.5	185	98	J. Colloid Interf. Sci. 2020, 566 , 296-303
FeP nanosheets	0.5	240	67	Chem. Commun., 2013, 49 , 6656–6658.
Ni ₁₂ P ₅ Spherical	0.5	175	69.9	CrystEngComm, 2019, 21 , 228–235.
NiCoP/NF	1 M KOH	85	46	Electrochim. Acta, 2019, 317 , 191–198.
NiCoP@FePx	0.5	96	50.16	ACS Sustain. Chem. Eng., 2018, 6 , 8847–8855.
Co doped VSe ₂	0.5	230	63.4	ACS Appl. Energy Mater. 2019, 2 , 644–653
NiCoP	0.5	160	70	This Work

The energy storage process about supercapacitors (SCs) measurements of a bimetallic phosphide material was performed in a biologic workstation of a three-electrode configuration. The electrolyte used for all the systematic measurements is 5 M KOH. However, the preparation of the working electrode for all the electrochemical studies was briefly described in the experimental section. Figure 4.9a presents the cyclic voltammograms curves of NiCoP electrode material at different scan values of (1, 2, 4, 8, 10, 20, 40, 80, 100 mV/s) respectively. The NiCoP sample displays two distinct

faradic peaks in the CV curves, which belong to the reversible change in the valence state of the Ni²⁺/Ni³⁺ and Co²⁺/Co³⁺. At higher scan rates, the polarization effects in measured CV curves occur due to the shifts of oxidation and reduction peaks towards more positive and negative potential within the potential window.³⁹⁻⁴¹ Galvanostatic charge-discharge process has been carried out at individual current density in Figure 4.9b. The value of specific capacitance (C_s) for this phosphide material was obtained from the recorded CV and GCD data using the equation as follows.^{30,41}

$$C_s = \frac{\int I dv}{2[mv(\Delta V)]} \quad (4.3)$$

$$C_s = \frac{I\Delta t}{m\Delta V} \quad (4.4)$$

Where $\int I dv$ the area of CV curve, m is the mass of sample used, v and ΔV are the various scan value and potential windows of the electrode material, respectively. In equation (4.4), the I term is used for applied current density and Δt gives discharge time. The obtained specific capacitance value at a current density of 1 A/g for NiCoP is 960 F/g. Moreover, the energy density (ED), and power density (PD), are the two key factors of a supercapacitor device investigating their energy storage and power delivered efficacy in practical application. Therefore by following the equation (4.5) and (4.6), the values of ED and PD were calculated.⁴¹

$$ED = \frac{C_s(\Delta V)^2}{2} \quad (4.5)$$

$$PD = \frac{C_s(\Delta V)v}{2} \quad (4.6)$$

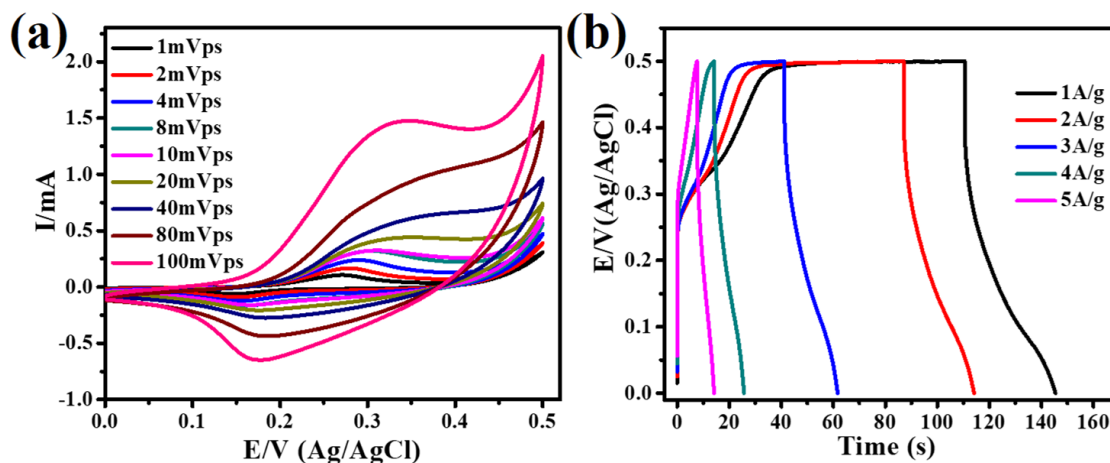


Figure 4.9 (a) CV cycles at different sweep rates, (b) CD plots at various applied current densities.

Figure 4.10a presents the Ragone plot of binary NiCoP, which gives the distinguishable value of energy density along with power density of 33.3 Wh kg^{-1} and 11.8 kW kg^{-1} , respectively. These observed values of specific capacitance (C_s) and energy with power density were much higher than other reported mono and binary metal phosphides. Particularly, Cheng groups reported Co_2P nanoflowers and nanorod types structured material with specific capacitance or energy storage values of 416 F g^{-1} and 284 F g^{-1} , respectively.⁴² Wang et al. investigated a two-step process for the design of Ni_2P and Ni_5P_4 electrode material with higher specific capacitance values.⁴³ Similarly, Yang and groups prepared bimetallic nickel-cobalt phosphides (NiCoP) and calculated the specific capacitance values of 646 F/g .⁴⁴ Table 4.2 displays the comparison of supercapacitor performance of as-synthesized NiCoP with other phosphide material. Figure 4.10b shows the cyclic stability of NiCoP in 5 M KOH of electrolyte solution. Its capacitance retention shows 95% of the initial value even after repeated 10000 charge-discharge cycles.

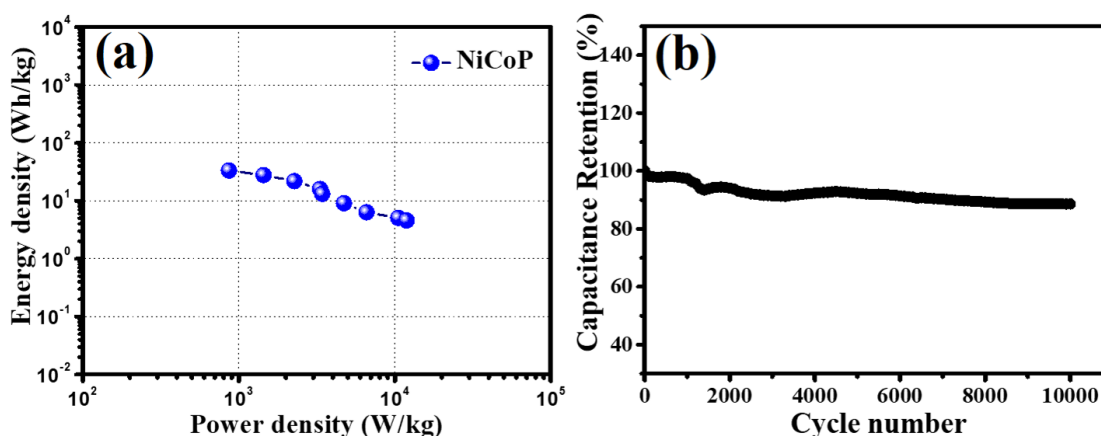
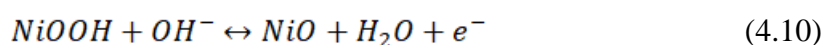
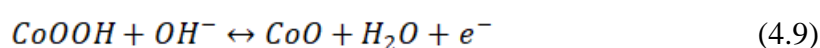
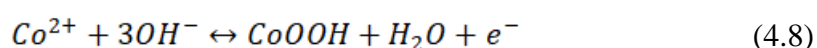
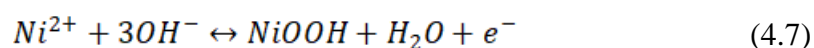


Figure 4.10 (a) Profile of Ragone plot for NiCoP and (b) durability test in 5 M KOH.

The sample of NiCoP was collected after the stability test and studied their further changes in phase purity and surface morphology by PXRD and FESEM analysis in Figure 4.11. In comparison, the post-stability analysis of the sample gives the actual catalytic active center of the electrode material. In the basic solution, the surface of the bimetallic NiCoP modified electrode material undergoes partial oxidation during the SCs measurements. Therefore NiCoP electrode materials are oxidized into the oxide or hydroxide intermediates of NiO, NiO(OH), CoO, respectively. The possible in-situ surface reaction mechanism in an alkaline solution is proposed and described. The active center of NiCoP is NiCoP/NiO, NiCoP/NiO(OH), and NiCoP/CoO or CoO(OH) by the following equations.⁴⁵⁻⁴⁷



The possible reaction mechanism of the post stability analysis indicates that NiCoP electrode surface getting oxidized into metal oxide or hydroxide in basic medium. The enhanced energy storage performances of the electrode material arise due to the combined effect of both phosphides and oxide or hydroxide electrode surfaces. In detail, the surface oxidation and reduction take place during the charging and discharging process, and the energy is stored because of the pseudocapacitive nature of the oxidized NiCoP surface. Scheme 1 displays the charging process in which oxidation of Ni^{2+} to Ni^{3+} or Co^{2+} to Co^{3+} and in discharging process reduction of metal cations occurs. These reactions occur on the oxidized surface in an alkaline medium, and the charge is stored efficiently.

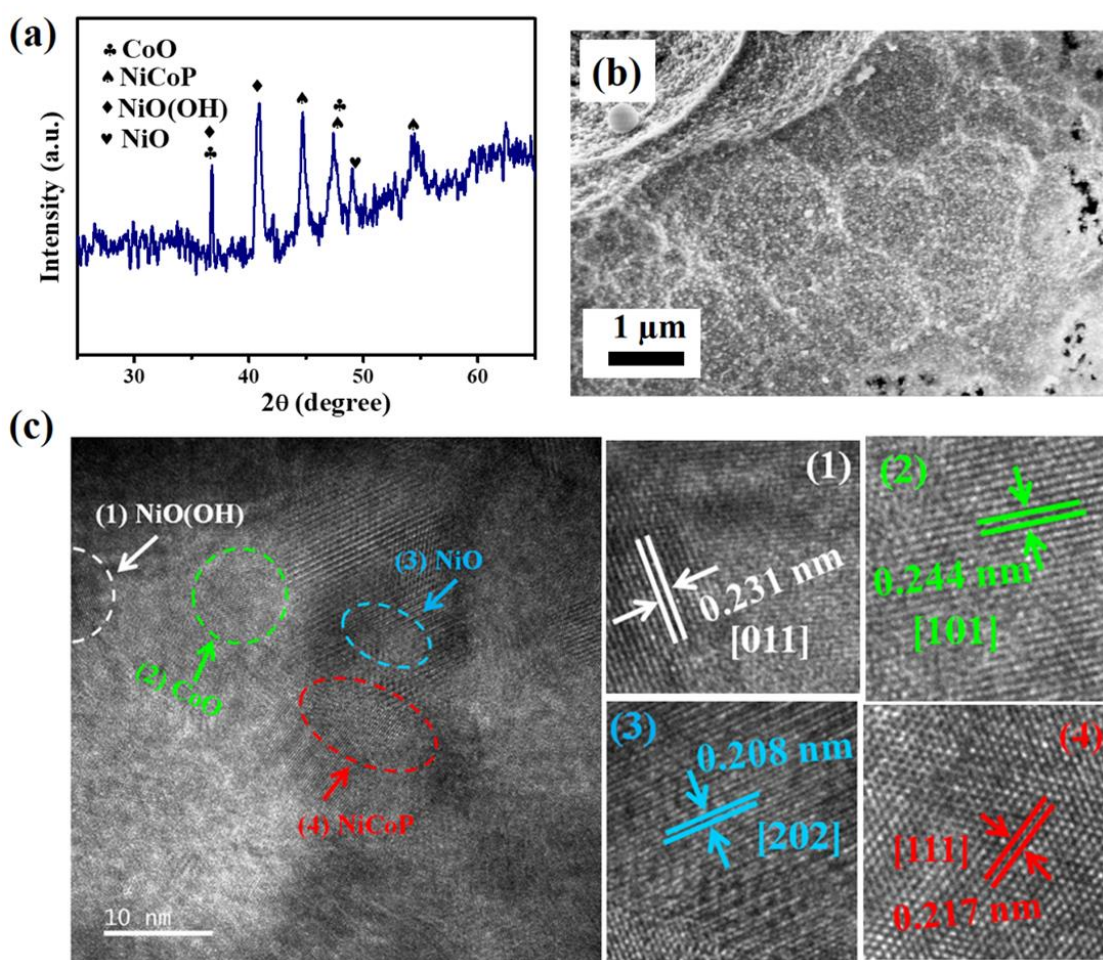
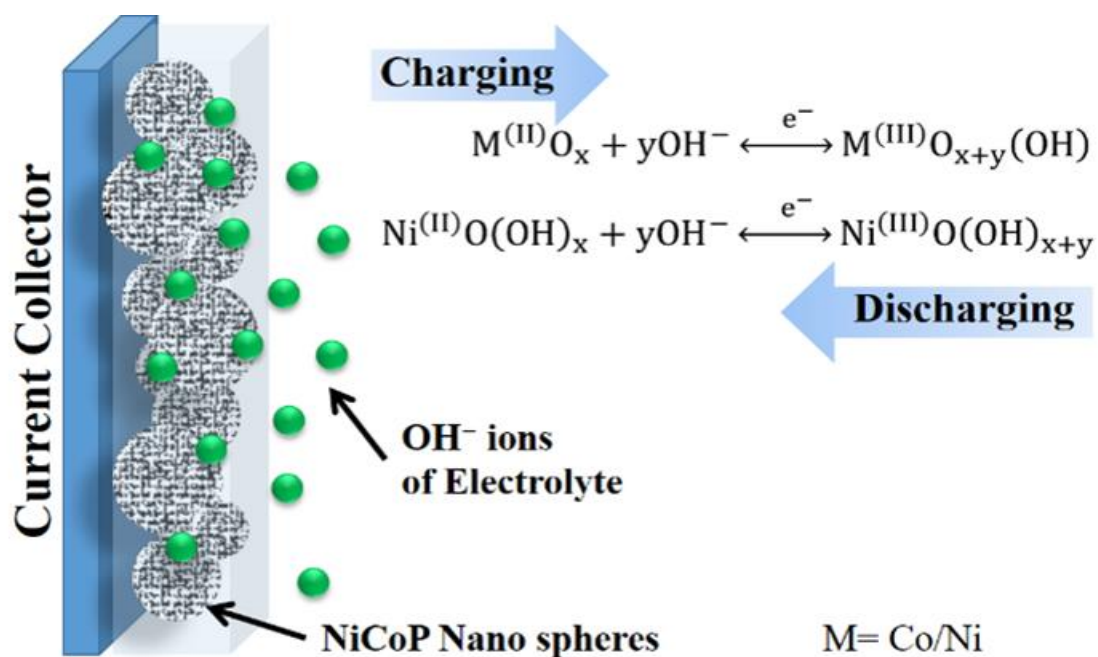


Figure 4.11 (a) X-ray diffraction pattern (b) FESEM study, with (c) HRTEM image of NiCoP microspheres after stability test in 5 M KOH electrolyte.



Scheme 1.1 Schematic diagram of surface oxidized NiCoP during electrochemical measurements towards SCs in 5 M KOH.

Table 4.2 Energy storage performance of NiCoP along with various transition metal phosphides.

Sample	Potential window	Specific capacitance (F/g)	References
Co ₂ P nanoflowers	0-0.5 V	416	Adv. Mater., 2017, 29 , 1605336.
NiCoP	0-0.6 V	653 C/g at 1A/g	Journal of Power Sources 467 (2020) 228324
Ni ₂ P nanorods	0- 0.475 V	799.2	Adv. Funct. Mater., 2012, 22 , 3927–3935.
Ni ₂ P@CNT	0-0.6 V	854	Front. Chem. Sci. Eng. 15 , 2021 1021–1032
Ni ₁₂ P ₅ hollow nanocapsules	0-0.55 V	949	Small, 2017, 13 , 1701530.
RuSe ₂ nanoparticles	0-1.0 V	100.8	Chem. Commun., 2019, 55 , 12320-12323
NiCoP nanoparticles	0.1-0.58 V	646	Adv. Mater., 2014, 26 , 6790–6797.
Ni-P microspheres@MnO ₂	0–0.35 V	1130	Angew. Chemie Int. Ed., 2014, 53 , 9352–9355.
Ni ₅ P ₄ particles	0-0.4 V	801.5	Adv. Energy Mater., 2014, 4 , 1300816.
Mn ₂ O ₃ @MnO ₂	0-1.0 V	225	ACS Appl. Energy Mater. 2020, 3 , 8190–8197
NiCoP hollow sphere	0-0.5 V	960	This Work

4.8 Conclusions

In conclusion, a 3D hollow sphere of NiCoP has been developed in a simple hydrothermal method, and all the systematic characterization techniques were observed a high crystalline nature of 3D sphere-like morphology and high phase purity. However, the use of NiCoP as a cathode electrode material shows enhanced

hydrogen evolution with low overpotential (160 mV at 10 mA/cm²) and a Tafel slope (70 mV dec⁻¹) which displays the Volmer-Heyrovsky reaction mechanism path followed for hydrogen evolution. Additionally, the energy storage performances of NiCoP achieved an excellent specific capacitance or energy value of 960 F/g at a particular current density of 1 A/g, obtained energy density of 33.3 Wh kg⁻¹, and the power supply capability of 11.8 kW kg⁻¹, respectively. Further, it exhibits a robust cyclic stability test during the electrolysis process. A small overpotential increase of 15 mV in HER even after 18 hours of constant electrolysis and the initial capacitance retained ~95% after a repeated 10000 charge-discharge cycle. The above study suggests that NiCoP nanostructures have excellent potential in electrocatalysis and energy storage, creating such a platform to prepare efficient electrode material in future research.

4.9 References

- 1 T. E. Mallouk, *Nat. Chem.*, 2013, **5**, 362–363.
- 2 M. Jefferson, *Handb. Energy Clim. Chang.*, 2013, 254–269.
- 3 K. Mazloomi and C. Gomes, *Renew. Sustain. Energy Rev.*, 2012, **16**, 3024–3033.
- 4 X. Zou and Y. Zhang, *Chem. Soc. Rev.*, 2015, **44**, 5148–5180.
- 5 R. Chen, C. Yang, W. Cai, H. Y. Wang, J. Miao, L. Zhang, S. Chen and B. Liu, *ACS Energy Lett.*, 2017, **2**, 1070–1075.
- 6 K. Li, Y. Li, Y. Wang, J. Ge, C. Liu and W. Xing, *Energy Environ. Sci.*, 2018, **11**, 1232–1239.
- 7 S. Ratha, A. K. Samantara, K. K. Singha, A. S. Gangan, B. Chakraborty, B. K.

- Jena and C. S. Rout, *ACS Appl. Mater. Interfaces*, 2017, **9**, 9640–9653.
- 8 A. Hasani, M. Tekalgne, Q. Van Le, H. W. Jang and S. Y. Kim, *J. Mater. Chem. A*, 2019, **7**, 430–454.
- 9 W. F. Chen, J. T. Muckerman and E. Fujita, *Chem. Commun.*, 2013, **49**, 8896–8909.
- 10 L. Yu, S. Song, B. McElhenny, F. Ding, D. Luo, Y. Yu, S. Chen and Z. Ren, *J. Mater. Chem. A*, 2019, **7**, 19728–19732.
- 11 J. K. Das, A. K. Samantara, A. K. Nayak, D. Pradhan and J. N. Behera, *Dalton Trans.*, 2018, **47**, 13792–13799.
- 12 J. Shi, J. Hu, Y. Luo, X. Sun and A. M. Asiri, *Catal. Sci. Technol.*, 2015, **5**, 4954–4958.
- 13 Y. Wang, B. Kong, D. Zhao, H. Wang and C. Selomulya, *Nano Today*, 2017, **15**, 26–55.
- 14 C. Ray, S. C. Lee, B. Jin, A. Kundu, J. H. Park and S. C. Jun, *ACS Sustain. Chem. Eng.*, 2018, **6**, 6146–6156.
- 15 C. Du, L. Yang, F. Yang, G. Cheng and W. Luo, *ACS Catal.*, 2017, **7**, 4131–4137.
- 16 A. Dutta, A. K. Samantara, S. K. Dutta, B. K. Jena and N. Pradhan, *ACS Energy Lett.*, 2016, **1**, 169–174.
- 17 X. Zhang, X. Yu, L. Zhang, F. Zhou, Y. Liang and R. Wang, *Adv. Funct. Mater.*, 2018, **28**, 1–8.
- 18 P. Jiang, Q. Liu and X. Sun, *Nanoscale*, 2014, **6**, 13440–13445.
- 19 M. Pi, T. Wu, D. Zhang, S. Chen and S. Wang, *Nanoscale*, 2016, **8**, 19779–19786.

- 20 J. Masud, S. Umapathi, N. Ashokaan and M. Nath, *J. Mater. Chem. A*, 2016, **4**, 9750–9754.
- 21 J. Mu, J. Li, E. C. Yang and X. J. Zhao, *ACS Appl. Energy Mater.*, 2018, **1**, 3742–3751.
- 22 B. Ma, Z. Yang, Y. Chen and Z. Yuan, *Nano Res.*, 2019, **12**, 375–380.
- 23 Z. Yin, C. Zhu, C. Li, S. Zhang, X. Zhang and Y. Chen, *Nanoscale*, 2016, **8**, 19129–19138.
- 24 P. Simon, Y. Gogotsi and B. Dunn, *Science (80-.)*, 2014, **343**, 1210–1211.
- 25 A. K. Samantara and S. Ratha, *Materials Development for Active/Passive Components of a Supercapacitor: Background, Present Status and Future Perspective*, 2017.
- 26 N. S. A. Manaf, M. S. A. Bistamam and M. A. Azam, *ECS J. Solid State Sci. Technol.*, 2013, **2**, M3101–M3119.
- 27 X. Zhang, A. Wu, X. Wang, C. Tian, R. An and H. Fu, *J. Mater. Chem. A*, 2018, **6**, 17905–17914.
- 28 Y. Lan, H. Zhao, Y. Zong, X. Li, Y. Sun, J. Feng, Y. Wang, X. Zheng and Y. Du, *Nanoscale*, 2018, **10**, 11775–11781.
- 29 R. K. Tripathy, A. K. Samantara and J. N. Behera, *Dalton Trans.*, 2019, **48**, 10557–10564.
- 30 A. K. Samantara, S. Kamila, A. Ghosh and B. K. Jena, *Electrochim. Acta*, 2018, **263**, 147–157.
- 31 Q. Liu, J. Tian, W. Cui, P. Jiang, N. Cheng, A. M. Asiri and X. Sun, *Angew. Chemie - Int. Ed.*, 2014, **53**, 6710–6714.
- 32 A. Lu, Y. Chen, H. Li, A. Dowd, M. B. Cortie, Q. Xie, H. Guo, Q. Qi and D. L.

- Peng, *Int. J. Hydrogen Energy*, 2014, **39**, 18919–18928.
- 33 J. Lin, Z. Peng, G. Wang, D. Zakhidov, E. Larios, M. J. Yacaman and J. M. Tour, *Adv. Energy Mater.*, 2014, **4**, 1–7.
- 34 Y. Xu, R. Wu, J. Zhang, Y. Shi and B. Zhang, *Chem. Commun.*, 2013, **49**, 6656–6658.
- 35 S. Anantharaj, S. R. Ede, K. Sakthikumar, K. Karthick, S. Mishra and S. Kundu, *ACS Catal.*, 2016, **6**, 8069–8097.
- 36 B. E. Conway and B. V. Tilak, *Electrochim. Acta*, 2002, **47**, 3571–3594.
- 37 Y. Zhang, B. Ouyang, J. Xu, S. Chen, R. S. Rawat and H. J. Fan, *Adv. Energy Mater.*, 2016, **6**, 1–6.
- 38 D. Hou, W. Zhou, X. Liu, K. Zhou, J. Xie, G. Li and S. Chen, *Electrochim. Acta*, 2015, **166**, 26–31.
- 39 T. Dang, L. Wang, D. Wei, G. Zhang, Q. Li, X. Zhang, Z. Cao, G. Zhang and H. Duan, *Electrochim. Acta*, 2019, **299**, 346–356.
- 40 J. Park, T. H. Ko, S. Balasubramaniam, M. K. Seo, M. S. Khil, H. Y. Kim and B. S. Kim, *Ceram. Int.*, 2019, **45**, 13099–13111.
- 41 J. K. Das, A. K. Samantara, S. R. K. A., C. S. Rout and J. N. Behera, *Dalton Trans.*, 2019, **48**, 15955–15961.
- 42 X. Chen, M. Cheng, D. Chen and R. Wang, *ACS Appl. Mater. Interfaces*, 2016, **8**, 3892–3900.
- 43 D. Wang, L. Bin Kong, M. C. Liu, Y. C. Luo and L. Kang, *Chem. - A Eur. J.*, 2015, **21**, 17897–17903.
- 44 C. Wang, Y. Qian, J. Yang, S. Xing, X. Ding and Q. Yang, *RSC Adv.*, 2017, **7**, 26120–26124.

- 45 A. Gopalakrishnan, D. Yang, J. C. Ince, Y. B. Truong, A. Yu and S. Badhulika, *J. Energy Storage*, 2019, **25**, 100893.
- 46 R. Ding, X. Li, W. Shi, Q. Xu and E. Liu, *Chem. Eng. J.*, 2017, **320**, 376–388.
- 47 W. Wei, L. Mi, Y. Gao, Z. Zheng, W. Chen and X. Guan, *Chem. Mater.*, 2014, **26**, 3418–3426.

Summary of Chapter-4

